# Studies on Coherent Population Trapping Resonance in Rubidium for Application in Atomic Clocks and Timekeeping Methodology for Satellite Navigation

**THESIS**

Submitted in partial fulfillment of the requirements for the award of the degree of

**DOCTOR OF PHILOSOPHY**


By

**Mr. Kaitha Rajaiah**

(Roll No: 717054)

**Supervisors:**

Prof. T. Venkatappa Rao (NITW)

Dr. Prashanth C Upadhya (ISRO)

**DEPARTMENT OF PHYSICS**

**NATIONAL INSTITUTE OF TECHNOLOGY**

**WARANGAL-506004, TELANGANA, INDIA**


**2024**

# Abstract

Atomic clocks with superior frequency accuracy and stability are essential for timekeeping applications. The application of clocks in satellite navigation demands the accurate predictability of clock behaviour and their utility in space necessitates miniaturization. Coherent population trapping (CPT) is a promising technique for developing miniaturized atomic clocks. Two main objectives are pursued in this thesis. The first objective is to investigate the characteristics of CPT resonance and derive optimum operating parameters as well as system configuration for improved frequency stability of CPT based atomic clock. The second one is the real-time characterization of on-board clock behaviour and development of optimum timekeeping methodology to ensure uninterrupted navigation service to the user.

An experimental investigation is carried out to study and optimize CPT resonance characteristics (quality figure and frequency shift) with respect to critical parameters such as dimension of Rubidium vapor cell, laser intensity, cell temperature, Radio Frequency (RF) power, buffer gas species and pressure inside the vapor cell. A theoretical model based on four-level atomic system is developed to understand the laser-atom dynamics that governs the CPT phenomena in alkali atoms. A new empirical parameter is introduced in the model to account for the influence of cell size on resonance characteristics. Designed and implemented a methodology to solve the differential equation governing four level atomic system through the utilization of Runge-Kutta $4^{th}$ order numerical integration method. Theoretical computation of quality figure is carried out for cells with different dimensions, buffer gas pressures, temperatures and compared with the experimental results. The outcome of this study helped in deriving optimum operating parameters and system configuration in order to achieve enhanced frequency stability of CPT based atomic clocks.

The performance of atomic clocks used in navigation satellites plays a crucial role in providing the desired position accuracy for navigation users. Continuous monitoring and real-time characterization of these clocks are necessary to provide uninterrupted navigation service to the users. In this regard, designed and developed a scheme for characterization and continuous monitoring of on-board clocks using one-way carrier phase measurements to sensitively detect the on-board clock anomalies. Devised and developed a single algorithm that detects anomalies present in the clock data. The characterization scheme developed in this study enables the timely generation and up-linking of clock correction parameters to ensure the user position accuracy within the specification.

In each navigation satellite, satellite clock offset is allowed to accumulate only up to the pre-allocated broadcast limit beyond which the range measurements are unreliable owing to significant error in user position. Hence, the clock offset needs to be maintained within the given broadcast limit, which is referred to as satellite timekeeping. A timekeeping methodology is established to maintain the satellite time optimally within the allocated broadcast limit. New mathematical model is derived to compute optimal frequency offset correction that provides maximum time interval between the two successive corrections to maintain the satellite clock offset always within the broadcast limit. The developed methodology facilitates the seamless navigation service to the user.

# Acknowledgement

I am extremely thankful to all the people who helped me during my journey in pursuing PhD.

Firstly, I am grateful to my supervisor Prof. Venkatappa Rao T for his firm support, guidance, continuous encouragement and cooperation throughout my PhD.

I would like to express my sincere gratitude to my supervisor Dr. Prashant C Upadhya who guided and supported me throughout my PhD. His comprehensive feedback, motivation and insightful perspectives are very precious and helped me a lot at each and every step of my research work.

I extend my appreciation to Mrs. Pragya Tiwari for her dedicated efforts and time in establishment of the experimental setup in the Laboratory. I am thankful to Mrs. Manjula R for her support during my work. I am also thankful to Mrs. Minni J Kappen, Dr. Praveen K C, and Mr. Rajendra for their support in performing the experiments during my research.

My sincere acknowledgment extends to members of the clock development team and management at Laboratory for Electro Optics Systems, ISRO, Bangalore, India.

My sincere appreciation also extends to Dr. Pradhan S, Bhabha Atomic Research Centre Facility, Visakhapatnam, for his support in technical discussions.

I would like to express my sincere appreciation to Mrs. Nirmala S for her encouragement, continuous support and guidance throughout my PhD. Further, I extend my gratitude to Mr. Manmohan V Kamat for supporting in technical aspects during my work.

I extend my sincere acknowledgement to Mr. Kartik A and Mr. Hemanth Kumar Reddy N for their continuous support during the course of my work.

My thankfulness also extends to all my colleagues at Space Navigation Group, U R Rao Satellite Centre, ISRO, Bangalore, India for their support.

I am grateful to Indian Space Research Organization for providing facilities to carry out this work.

My sincere acknowledgement extends to the Head, Dept. of Physics, Chairman of Doctoral Scrutiny Committee (DSC), and DSC members Prof. Dinakar D, Prof. Abdul Azeem P and Prof. Venugopal A for their valuable suggestions and evaluation of my research work.

I would like to express my sincere appreciation to all the faculty members, Dept. of Physics, NIT Warangal, Telangana, India for their support.

I extend my appreciation to Dr. Jayarambabu N for his support. I am thankful to all research scholars, Dept. of Physics, NIT Warangal for their support. I also extend my acknowledgement to administrative staff, NIT Warangal.

Finally, I extend my gratitude to my family for their support, patience and sacrifices in completing my research work.

# Contents

# List of Figures

# List of Tables

# Chapter-1

# Precision Timekeeping and Satellite Navigation

Time is an integral part of daily life, which enables the systematic execution of activities falling in the interval from nanoseconds to years. Time is one of the fundamental physical quantities, with second as the S.I. unit. In general, the time is realized by counting the systematic oscillations. A clock is a device that counts these oscillations and displays the time. Figure 1.1 shows the typical mechanism of a clock. In a clock, an oscillator, known as resonator which is driven by an energy source, undergoes periodic motion that nearly repeats at a constant rate. The time interval between two successive oscillations is known as the time period. The number of oscillations made by the resonator in one second is known as the resonance frequency ($\nu_0$) of oscillator. The counter increments time based on the cumulative number of oscillations. However, the time provided by a clock purely depends on the consistency of oscillator's frequency, i.e., ability to produce the same number of oscillations per unit time over a prolonged interval which is termed as stability of the oscillator.

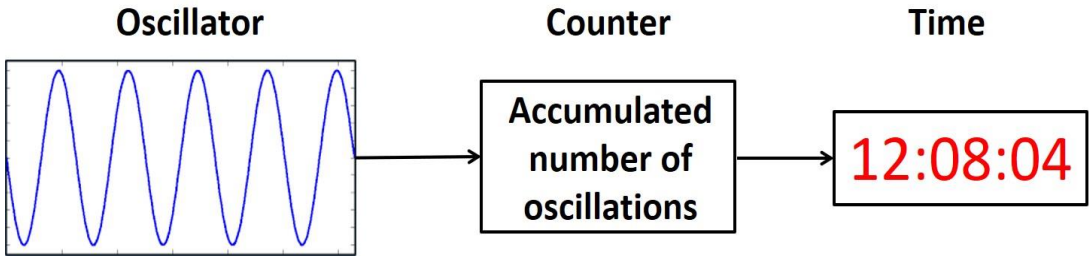


Figure 1.1: Basic block diagram of a clock containing an oscillator, counter and display of time.

A reliable and stable clock can be realized by designing a system whose frequency of oscillation is not perturbed by environmental as well as operating conditions [1]. Depending on the type of frequency source, the clocks can be categorized as natural clocks and man-made clocks.

## 1.1 Evolution of timekeeping methods

In nature, there are different types of oscillators that produce periodic motions which we observe daily - for example, the movements of the Sun, Moon, and Stars. The Earth's rotation around its axis provides the measurement of day, and its revolution around the Sun provides year. Similarly, the revolution of moon around the Earth provides measurement of month. The earliest device (around 3000 B.C.) to measure the time was based on a shadow clock where the shadow of a vertical straight pole (called a *gnomon*) changes with the movement of Sun from sunrise to sunset and repeats daily, later developed as sundial [2], [3]. In a sundial, a vertical pole is fixed on a horizontal plane where the different sub-divisions of the day are marked. However, sundials cannot be used in the absence of Sun, i.e., during nights and cloudy weather.

Egyptians developed water clocks in 2000 B.C., the earliest non-astronomical devices. The water clock measures the time based on water level in a conical stone vessel containing a small hole through which water escapes slowly. The side of the vessel is marked with a uniform scale. The assumption made for using water clocks was that the water flow rate is constant. However, this flow rate depends on pressure and the viscosity of water, which changes with depth and temperature, respectively [3], [4]. Over time, some improvements were made to the design of water clocks to improve the accuracy. Since the time measured using water clock is not absolute, it had to be calibrated with time based on astronomical observations. Another device based on material flow through a small hole is the hourglass, where sand is used as flow material. Hourglasses were mainly used to determine a fixed interval of time.

The pendulum clock was invented in 1656 by Huygens, where time is measured based on oscillations made by a pendulum. The pendulum is a pivoted or suspended object via a string that swings freely. The pendulum clock cannot be used as a reliable time reference because its time period of oscillation depends on gravity, which varies with location on Earth. The time period of oscillations of the pendulum also depends on air resistance (drag) which in turn depends on atmospheric pressure. The performance of the pendulum clock was further improved with the modified design containing an anchor escapement [4]. The pendulum clock was an accurate time-keeping device until the development of crystal oscillator based clock in 1927.

A significant improvement in time measurement with accurate frequency was realized with the invention of quartz crystal oscillator. Quartz is a crystal that has excellent elastic properties with low internal friction. It exhibits a piezoelectric effect in which a pressure applied along a particular direction produces electric polarization proportional to the applied pressure. Thus,

the mechanical vibrations in the crystal produce an oscillating current. Similarly, if the crystal is placed between two metallic plates carrying opposite charges, it undergoes mechanical vibrations. This effect is used to generate oscillations required to measure time by applying an alternate voltage to the metal plates [4].

The frequency of oscillations produced by a quartz crystal depends on various factors such as its dimension, type of cut and environmental conditions, in particular the temperature. The effect of temperature can be reduced by compensating temperature sensitivity, called a temperature-compensated crystal oscillator (TCXO). Further improvement in frequency accuracy was achieved by using an oven-controlled crystal oscillator (OCXO), which is operated in an oven by keeping the temperature constant with a thermostat [1]. The frequency generated by quartz crystal changes over time due to ageing, which is referred to as drift. Thus, the frequency of crystal oscillator varies with environmental conditions as well ageing.

## 1.2 Timekeeping using atoms

It was essential to find a suitable oscillator whose frequency is not influenced by external factors. In this regard, the frequency related to the energy difference between two quantum states in an atom is considered as an ideal choice of reference. The influence of external parameters on the quartz oscillator can be controlled by stabilizing its frequency using the electromagnetic transitions in the free atoms, ions or molecules. These free atoms are also called quantum oscillators, where the electromagnetic transitions occur at well-defined frequencies specific to each species.

The following are the advantages of oscillators derived from atomic resonant transitions. An unperturbed atomic transition is identical among all the atoms of same species. Unlike other electrical or mechanical oscillators, atoms do not degrade over time. In contrast to quartz oscillators, atoms do not change their properties over time.

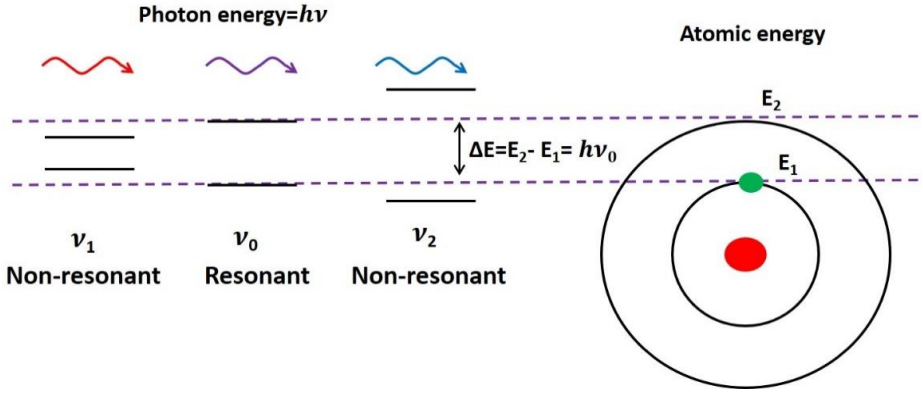


Figure 1.2: Atomic transition energy in discrete form. $E_1$ and $E_2$ are the energies corresponding to initial and final states of electron, respectively.

According to the quantum mechanics established at the beginning of the 20th century, the electron can transfer from one state to another by absorbing or emitting a photon. The energy of this photon is equal to the difference between the energies of initial and final states, i.e., $\Delta E=E_2-E_1$. Here, $E_1$ and $E_2$ are the energies corresponding to the initial and final states. The electron can take the energies only in discrete values. As a result, atoms can absorb or emit a particular electromagnetic wave of frequency $v_0=(E_2-E_1)/h$, referred to as the resonance frequency of transition, as shown in Figure 1.2. Using this atomic transition frequency as a reference, the crystal oscillator can be tuned to provide a stable output frequency. Thus, the realization of a stable clock is made possible by a unique frequency of electromagnetic (EM) waves that are absorbed or emitted by the atom.

### 1.2.1 Principle of atomic clock

Atomic clock is an atomic system that provides a stable output frequency generated by a quartz crystal oscillator, such as TCXO or OCXO, which is locked to an atomic transition frequency, as shown in Figure 1.3.

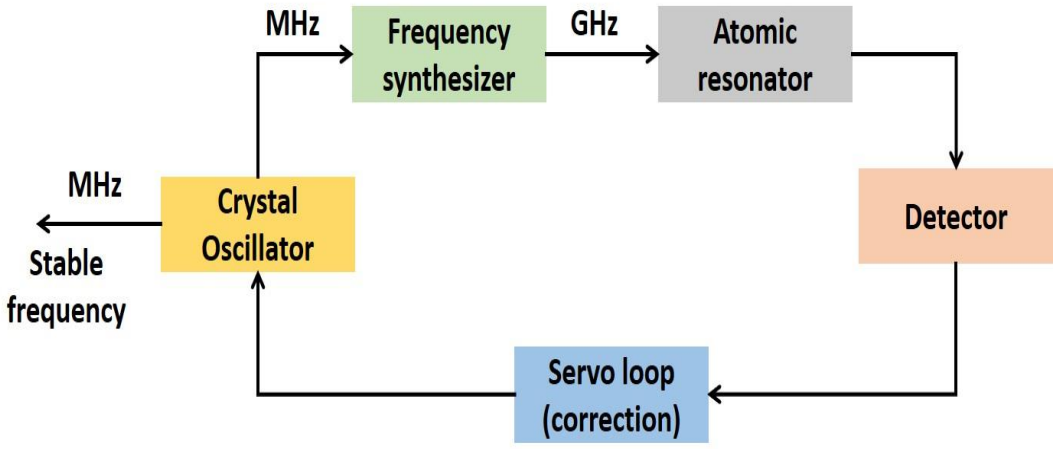


Figure 1.3: Basic block diagram of an atomic clock. Output frequency of oscillator is stabilized by locking it to stable reference frequency of atomic resonator.

The frequency of the crystal oscillator is in MHz (typically 10 MHz), which is converted into the microwave frequency that corresponds to chosen atomic transition using a frequency synthesizer. If this microwave frequency matches with the frequency of atomic resonance, the detector experiences maximum change in its response with respect to the background. Any deviation in crystal oscillator frequency with respect to atomic resonance is derived from the

detector response. This deviation serves as a correction signal that is applied to crystal oscillator in a feedback loop to control its frequency. Thus, in atomic clock, the crystal oscillator is locked to the atomic resonance to produce stable output frequency. The evolution of the clocks with accuracy per day is represented in Figure 1.4.

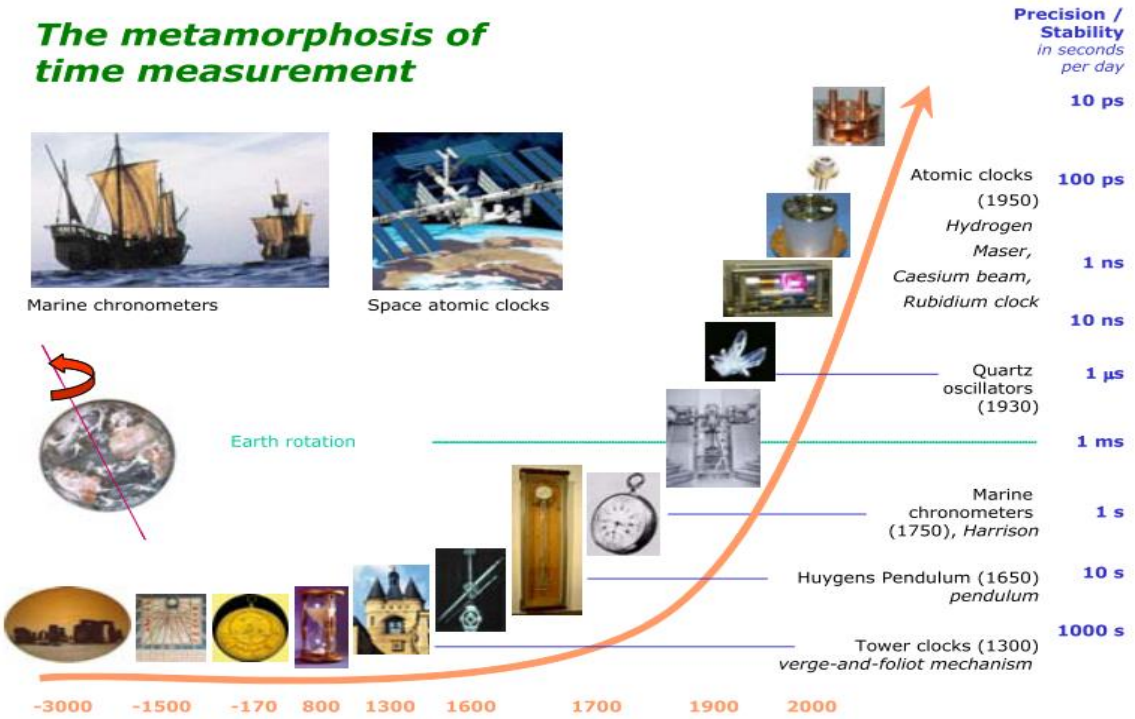


Figure 1.4: The evolution of clocks and corresponding accuracy per day [5].

## 1.2.2 Atomic clocks in satellite navigation

Satellite navigation is a system that provides user with position and timing information derived from signals transmitted by the satellites. In order to provide accurate and reliable navigation service, satellites require precision timekeeping systems such as atomic clocks. However, space application requires robust, compact, and low power atomic clocks. In addition, these clocks are required to sustain with initial launch vehicle and harsh space environment. Atomic clocks based on Cesium (Cs), Hydrogen (H) and Rubidium (Rb) atoms are well suited for space application and are the most commonly used timekeeping solutions in navigation satellites. The following section discusses the working principle of these three types of atomic clocks.

### 1.2.2.1 Cs beam clock

The schematic of the working principle of Cs beam atomic clock is shown in Figure 1.5b. Hyperfine splitting frequency of 9192631770 Hz between $F$=3 and $F$=4 states is used as clock

reference (Figure 1.5a). A few grams of Cs are filled in an oven. The Cs atoms emerge from the oven, which is heated up to a temperature of ~100 $^0$C or above. In the thermal beam, the Cs atoms are equally populated in states $F$=3 and $F$=4. The working principle of Cs beam clock can be explained in three steps as follows. The first step is the state selection process where the Cs atoms pass through a strong inhomogeneous magnetic field (magnet-A in Figure 1.5b). This magnetic field deflects the atoms in $F$=4 state due to the interaction between the magnetic field and the magnetic moment of Cs atoms. Thus, it selects the atoms in the remaining state ($F$=3) in the beam, called as state selection magnet or polarizer. The second step is the interaction process, wherein the Cs atoms pass through the microwave cavity which is also known as the Ramsey cavity. A radio frequency close to the Cs atomic resonance that derived from an OCXO as shown in Figure 1.5b is coupled to this microwave cavity.

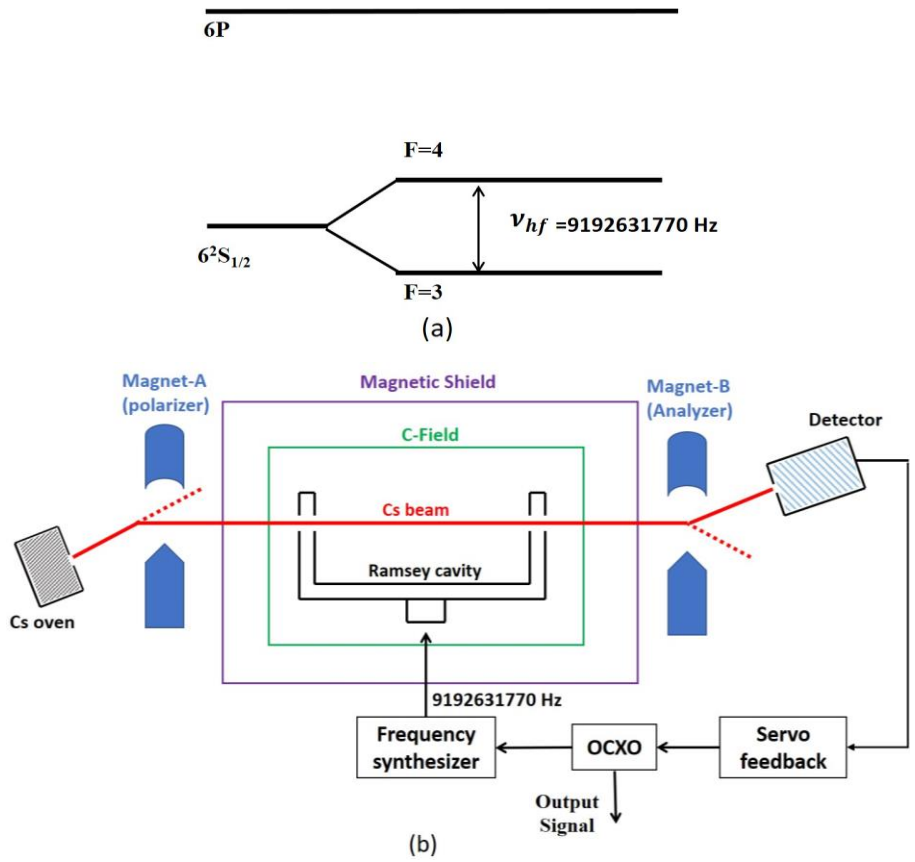


Figure 1.5: (a) Hyperfine ground state energy level diagram of Cs atoms. (b) Simplified layout of Cs beam atomic clock. Atomic state selection is done by strong inhomogeneous magnetic field. Source: [6].

When the frequency coupled to this cavity matches with the hyperfine ground state transition frequency of Cs atoms (resonance frequency), their energy state changes from $F$=3

to $F$=4. In the third step, a second state selection magnet (magnet-B) also known as an analyzer, deflects the atoms that have changed their state and directs them to a hot-wire detector that produces current in the external circuit. Any deviation in the coupled frequency would place the Cs atoms in some other magnetic energy state allowing them to be routed away from the detector. Based on the number of atoms reaching the detector and subsequent current generated, a servo feedback is provided to the OCXO to tune its output frequency so as to maximize the number of atoms detected. Thus, it is a continuous process that controls OCXO with respect to transition frequency of Cs atoms and ensures a stable output frequency.

### 1.2.2.2 Hydrogen maser

The hydrogen maser is based on a phenomenon known as MASER (Microwave Amplification by Stimulated Emission of Radiation). The hydrogen maser utilizes the atomic transition between two hyperfine ground states of atomic hydrogen, i.e. ($F$=0, $m_F$=0) and ($F$=1, $m_F$=0) as shown in Fig 1.6a. The frequency corresponding to this atomic transition is 1.420405752 GHz. Two types of hydrogen masers exist, namely active hydrogen maser and passive hydrogen maser. In an active hydrogen maser, the cavity oscillates at the atomic resonance frequency to provide active signal output. In contrast, the cavity in a passive hydrogen maser is stimulated passively by electromagnetic energy at atomic resonance in a manner similar to that described in Cs beam atomic frequency standards.

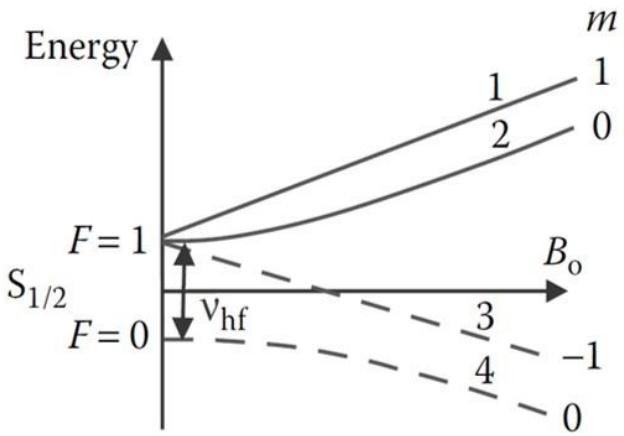


(a)

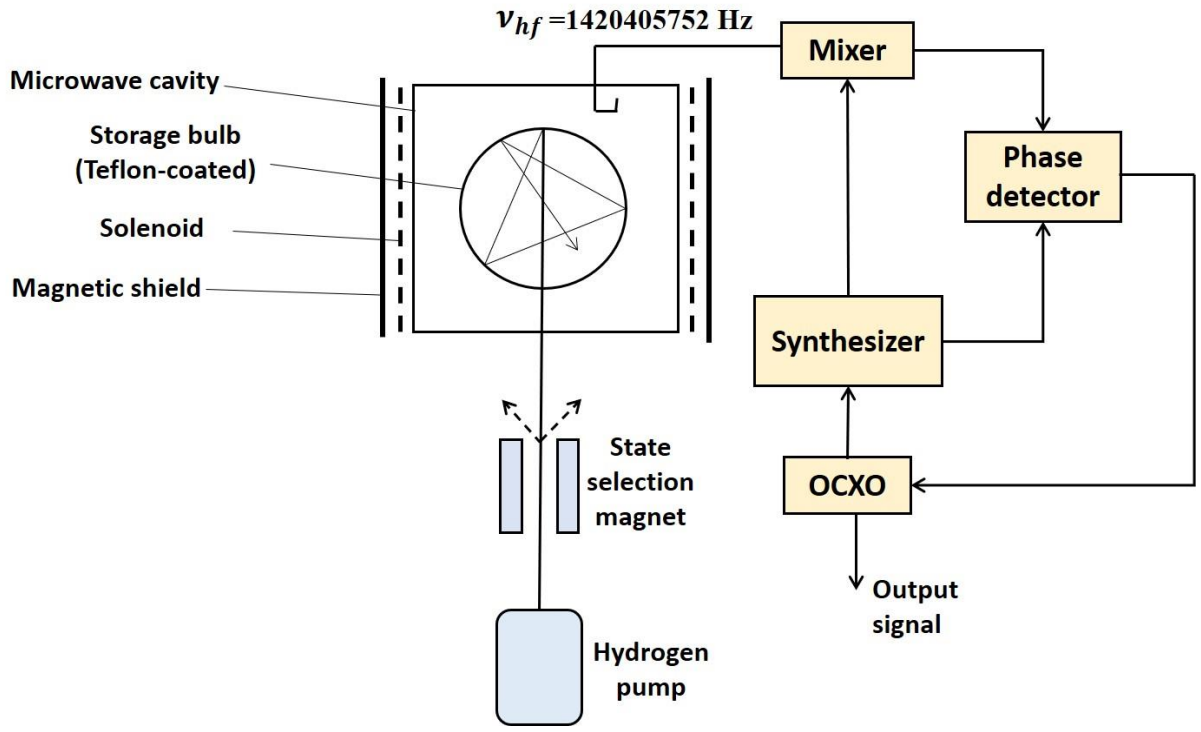


(b)

Figure 1.6: (a) Hyperfine ground state energy levels of atomic hydrogen. (b) Simplified layout of active hydrogen maser. Source: [7].

## Active hydrogen maser

As shown in Figure 1.6b, the molecular hydrogen in the hydrogen pump is dissociated into atomic hydrogen using RF discharge. These atoms are collimated into a beam and then guided through an inhomogeneous magnetic field. Due to the applied magnetic field, the higher hyperfine ground state atoms are directed into a storage bulb, which is placed in a microwave resonator. The storage bulb is coated with Teflon to prevent atomic collisions with bulb walls.

In the storage bulb, a few atoms drop to a lower energy level and release the photons with electromagnetic energy corresponding to atomic transition. These photons stimulate other atoms to de-excite to their lower energy level by releasing more photons. As a result of this repeated process, a self-sustaining microwave field is created in the cavity resonator. The quality factor (Q) of cavity resonator is crucial in self-sustaining these active oscillations. The 'Q' must have fairly high value in order to sustain a sufficiently large RF field to stimulate the atoms and sustain active oscillations. A small portion of the cavity resonator energy is partly dissipated into the cavity walls and partly given to the external circuit via the pickup coil. The loss in this microwave field is compensated with the incoming hydrogen atoms. The signal from the pickup coil is mixed and compared with the atomic resonance signal generated by

OCXO via the synthesizer. The error signal between the cavity signal (extracted through pickup coil) and OCXO signal is used as feedback to control the output frequency of OCXO.

### Passive hydrogen maser

The size of hydrogen maser is limited by size of cavity resonator. Cavity resonator size can be reduced by filling it with a dielectric material. However, cavity 'Q' will be lower and beneath the self-oscillating limit due to the presence of dielectric material. Thus, the cavity loaded with dielectric material does not support self-sustained oscillations. In such a case, the hydrogen maser operates in a passive mode, utilizing two coupling loops for energy transfer. Microwave energy generated by OCXO, corresponding to the atomic transition is provided to the cavity from one loop, which enables the stimulated emission from the hydrogen atoms in the cavity. The second coupling loop is used to detect the amplified signal within the cavity. The error signal between these two signals is employed to stabilize the OCXO output signal (frequency).

## 1.2.2.3 Rb atomic clock

Rubidium vapor cell clocks are the most commonly used commercial atomic clocks. Double Resonance (DR) based rubidium clock is the first atomic clock used in satellites [8]. The hyperfine ground states used for atomic transition in $^{87}$Rb are $F$=1 and $F$=2, with the corresponding transition frequency of 6.834682608 GHz as shown in Figure 1.7b. Coincidently, the frequency corresponding to transition from excited state to hyperfine ground state $F$=3 in $Rb^{85}$ is approximately same as that of $F$=2 level in $Rb^{87}$ (see dotted lines in Figure 1.7).

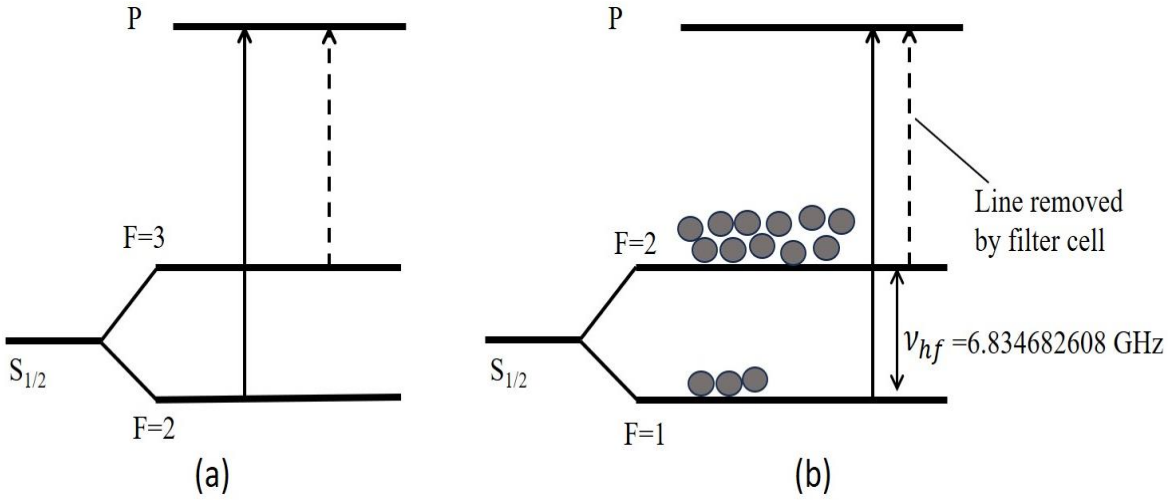


Figure 1.7: Hyperfine energy level structure in (a) $^{85}$Rb and (b) $^{87}$Rb atoms.

The functional block diagram of double resonance based Rb atomic clock is shown in Figure 1.8. It consists of two vapor cells called a filter cell ($^{85}$Rb) and a resonance cell ($^{87}$Rb), which are filled with buffer gas. The advantage of the buffer gas is to prevent Rb collisions with cell walls [9]. Atomic interrogation is achieved through a technique known as intensity optical pumping (IOP). The $^{87}$Rb lamp excited by RF energy provides Rb light corresponding to two transitions of hyperfine ground states as shown in Figure 1.7b. The light corresponding to the transition from ground state $F$=2 to excited state is filtered by the $^{85}$Rb cell ($F$=3 to excited state (Figure 1.7a)). The light corresponding to the $F$=1 transition passes through the $^{87}$Rb cell. $^{87}$Rb atoms in the $F$=1 state absorb this light and are pumped to the excited state, from which they decay into both ground states. Due to continuous optical pumping, all atoms in the $F$=1 state are pumped to the $F$=2 state via an excited state. Under the equilibrium condition, the light transmitted through the $^{87}$Rb cell, which is detected by a photodetector is maximum and remains constant. Now the microwave energy corresponding to transition $F$=2→$F$=1 is derived from OCXO and coupled to the microwave resonator. When microwave energy matches with the above transition, the atoms in $F$=2 are pumped into $F$=1 state, which allows minimum transmission at the photodetector. Thus, the output of the photodetector indicates a resonance signal which is in Lorentzian shape as function of detuning frequency. The peak value of resonance in a feedback loop, OCXO is locked and continuously corrected to provide the atomic transmission. The 10 MHz output of OCXO serves as output frequency of Rb atomic clock. During the entire process, the atoms are resonant with both the optical field and microwave field, hence the clock is called as double resonance based atomic clock.

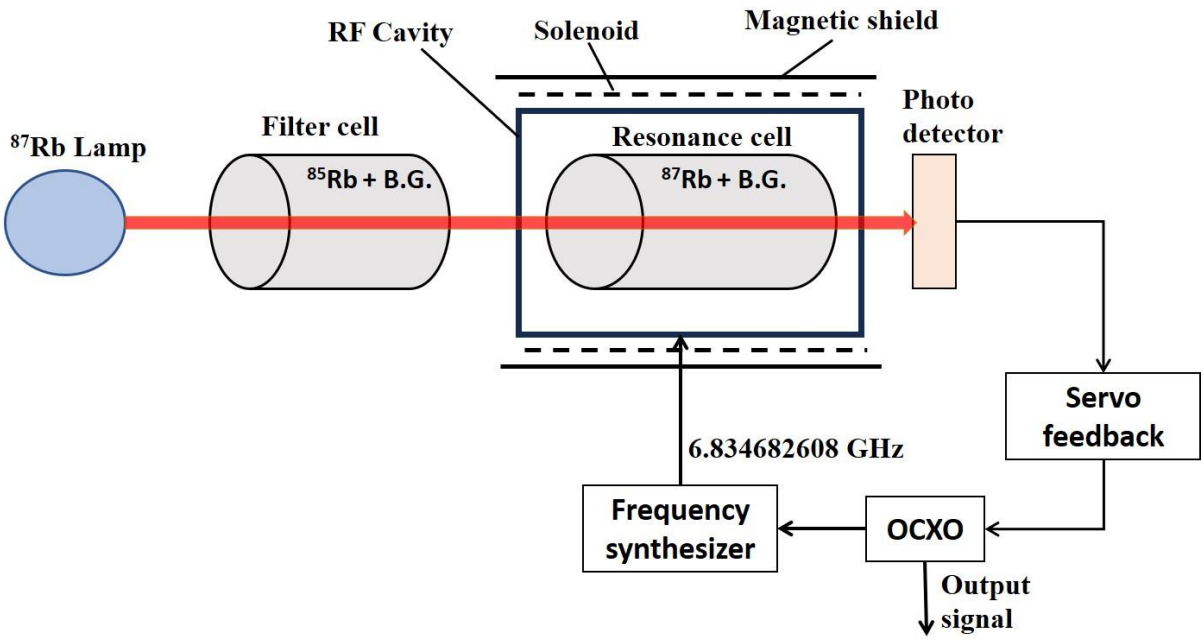


Figure 1.8: Functioning scheme of double resonance Rb clock. Source: [1].

Construct of space grade atomic clocks is different from ground clocks. The differentiating factors include reduced size, less weight and low power consumption. In addition, space clocks are required to sustain the launch process and harsh space environment, and provide reliable service throughout the mission life. Table 1.1 provides the typical size, weight and power (SWaP) of double resonance Rb clock, Cs beam clock and PHM space grade clocks used in satellite navigation [10], [11], [12].

Table 1.1: Typical size, weight and power (SWaP) of space grade atomic clocks used in satellite navigation.

| Clock type | Size ($cm^3$) | Weight (kg) | Power (W) |
|---|---|---|---|
| Rb (Double resonance) | 1600-1800 | 6-8 | 30-35 |
| Cs beam clock | 6500-7000 | 9-10 | 25-30 |
| PHM | 27500-28500 | 18-20 | 60-65 |

## 1.3 Characterization of atomic clocks

The performance of atomic clock output frequency is critical in timing applications. Clock characterization includes continuous monitoring of clock frequency and detection of anomalies

such as outliers, frequency and phase jumps. Frequency stability and accuracy are the essential parameters when assessing the clock performance. Frequency stability is studied in terms of stochastic (noise) behaviour. On the other hand, frequency accuracy is studied using deterministic (systematic) behaviour. Stochastic behaviour is described in this section, while the deterministic behaviour and clock anomaly detection are discussed in Chapter 5.

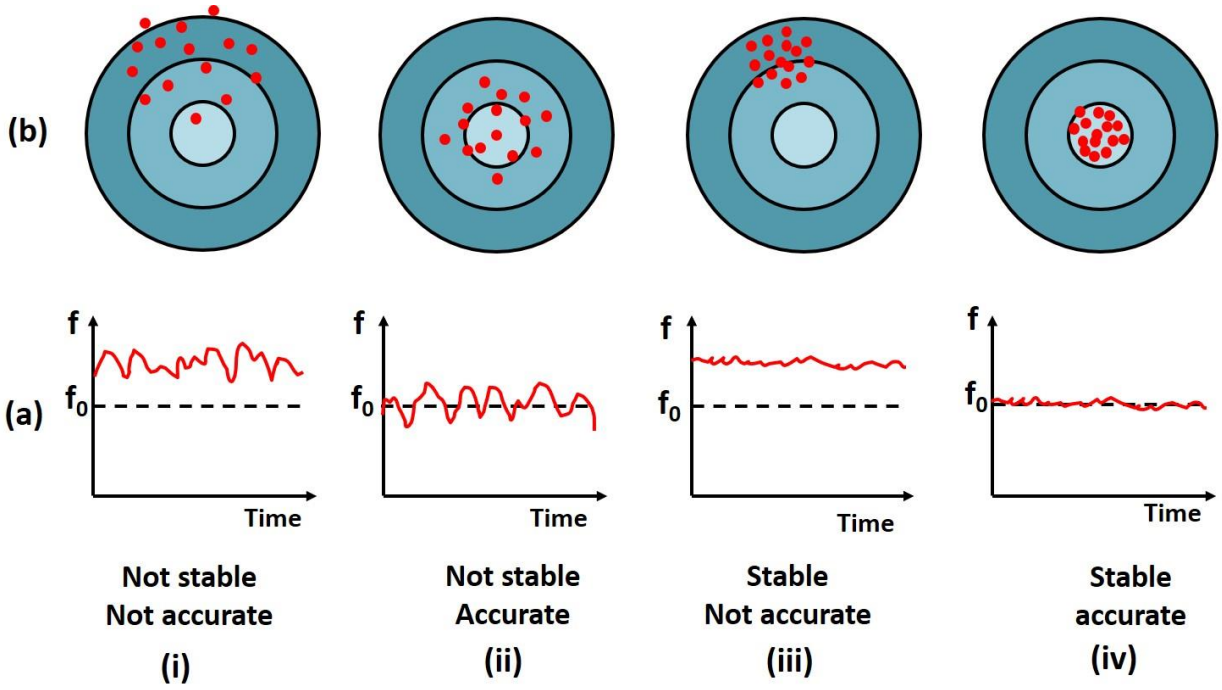


Figure 1.9: Pictorial representation of stability and accuracy [13]. (a) Four possibilities of a frequency source behaviour that are (i) not stable and not accurate, (ii) not stable but accurate, (iii) stable but not accurate, (iv) stable and accurate. (b) Visual representation of corresponding behaviour using bullet holes on a target.

Frequency stability is defined as the degree to which an atomic clock can provide the same frequency over a specific time interval [7]. Frequency accuracy is a measure of how good the frequency is close to the true value. Figure 1.9a shows the schematic explanation of stability and accuracy of a frequency source. The behaviour of a frequency source can have four possibilities as shown in Figure 1.9a. The corresponding behaviour can be visually represented using bullet holes on a target, as shown in Figure 1.9b.

### 1.3.1 Frequency noise

The noise of a frequency source can be treated as the time dependent phase and frequency fluctuations caused by a superposition of random signals generated in the clock. Frequency

stability is analysed using a standard noise model, as explained below. The output frequency of a source that produces a sinusoidal voltage signal can be represented as in Equation 1.1 [14], [15].

$$V(t) = [V_0 + \varepsilon(t)]\sin(2\pi\nu_0 t + \phi(t)) \tag{1.1}$$

Where,

$V_0$: true amplitude of the signal

$\nu_0$: true frequency of the signal

$\varepsilon(t)$: random variations in amplitude

$\phi(t)$: random variations in phase

For frequency stability analysis of precision oscillators, it is assumed that the amplitude fluctuations are negligible compared to the magnitude of the true amplitude. The instantaneous angular frequency of the source due to fluctuations in phase is represented as the time derivative of its total phase according to Equation 1.2 [16].

$$\omega(t) = \frac{d}{dt}[2\pi\nu_0 t + \phi(t)] = 2\pi\nu_0 + \frac{d\phi}{dt} \tag{1.2}$$

Thus, the instantaneous frequency $\nu(t) = \frac{\omega(t)}{2\pi}$ is given by

$$\nu(t) = \nu_0 + \frac{1}{2\pi}\frac{d\phi}{dt} \tag{1.3}$$

The normalized or fractional frequency deviation $y(t)$ is defined as the normalized deviation of oscillator frequency $\nu(t)$ from nominal value $\nu_0$ as given in Equation 1.4.

$$y(t) = \frac{\nu(t) - \nu_0}{\nu_0} = \frac{1}{2\pi\nu_0}\frac{d\phi}{dt} \tag{1.4}$$

The time deviation (time offset) can be represented using normalized phase deviation as $x(t) = \frac{\phi(t)}{2\pi\nu_0}$. Hence, the fractional frequency can be given as the derivative of time deviation which is given by Equation 1.5.

$$y(t) = \frac{dx}{dt} \tag{1.5}$$

In the discrete time domain, the fractional frequency can be computed using time offset given by $y_i = \frac{x_{i+1} - x_i}{\tau_0}$. Where, $\tau_0$ is the time interval (sampling time) between two consecutive time offsets $x_i$ and $x_{i+1}$.

In this thesis, fractional frequency is used as a base measurement to characterize the performance of the atomic clock (see Chapter 5). If fractional frequency is provided, the time deviation can be derived by integrating it, according to Equation 1.6.

$$x(t) = \int_0^t y(t)dt \tag{1.6}$$

### 1.3.2 Power law noise

Section 1.3.1 describes the noise of frequency source based on fluctuations in phase. Alternatively, the noise can also be described by frequency fluctuations. As per the IEEE recommendation, the frequency domain stability of a source can be studied using power spectral density (PSD) of frequency $S_y(f)$ and time offset $S_x(f)$ [7], [16], [17]. Following is the relationship between time offset and frequency power spectral densities.

$$S_x(f) = \frac{S_y(f)}{(2\pi f)^2}$$

Here, $S_x(f)$ is PSD of time offset fluctuations. PSD of the phase fluctuations also can be related to $S_x(f)$ and $S_y(f)$ as shown below.

$$S_\phi(f) = (2\pi\nu_0)^2 . S_x(f) = (\frac{\nu_0}{f})^2 . S_y(f)$$

Here $\nu_0$ is the carrier frequency. Single side band (SSB) phase noise can be computed using PSD of phase fluctuations as given by $\mathcal{L}(f) = 10.\log[\frac{1}{2}S_\emptyset(f)]$ in units of dBc/Hz. It is the most commonly used expression to compute the phase noise.

The power law spectral density $S_y(f)$ is given by Equation 1.7 [16].

$$S_y(f) = h(\alpha) f^{\alpha} \tag{1.7}$$

Here, $f$ is the Fourier frequency, $\alpha$ is an integer, and $h(\alpha)$ is the intensity coefficient. Typically, $\alpha$ values are 2, 1, 0, -1, -2, and -3, and the corresponding noise types are White phase modulation (PM), Flicker PM, White frequency modulation (FM), Flicker FM, Random walk FM and frequency drift, respectively. Further details on these statistical noise characteristics are available in Reference [16] . The possible reason for these typical noises and their impact on frequency stability is explained as below [18].

White noise is due to thermal fluctuations in the clock components, such as oscillators and amplifiers. It has constant power spectral density across all frequencies. Thus, it introduces random voltage fluctuations in the components across all frequencies and affects the short-term frequency stability of clock.

Flicker noise can arise from various sources such as electronic components of the clock, interface traps between the components and thermal noise in resistive components. It has a spectral density that decreases with an increase in frequency (proportional to 1/f), affects the long-term frequency stability of clock.

Random fluctuations in frequency over time represent the random walk noise. This is generated by fluctuations in the operating parameters of clock such as temperature and other environmental factors. It affects the long-term frequency stability and accuracy of the source over long periods of time.

The combination of flicker noise and random walk noise results in flicker walk noise. It also affects the long-term frequency stability and accuracy of the source over long periods of time.

The above noises cannot be completely eliminated. However, they can be minimized using techniques such as temperature stabilization, noise reduction techniques, phase locked loops, frequency stabilization techniques, filtering techniques and the use of low noise components [18].

### 1.3.3 Methodologies to estimate frequency stability

Frequency stability primarily deals with the characterization of statistical nature of phase and frequency fluctuations with time [16]. There are different statistical variances available to study the frequency stability of a clock.

**Standard Variance**

The standard variance or ordinary variance is given by

$$s^2 = \frac{1}{M-1}\sum_{i=1}^{M}(y_i - \bar{y})^2 \tag{1.8}$$

Where, $y_i$ is the $i^{th}$ frequency value, $M$ is the total number of samples in frequency data, $\bar{y} = \frac{1}{M}\sum_{i=1}^{M} y_i$ is the mean of total frequency data. Standard deviation ($s$) is the square root of the standard variance. Generally, standard deviation is not recommended for frequency stability analysis of oscillators as it is non-convergent for few types of noises [19]. As the standard deviation considers the deviations from the mean value, it is not stationary and diverges for some noise types such as flicker and random walk.

**Allan Variance**

Allan variance or two-sample variance is the most commonly used technique to measure the frequency stability of a source [20]. It considers deviation between samples instead of deviation of sample from the average, which overcomes the divergence issue for most types of clock noises. The Allan variance (AVAR) is given by Equation 1.9 [19], [21].

$$\sigma^2{}_y(\tau) = \frac{1}{2(M-1)}\sum_{i=1}^{M-1}(y_{i+1} - y_i)^2 \tag{1.9}$$

Where, $M$ is the number of frequency values, $y_i$ is $i^{th}$ frequency value. Equation 1.9 can be written in terms of time offset as given in Equation 1.10.

$$\sigma^2{}_y(\tau) = \frac{1}{2(N_x-2)\tau^2}\sum_{i=1}^{N_x-2}(x_{i+2} - 2x_{i+1} + x_i)^2 \tag{1.10}$$

Here, $x_i$ is the $i^{th}$ time offset, $N_x$ is the number of time offset values and $\tau$ is the averaging time. Frequency stability is represented using Allan deviation (ADEV), $\sigma_y(\tau)$, which is the square root of the AVAR. For white frequency modulation (FM), the behaviour of Allan variance and standard variance is the same. However, AVAR has the advantage that it converges for all divergent noises. This convergence value is independent of total number of samples available in frequency or time offset data. The confidence interval of the ADEV estimate depends on the type of noise present, but in general, it is computed as $\pm\sigma_y(\tau)/\sqrt{N_x}$.

## Overlapping Allan deviation

The confidence of the ADEV estimate can be improved by taking overlapping samples. Overlapping Allan deviation (OADEV) considers all possible combinations of samples at each averaging time $\tau$ to compute the frequency stability. Thus, OADEV takes more computational time compared to ADEV. If $\tau_0$ is the basic sampling period, the averaging time ($\tau$) is calculated using $\tau = m\tau_0$. Here, $m$ is the averaging factor. For a given frequency data with *M* number of samples, OADEV is computed using Equation 1.11.

$$\sigma_y(\tau) = \sqrt{\frac{1}{2m^2(M-2m+1)} \sum_{j=1}^{M-2m+1} \left\{ \sum_{i=j}^{j+m-1} [y_{i+m} - y_i] \right\}^2} \tag{1.11}$$

The confidence interval of OADEV is better than ADEV due to the participation of overlapping sample differences, which increase the number of degrees of freedom. However, not all additional overlapping differences are statistically independent here.

The time domain frequency stability of a source is expressed by plotting OADEV ($\sigma_y(\tau)$) as a function of averaging time ($\tau$), and it is also known as stability curve or sigma-tau plot. The plot between log sigma and log tau indicates the frequency stability at a given averaging time, and its slope provides the type of noises [16], [22], [23]. Figure 1.10 shows the typical log sigma and log tau plot and the corresponding noise types based on the slope value.

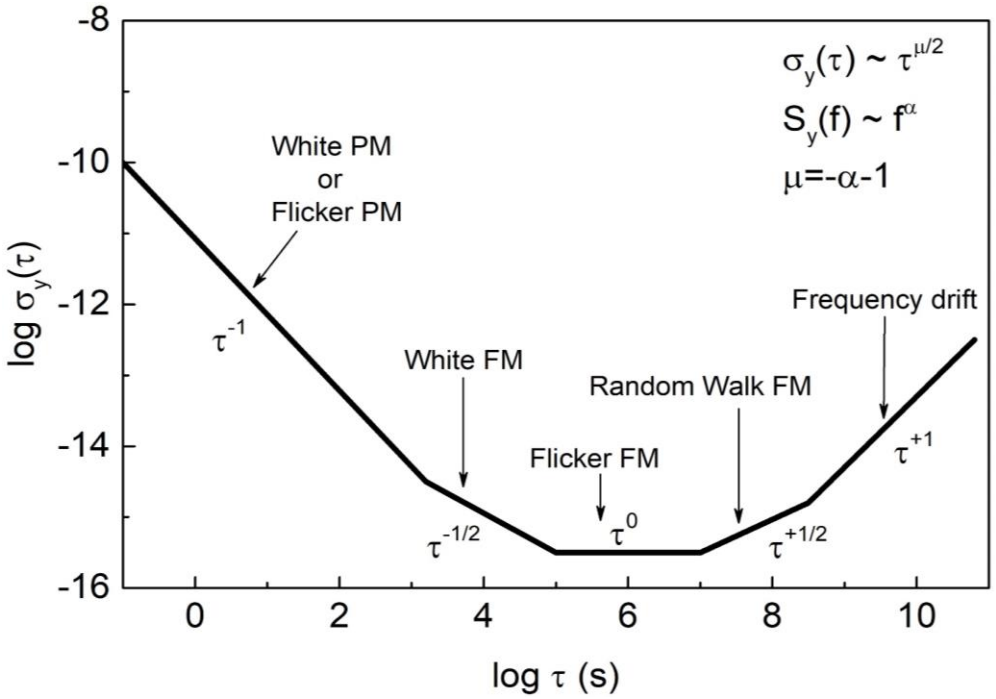


Figure 1.10: Frequency stability and type of noise using OADEV as function of averaging time. Slope of stability curve provides the type of noise present at corresponding averaging time. Source: [16].

Figure 1.10 shows the relationship between OADEV and the type of noise with averaging time as given by $\sigma_y(\tau) \propto \tau^{\frac{\mu}{2}}$. The relation between $\mu$ and $\alpha$ is given as $\mu = -\alpha - 1$. Thus, to find the type of noise, one can compute OADEV and calculate the slope of the stability curve.

## Modified Allan deviation

It is clear from Figure 1.10 that OADEV cannot distinguish between white PM and flicker PM as the slope is same for both types. However, Modified ADEV (MADEV) as given in Equation 1.12 [24] can distinguish these two noises.

$$Mod\sigma_{\mathrm{y}}(\tau) = \sqrt{\frac{1}{2\mathrm{m}^4(\mathrm{M}-3\mathrm{m}+2)} \sum_{\mathrm{j}=1}^{\mathrm{M}-3\mathrm{m}+2} \left\{ \sum_{\mathrm{i}=\mathrm{j}}^{\mathrm{j}+\mathrm{m}-1} \left( \sum_{k=i}^{i+m-1} [\mathrm{y}_{\mathrm{k}+\mathrm{m}} - \mathrm{y}_k] \right) \right\}^2} \tag{1.12}$$

Figure 1.11 shows the typical MADEV with averaging time where white and flicker phase noise types exhibit different slopes.

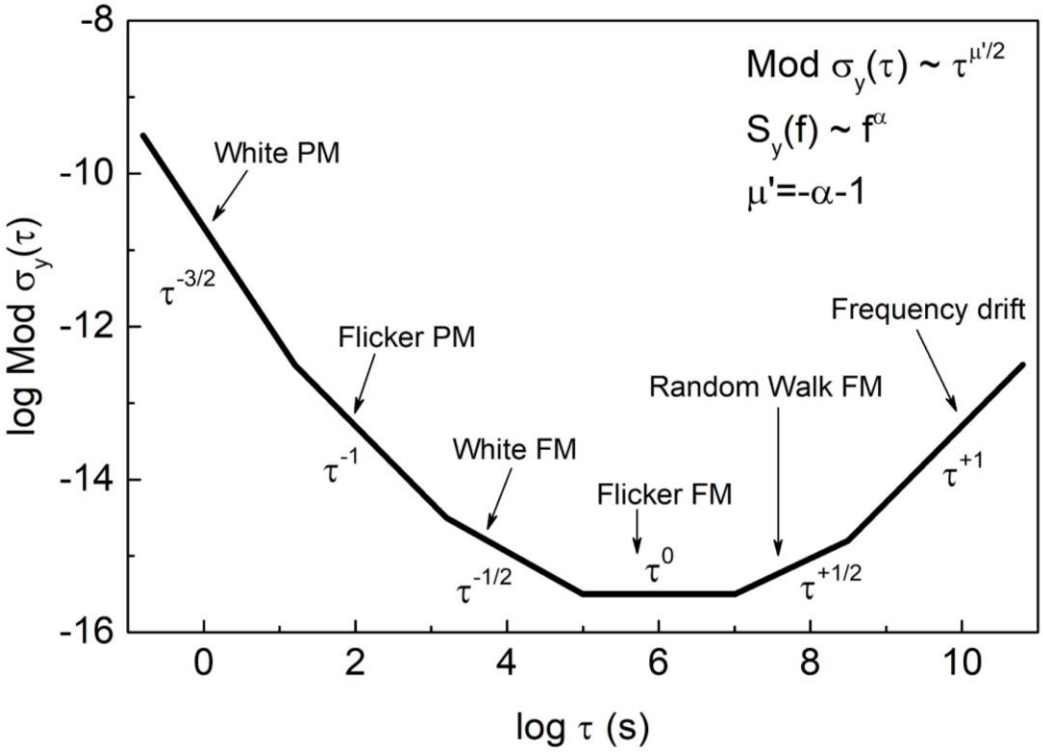


Figure 1.11: Frequency stability and type of noise using MOADEV as function of averaging time. White PM and Flicker PM are distinguished with different slopes of stability curve. Source: [16].

## Overlapping Hadamard Deviation

Overlapped Hadamard variance is a three-sample variance which is insensitive to linear frequency drift of frequency source [25]. Its square root is known as overlapped Hadamard deviation (OHDEV), which is used to compute the frequency stability of sources that exhibit linear frequency drift [26], [27]. Moreover, the power law noise types such as Flicker Walk FM ($\alpha = -3$) and Random Run FM ($\alpha = -4$) are convergent with OHDEV. OHDEV of frequency output of a source for *M* number of samples is computed using Equation 1.13.

$$H\sigma_y(\tau) = \sqrt{\frac{1}{6m^2(M-3m+1)} \sum_{j=1}^{M-3m+1} \left\{ \sum_{i=j}^{j+m-1} [y_{i+2m} - 2y_{i+m} + y_i] \right\}^2} \quad (1.13)$$

## Dynamic Allan deviation

OADEV cannot be used to monitor the instantaneous (real-time) frequency variations as it provides frequency stability by averaging the frequency fluctuations over a period of time. On the other hand, Dynamic Allan Deviation (DADEV) [28], [29], [30], [31] is used for

monitoring the clock behaviour in real-time as it captures the instantaneous variations in the clock frequency. This algorithm captures all the variations present in the clock frequency data. It also calculates the frequency stability even in the case of data gaps. An estimate of dynamic Allan variance (DAVAR) is expressed using Equation 1.14 [32].

$$\sigma_y^2[n,k] = \frac{1}{2k^2{\tau_0}^2}\frac{1}{N_w - 2k} \times \sum_{m=n-\frac{N_w}{2}}^{n+\frac{N_w}{2}-2k-1} (x[m+2k] - 2x[m+k] + x[m])^2 \qquad (1.14)$$

Where, $k = 1, \ldots, \frac{N_w}{2} - 1$ , $\tau = k\tau_0$ and $n$ is discrete time at which DAVAR is computed. $N_w$ is analysis window length. The square root of DAVAR is DADEV. If the window length is too long, the computational time is longer. Hence, there is a trade-off between window length and computational time. More details on the implementation of DADEV are available in [32], [33].

## 1.3.4 Identification of noise

As discussed in Section 1.3.3, the types of noises in a clock are derived from the slopes of the sections of modified Allan deviation versus averaging time plot. Further, the identification of noise type is influenced by the frequency stability (see Figure 1.11). Two analytical methods that overcome the above limitation are described below.

### Identification of noise using *B1* and *R(n)*

The functions Barnes $B_1$ and *R(n)* are used to identify the types of noise [18], [34]. The ratio between the standard (*N*-sample) variance and the Allan (two-sample) variance is defined as $B_1$ function. Similarly, the ratio between the modified Allan variance and the normal Allan variance is defined as *R(n)* function. The detailed procedure to identify the noise types using $B_1$ and *R(n)* functions can be found in Reference [34]. The linear frequency drift must be removed before applying this method.

### Lag-1 autocorrelation method

The limitation of using $B_1$ and *R(n)* functions in identifying the noise is that it cannot distinguish between white PM and flicker PM noises when the sampling period and averaging

times are equal. This limitation is overcome by using the autocorrelation function (ACF). Detailed methodology of implementation of ACF using frequency data is described as follows. The autocorrelation function is calculated using Equation 1.15 as given below [35], [36].

$$r_1 = \frac{\frac{1}{N_S}\sum_{k=1}^{N_S-1}(z_k - \bar{z})(z_{k+1} - \bar{z})}{\frac{1}{N_S}\sum_{1}^{N_S}(z_k - \bar{z})^2} \tag{1.15}$$

Here, $z_k$ is given by

$$z_k = \frac{1}{M_A}\sum_{j=1}^{M_A} X_{(k-1)M_A+j} \quad (\mathrm{k} = 1,2, \ldots, N_S)$$

Here, $X$ is the time series of frequency data with length $N_X$, $M_A$ is the averaging factor, $\bar{z}$ is the mean of $z_k$, $N_S$ is the number of samples based on $M_A$ given by, $N_S = int(\frac{N_X}{M_A})$. The types of noise present in frequency data are estimated using $\sigma = \frac{r_1}{1+r_1}$. Here, $\sigma$ is a status flag used for convergence check for the type of noise. The condition for the convergence of noises (i.e., stationary condition) is to satisfy $\sigma < 0.25$. If this condition is not met, successive differences of $z_k$ are taken until the stationary process is reached (i.e., to satisfy $\sigma < 0.25$), as shown below.

$$z_1 = z_2 - z_1, z_2 = z_3 - z_2, \ldots \ldots, z_{N_S-1} = z_{N_S} - z_{N_S-1}$$

Noise identification is done by considering $p = -\mathrm{round}(2\sigma) - 2d$, i.e., rounding value of $2\sigma$ with negative sign is added with negative value of $2d$. Here, $d$ is the number of times data differenced and $p$ is an integer used for intermediate calculations. If the frequency data is used in calculating the ACF, then $\alpha = p$. On the other hand, if the phase data is used in the calculation, then $\alpha = p + 2$. The $\alpha$ is power law exponent as given in Equation 1.7. Estimation of the noise ID algorithm to identify the noise present in the phase or frequency data is shown in Figure 1.12.

$Done = False, \qquad d = 0$

While not done

$$z_i = \frac{1}{M_A}\sum_{j=1}^{M_A} X_{(i-1)M_A+j} \qquad (i = 1,2,3, \ldots \ldots N_S)$$

$$\bar{z} = \frac{1}{N_S}\sum_{i=1}^{N_S} Z_i \qquad N_S = int(\frac{N_x}{M_A})$$

$$r_1 = \frac{\sum_{k=1}^{N_S-1}(z_k - \bar{z})(z_{k+1} - \bar{z})}{\sum_{k=1}^{N_S}(z_k - \bar{z})^2} \qquad \sigma = \frac{r_1}{1 + r_1}$$

$if\ d \geq d_{min}\ \&\ (\sigma < 0.25 \mid d \geq d_{max})$

p=round(2$\sigma$)-2d

Done=True

else

$Z_1 = Z_2 - Z_1, \ldots\ldots\ldots, Z_{N_S-1} = Z_{N_S} - Z_{N_S-1}$

$N_S = N_S - 1, \qquad d = d + 1$

End if

End while

Figure 1.12: Noise identification algorithm using Lag-1 autocorrelation method.

There are following limitations when using the standard Lag-1 autocorrelation method. The noise results show jumps and frequent variations with an increase in averaging time, which affects the identification of noise type. The minimum number of samples required for a standard method is more than or equal to 32 [35]. This makes it difficult to compute noise type with long averaging times. The above limitations can be avoided by calculating the coefficient of noise type using a modified Lag-1 autocorrelation method that uses overlapping samples [36]. Estimation of the noise ID algorithm using overlapping samples is shown in Figure 1.13. Lag-1 autocorrelation algorithms using non-overlapping and overlapping samples are implemented and the corresponding results are discussed in Section 5.6.2.

$Done = False, \qquad d = 0$

While not done

$$z_i = \frac{1}{M_A}\sum_{j=1}^{i+M_A-1} X_j \qquad (i = 1,2,3, \dots \dots N_S)$$

$$\bar{z} = \frac{1}{N_S}\sum_{i=1}^{N_S} Z_i \qquad N_S = N_x - M_A + 1$$

$$r_1 = \frac{\sum_{k=1}^{N_S-M_A}(z_k - \bar{z})(z_{k+M_A} - \bar{z})}{\sum_{k=1}^{N_S}(z_k - \bar{z})^2} \qquad \sigma = \frac{r_1}{1 + r_1}$$

$if\ d \geq d_{min}\ \&\ (\sigma < 0.25 \mid d \geq d_{max})$

p=round(2$\sigma$)-2d

Done=True

else

$Z_1 = Z_{1+M_A} - Z_1, Z_2 = Z_{2+M_A} - Z_2, \dots\dots, Z_{N_S-M_A} = Z_{N_S} - Z_{N_S-M_A}$

$N_S = N_S - M_A, \qquad d = d + 1$

End if

End while

Figure 1.13: Modified noise identification algorithm using Lag-1 autocorrelation method with overlapping samples.

## 1.4 Atomic clock in time scales

Time scale is generally referred to as a combination of time origin and basic time interval [37]. International Bureau of Weights and Measures (BIPM) is recommended second as the basic time interval. Based on Earth's rotation with respect to Sun, universal time (UT0) is determined to provide uniform time across the globe for civilian timekeeping. UT0 is derived such that zero hour corresponds to mean midnight at the Meridian Line in Greenwich, UK, and its 24 hours is close to the average duration of a day. The UT0 second was defined by early astronomers as a fraction (1/86400) of the length of the solar day, which is based on Earth's rotation about its axis. Thus, the solar day is the time interval between two consecutive solar Noons [37]. The contribution from periodic motion of Earth's polar axis is corrected in UT0 and referred to as UT1. UT1 is calculated and maintained by the International Earth Rotation and Reference Systems Service (IERS). UT1 was accepted as the world's reference time scale

until 1972. In addition, UT1 is also corrected for seasonal variations of Earth's rotation and known as UT2.

Due to the seasonal variations in the length of the day, the definition of second was further modified as the fraction of the mean solar day. Additionally, to establish a more stable definition of the second, astronomers selected Earth's revolution period around the Sun as a basis in 1956, known as ephemeris time (ET). This means that time is maintained more accurately by using Earth's revolution around the Sun rather than rotation about its axis. The ephemeris second is defined as the fraction (1/31556925.9747) of the length of the tropical year 1900, which was formally considered as the S.I. second by the General Conference of Weights and Measures (CGPM).

Later on, International Atomic Time (TAI) was developed, which is based on atomic time derived from a network of 450 atomic clocks located in 85 countries. The atomic second was then introduced which is defined as the duration of 9192631770 periods of radiation corresponding to the transition between two hyperfine levels of a Cesium-133 atom. Atomic second has been the S.I. unit of time since 1967. TAI and UT1 were officially agreed to coincide starting on the 1st January 1958. TAI is maintained by the International Bureau of Weights and Measures (BIPM).

In 1972, a new coordinated global time standard was adopted to unify the different time scales. Coordinated Universal Time (UTC) is similar to TAI but accounts for an integer number of leap seconds to maintain approximate agreement with UT1. Based on variation in the Earth's rotation speed, IERS decided to add or subtract a leap second to UTC such that the difference between UTC and UT1 is always maintained within 0.9 seconds. The following is the system of equations for UTC.

$$\begin{aligned} UTC(t) - TAI(t) &= n * s \\ UTC(t) - UT1(t) &< 0.9\, s \end{aligned} \tag{1.16}$$

Here, *n* is integer number. UTC is calculated and distributed by the BIPM, and the users can access local UTC through national laboratories (UTC(k)). Here, *k* is the national timing laboratory that is contributing to TAI. Each satellite navigation system uses its dedicated time scale and then linked to UTC (k). For a given satellite navigation system, the time scale is its ground reference time.

## 1.5 Satellite navigation

Satellite navigation is a system that provides positioning and timing services to the user by broadcasting navigation signals through satellites. There are Global Navigation Satellite Systems (GNSS) and Regional Navigation Satellite Systems (RNSS). GNSS includes Global Positioning System (GPS) by the United States of America (USA), Global'naya Navigatsionnaya Sputnikova Sistema (Global Navigation Satellite System, GLONASS) by Russia, BEIDOU (Big Dipper asterism) by China, and GALILEO by Europe. RNSS includes Quasi-Zenith Satellite System (QZSS) by Japan and Navigation with Indian Constellation (NavIC) by India. Satellite navigation system consists of three components called as space segment, control segment and user segment as shown in Figure 1.14.

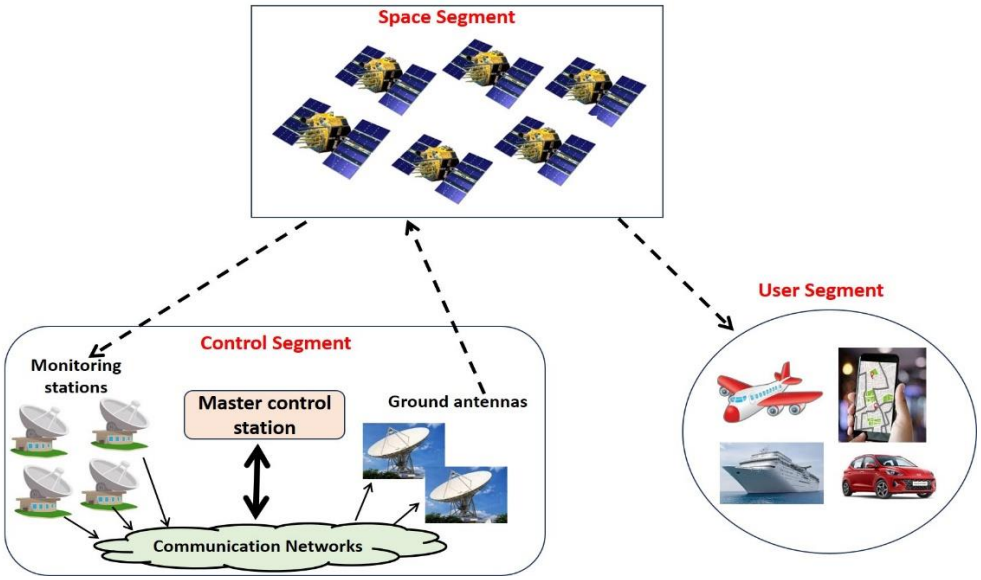


Figure 1.14: Simplified architecture of satellite navigation system. It consists of three segments named as space segment, control segment and user segment. Source: [38]

### Space segment

It comprises satellites in specific orbits above the Earth's surface. These navigation satellites are equipped with stable atomic clocks on-board as a timing source. Each navigation satellite transmits ranging signals with navigation data on at least two frequency bands. Navigation data consists of information about satellite's position, its health status and time of its clock.

### Control segment

The control segment is primarily responsible for generating navigation data, monitoring and maintaining the satellites in predefined constellation. It consists of ground ranging and monitoring stations, master control station and ground antennas. Ranging and monitoring stations track the satellites and provide one way ranging measurement data. These stations are also utilized to monitor the reliability of broadcast signals. Ranging data from all the stations is transmitted and collected at master control station. This ranging data is processed and used by master control station to estimate orbit and time of clock for each satellite. This orbit and clock information is predicted for a future period (typically 24 hrs), structured into navigation message (also called as navigation data) and then up-linked to the satellites via ground antennas.

Each satellite navigation system comprises its own ground reference time referred to as system time. System time is a reference time scale generated using the ensemble of ground atomic clocks. Navigation parameters are generated and uploaded to the satellites with respect to system time.

### User segment

User segment consists of GNSS/RNSS receivers that are capable of receiving satellite navigation signals. User receiver computes its position and timing information by tracking and processing the navigation signals based on the algorithms provided by the corresponding navigation system via Interface Control Document (ICD). User segment includes receivers on ground, air, water and space. Low Earth Orbit (LEO) satellites also carry GNSS receiver to compute its real time position.

## 1.5.1 Principle of satellite navigation

Satellite navigation enables the estimation of three-dimensional position and time of user receiver in real-time. In every satellite navigation system, satellites broadcast the navigation signals that are time stamped with corresponding satellite time. Further details on satellite time are discussed in Section 1.5.2. User receiver uses these signals from different satellites simultaneously and compares them with the time stamp generated by local clock known as receiver clock. Therefore, it computes its position based on the time of arrival (TOA) of navigation signals. Three basic measurements such as pseudorange, carrier phase and Doppler are derived from navigation signals. Pseudorange is determined by multiplying the speed of light by time difference between receiver clock time when signal is received and satellite time

when signal is transmitted. Carrier phase measurement provides the range information in terms of accumulated number of carrier cycles (i.e., wavelengths) and phase difference within the cycle. Doppler measurement is the change in received frequency due to the Doppler effect which provides the information about range rate (i.e., variation of range with time). These three measurements enable the user receiver to compute its position, velocity and time offset with respect to system time.

In order to compute the receiver's three-dimensional position $(x_u, y_u, z_u)$, a minimum of three navigation satellite signals are required (in principle) as explained below. The position of receiver (Rx) is the intersection of spheres formed by the navigation signals transmitted by satellites as shown in Figure 1.15 which is referred to as trilateration method. With a single satellite, the user position is somewhere on the surface of the sphere formed by a radius equal to the distance from satellite to receiver ($\rho_1$) and satellite as the centre ($s_1$). Similarly, if a second satellite is considered simultaneously, the receiver must also be somewhere on the sphere formed by it, same as that of first satellite. These two spheres intersect and form a circle that contains interconnecting points common to both spheres and the receiver position is anywhere on this circle. Now, if we consider a simultaneous third satellite that forms a sphere intersecting with others, it forms two points on the circle common to all three spheres. One of these two points can be ignored as its location is in space far away from the Earth's surface, while the other point provides the user position.

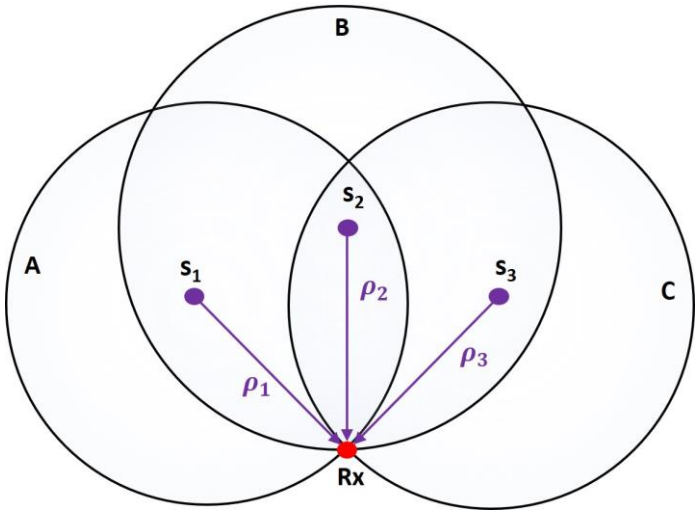


Figure 1.15: User receiver positioning through trilateration method. In principle, minimum three satellites are required to compute user position (Rx). *A*, *B* and *C* are three spheres formed by satellites $s_1$, $s_2$, $s_3$, respectively.

The distance from satellite to the receiver is calculated by multiplying the signal transit time (τ) by the speed of light. Here, the signal travel time is measured based on the satellite

timestamp (generated by satellite clock) and receiver time stamp (generated by receiver clock). Satellite clocks are stable and synchronized with system reference time (see Section 6.2). On the other hand, the receiver clocks are not synchronized with the system time. Therefore, the calculated distance is a pseudorange that includes geometric range and range due to the receiver clock's time offset ($\delta t_u$) with respect to system time. In addition to position ($x_u, y_u, z_u$), a fourth unknown parameter ($\delta t_u$) also needs to be computed, therefore at least four satellites are required to estimate the position and time offset of user receiver. The simplified equations for the pseudorange between receiver and satellite can be written as given in Equation 1.17.

$$\begin{aligned}
\rho_1 &= \sqrt{(x_u - x^{S_1})^2 + (y_u - y^{S_1})^2 + (z_u - z^{S_1})^2} + c.\delta t_u \\
\rho_2 &= \sqrt{(x_u - x^{S_2})^2 + (y_u - y^{S_2})^2 + (z_u - z^{S_2})^2} + c.\delta t_u \\
\rho_3 &= \sqrt{(x_u - x^{S_3})^2 + (y_u - y^{S_3})^2 + (z_u - z^{S_3})^2} + c.\delta t_u \\
\rho_4 &= \sqrt{(x_u - x^{S_4})^2 + (y_u - y^{S_4})^2 + (z_u - z^{S_4})^2} + c.\delta t_u
\end{aligned} \tag{1.17}$$

Here, $(x_u, y_u, z_u)$ are the coordinates of user receiver, and $(x^{S_i}, y^{S_i}, z^{S_i})$ are the coordinates of $i^{th}$ satellite. Four simultaneous equations (given in Equation 1.17) are solved to estimate position and time offset of user receiver [39]. In reality, the pseudorange includes the time offset of satellite clock and receiver clock with respect to system time, atmosphere (ionosphere and troposphere) delay and errors due to receiver (noise and multipath). Therefore, the complete pseudorange equation can be represented as follows.

$$\rho = r + c[\delta t_u - \delta t^s] + I + T + \varepsilon \tag{1.18}$$

Here, $r = \sqrt{(x_u - x^S)^2 + (y_u - y^S)^2 + (z_u - z^S)^2}$ is the geometric range between receiver $(x_u, y_u, z_u)$ and satellite $(x^S, y^S, z^S)$, $\delta t_u$ and $\delta t^s$ are the receiver and satellite clock offsets with respect to ground reference time, $I$ is the ionospheric delay, $T$ is the tropospheric delay and $\varepsilon$ represents measurement noise together with unmodeled errors. The satellite coordinates $(x^S, y^S, z^S)$ are calculated from the satellite ephemeris broadcasted through the navigation signals. The broadcasted clock correction parameters are used to compute offset ($\delta t^s$) using the quadratic model according to Equation 1.19 [40]. Further details about $\delta t^s$ are discussed in Section 1.5.2.

$$\delta t^s(t_{sys}) = af_0 + af_1(t_{sys} - t_c) + af_2(t_{sys} - t_c)^2 \quad (1.19)$$

Where, $t_{sys}$ is the system time (ground reference time) broadcasted by the satellite, $\delta t^s(t_{sys})$ is satellite clock offset accumulated at time $t_{sys}$, $t_c$ is the time $t_{sys}$ at which the recent clock correction parameters are applicable. Here, $af_0$ is the initial time offset or time bias, $af_1$ is clock drift or fractional frequency offset, and $af_2$ is clock drift rate or frequency drift. More details on these clock correction parameters are discussed in Section 6.3. For the dual frequency receivers, the ionosphere delay is compensated by using a suitable combination of dual frequency measurements [39]. However, the single frequency user receivers compute the ionospheric delay using broadcasted ionospheric correction parameters. Troposphere delay is computed by using different algorithms [41], [42], [43], [44]. Finally, the unknown parameters to be estimated are $(x_u, y_u, z_u, dt_u)$.

The position accuracy of the user depends on the errors present in the broadcasted parameters (satellite ephemeris, satellite clock correction parameters and ionospheric correction parameters) and the models used for correcting tropospheric delay. The combined line of sight error seen by the user for a given satellite due to all these errors is known as User Equivalent Range Error (UERE) [45]. In addition, dilution of precision (DOP) also contributes to the user positioning accuracy. It is the measure of satellites geometry in a particular constellation. The accuracy of user position is given by the following equation [39].

$$Position\ accuracy = UERE \times DOP \quad (1.20)$$

Thus, the position accuracy of a user from given satellite navigation system depends on the accuracy of its broadcast parameters and the satellite geometry.

## 1.5.2 Satellite timekeeping

Each navigation satellite operates in its local time, which is generated by a free running on-board atomic clock (satellite clock) and is referred to as satellite time. All time-related data in the navigation message is executed with respect to satellite time. For example, the service provider uplinks twelve sets of navigation data to satellites predicted for next 24 hours. Each set consists of specific time of applicability and validity period. Satellite broadcasts the specific

navigation data set when its local time matches with the time of applicability of corresponding data set.

In navigation system, satellite clock time is synchronized to system time once the satellite is put in its intended orbit. Over time, satellite time deviates from system time due to frequency drift and ageing. The difference between system time and satellite time is referred to as satellite clock time offset or satellite clock offset denoted by $\delta t^s$. Service provider monitors the behaviour of satellite clock offset and correction parameters to the clock ($af_0, af_1, af_2$) are derived based on its past behaviour over a period. They are then predicted for the future 24 hours and broadcasted to the user. These predictions in the form of coefficients that are used by receiver to correct $\delta t^s$ to synchronize the signal reception time with respect to system time. If the instantaneous behaviour of clock changes during the prediction period, then position accuracy is degraded. Real-time satellite clock behaviour is monitored by the service provider. Any deviation in clock behaviour is detected instantly that would activate the timekeeping system to generate and up-link new clock correction parameters to the satellite. The detailed methodology for real-time computation of $\delta t^s$ and characterization of its behaviour is discussed in Chapter 5.

Since the satellite clock is a free running clock, its time offset with respect to system time accumulates over time. However, satellite navigation system allocates predefined limits for the maximum values of broadcast parameters. Thus, satellite clock offset is allowed to accumulate only up to the pre-allocated broadcast limit. The range measurements are not reliable if satellite clock offset is beyond the maximum allocated broadcast limit which contributes to large error in user position. Hence, satellite clock offset needs to be maintained within the allocated broadcast limit, which is referred to as satellite timekeeping. A detailed description of satellite timekeeping methodology is provided in Chapter 6.

### 1.5.2.1 Criticality of satellite clocks

Satellite clock offset, $\delta t^s$ is critical parameter in computing the UERE (see Equation 1.18) and then position accuracy of receiver (see Equation 1.20). User receiver computes the $\delta t^s$ in real-time using broadcasted clock coefficients according to Equation 1.19. For better position accuracy, the real-time behavior of satellite clock should comply with the broadcast clock correction parameters. The deviation between true clock offset (real time $\delta t^s$ as seen from the range measurements) and the predicted clock offset ($\delta t^s$ as predicted by the service provider) can occur mainly due to the change in deterministic and stochastic behavior of satellite clock.

The error in the deterministic behaviour (characterized by the broadcast clock parameters) can be attributed to estimation error and prediction error. The estimation error depends on various factors such as measurement accuracy, the model used and frequency stability of clock. Prediction error depends on initial estimation error, variation in frequency drift and frequency stability of clock. The stochastic behaviour entirely depends on the frequency stability of clock and it is an inherent property of clock and cannot be corrected on-board. Therefore, the satellite clock must be selected suitably to ensure its frequency stability is within the desired specifications that would meet the user requirements.

From the above discussion, it is evident that the clock must fulfil two conditions to be considered as satellite (on-board) clock. The first condition is that the clock offset should comply with the quadratic polynomial model for the next 24 hrs. More specifically, its frequency drift should not deviate from its past accepted behaviour for a certain period of time. Second, it should exhibit frequency stability that meets the desired user position accuracy. In other words, its stochastic noise should be within the limit. Consider an example of 1.0 m (i.e., 3 ns) as a limit on the accumulated line of sight error due to satellite clock over 24 hrs. This can be only achieved if the clock frequency stability is around 4.0E-14/day (3ns/86400s). In order to meet the above two requirements, all GNSS and RNSS generally use atomic clocks (rubidium/cesium/hydrogen maser) with good long-term stability as on-board clocks.

## 1.6 Atomic clocks in GNSS and RNSS

Major application of space-grade atomic clocks is in GNSS and RNSS [5], [8]. These navigation systems use different combinations of atomic clocks as satellite clocks [7]. The Rb clock was the first atomic clock used as on-board clock in satellites and has become the primary on-board atomic clock in various GNSS and RNSS systems. The GPS satellites that are launched in a particular generation known as blocks. Satellites from blocks I to IIA and block IIF used the combination of Rb and Cs atomic clocks as satellite clocks. The satellites in IIR, IIR-M and III blocks are equipped with Rb clocks. GLONASS satellites initially used Cs atomic clocks and currently use Rb atomic clocks. GLONASS-M and GLONASS-M+ generation satellites employ Cs atomic clocks, and GLONASS-K1 satellites employ Cs and Rb atomic clocks. BEIDOU and GALILEO navigation satellites use Rb and passive hydrogen maser (PHM) atomic clocks. The regional navigation systems QZSS and NavIC use Rb atomic clocks. Table 1.2 contains the list of atomic clocks used in various satellite navigation systems.

Table 1.2: Types of atomic clocks used as on-board clocks in GNSS and RNSS. Here, * indicates the regional navigation satellite systems, whereas the rest are global navigation satellite systems.

| S. No | Navigation System | Type of on-board clock | Country |
|---|---|---|---|
| 1 | GPS | Cs, Rb | USA |
| 2 | GLONASS | Cs | RUSSIA |
| 3 | BEIDOU | Rb, PHM | CHINA |
| 4 | GALILEO | Rb, PHM | EUROPE |
| 5 | QZSS* | Rb | JAPAN |
| 6 | NavIC* | Rb | INDIA |

Table 1.2 shows that most of the satellite navigation systems employ Rb atomic clocks, mainly for two reasons. First, the performance of Rb atomic clock meets the navigation accuracy requirements. The second reason is lower cost, lower power requirement and lower volume compared to Cs and PHM atomic clocks. For the last few decades, double resonance technique in Rubidium (Rb) atoms has been the widely used approach to realize clock resonance for space applications.

The application of atomic clock in space demands the miniaturization. Coherent Population Trapping (CPT) phenomenon in alkali atoms is another promising technique for the development of atomic clocks [46], [47], [48]. In this approach, hyperfine ground state atomic transitions are excited by optical fields generated by a laser diode, in contrast to a microwave cavity in double resonance clock. Thus, a CPT based atomic clock has the potential for miniaturization since it does not require a microwave cavity.

This thesis discusses about the study of CPT in $^{87}$Rb, optimization of its characteristics with respect to operating parameters for improved frequency stability and its utility as atomic clock for satellite navigation. The second part of the thesis deals with the real-time characterization of satellite clock behaviour and optimum satellite timekeeping methodology while maintaining uninterrupted service to the user.

## Outline of the thesis:

### Chapter-2: Coherent Population Trapping in Alkali Atoms

Coherent Population Trapping (CPT) as a quantum interference phenomenon in three-level atomic system is described. A four-level atomic model is discussed to simulate the CPT resonance with various operating parameters. A new scaling parameter is introduced in the

model to account for the influence of cell size on resonance characteristics. The theoretical limit of cell length where the quality figure saturates is predicted for different laser intensities. A theoretical computation of ground state relaxation rate ($\gamma_2$) is carried out by considering the effect of collisional mechanisms among Rb atoms, buffer gas and cell walls. Finally, the influence of each of the operating parameters on the characteristics of CPT resonance and the underlying laser-atom interaction mechanisms are discussed in this chapter.

### Chapter-3: Experimental Methods

The CPT excitation scheme employed in this study is discussed. A detailed scheme is devised to perform a thorough experimental investigation of CPT phenomena in Rb vapor cells with respect to range of operating parameters. A description of dedicated tabletop CPT setup used in this study is provided. Also, description on the configuration and parameters of Rb vapor cells, optical excitation schemes considered in the study are also discussed. Practical implementation of CPT scheme employing VCSEL diode, RF modulation of laser injection current, phase sensitive detection, laser frequency stabilization etc. are presented in detail.

### Chapter-4: Parametric Study of CPT Characteristics

This chapter provides the experimental and theoretical investigation on optimizing the control/operating parameters with respect to quality figure and frequency shift of CPT resonance. Experimental investigation carried out on the cells with different radii (R=5.0, 7.5 and 12.5 mm) filled with Ne buffer gas at 50 Torr pressure. The cells with chosen optimum dimension (R=12.5 mm) and filled with Ar+$N_2$ buffer gas mixture at different pressures (P=15, 17, 20 and 22 Torr) are investigated to optimize the characteristics of CPT resonance. CPT resonance and its corresponding quality figure are modelled in all the cells by accounting radius, temperature and buffer gas pressure.

### Chapter-5: Characterization of On-board Clocks

This chapter provides a detailed methodology for monitoring the behaviour of satellite clock and detection of anomalies using one-way carrier phase range measurements in real-time. Detailed description is provided on the algorithm that was developed to detect anomalies such as outlier, phase jump and frequency jump in satellite clock, using fractional frequency data. The implementation and demonstration of clock characterization methodology are carried out using NavIC (Navigation with Indian Constellation) satellites and discussed the relevant

results. Stochastic behaviour of on-board clocks is described using overlapping Allan deviation, dynamic Allan deviation and Lag-1 autocorrelation methods.

### Chapter-6: Satellite Timekeeping Methodology

This chapter describes a suitable timekeeping methodology to maintain the accuracy of satellite clock offset. A brief discussion is provided on various timekeeping methods and the advantages as well as limitations on implementation of these methods. This chapter then describes the optimum timekeeping methodology employed in NavIC satellites. A new mathematical model is derived to compute the optimal frequency offset correction such that the time interval between two consecutive corrections would be as long as possible. This methodology is demonstrated by implementing in IRNSS-1B satellite of NavIC constellation.

### Chapter-7: Summary

This chapter summarizes the overall work discussed in the thesis. The key observations on the measured quality figure and frequency shift of CPT resonance are highlighted with respect to laser-atom interaction mechanisms. The necessity of clock characterization and timekeeping methodology for providing desired position accuracy to the user is summarized. The thesis concludes with a brief discussion on future activities.

# Chapter-2

# Coherent Population Trapping in Alkali Atoms

This chapter provides a brief description about Coherent Population Trapping (CPT) in three level system along with the associated mathematical equations. Subsequently, the need for considering four-level atomic system under practical operating conditions is discussed to realize CPT phenomena. Implemented a four-level atomic model to compute the theoretical CPT resonance. Developed and introduced an empirical parameter into four-level atomic model to account for the dimension of the cell. Devised and implemented algorithm for solving this four-level model using Runge-Kutta $4^{th}$ order numerical integration method. With the developed model, CPT resonances are simulated for different lengths of the cell and the corresponding behavior is discussed. Further, various factors effecting CPT resonance performance for application in atomic clock are highlighted. Theoretical computation of ground state relaxation is carried out with respect to dimension of the cell, cell temperature and buffer gas pressure.

## 2.1 Coherent Population Trapping

This section describes the phenomenon of CPT in alkali atoms. The energy level structure of alkali atoms is discussed along with relevant energy transitions between hyperfine energy levels (i.e., *D1* and *D2* lines in Rb atoms) that can excite the CPT phenomenon in these atoms. CPT phenomenon is a demonstration of quantum interference due to coherence in multi-level quantum systems. The CPT phenomenon was first observed in sodium (Na) atoms as a decrease in fluorescence emission [49]. This phenomenon can be easily understood by considering a three-level atomic configuration in alkali atoms, called as Lambda system. A detailed description of the quantum interference phenomenon in three-level as well as four-level atomic configurations is provided in the subsequent sections.

### 2.1.1 CPT phenomenon in three level system

**Hyperfine structure in alkali atoms**

Alkali atoms are the Group-1A elements in the periodic table namely, Hydrogen (H), Lithium (Li), Sodium (Na), Potassium (K), Rubidium (Rb), Cesium (Cs) and Francium (Fr). These elements consist a single valence electron in their outermost electronic orbit. This chapter focuses on the CPT phenomenon in Rb alkali atoms. The atomic number of the Rb atom is 37, which indicates the total number of electrons distributed among different electron orbitals as given by $1s^2 2s^2 2p^6 3s^2 3p^6 3d^{10} 4s^2 4p^6 5s^1$. Here, the integers 1 to 5 indicate the principal quantum numbers. The symbols '$s$', '$p$' and '$d$' correspond to the orbital angular momentum ($l$) of electron and their values are given by 0, 1 and 2, respectively. The superscripts indicate the number of electrons available in the corresponding orbitals. In the ground state electronic configuration of Rb, the electrons are filled up to $4p$ orbitals (i.e., 36 electrons), and a single valence electron is available in the $5s$ orbital. Under the excitation condition, the single $5s$ electron can jump to the next available $5p$ orbital.

Within the orbital, the energy levels split further and are called as fine levels. These fine structure energy levels are due to Coulomb and spin orbit interactions. The Coulomb interaction is related to the electrostatic potential energy between electron-electron pair and electron-nucleus. The Spin-orbit interaction is associated with the orientation energy of the electron magnetic dipole moment in the internal magnetic field of the atom. Fine structure energy levels are commonly described by the $L - S$ coupling scheme, where $\boldsymbol{L}$ and $\boldsymbol{S}$ are the quantum numbers that indicate the magnitudes of total orbital angular momentum and total electronic spin angular momentum, respectively.

Furthermore, the total electronic angular momentum quantum number ($\boldsymbol{J}$) is defined as $\boldsymbol{J} = \boldsymbol{L} + \boldsymbol{S}$. Fine structure energy states are indicated by the notation $^{2S+1}L_J$, where ($2S$+1) is called multiplicity. The value of $S$ is 1/2, and that of $L$ are 0, 1 and 2 for the orbitals '$s$', '$p$' and '$d$', respectively. The values of $J$ are taken from $|L - S|$ to $L + S$. The ground state $5s$ of Rb is described by the fine structure state $^2S_{1/2}$ with the values $L$=0, $S$=1/2 and $J$=1/2. Similarly, the fine structure states for the next energy level $5p$ are denoted by $^2P_{1/2}$ and $^2P_{3/2}$ with values $L$=1, $S$=1/2 and $J$=1/2 (i.e., 1-1/2), and 3/2 (i.e., 1+1/2), respectively.

In addition, each fine structure energy level is split into sub-levels known as hyperfine energy levels [50]. The hyperfine structure is due to the splitting of orientation energy of the nuclear magnetic moment in the magnetic field of an atom. The hyperfine energy splitting is smaller than fine splitting because the nuclear magnetic moment is smaller than the electron magnetic moment. The nuclear magnetic moment depends on the nuclear spin angular momentum ($I$), the magnitude of which depends on the nuclear structure and the isotope. Thus,

hyperfine energy levels depend on the total angular momentum ($\boldsymbol{F}$), which is defined as $\boldsymbol{F} = \boldsymbol{J} + \boldsymbol{I}$ and it takes values from $|J - I|$ to $J + I$.

Naturally occurring Rb contains two isotopes $^{85}$Rb and $^{87}$Rb which exists in the percentage ratio of ~72:28. The values of $I$ for $^{87}$Rb and $^{85}$Rb are 3/2 and 5/2, respectively. Thus, two hyperfine levels exist for $^{87}$Rb in each of the fine structure levels $^2S_{1/2}$ and $^2P_{1/2}$ ($F$=1, 2). Likewise, there are four hyperfine levels that exist in the fine structure level $^2P_{3/2}$ ($F$=0, 1, 2, 3). Figure 2.1 shows the complete energy level structure for $^{87}$Rb.

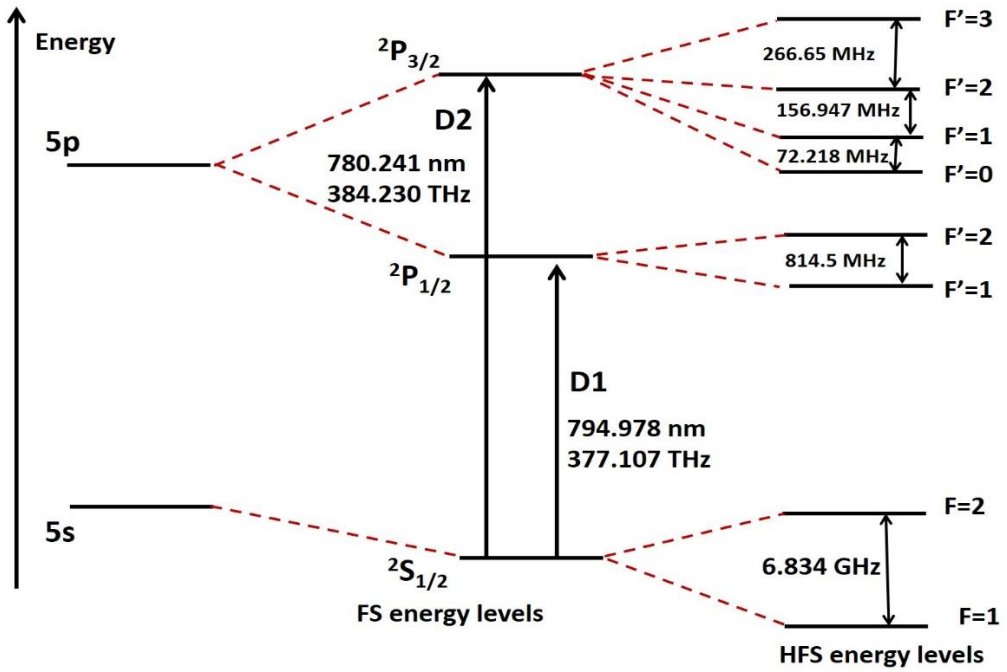


Figure 2.1: Energy levels structure in $^{87}$Rb (not to scale). FS: Fine Structure and HFS: Hyper Fine Structure. *D1* and *D2* are the fine level transitions between $^2S_{1/2} \rightarrow {}^2P_{1/2}$ and $^2S_{1/2} \rightarrow {}^2P_{3/2}$, respectively [50].

## D1 and D2 excitations in $^{87}$Rb

The *D1* and *D2* lines in $^{87}$Rb are defined as the excitations corresponding to $5^2S_{1/2} \rightarrow 5^2P_{1/2}$ and $5^2S_{1/2} \rightarrow 5^2P_{3/2}$, respectively, as shown in Figure 2.1. The wavelengths (frequencies) corresponding to the *D1* and *D2* lines are 794.978 nm (377.107 THz) and 780.241 nm (384.230 THz), respectively. Table 2.1 provides a comparison of the optical transition properties between *D1* and *D2* lines [50].

Table 2.1: Transition optical properties for *D1* and *D2* excitation lines of $^{87}$Rb atoms. Source: [50].

| Parameter | Symbol | D1 line | D2 line |
|---|---|---|---|
| Frequency | $\omega_0$ | $2\pi$ . 377.107 THz | $2\pi$ . 384.230 THz |
| Transition energy | $\hbar\omega_0$ | 1.559 eV | 1.589 eV |
| Wavelength | $\lambda$ | 794.978 nm | 780.241 nm |
| Life time | $\tau$ | 27.679 ns | 26.2348 ns |
| Decay Rate/Natural line width (FWHM) | $\Gamma$ | 36.129x10$^{-6}$ s$^{-1}$<br>$2\pi$ . 5.75 MHz | 38.117x10$^{-6}$ s$^{-1}$<br>$2\pi$ . 6.0666 MHz |

The significant difference between the excitation lines *D1* and *D2* is in the hyperfine structure of excited states, that is $^2P_{1/2}$ and $^2P_{3/2}$. The excited state $^2P_{1/2}$ comprises only two hyperfine levels ($F'$=1, 2), whereas the state $^2P_{3/2}$ exhibits four hyperfine levels ($F'$=0, 1, 2, 3). The selection rules for energetic transition among these levels are, $\Delta F$=0, ±1. *D1* transitions can occur between $^2S_{1/2}$ hyperfine ground states and both hyperfine levels of $^2P_{1/2}$ (i.e., $F'$=1, 2). Whereas the *D2* transitions can occur between $^2S_{1/2}$ hyperfine ground states and only two hyperfine levels of $^2P_{3/2}$ (i.e., $F'$=1, 2). Uncoupled hyperfine levels of $^2P_{3/2}$ (i.e., $F'$=0, 3) do not participate in the preparation of coherence. Therefore, atoms which are trapped in these uncoupled levels due to direct, i.e., one photon absorption, can reduce the number of atoms participating in CPT phenomenon involving *D2* transitions. In addition, this also reduces the lifetime of resulting coherent dark state. The effect of these light-atom interaction would lead to decrease in CPT resonance contrast and an increase in its linewidth when compared to the *D1* line excitation [51]. The detailed discussion on CPT dynamics is provided in the subsequent sections. Further, Stahler et al. [51] also discusses another major difference between these two excitation schemes in terms of Clebsch - Gordan (C-G) coefficients. They have concluded that *D1* line is more advantageous than *D2* line with respect to superior CPT resonance characteristics. The work presented in this thesis focuses on CPT phenomena with respect to *D1* excitation in $^{87}$Rb atoms.

## Quantum interference and dark resonance

As stated earlier, CPT phenomenon is a quantum interference process in a three-level energy system under optical pumping. Consider two long lived hyperfine ground states $|1>$, $|2>$ and a common excited state, $|3>$ in the $^{87}$Rb atom as shown in Figure 2.2 (known as ʌ-

configuration). Quantum interference can be excited in these atoms when there are two coherent laser fields that can couple these two ground states to a common excited state. When the first laser field corresponding to the transition from $|1>$ to $|3>$ is applied, the atoms in state $|1>$ absorb the light and are pumped to an excited state $|3>$, from which they decay to both the ground states $|1>$ and $|2>$. Due to the continuous pumping of the laser field, all the atoms in state $|1>$ are pumped to $|2>$ via the excited state, resulting in a decrease in absorption. Now, when the second laser field corresponding to the transition from $|2>$ to $|3>$ is applied, all the atoms in $|2>$ are pumped to $|3>$ and then back to $|1>$ and $|2>$. Thus, the absorption of both laser fields is observed under simultaneous excitation of these fields. When the condition for Raman resonance occurs, i.e., the frequency difference between synchronized laser fields is equal to the separation of hyperfine ground states, then the atoms do not absorb light. This is because these two transition probabilities interfere destructively and atoms are therefore trapped in a new state called the dark state, which is referred to as non-coupled state. This phenomenon is referred to as Coherent Population Trapping (CPT) [48], [52], [53], [54], [55].

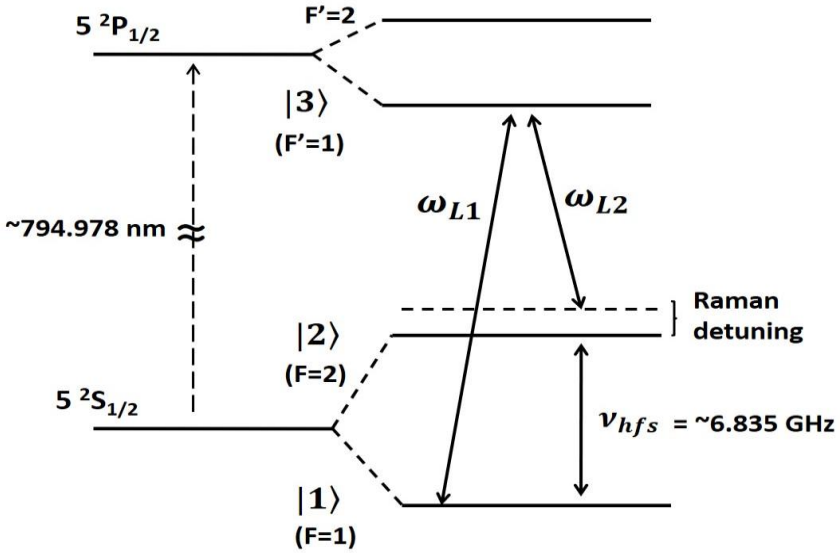


Figure 2.2: A ʌ-system involving $^{87}$Rb hyperfine energy levels for CPT excitation.

The CPT phenomenon can be described in detail by considering a semi-classical approach, i.e., the light field is treated classically, and the atomic levels are described using quantum mechanics. As depicted in Figure 2.2, two ground states, $|1>$ and $|2>$ are coupled to a common excited state $|3>$ by a bi-chromatic laser field. Here, the frequency components of laser field are $\omega_{L1}$ and $\omega_{L2}$, acting on $|1> \rightarrow |3>$ and $|2> \rightarrow |3>$, respectively. The amplitude of the optical field, $E(t)$, can be described as [52],

$$E(t) = \varepsilon_{L1} e^{-i(\omega_{L1} t + \varphi_1)} + \varepsilon_{L2} e^{-i(\omega_{L2} t + \varphi_2)} \quad (2.1)$$

Here $\varepsilon_{L1}, \varepsilon_{L2}$, $\omega_{L1}$, $\omega_{L2}$ and $\varphi_1$, $\varphi_2$ are the (complex) amplitude, angular frequencies, and phases of the applied laser fields respectively. The Raman detuning, $\delta_R$ between the levels can be written as

$$\delta_R = \omega_{L1} - \omega_{L2} - (\Omega_2 - \Omega_1) \quad (2.2)$$

Where, $\Omega_1 = 2\pi\nu_1$ and $\Omega_2 = 2\pi\nu_2$ are the angular frequencies corresponding to the transitions $|1> \rightarrow |3>$ and $|2> \rightarrow |3>$, respectively such that $\nu_1 - \nu_2 = \nu_{hfs}$. $\nu_{hfs}$ is the ground state hyperfine splitting, i.e., clock reference frequency.

The laser-atom interaction Hamiltonian ($\hat{H}_{int}$) for the optical field can be written as [56]:

$$\hat{H}_{int} = \frac{\hbar\omega_{R1}}{2} e^{-i(\omega_{L1} t + \varphi_1)} |3><1| + \frac{\hbar\omega_{R2}}{2} e^{-i(\omega_{L2} t + \varphi_2)} |3><2| + h.c. \quad (2.3)$$

Here, $h.c.$ is the Hermitian conjugate. $\omega_{R1}$, $\omega_{R2}$ are the Rabi frequencies that indicate the strength of laser-atom interaction of electric dipole transition between excited state $|3>$ and ground levels $|1>$ and $|2>$, respectively. The non-coupled state $|NC>$ is expressed as given in Equation 2.4.

$$|NC> = \frac{1}{\sqrt{|\omega_{R1}|^2 + |\omega_{R2}|^2}} (\omega_{R2} e^{-i\Omega_1 t} |1> - \omega_{R1} e^{-i\Omega_2 t + i(\varphi_2 - \varphi_1)} |2>) \quad (2.4)$$

The transition amplitude of the non-coupled state to the excited state $|3>$ is given by

$$\langle 3|H_{int}|NC\rangle = \frac{\hbar\omega_{R1}\omega_{R2}}{2\sqrt{|\omega_{R1}|^2 + |\omega_{R2}|^2}} e^{-i(\Omega_1 + \omega_{L1})t - i\varphi_1} (1 - e^{i\delta_R t - i(\varphi_2 - \varphi_1)}) \quad (2.5)$$

When the two-photon Raman resonance condition is fulfilled, i.e., Raman detuning, $\delta_R$=0 ($\omega_{L1} - \omega_{L2} = \Omega_2 - \Omega_1$), and phase difference $\varphi_2 - \varphi_1 = 2n\pi$ (where, n=0, 1, 2 ….), the transition amplitude is given by Equation 2.6.

$$< 3|\hat{H}_{\text{int}}|\text{NC} > = 0 \tag{2.6}$$

Thus, under the resonance condition, the transition amplitude from the $|\text{NC}>$ state to the excited state $|3>$ is zero and therefore an atom in the $|\text{NC}>$ state cannot absorb photons. More specifically, this condition is the result of "quantum interference" between the transitions from states $|1>$ and $|2>$ to state $|3>$ under the influence of an exciting optical field. Therefore, the $|\text{NC}>$ state is called a dark (or "non-coupled") state, and the corresponding dark resonance (CPT resonance) has a narrow linewidth, which is determined by the properties of the ground state. This feature makes CPT phenomena very attractive for its application in atomic clocks.

When the absorption of the optical field in an atomic cell is measured as a function of two-photon detuning, a sharp change (reduction) in the absorption will appear near the resonance condition, as shown in Figure 2.3. This is referred to as CPT (dark) resonance, and its peak is used as clock reference frequency in the CPT based atomic clock.

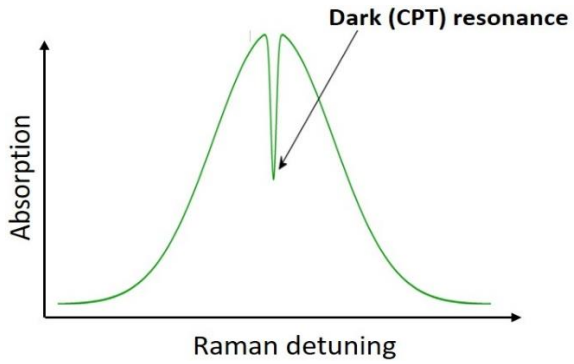


Figure 2.3: CPT resonance curve in an atomic system with ∧-configuration.

The density matrix formalism is another approach to describe the CPT phenomena [57]. For an ideal symmetric three-level system, the solution of the density matrix equations provides the linewidth and amplitude of CPT resonance as given in Equations 2.7 and 2.8, respectively [58]. Further details on linewidth and amplitude are discussed in Section 2.1.2.

$$\Delta\nu_{FWHM} = \frac{1}{\pi}\left(\gamma_2 + \frac{{\omega_R}^2}{\Gamma^*}\right) \tag{2.7}$$

$$\text{H} \propto n_{Rb}\frac{{\omega_R}^4}{{\Gamma^*}^3}\frac{1}{\left(\gamma_2 + \frac{{\omega_R}^2}{\Gamma^*}\right)} \tag{2.8}$$

Here, $\gamma_2$ and $\Gamma^*$ are the relaxation rates in the ground and excited states, respectively. H is amplitude of CPT resonance. Assumption for an ideal symmetric three-level system is $\omega_{R1} = \omega_{R2} = \omega_R$. The Rabi frequency, $\omega_R$ is proportional to the laser excitation intensity and represents the strength of laser-atom interaction and, $n_{Rb}$ is the Rb atomic density. From Equation 2.7 it is clear that Full Width at Half Maximum (FWHM) is predominantly limited by $\gamma_2$ at much lower laser excitation intensity values. The magnitude of $\gamma_2$ depends on contributions from various relaxation mechanisms in the atomic vapor cell, i.e., relaxation by alkali atom-buffer gas collisions ($\gamma_{2\mathrm{BG}}$), alkali atoms spin-exchange interaction ($\gamma_{2\mathrm{SE}}$) and alkali atom-cell wall collisions ($\gamma_{2\mathrm{W}}$) [59], [60], [61], [62]. Thus, for a Rb vapor cell filled with buffer gas, the ground state relaxation rate, $\gamma_2$, is given by Equation 2.9. In atomic clocks based on alkali vapor cells, buffer gas is added to vapor cells to reduce the ground state relaxation and Doppler broadening [63]. Section 2.3 provides the contribution of the individual mechanisms based on theoretical calculations taking into account different cell dimensions and buffer gas pressure values.

$$\gamma_2 = \gamma_{2BG} + \gamma_{2SE} + \gamma_{2W} \tag{2.9}$$

## Comparison between CPT and EIT

CPT and Electromagnetically Induced Transparency (EIT) [64], [65] are two important phenomena based on quantum interference. The fundamental physics underlying in both phenomenon is related but have few differences. Both phenomena involve the coupling of two ground states to common excited states using two laser sources. The major difference is that the CPT uses two laser sources of equal strengths, while EIT uses, one strong and the other one weak. CPT is well explained using Lambda ($\Lambda$) system. EIT can also be explained using Lambda ($\Lambda$), Ladder and vee (V) systems as well [66], [67] .

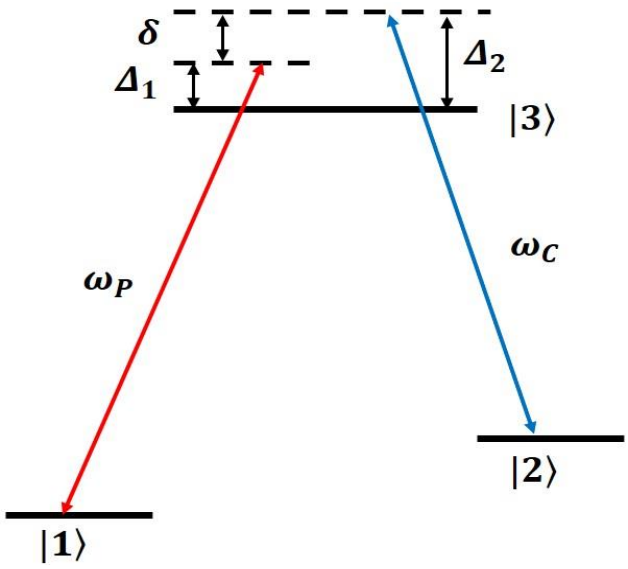


Figure 2.4: A three level system (hyperfine Λ system) for CPT and EIT phenomenon. $\boldsymbol{\delta}$ is Raman detuning.

Figure 2.4 shows a three-level system considered to explain the working principles of CPT and EIT. Here, $|1\rangle$, $|2\rangle$ are the ground states and $|3\rangle$ is excited state. $\omega_P$ and $\omega_C$ are the Rabi frequencies of probe and control laser sources coupling the transitions $|1\rangle \rightarrow |3\rangle$ and $|2\rangle \rightarrow |3\rangle$ with corresponding single photon detuning's $\Delta_1$and $\Delta_2$, respectively. In CPT phenomenon, two long lived ground states are coupled to a common excited state by two coherent laser sources of equal strengths i.e., $\omega_P = \omega_C$ . The corresponding transition probabilities undergo destructive quantum interference and create a new state in which the atoms are trapped and not seen by laser sources. This state is called dark state and under this condition the transmission of laser field through atomic medium increases.

In an EIT phenomenon, two near resonant laser sources are also used to excite atoms but with different strengths (strong control and weak probe, i.e., $\omega_P \ll \omega_C$) [66], [67]. By applying a strong control field, the energy levels of atom shift from line centre due to AC stark effect. Then, the applied weak probe field shows enhanced transparency. It is therefore referred to as electromagnetically induced transparency, since the transparency is induced by the control laser. Thus, both CPT and EIT are two photon processes as the transitions involve two different levels. Both control and probe lasers have equal significance in CPT. Conversely, in EIT, strong control laser induces the entire transparency, while weak probe laser is used to measure this transparency.

Both EIT and CPT phenomena find various applications in atomic physics and quantum optics. EIT is also used in the development of magnetometers, quantum information

processing, quantum memory, slow light, light storage, and optical switches [68], [69], [70], [71], [72], [73], [74], [75]. CPT is most commonly used in the development of atomic clocks and magnetometers [48], [58], [76], [77], [78], [79], [80] because most experiments use a balanced Λ-system with equal intensities of the two optical fields. This configuration allows reduction of some systematic effects such as light shifts and can be realized experimentally by direct frequency modulation of a single laser. CPT is also used in atom laser cooling, quantum information processing, and precision spectroscopy [57], [81], [82], [83], [84].

## 2.1.2 Characteristics of CPT resonance

The performance of CPT resonance is studied in terms of its characteristics such as contrast, FWHM, quality figure, and frequency shift. Figure 2.5 shows the typical CPT resonance, i.e., the transmission of laser field as a function of the Raman detuning (see Figure 2.3).

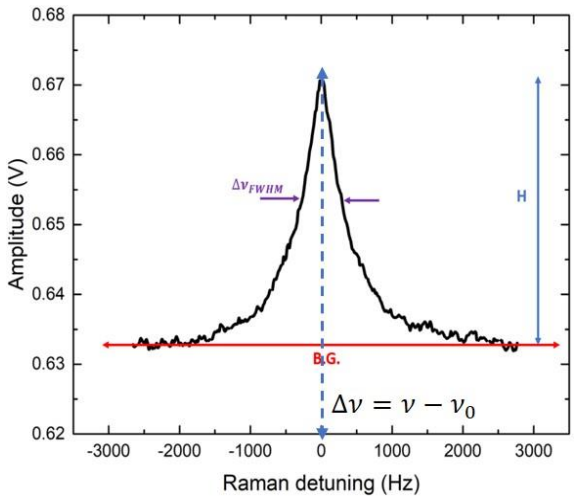


Figure 2.5: CPT resonance measured as transmission of laser excitation field through atomic vapor as function of Raman detuning. B.G. is background. *H* is height/amplitude. $\boldsymbol{\Delta\nu_{FWHM}}$ is FWHM and $\boldsymbol{\Delta\nu}$ is frequency shift.

Contrast (*C*) is defined as the ratio of amplitude (*H*) of resonance to its background. $\Delta\nu_{FWHM}$ indicates the FWHM of resonance. One of the important parameters is the quality figure (*q*) of CPT resonance, which is defined as the ratio between contrast and FWHM.

$$C = \frac{Amplitude\ above\ background\ (H)}{Back\ ground\ level\ (B.G.)} \tag{2.10}$$

$$q = \frac{Contrast\ (C)}{FWHM} \tag{2.11}$$

The frequency shift (Δν) is the deviation of resonance centre frequency from the theoretical value. Further details on the significance of quality figure and frequency shift are discussed in Section 2.3.

### 2.1.3 Application of CPT in atomic frequency standard

The CPT phenomenon in alkali atoms is widely employed in developing atomic frequency standard (atomic clock) [46], [47], [48], [58], [76], [85], [86]. The CPT resonance can be used as a reference to lock the crystal oscillator and control its output frequency. Since the CPT resonance depends on the characteristics of long lived hyperfine ground states, a narrower line width (~ Hz) is achievable. CPT based atomic clocks have few advantages over double resonance (DR) Rb atomic clocks. One of the major advantages is the absence of a microwave cavity, which enables miniaturization and reduces the power requirements. The requirement of Rb lamp, filter cell and microwave cavity (see Section 1.2.2.3) is replaced by a single laser diode (see Section 3.1). The short-term frequency stability of the clock depends primarily on the characteristics of CPT resonance, and it is given by [48], [60]

$$\sigma(\tau) = \frac{1}{4\nu_{\mathrm{hfs}}}\sqrt{\frac{e}{I_{\mathrm{bg}}}}\frac{1}{q}\tau^{-1/2} \tag{2.12}$$

where $\nu_{hfs}$ is primarily clock reference frequency which is the frequency separation between hyperfine ground states, $I_{bg}$ is background current generated by photodetector, $e$ is electron's charge, $\tau$ is averaging time and $q$ is the quality figure as defined in Section 2.1.2. Thus, the short-term frequency stability of atomic clock can be improved by maximizing $q$ of CPT resonance which can be achieved by improving its contrast and reducing FWHM. A detailed discussion on the factors that affect the quality figure is provided in Section 2.3.

## 2.2 Four level atomic model

It may be noted that when atomic vapor cells are operated at elevated temperatures and relatively higher laser excitation intensities, the atomic medium in the vapor cell becomes optically thick. In such cases, the three-level atomic model is not adequate to model the CPT

resonance and the four-level atomic model provides the realistic behaviour of CPT resonance. This section describes the construction of a modified four-level theoretical model to simulate the CPT resonance which accounts for parametric variation in the atomic vapor cell. Theoretical analysis is carried out by modelling the evolution of laser-atom interaction in the atomic ensemble along the length of atomic vapor cell. To simulate the CPT resonance, the variation of Rabi frequency that corresponds to the *D1* hyperfine transition in $^{87}$Rb atoms is estimated as a function of Raman detuning frequency.

## 2.2.1 Theory

The Rabi frequency of a given atomic transition is proportional to the amplitude of laser radiation given by Equation 2.13 [87].

$$\omega_{Ri} = \left(\frac{\mathcal{E}_{Li}}{\hbar}\right) < i|\boldsymbol{er}.\boldsymbol{e_\lambda}|j > \tag{2.13}$$

Here, $\varepsilon_{Li}$ is the amplitude of laser radiation, $\hbar$ is modified Planck's constant and $< i|\boldsymbol{er}.\boldsymbol{e_\lambda}|j > = d_{ij}$ is the electric dipole matrix element of the transition from ground state $i$ to excited state j. $\omega_{R1}$, $\omega_{R2}$ are the Rabi frequencies corresponding to the transitions from ground states $|1>$, $|2>$ to excited state $|3>$, respectively. Using the relation $I_L = \frac{1}{2}c\varepsilon_0{\varepsilon_{Li}}^2$ [50], and with assumption $\omega_{R1} = \omega_{R2} = \omega_R$, Rabi frequency can be expressed using Equation 2.14.

$$\omega_R = \sqrt{\frac{2I_L{d_{ij}}^2}{c\varepsilon_0\hbar^2}} \tag{2.14}$$

The Rabi frequency varies as a function of laser excitation intensity ($I_L$), and Equation 2.14 provides the Rabi frequency that corresponds to the incident laser light at the entrance of the vapor cell. When laser frequency is tuned to CPT resonance, Rabi frequency varies along the length of vapor cell as CPT phenomena changes light absorption in the cell. Moreover, for application in atomic clocks, the propagation effect is of concern as clocks are operated at relatively higher temperature for improving the amplitude of the signal which increases Rb density that affects the Rabi frequency. For each incident laser excitation intensity, the resulting CPT resonance is modelled by estimating the Rabi frequency at the exit of the vapor cell after

transmitting through the length of the cell as function of Raman detuning. The resonance characteristics are then extracted by performing a suitable curve fit.

The four-level atomic system [48] used in the modelling of CPT resonance is shown in Figure 2.6. The collisions between buffer gas atoms and Rb atoms cause the atoms in the excited state (F′ = 1) to decay to all possible ground state (F = 1&2) Zeeman levels. Under circular polarization $\sigma^+$ (or $\sigma^-$), the transitions from $m_F = +2$ (or $m_F = -2$) are forbidden i.e., the atoms in these states do not contribute to CPT phenomenon. These atoms are referred to as trapped atoms and are represented by a fourth level known as "trap level" [48], [60] as shown in Figure 2.6. The three-level model with this trap is called as four level atomic system.

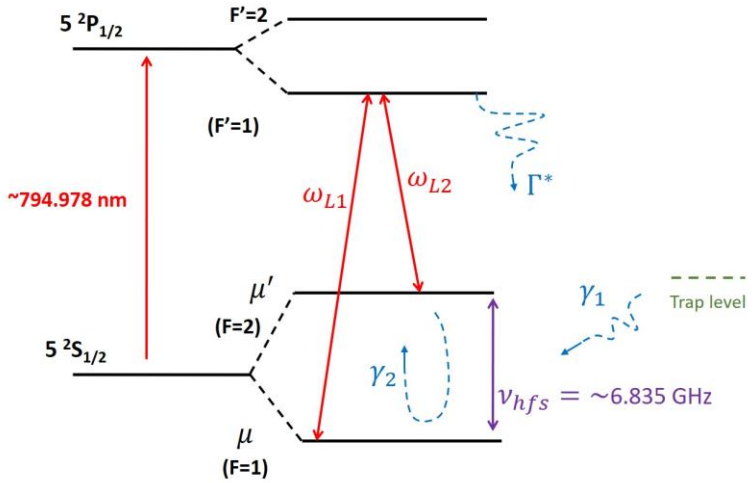


Figure 2.6: Four level atomic system used to theoretically calculate the CPT resonance. The trap level represents the fourth level of trapped atoms that do not contribute to CPT phenomena.

With four level model, characteristics of CPT resonance can be studied by estimating the variation in Rabi frequency of transmitted laser light due to absorption along the length of vapor cell which is represented by Equation 2.15 [48], [88].

$$\frac{\partial \omega_R}{\partial z} = \alpha_a \, Im\delta_{\mu m} \tag{2.15}$$

Where, $\alpha_a$ is the absorption coefficient, and $Im\delta_{\mu m}$ is the imaginary part of the density matrix element in which $\delta_{\mu m}$ describes the induced coherence in the atomic medium due to laser excitation. $Im\delta_{\mu m}$ is given by Equation 2.16 [48].

$$Im\delta_{\mu m} = -\frac{\omega_R(z)}{\Gamma^*}\left[\frac{1}{3} - \frac{\left(\frac{2}{9}\right)\frac{\omega_R^2(z)}{2\Gamma^*\gamma_1}}{1+\left(\frac{2}{3}\right)\frac{\omega_R^2(z)}{2\Gamma^*\gamma_1}} + \delta_{\mu\mu'}^r\right] \tag{2.16}$$

Here, $\delta_{\mu\mu'}^r$ is the real part of $\delta_{\mu\mu'}$, i.e., the ground state coherence created by the CPT phenomenon which is expressed as

$$\delta_{\mu\mu'} = \frac{-\left(\frac{2}{3}\right)\frac{\omega_R^2(z)}{2\Gamma^*}\left(\gamma_2+\frac{\omega_R^2(z)}{\Gamma^*}\right) + \left(\frac{4}{9}\right)\frac{\frac{\omega_R^4(z)}{4{\Gamma^*}^2}\left(\gamma_2+\frac{\omega_R^2(z)}{\Gamma^*}\right)}{\gamma_1\left(1+\frac{\omega_R^2(z)}{3\Gamma^*\gamma_1}\right)}}{\left(\gamma_2+\frac{\omega_R^2(z)}{\Gamma^*}\right)^2+(\omega_{12}-\omega_{\mu'\mu})^2} + i\frac{\left(\frac{2}{3}\right)\frac{\omega_R^2(z)}{2\Gamma^*} - \left(\frac{4}{9}\right)\frac{\frac{\omega_R^4(z)}{4{\Gamma^*}^2}}{\gamma_1\left(1+\frac{\omega_R^2(z)}{3\Gamma^*\gamma_1}\right)}(\omega_{12}-\omega_{\mu'\mu})}{\left(\gamma_2+\frac{\omega_R^2(z)}{\Gamma^*}\right)^2+(\omega_{12}-\omega_{\mu'\mu})^2} \tag{2.17}$$

By substituting the expression of $\delta_{\mu\mu'}^r$ i.e., real part of $\delta_{\mu\mu'}$ from Equation 2.17, the variation in Rabi frequency can be written as shown in Equation 2.18.

$$\frac{\partial\omega_R}{\partial z} = -\beta\alpha_a\frac{\omega_R(z)}{\Gamma^*}\left[\frac{1}{3} - \frac{\left(\frac{2}{9}\right)\frac{\omega_R^2(z)}{2\Gamma^*\gamma_1}}{1+\left(\frac{2}{3}\right)\frac{\omega_R^2(z)}{2\Gamma^*\gamma_1}} + \frac{-\left(\frac{2}{3}\right)\frac{\omega_R^2(z)}{2\Gamma^*}\left(\gamma_2+\frac{\omega_R^2(z)}{\Gamma^*}\right) + \left(\frac{4}{9}\right)\frac{\frac{\omega_R^4(z)}{4{\Gamma^*}^2}\left(\gamma_2+\frac{\omega_R^2(z)}{\Gamma^*}\right)}{\gamma_1\left(1+\frac{\omega_R^2(z)}{3\Gamma^*\gamma_1}\right)}}{\left(\gamma_2+\frac{\omega_R^2(z)}{\Gamma^*}\right)^2+(\omega_{12}-\omega_{\mu'\mu})^2}\right] \tag{2.18}$$

Here, $\Gamma^*$: Decay rate of excited state

$\omega_R(z)$: Rabi frequency at a position $z$ along the length of vapor cell

$\gamma_1$: Relaxation rate of ground state population

$\gamma_2$: Relaxation rate of ground state coherence and is the measure of collisional interactions in the atomic vapor cell

$\omega_{\mathrm{L}1}, \omega_{\mathrm{L}2}$: Angular frequencies of laser sidebands ($\omega_{12} = \omega_{\mathrm{L}1} - \omega_{\mathrm{L}2}$)

$\omega_{\mu'\mu}$: Angular frequency of hyperfine ground state

Here, a new empirical parameter $\beta$ is developed and incorporated into Equation 2.18 to account for the cell dimension (radius). This parameter is referred to as cell dimension dependent scale factor and represented by $\beta = b_0 + b_1R + b_2R^2$. Here, $R$ is the cell radius and $b_0$, $b_1$, $b_2$ are constants dependent on cell dimension.

## 2.2.2 Solving four-level model

An analytical solution to Equation 2.18 is not possible because it is highly non-linear and complex. To solve this model Runge-Kutta 4$^{th}$ order (RK4) numerical integration method [89] is used. RK4 is a numerical integration technique for solving the differential equation of the form, $\frac{dy}{dx} = f(x, y)$, with the initial condition $y(0) = y_0$. Mathematical expressions involved in RK4 method are derived based on Equation 2.19.

$$y_{i+1} = y_i + (a_1 k_1 + a_2 k_2 + a_3 k_3 + a_4 k_4)h \tag{2.19}$$

By knowing the value of $y = y_i$, at $x_i$, the value of $y = y_{i+1}$, at $x_{i+1}$ can be found. Here, $h = x_{i+1} - x_i$. By applying the Taylor series, Equation 2.19 can be written in the form of a solution, as shown in Equation 2.20.

$$y_{i+1} = y_i + \frac{1}{6}(k_1 + 2k_2 + 2k_3 + k_4)h \tag{2.20}$$

Here $k_1$, $k_2$, $k_3$ and $k_4$ are intermediate slopes of integrating function which are given by

$$\begin{aligned} k_1 &= f(x_i, y_i) \\ k_2 &= f\left(x_i + \frac{h}{2}, y_i + \frac{h}{2}k_1\right) \\ k_3 &= f\left(x_i + \frac{h}{2}, y_i + \frac{h}{2}k_2\right) \\ k_4 &= f(x_i + h, y_i + hk_3) \end{aligned} \tag{2.21}$$

Similarly, RK4 numerical integration method has been employed to calculate the Rabi frequency along the length of vapor cell. For each incident laser intensity, the Rabi frequency at any position ($z$) along the length of vapor cell is given by

$$\omega_R(z = l) = \omega_R(z = l - \delta l) + \delta\omega_R \tag{2.22}$$

Where, $\delta\omega_R = \frac{\delta l}{6}(k_1 + 2k_2 + 2k_3 + k_4)$ and $k_1, k_2, k_3, k_4$ are given by

$$k_1 = f\big(\omega_R(z = l - \delta l)\big) = \frac{\partial \omega_R(z = l - \delta l)}{\partial z}$$
$$k_2 = f\left(\omega_R(z = l - \delta l) + \frac{\delta l}{2} k_1\right)$$
$$k_3 = f\left(\omega_R(z = l - \delta l) + \frac{\delta l}{2} k_2\right) \quad (2.23)$$
$$k_4 = f(\omega_R(z = l - \delta l) + \delta l k_3)$$

$\delta l$ is the incremental length of vapor cell ($\delta l = 1$ mm in our calculation) and $l = 1\delta l, 2\delta l, 3\delta l, \ldots\ldots, L$. Rabi frequency at the exit of a vapor cell with length $L$ (i.e., $\omega_R(z = L)$) is then calculated through the iterative process by considering $l = \delta l$ to $L$.

### 2.2.3 Simulation

The variation of Rabi frequency is simulated as a function of Raman detuning. Below is the step-by-step procedure followed to solve the four-level atomic model.

Rabi frequency ($\omega_R$) changes along the length of the cell as laser intensity changes due to absorption. For a given laser intensity value the variation of Rabi frequency ($\omega_R$) is calculated. The initial value of Rabi frequency $\omega_R(0)$ is calculated using Equation 2.14. Raman detuning (RD) values are selected with a range from -2000 Hz to +2000 Hz. For a given RD value, the variation of Rabi frequency is calculated along the length of the cell i.e., from z=0 ($\omega_R(0)$) to z=L ($\omega_R$(L)) (see Figure 2.7) iteratively. This calculation is carried out by using Equation 2.23 together with Equation 2.18 by considering step size $\delta l$=1 mm. A similar process is followed to calculate Rabi frequency at the end of the cell for all values of the incident laser intensity values.

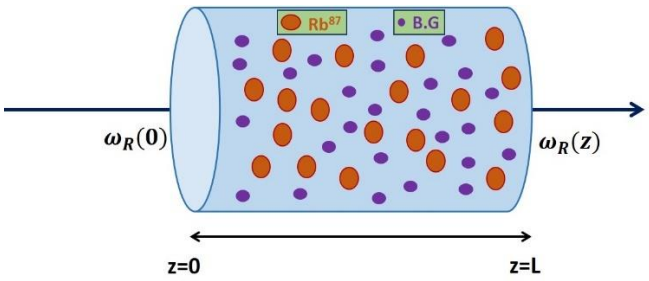


Figure 2.7: Vapor cell filled with $^{87}$Rb atoms (big size circles) and buffer gas (small size circles). $\boldsymbol{\omega_R(0)}$ and $\boldsymbol{\omega_R(z)}$ are the Rabi frequencies corresponding to the laser intensities at the entrance and exit of the vapor cell.

An approximation of $\gamma_1 = \gamma_2$ is used in our theoretical calculation [87]. The values considered for the simulation are $\gamma_2$=630 rad/s and $\Gamma^*$=1.5E10 $s^{-1}$, $\alpha_a$=4.5E11 (at T=71 $^0$C), cell radius, R=12.5 mm, and laser intensity of 5.0 W/m$^2$. Figure 2.8 shows the simulated CPT resonances (Rabi frequencies) with respect to Raman detuning for cells with different lengths ($L$). These CPT resonances follows the Lorentzian form and its characteristics are extracted by performing corresponding mathematical fit. Further details on extraction of CPT resonance characteristics are discussed in Section 3.7. Figure 2.8 indicates that the contrast is increasing and FWHM is reducing with increase in cell length.

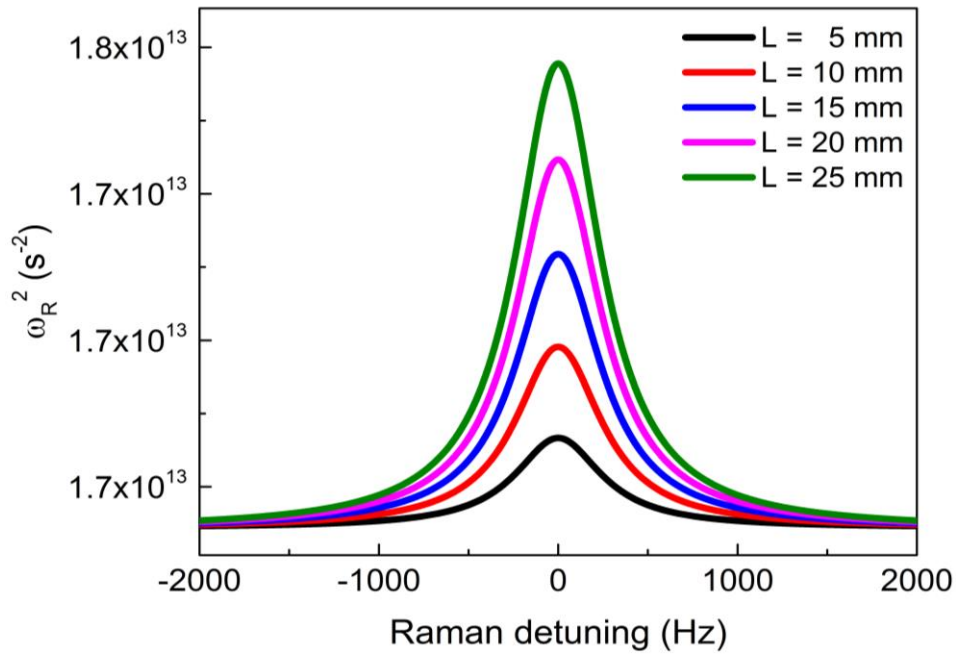


Figure 2.8: CPT resonances (Rabi frequencies) simulated by RK4 numerical integration (Equation 2.23) using four level atomic model (Equation 2.18) for cells with different lengths (L).

## Effect of cell length on quality figure

The effect of cell length on the quality figure, $q$ is studied by theoretical computation of the CPT resonances as explained above with length up to 300 mm. The quality figure, $q$ is then calculated by extracting contrast and FWHM using a Lorentzian fit to the computed CPT resonances as discussed in Section 3.7.

The $q$ values of CPT resonances in cells with lengths up to 300 mm are calculated under various values of the laser excitation intensity ($I_L$) and plotted in Figure 2.9. For cell length values up to 30 mm, $q$ increases with the intensity of laser excitation at lower intensity values.

At higher intensity values, it decreases with increase in laser intensity due to power broadening. However, the quality figure saturates beyond a threshold value of cell length. At higher excitation intensities, this saturation length becomes longer and the quality figure tends to increase non-linearly. Though the longer cells at higher excitation intensities exhibit results in superior quality figure, they may not be suitable for application in space borne atomic clock. Moreover, light intensity dependent light shift effect could also become dominant contributor to medium and long-term frequency instability [53], [90].

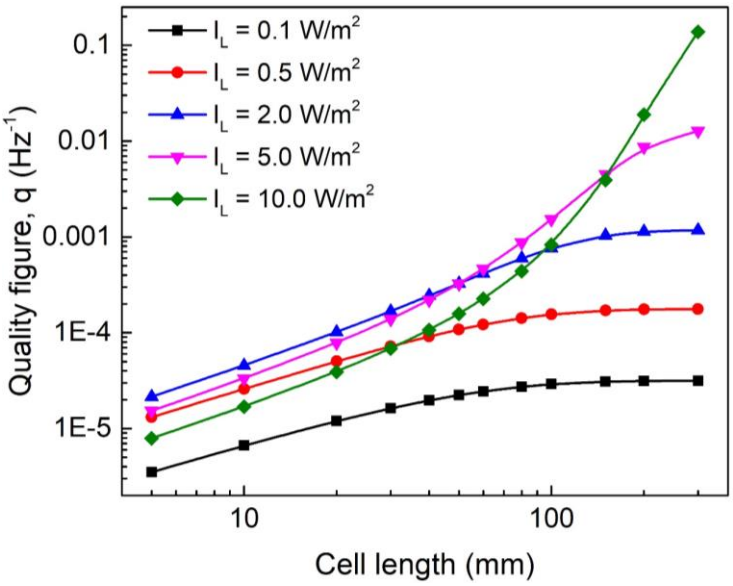


Figure 2.9: Variation of the quality figure of CPT resonance as function of cell length at different incident values of laser excitation intensities. The data points are computed using a theoretical model. Solid lines connecting the data points are provided to guide the eye.

The theoretical model developed in this section is utilized to simulate the CPT resonances for different cell dimensions (radii), cell temperatures and buffer gas pressures. Detailed discussion on these simulated results and their comparison with experimental results is provided in Chapter-4.

## 2.3 Factors affecting CPT resonance

According to Equation 2.12, short-term frequency stability of clock depends primarily on the quality figure ($q$), and thus on contrast ($C$) and full width at half maximum (FWHM) of CPT resonance (see Equation 2.11). On the other hand, medium to long-term stability of clock depend on the shift in centre frequency of resonance, known as frequency shift ($\Delta\nu$). Thus, it is essential to understand the underlying physics and optimize the operating parameters that

influence CPT resonance characteristics to improve the frequency stability of atomic clock [60], [90], [91]. The quality figure of CPT resonance is determined by the nature of laser-atom interaction in an atomic vapor cell that depends on variety of factors, viz. laser intensity [48], cell temperature [92], [93], cell dimension [62], [92], buffer gas species and its pressure in the atomic cell [9], [59], [61], [84]. The effect of control/operating parameters on CPT resonance characteristics is represented in Figure 2.10 and discussed in the following sections.

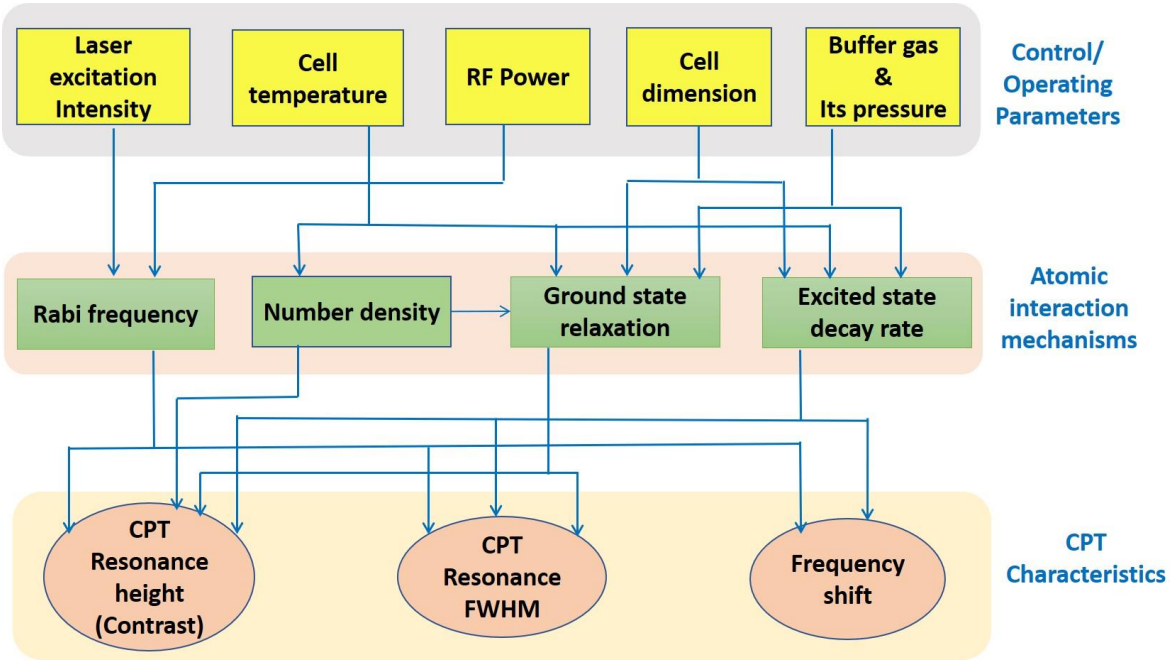


Figure 2.10: Flow chart depicting control/operating parameters that affect the CPT resonance characteristics via various atomic interaction mechanisms.

## 2.3.1 Laser excitation intensity

Rabi frequency of atomic transition is directly proportional to the amplitude of the laser excitation intensity (see Equation 2.14). According to Equations 2.7 and 2.8 both FWHM and contrast (amplitude) of CPT resonance are linearly proportional to the Rabi frequency. Therefore, the laser intensity directly influences both the amplitude of CPT resonance as well as its FWHM [58], [94]. Further, temperature of the atomic medium also influences the variation of contrast with respect to laser intensity. A detailed analysis on the dependency of CPT resonance characteristics on laser intensity is provided in Chapter 4.

In addition, the laser intensity also contributes significantly to the shift of centre frequency (peak) of CPT resonance. Frequency shift due to laser intensity is the result of AC stark effect

caused by change in amplitude of electric field which leads to shift in the atomic energy levels. The interaction of the atomic dipole moment induced by light field with the electric field of the light leads to a frequency shift in the CPT resonance, termed as light shift. Light shift can be represented as a function of laser frequency and laser intensity, as given in Equation 2.24 [95], [96]

$$\Delta\nu(\omega_L, I_L) = \frac{1}{4}|\omega_R|^2 \frac{\omega_L - \nu_0}{(\omega_L - \nu_0)^2 + \frac{\Gamma^{*2}}{4}} \tag{2.24}$$

Here, $\omega_R$ is Rabi frequency (where $|\omega_R|^2 \propto I_L$), $\omega_L$ is laser frequency, $\nu_0$ is resonance frequency, and $\Gamma^*$ is the excited state decay rate to the ground states. Equation 2.24 indicates that light shift is directly proportional to the laser intensity.

## 2.3.2 Temperature of atomic vapor

The amplitude of CPT resonance primarily depends on the number of atoms (see Equation 2.8) in the vapor cell participating in CPT phenomena which is function of temperature of vapor cell (see Equation 2.27). Cell temperature directly affects the atomic number density which in turn influences the ground state relaxation rate resulting from spin exchange collision ($\gamma_{2SE}$) as given by [59], [61], [62]

$$\gamma_{2SE} = \frac{6I+1}{8I+4}\bar{v}_{Rb-Rb}\sigma_{ex}n_{Rb} \tag{2.25}$$

Here, $I$ is nuclear spin ($I = \frac{3}{2}$ for $^{87}$Rb isotope), $\bar{v}_{Rb-Rb}$ is relative velocity of alkali-alkali atoms, $\sigma_{ex}$ is corresponding spin exchange cross section ($\sigma_{ex}$ =1.6 x $10^{-18}$ $m^2$ [61] and $n_{Rb}$ is atomic density. Thus, temperature of the atomic vapor directly impacts the FWHM of CPT resonance.

Atomic number density is a function of atomic vapor pressure in the cell which is also function of cell temperature ($T$). The vapor pressure (in Torr) for Rb atoms is given by [97]

$$\log_{10} p = A - \frac{B}{T} + CT + D\log_{10} T \tag{2.26}$$

Here, the values of constants $A$, $B$, $C$ and $D$ are different for solid and liquid phase of Rb. The values are given by $A$=-94.04826, $B$=1961.258, $C$=-0.03771687 and $D$=42.57526 (for

solid Rb, $T$<312.46 $K$) and $A$=15.88253, $B$=4529.635, $C$=0.00058663 and $D$=-2.99138 (for liquid Rb, $T$>312.46 $K$) [97].

Using ideal gas equation, the number density of Rb atoms can be computed as

$$n_{Rb} = \mathrm{F}\frac{p}{k_B T} \tag{2.27}$$

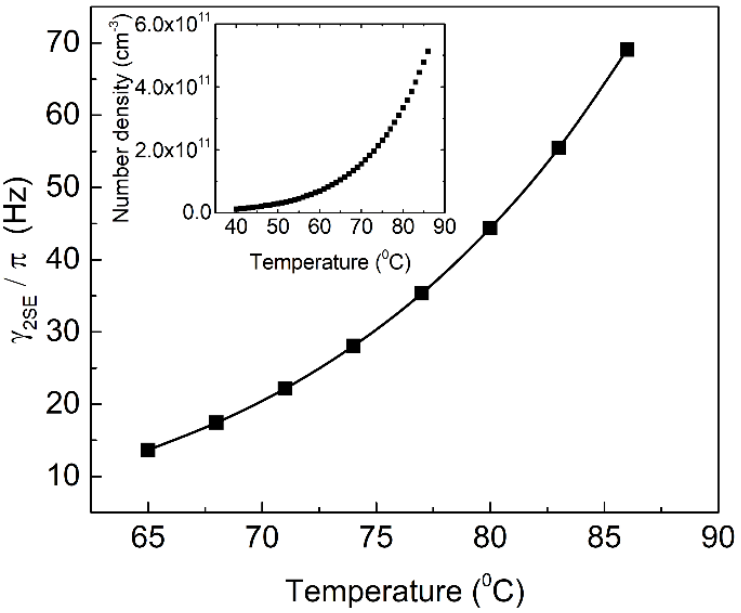


Figure 2.11: The variation of relaxation rate due to spin exchange collision ($\boldsymbol{\gamma_{2SE}}$) with respect to cell temperature. Inset: Atomic number density of $^{87}$Rb atoms as function of cell temperature.

Here, $k_B$ is Boltzmann's constant, $p$ is atomic vapor pressure, $T$ is cell temperature and $F$ is the fraction that indicates abundance of $^{87}$Rb isotope ($F \cong 0.2783$). From Equations 2.26 and 2.27, it is clear that number density of $^{87}$Rb atoms increases exponentially with cell temperature (as shown in the inset of Figure 2.11). Thus, $\gamma_{2SE}$ also increases exponentially with temperature (see Figure 2.11).

Cell temperature also influences the collisions between alkali atoms and buffer gas which results in shift of atomic hyperfine splitting. This frequency shift is referred to as temperature shift. The effect of cell temperature on contrast, FWHM and frequency shift are discussed in Chapter 4 along with the experimental results.

### 2.3.3 Dimension of vapor cell

Cell dimension is one of the important parameters that influences both the ground state relaxation rate and excited state decay rate. This results in the change in contrast, FWHM and centre frequency.

The ground state relaxation rate ($\gamma_{2W}$) due to collision of Rb atoms with cell wall depends on cell dimension which is given by [59], [62]

$$\gamma_{2W} = \left(\frac{(2.405)^2}{R^2} + \frac{\pi^2}{L^2}\right) D_0 \frac{P_0}{P} \tag{2.28}$$

Where, $L$ and $R$ are length and radius of cell, respectively; $P_0$ is reference gas pressure ($760 \times 133.323$ Pa); $P$ is buffer gas pressure in the cell; $D_0$ is diffusion constant for Rb atoms through buffer gas. The computation of $\gamma_{2W}$ with respect to buffer gas pressure is shown in Figure 2.12 for vapor cells with three different dimensions ($L$= 25 mm and $R$ = 12.5 mm, 7.5 mm, 5.0 mm) filled with Neon (Ne) buffer gas. The $D_0$ for Ne buffer gas is 2.0 x $10^{-5}$ $m^2s^{-1}$ [9], [98], [99].

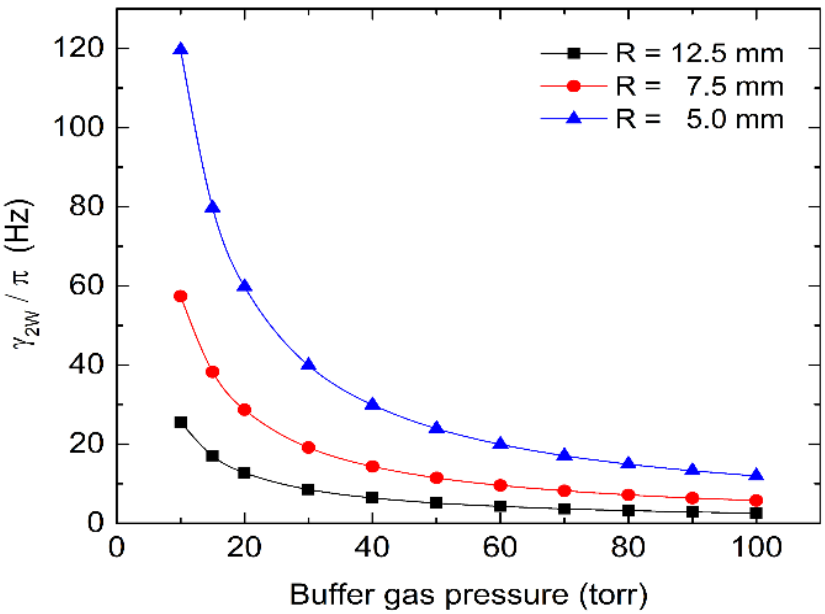


Figure 2.12: The variation of relaxation rate due to collision of Rb atoms with cell wall ($\boldsymbol{\gamma_{2W}}$) with respect to buffer gas pressure for three cells (R = 12.5 mm, 7.5 mm, and 5 mm) maintained at T = $71^0$ C. $\boldsymbol{\gamma_{2W}}$ is more dominant in lower dimension cells, particularly at lower buffer gas pressure.

The ground state relaxation rate due to collision of Rb atoms with cell wall is very significant in cells with lower dimension (radius), particularly at lower buffer gas pressure. Therefore, smaller or miniature vapor cells require buffer gas at higher pressure to mitigate the

effect of wall collision on CPT resonance. All the characteristics of CPT resonance with respect to cell diameter are discussed in Chapter 4 along with experimental results.

### 2.3.4 Buffer gas

In atomic clocks based on a vapor cell, buffer gas is added to slow down the diffusion of alkali atoms in the vapor cell that would enhance the laser-atom interaction time. This would also help in minimizing relaxation due to atom-wall collisions. However, collision between buffer gas and alkali atoms influence the excited state decay rate of alkali atoms and thus the CPT resonance characteristics.

The relaxation rate due to collision between alkali atom-buffer gas is given by [59], [62]

$$\gamma_{2BG} = L_0 \bar{v}_{Rb-Ne} \sigma_{Rb-Ne} \frac{P}{P_0} \tag{2.29}$$

Here, $L_0$ is Loschmidt's constant (2.6867774 x $10^{25}$ $m^3$), $\bar{v}_{Rb-Ne} = \sqrt{\frac{8k_BT}{\pi\mu}}$ ( $k_B$ is Boltzmann's constant, T is cell temperature and μ is reduced mass of alkali-buffer gas atoms) is relative velocity of alkali and buffer gas atoms, $\sigma_{Rb-Ne}$ is collisional cross section for Rb atoms with Ne buffer gas (5.55 x $10^{-26}$ $m^2$ [9], [63], $P$ is buffer gas pressure in the vapor cell and $P_0$ is reference gas pressure (760 × 133.323 Pa).

Variation of $\gamma_{2BG}$ with buffer gas pressure is plotted in Figure 2.13a and it can be noted that $\gamma_{2BG}$ increases linearly with buffer gas pressure, as expected from Equation 2.29. Further, $\gamma_{2BG}$ values are also computed as function of cell temperature at constant buffer gas pressure (P = 40, 50 and 60 Torr). As seen in Figure 2.13b, for a given buffer gas pressure, $\gamma_{2BG}$ also increases with temperature. However, rate of change of $\gamma_{2BG}$ with buffer gas pressure is more compared to its change with respect to temperature. Consequently, FWHM of CPT resonance is highly sensitive to buffer gas pressure.

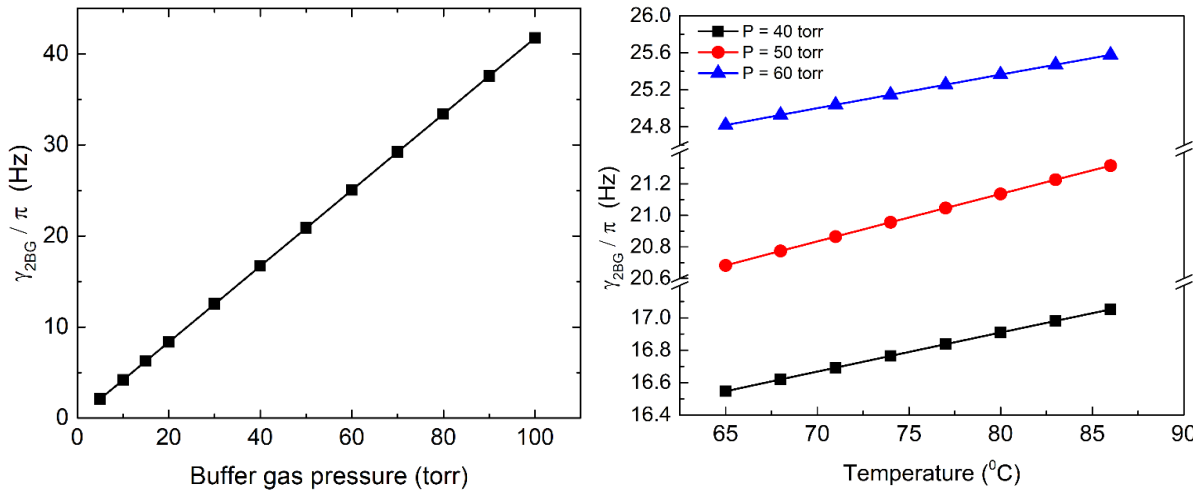


(a) (b)

Figure 2.13: Effect of buffer gas and cell temperature on relaxation rate. (a) Relaxation rate due to the collision between alkali atom-buffer gas ($\boldsymbol{\gamma_{2BG}}$) with respect to buffer gas pressure at T=71 $^0$C. (b) The variation of $\boldsymbol{\gamma_{2BG}}$ with respect to vapor cell temperature at constant buffer gas pressure.

From Equations 2.29 and 2.28 it is observed that $\gamma_{2BG}$ varies linearly with buffer gas pressure whereas $\gamma_{2W}$ varies inversely. Therefore, to optimize the contribution of these two relaxation rates to the CPT resonance broadening the pressure would need to be carefully chosen such that combined effect of $\gamma_{2BG}$ and $\gamma_{2W}$ onto the ground state relaxation is minimum. Figure 2.14 shows the values of $(\gamma_{2BG} + \gamma_{2W})$ at different buffer gas pressures for a cell with radius, $R$ = 12.5 mm maintained at $71^0$ C. As can be seen in Figure 2.14, $\gamma_{2W}$ affects the ground state relaxation significantly at lower buffer gas pressure while $\gamma_{2BG}$ dominates at higher pressures. It is also observed that the combined effect of alkali atom collision with buffer gas and cell wall contributes minimally to the ground state relaxation rate in the intermediate pressure range, i.e.,15 - 50 Torr.

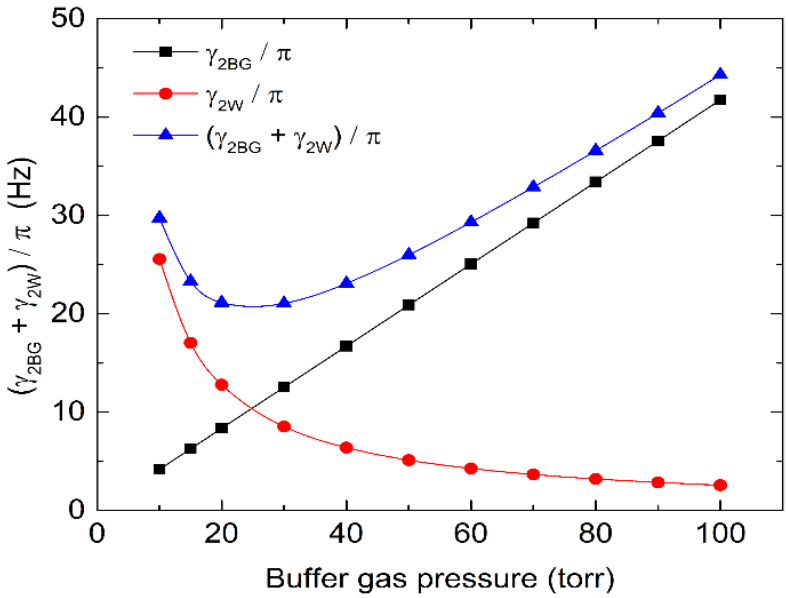


Figure 2.14: Contribution of $\boldsymbol{\gamma_{2BG}}$ and $\boldsymbol{\gamma_{2W}}$ to the ground state relaxation rate at different buffer gas pressures in a cell with radius, R=12.5 mm with temperature = $71^0$ C.

The overall ground state relaxation ($\gamma_2$) due to all the three collision mechanisms, i.e., $\gamma_{2BG}$, $\gamma_{2SE}$ and $\gamma_{2W}$, is calculated as function of cell temperature and dimension (see Figure 2.15). $\gamma_2$ decreases with increase in cell dimension.

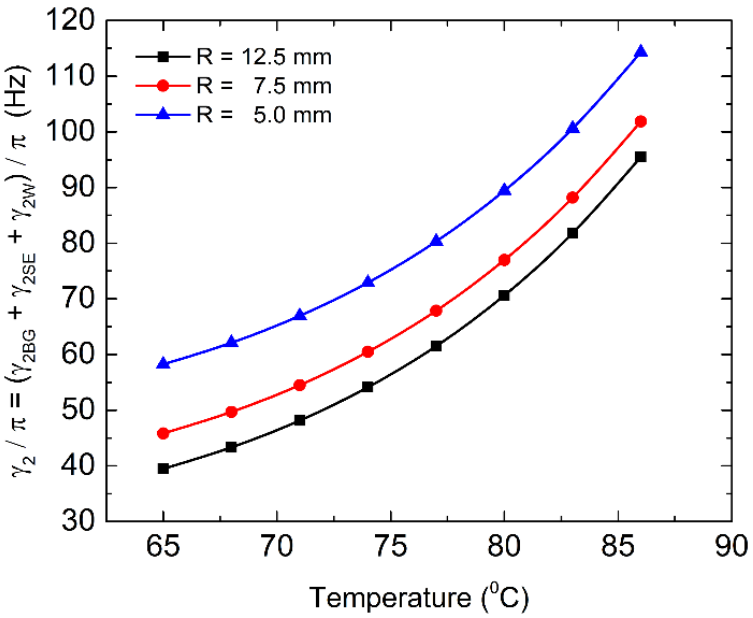


Figure 2.15: The overall ground state relaxation rate due to all the three collisional effects, $\boldsymbol{\gamma_2}$ ($= \boldsymbol{\gamma_{2BG} + \gamma_{2SE} + \gamma_{2W}}$), with respect to cell temperature filled with buffer gas at pressure, P = 50 Torr.

Additionally, buffer gas induces the temperature dependent frequency shift owing to the temperature dependent interaction between buffer gas and alkali atoms [62], [63]. These interactions would shift the hyperfine splitting because of the combined effects of attractive long-range Van der Waals interactions and repulsive short range Pauli exclusion forces [63], [100] in the vapor cell.

Whilst Van der Waals interactions reduce the hyperfine splitting by decreasing the electronic density at the nucleus, Pauli exclusive forces increase hyperfine splitting by increasing the electronic density at nucleus. These effects cause either a negative or positive frequency shift which depends on the type of buffer gas, its pressure and operating temperature [63], [101]. The lighter buffer gases, such as Helium (He), Ne and Nitrogen ($N_2$), produce positive frequency shift dominated by Pauli exclusion forces, whereas the heavier buffer gases like Argon (Ar), Krypton (Kr) and Xenon (Xe) produce a negative frequency shift dominated by Van der Waals interactions [63]. The empirical formula that represents the frequency shift produced by buffer gas ($\Delta\nu_{BG}$) is given by Equation 2.30 [63], [102]. Here, $P_0$ is buffer gas pressure measured at the reference temperature $T_0$. $\beta_{BG}$, $\delta_{BG}$, and $\gamma_{BG}$ are the pressure coefficient, the linear temperature coefficient, and the quadratic temperature coefficient of given buffer gas, respectively.

$$\Delta\nu_{BG} = P_0[\beta_{BG} + \delta_{BG}(T - T_0) + \gamma_{BG}(T - T_0)^2] \tag{2.30}$$

A detailed analysis on the effect of buffer gas pressure on CPT resonance characteristics is described in Chapter 4. The experimental analysis is carried out by considering different buffer gas types (Ne and mixture of Ar and $N_2$) and magnitude of pressure.

### 2.3.5 Modulating RF field

In the work presented in this thesis, CPT resonance is realized by generating two resonant optical laser fields by modulating the laser drive current at Radio Frequency (RF) field such that, the separation between first harmonics corresponds to the ground state hyperfine separation in alkali atoms (Rb) (see Section 3.4). The amplitude of RF field contributes to the intensity of first harmonics, and thus it influences the CPT characteristics similar to that of laser intensity. In addition, every side band generated by modulation contributes to light shift similar to first harmonics but with different magnitudes depending on their individual

intensities [103], [104], [105]. Thus, the sum of intensities from all subharmonics contributes to the total light shift which can be expressed as [105]

$$\Delta\nu_{total} = \cdots + \Delta\nu_{-2} + \Delta\nu_{-1} + \Delta\nu_0 + \Delta\nu_{+1} + \Delta\nu_{+2} + \cdots \tag{2.31}$$

$$\Delta\nu_{total} = \cdots + C_{-2}I_{-2} + C_{-1}I_{-1} + C_0I_0 + C_{+1}I_{+1} + C_{+2}I_{+2} + \cdots \tag{2.32}$$

Here, $\Delta\nu_{\pm n}$ is the light shift due to side bands, $\pm n$. $C_{\pm n}$ is the coefficient of side band $\pm n$, and $I_{\pm n}$ is the intensity of corresponding side band.

Therefore, the CPT resonance characteristics such as contrast, FWHM and frequency shift depend on various control/operating parameters as explained above. Thus, it is important to understand the underlying physics and then carefully optimize the configuration of system. This thesis reports an experimental investigation on understanding the impact of these critical parameters on the quality factor and frequency shift of CPT resonance and their optimization, which would lead to achieving superior frequency stability of CPT based atomic clock.

# Chapter-3

# Experimental Methods

This chapter discusses the experimental methodologies employed in this study to excite CPT resonance, its measurement and characterization for application in atomic clock. A brief introduction is provided on the various CPT excitation schemes and application of CPT in both atomic clock and magnetometer. The chapter then discusses the architecture of CPT scheme implemented in this study and its practical realization. A detailed methodology is established for conducting experiments with various combinations of operating parameters to excite CPT resonance in Rb atoms. An in-house MATLAB software is devised to extract the CPT resonance characteristics using batch least square technique. The chapter concludes with discussion on characterization of CPT atomic clock and development of processing algorithms to evaluate the performance CPT clock.

As explained in Section 2.1.1, CPT phenomena occurs when two coherent laser fields couple the two ground states of alkali atoms to a common excited state. Various schemes exist to generate these coherent laser fields, either from two independent laser sources or from a single laser source, each of which have their own advantages and disadvantages. A brief description on these different methods is provided below.

One of the approach would be to utilize two independent laser sources. In this configuration, two different laser sources with optical phase locking are used to generate the coherent optical fields [84], [106], [107], [108]. The phase of second laser is precisely controlled with respect to the first laser. An Optical Phase Locked Loop (OPLL) synchronizes the phases of two laser fields, allowing an adjustable frequency difference while maintaining a constant phase relationship. Phase locking of two lasers is a complicated system and limits the application for miniaturization. Fig 3.1 shows the experimental setup demonstrating optical phase locking of two lasers referred to as master and slave, as documented in reference [106].

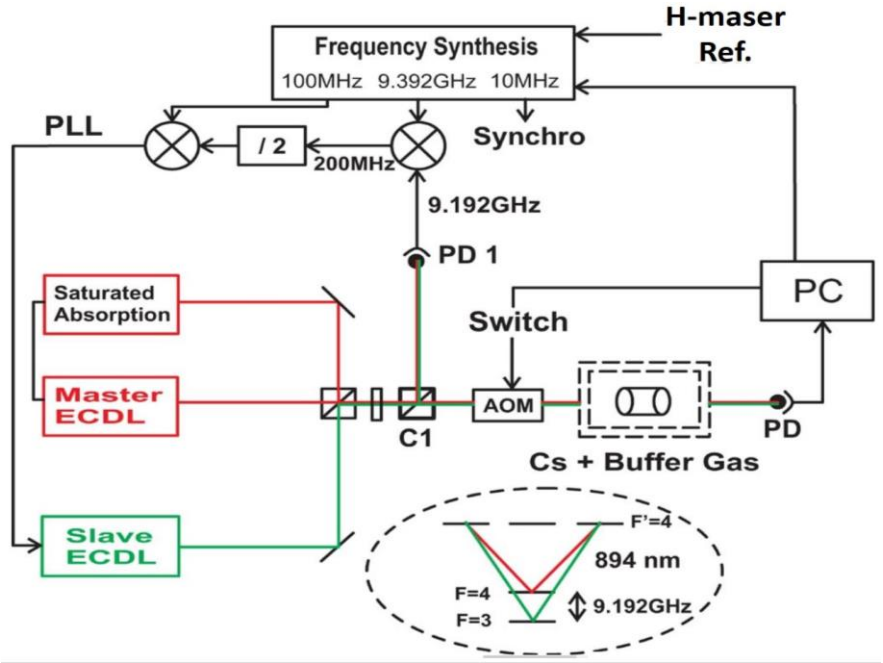


Figure 3.1: Experimental setup showing optical phase locking of two laser sources for CPT excitation. Figure is extracted from Reference [106].

Another method involves employing a single laser source. Coherent optical fields from a single laser source can be generated in two distinct mechanisms such as external modulation and direct modulation. External modulation is when the modulation is imposed on the output of laser source. Conversely, direct modulation involves the modulation of input source to the laser itself.

Electro-Optic Modulation (EOM) and Acousto-Optic Modulation (AOM) represent two modulation techniques to modulate laser output using electric fields and sound waves, respectively. Thus, laser source undergoes external modulation through either EOM or AOM to generate the coherent optical fields [85], [109]. Figure 3.2 shows the experimental setup, wherein the laser light is externally phase modulated at half of the ground state splitting by an electro-optic modulator [85]. This results in the generation of two side bands resonant with transitions from two ground states to excited state. External modulator leads to complexity in the system architecture and thus limits the implementation for compact atomic clocks.

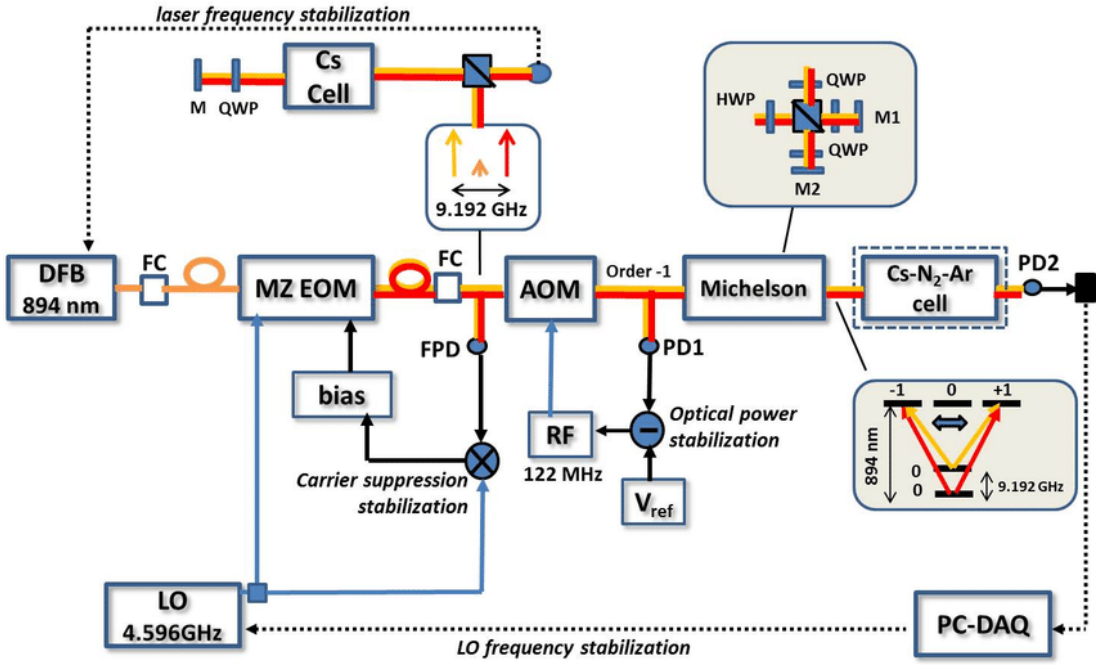


Figure 3.2: Experimental setup illustrating generation of coherent optical fields for CPT excitation using external modulation (EOM). Figure is extracted from Reference [85].

An alternative approach involves the utilization of a single laser source with direct modulation. It is the simplest method to implement, where, typically, a Vertical Cavity Surface Emitting Laser (VCSEL) diode generates the coherent optical fields by modulating its injection current with radio frequency (RF) [47], [110], [111]. The work carried out in this thesis is based on this method for its ease of implementation and potential for miniaturization.

Figure 3.3a depicts the simplified functional block diagram of the CPT excitation scheme employed in this study. In this approach, coherent optical fields are generated by a VCSEL diode through the modulation of its injection current (DC) with RF frequency ($f_m$), i.e., half of the hyperfine ground state splitting ($f_m = \frac{\nu_{hfs}}{2}$) [47], [110]. For example, the injection current of laser diode emitting light at ~ 794.8 nm is modulated with $\frac{\nu_{hfs}}{2}$ ~ 3.417 GHz such that the separation between resulting first-order sidebands is equal to the hyperfine ground state splitting ($\nu_{hfs}$) of $^{87}$Rb as shown in Figure 3.3b. These sidebands in the laser output are resonant with the transitions from ground states to the excited state (Figure 3.3c). The atomic $\Lambda$-system needed for CPT excitation used in this study is formed by the *D1* transitions ($5^2S_{1/2} \rightarrow 5^2P_{1/2}$) in $^{87}$Rb atoms in which the two hyperfine ground states ($F$=1 and 2) couple to a common excited state ($F'$=1) as shown in Figure 3.3c.

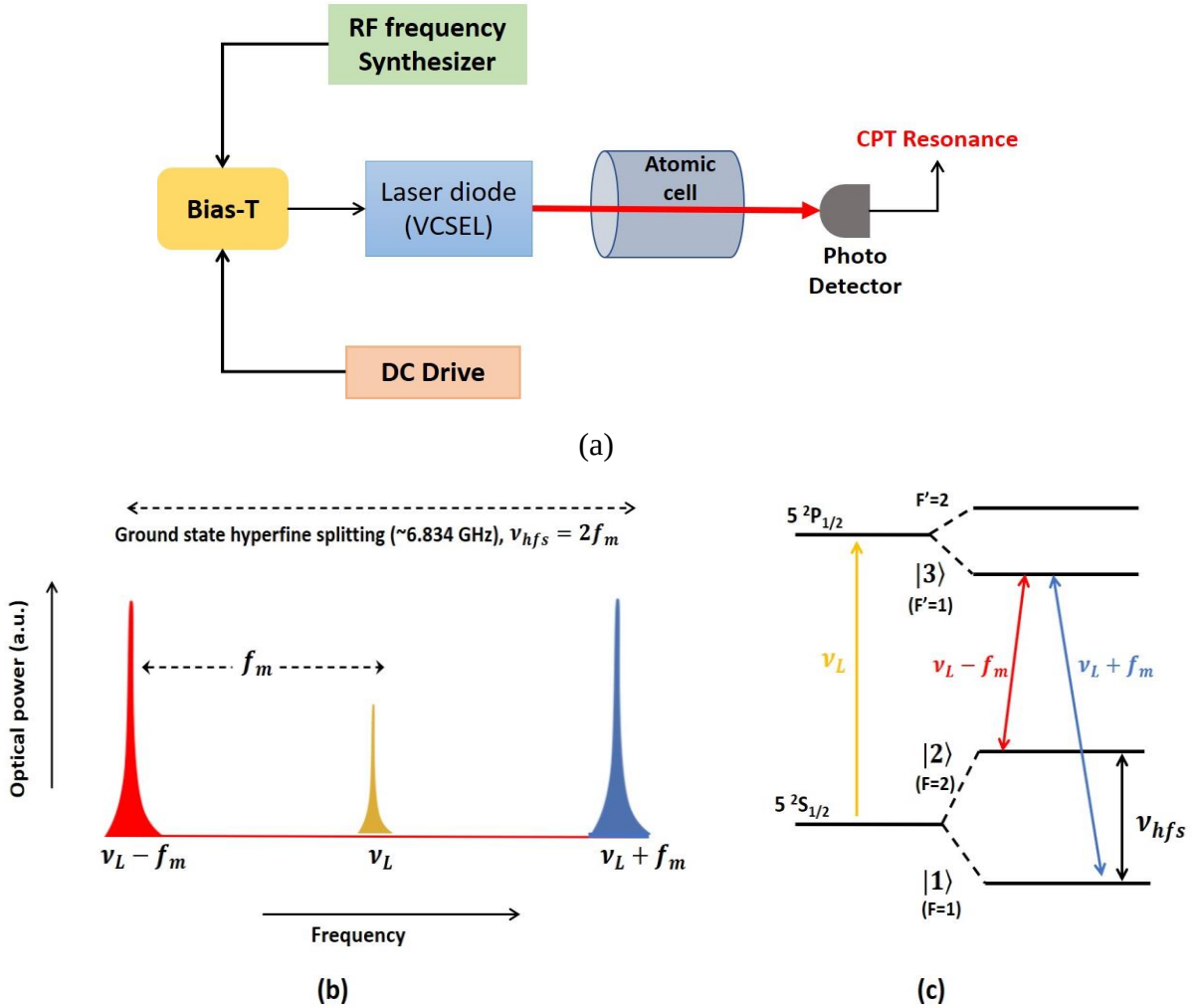


Figure 3.3: (a) Functional block diagram of CPT excitation scheme. (b) Laser spectrum with RF modulation. $\nu_L$ is laser carrier frequency and $f_m$ (~3.417 GHz) is modulation frequency. (c) Hyperfine energy levels in $^{87}$Rb.

The bi-chromatic coherent light field thus generated passes through an atomic vapor cell placed in a controlled magnetic field environment at elevated temperature. The transmitted light is recorded by a photodetector. When the RF modulation frequency is scanned such that the first order-sidebands in the emitted laser field are resonant with two ground state hyperfine transitions of $^{87}$Rb atoms (as shown in Figure 3.3c & 3.4a), CPT resonance is observed [55], [112]. A series of CPT resonances (Figure 3.4b) are generated when the laser field is made resonant with transitions from magnetic field independent as well as field dependent Zeeman levels (Figure 3.4a).

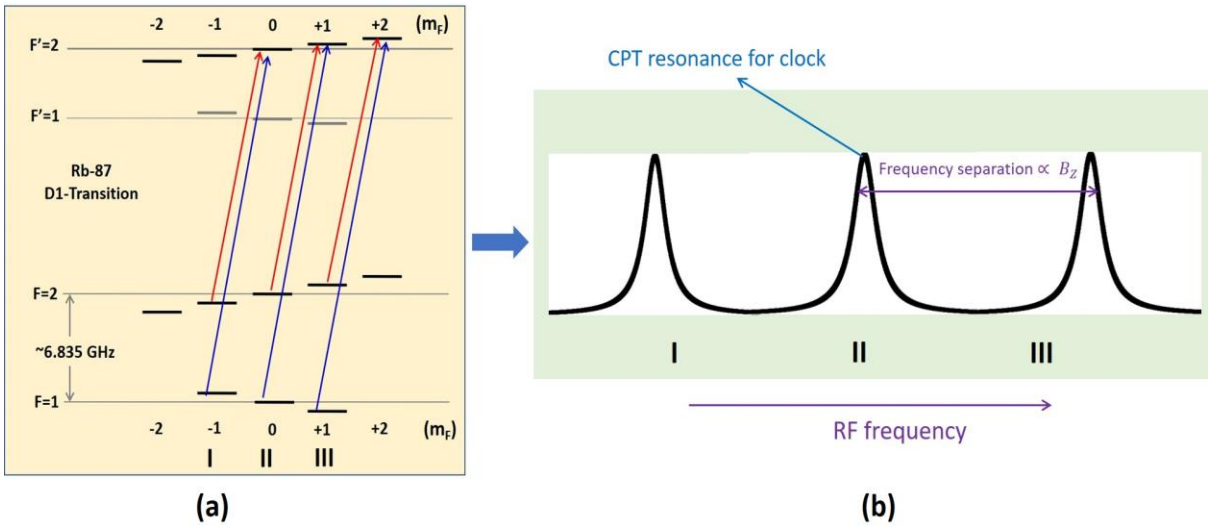


Figure 3.4: (a) CPT excitations from magnetic field independent ($m_F$=0) and field dependent ($m_F \neq 0$) Zeeman levels in $^{87}$Rb. (b) Corresponding CPT resonances. The frequency separation between the consecutive resonances correspond to the external magnetic field ($B_Z$).

The CPT resonance is employed in realizing miniaturized precision atomic sensors, including atomic clocks [46], [47], [80], [113] and atomic magnetometers [77], [78], [79], [80]. CPT resonance originating from transitions involving magnetic field independent Zeeman levels serves as reference for atomic clock and is thus called as clock resonance. This clock resonance is used to lock the crystal oscillator to stabilize its output frequency as shown in Figure 3.5. The presence of external magnetic field ($B_Z$) induces shift in the Zeeman levels (Figure 3.4a) leading to the separation between CPT resonances (Figure 3.4b). This frequency separation is used to calculate the external magnetic field using Breit-Rabi formula [114].

The performance of CPT based atomic clock or magnetometer is primarily depends on the CPT resonance characteristics, i.e., amplitude, linewidth, shift in center frequency etc. The CPT resonance with large amplitude and narrow line width results in better short-term stability [48] for clock and superior sensitivity for a magnetometer [79]. The shift of center frequency from theoretical reference influences the long-term stability of atomic clock [90] and accuracy of magnetic field measurement [114]. The work discussed in this thesis is mainly focussed on experimental study of CPT resonance characteristics for improved stability of CPT based atomic clock.

## 3.1 Architecture of CPT based atomic clock

Figure 3.5 shows the architecture of CPT based atomic clock [115] employed in this study. The constituents of CPT based atomic clock are classified into three main sections, namely physics package, laser stabilization and crystal oscillator stabilization. Physics package consists of source assembly, atomic cell assembly and detector assembly, mounted onto a common base plate.

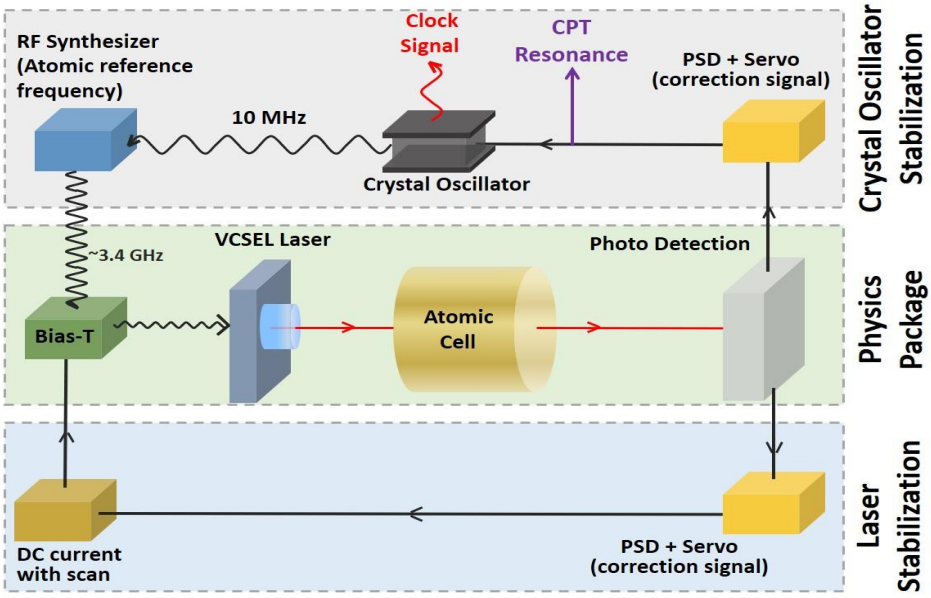


Figure 3.5: Architecture for CPT based atomic clock which includes three major sections: physics package, laser stabilization and crystal oscillator stabilization.

In this CPT architecture, the output of a crystal oscillator (10 MHz) is fed to frequency synthesizer to generate required RF frequency for modulation via a Bias-T as shown in Figure 3.5. Any fluctuations in the emission frequency of laser diode leads to instability of the CPT resonance. This emission frequency of laser diode primarily depends on the injection current and the junction temperature. Laser frequency stabilization includes its temperature control and drive current stabilization. Stabilization of laser drive current is achieved by locking its frequency to a chosen atomic hyperfine transition by employing phase-sensitive detection (PSD) and a servo mechanism, as shown in Figure 3.5.

The stability of a CPT based clock would depend primarily on the characteristics of the CPT resonance and its interrogation. The CPT resonance characteristics are influenced by various control/operating parameters such as laser intensity, cell temperature and its dimension, RF power, buffer gas, and its pressure (see Section 2.3). To improve the stability of CPT based

clock, it is essential to study and understand the effect of all these parameters and then optimize the CPT resonance characteristics. Therefore, the experimental realization of CPT resonance, its measurement and extraction of resonance characteristics are very crucial. The following sections describe the implementation scheme (experimental setup), CPT resonance measurement, and characterization methodology.

## 3.2 Experimental setup

The block diagram of the experimental setup for CPT scheme used in this study is shown in Figure 3.6 [112]. A phase locked loop (PLL) RF synthesizer seeded by crystal oscillator (OCXO) @ 10 MHz is used to generate the required modulating radio frequency ($f_m$). The collimated laser light with beam diameter of ~3 mm first passes through a neutral density (ND) filter to change the laser intensity to a desired value. The attenuated laser light then passes through a quarter-wave (λ/4) plate which converts the polarization of light from linear to circular for state selection. The circularly polarized light passes through a vapor cell filled with Rb and buffer gas at elevated temperature. A silicon photodetector then detects the transmitted light. A solenoid coil is used to generate a constant magnetic field that is applied along the direction of laser beam for exciting CPT among field independent Zeeman lines ($m_F = 0$).

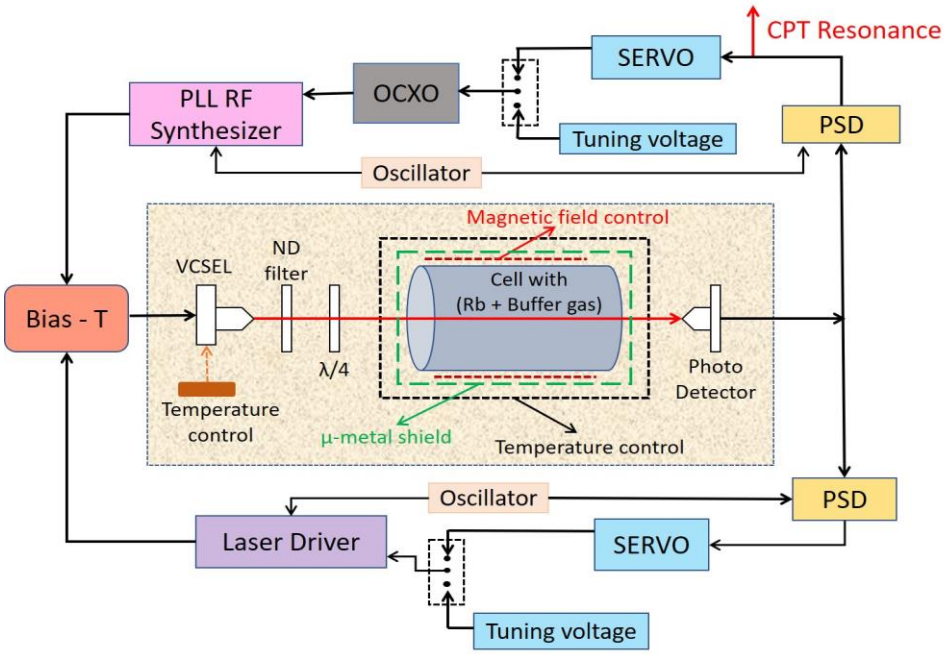


Figure 3.6: Detailed functional block diagram of CPT scheme employed in this study.

The characteristics of CPT resonance are investigated experimentally by measuring its quality figure and frequency shift by varying different operating parameters mentioned in Section 2.3. The description on the physics package, RF frequency synthesis and laser frequency stabilization scheme which are crucial for the realization of CPT resonance, is provided in the following sections.

## 3.3 Physics package

The physics package is very crucial in atomic clock where the interaction of laser field with atomic medium leads to the excitation of CPT resonance. It consists of laser excitation source, collimating and polarizing optics, atomic cell assembly, and photodetector. Figure 3.7 shows the engineering model of physics package. The individual elements of physics package are described in the following sections.

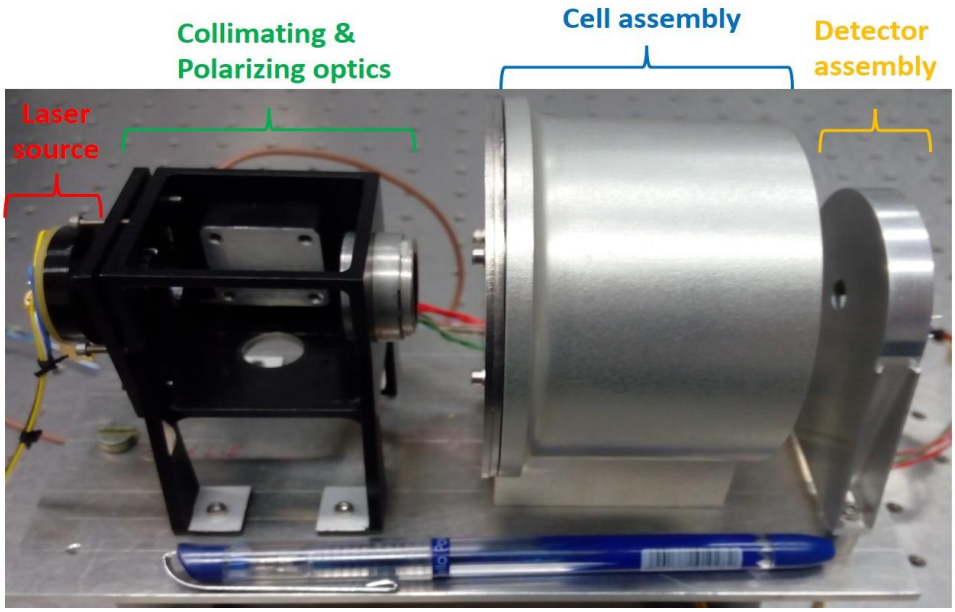


Figure 3.7: Photograph showing the engineering model of physics package.

### 3.3.1 Source assembly

Source assembly consists of laser source, collimating and polarizing optics. A VCSEL diode is used to generate the required optical fields for atomic excitation. VCSEL is a type of semiconductor diode laser in which the light is emitted vertically from the surface of the semiconductor. Typical VCSELs are with GaAs substrate, side n-contact and top annular p-

contact featuring a circular light output aperture (see Figure 3.8). It has several advantages as mentioned below:

- Works at low operating currents and hence, lower power consumption.
- Ease of its current modulation at RF frequencies.
- Higher modulation bandwidth which ensures a significant amount of optical power in first sidebands even with small RF modulation power.
- Its compactness is advantageous for application in miniaturized clocks.

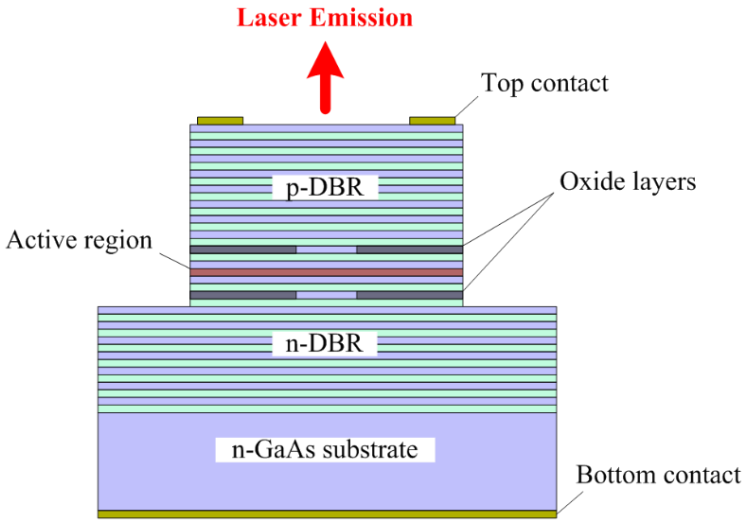


Figure 3.8: Internal structure of a typical VCSEL diode [115]. DBR: Distributed Bragg Reflector.

In this work, an oxide-confined VCSEL diode (see Figure 3.8) [116] from the Frankfurt company is used. VCSEL diode consists of an inbuilt thermistor and Thermo Electric Cooler (TEC). Emission frequency of VCSEL corresponding to the desired atomic transition can be achieved by tuning its junction temperature and injection current. Its emission wavelength (frequency) can be varied by tuning both injection current (@ 0.6 nm/mA) and junction temperature (@ 0.06 nm/K). The linewidth of VCSEL diode is around 30 MHz and optical power is about 500 μW. The junction temperature is maintained within 5 mK by using a Proportional Integral (PI) temperature control. The wavelength is tuned by changing the diode injection current using a drive control. Generally, a drive current ~2 mA and junction temperature ~45 $^{0}$C would result in an emission frequency that corresponds to D1 transitions in $^{87}$Rb atoms. However, these values can vary among different units of laser diode.

## 3.3.2 Atomic cell assembly

Atomic cell assembly includes atomic cell, cell chamber as well as solenoid, mu metal shield for magnetic shield and heating foil (see Figure 3.9). Atomic cell is securely placed within the cell chamber using lock nuts and RTV moulds which can withstand high temperature. Atomic cell assembly is placed in between source and detector assembly and mounted on to the common base plate (see Figure 3.7).

Rb cells with different dimensions (length=25 mm, radius=5, 7.5 and 12.5 mm) and buffer gas pressure values (Ne@50 Torr, Ar+$N_2$@15 to 22 Torr) are used in the experimental analysis. More details about these Rb cells are provided in section 3.6. The cells are heated using a foil heater. Heater has bifilar heating element with equivalent resistance of 42 Ω. Cell temperature is maintained well within $\pm 0.01\ ^0$C by using a PI controller. Thermistor is mounted on the surface of the cell to monitor its temperature.

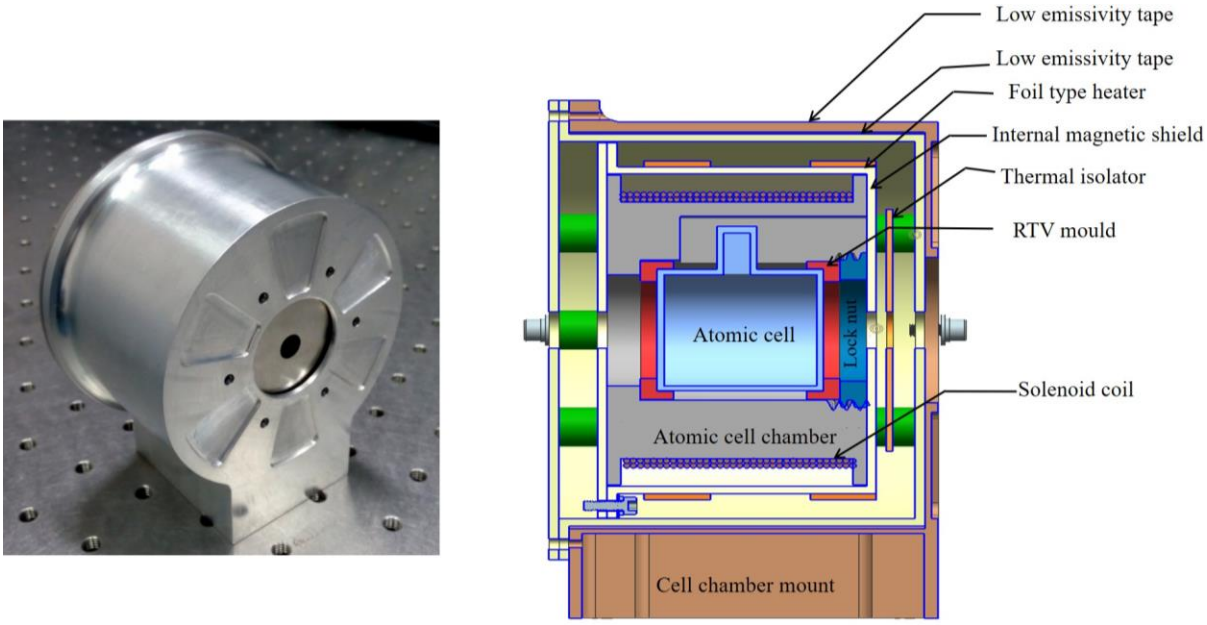


Figure 3.9: Integrated structure of atomic cell assembly (left) and cross-sectional view of its design structure (right).

### Magnetic shields

External non-homogeneous magnetic fields can split the magnetic levels that affect the laser-atom interaction in Rb vapor cell and thus the CPT resonance. High permeability mu-metal shields are used to isolate the Rb vapor cell from external magnetic fields. These shields are made of nickel-iron alloy. Two layers of magnetic shields are used with thick ness of 0.8 mm and an attenuation ~ 80 dB.

### Solenoid

Rb atomic cell is placed inside a solenoid that provides a constant magnetic field along the Z-direction of the cell. Applied field separates the magnetic field dependent states ($m_F \neq 0$) from field independent states ($m_F$=0). The length and radius of solenoid are 34.5 mm and 28.5 mm, respectively, with 34 number of turns, over two number of layers. The magnetic field is produced by passing a constant current through the solenoid and its magnitude is proportional to the magnitude of the current. The constant magnetic field maintained in the experimental setup is ~50 $\mu T$.

## 3.3.3 Detector assembly

The detector assembly comprises the silicon photodetector and detector drive electronics. The current generated in the photodetector is converted into a voltage signal using a Trans-Impedance Amplifier (TIA). A commercial silicon photodetector (Thorlabs) with responsivity of approximately 0.5A/W is used for photodetection.

# 3.4 Synthesis of RF frequency for laser modulation

The injection current of the laser diode is modulated by RF frequency ( $f_m$ = 3.417341305 $GHz$) as shown in Figure 3.3b. This modulating RF frequency is generated by RF synthesizer. Figure 3.10 shows the block diagram for generation of required RF frequency.

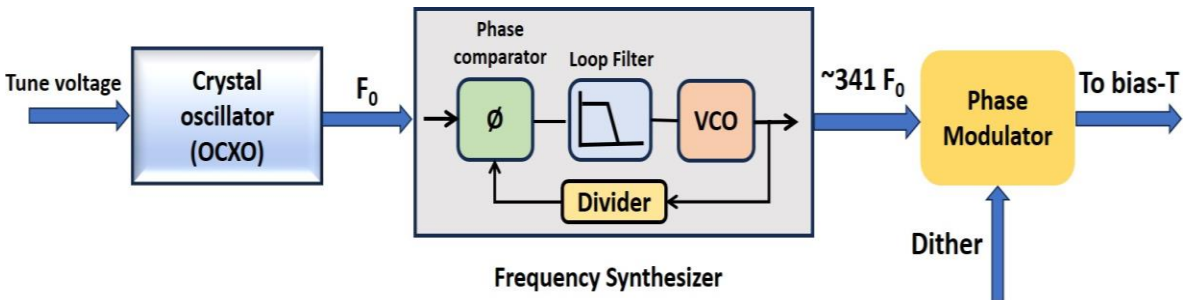


Figure 3.10: Schematic showing the generation of required RF which would modulate the laser drive current via bias-T.

In this scheme, a crystal oscillator generates 10 MHz frequency which has provision to adjust its output frequency up to 3 Hz by changing its input tuning voltage. Crystal oscillator output is provided to a Phase locked Loop (PLL) frequency synthesizer which is designed to

generate required RF frequency by configuring the appropriate multiplication factor. The PLL consists of phase comparator, loop filter and VCO to synthesize desired frequency ($f_m$). Synthesized RF frequency, $f_m$, is achieved by configuring a multiplication factor of ~341.7. This RF signal is provided to a phase modulator to modulate with a dither frequency for phase sensitive detection. Modulated RF signal is couple with DC drive current in a Bias-T which combines the two for driving the laser diode. By changing the input tuning voltage of crystal oscillator, the output RF frequency can be scanned.

## 3.5 Laser frequency stabilization

$^{87}$Rb absorption spectrum is obtained by varying the laser frequency which is achieved by scanning the injection current of laser diode. The output of the photodetector, i.e., absorption spectrum, as function of sweep current is monitored on the oscilloscope as shown in Figure 3.11a. Two transmission dips (or absorption peaks) are observed as a result of hyperfine transitions from ground states to excited state.

In general, the absorption spectrum is affected by laser frequency fluctuations. The instabilities associated with these laser frequency fluctuations can be minimized by locking the laser frequency to a chosen atomic hyperfine transition [54], [55]. As discussed in the previous section, the laser diode generates the coherent optical fields by modulating its laser injection current with half of the ground-state hyperfine splitting of $^{87}$Rb. A series of resonance peaks (complex spectrum) are observed as the RF modulated laser's drive current is swept from low to high frequency. This is due to the transitions from each of the ground states to the excited state caused by both the carrier and sidebands. However, the complexity of the spectrum also depends on the RF power. Figure 3.11b shows the typical absorption spectrum observed when the laser is modulated with RF frequency of ~3.417 GHz which is also referred to as RF coupled spectrum.

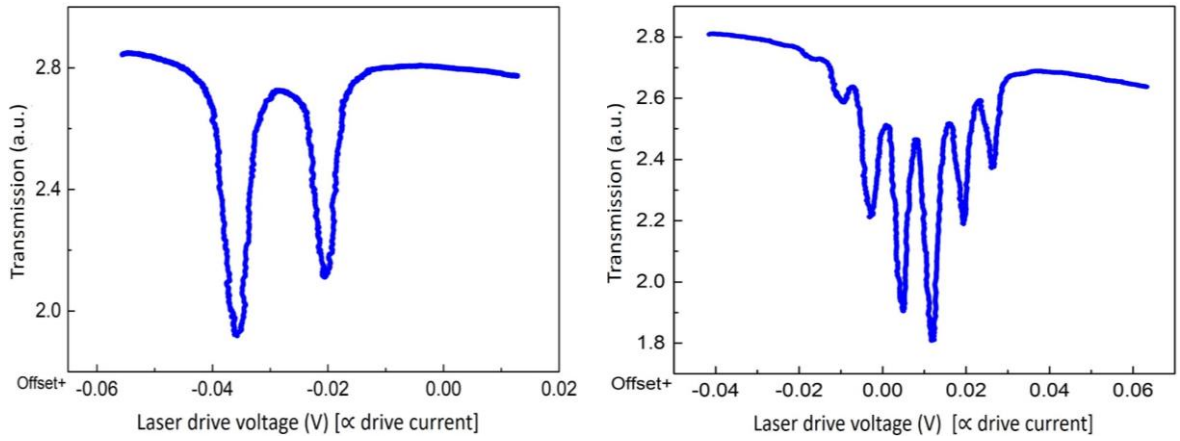


(a) (b)

Figure 3.11: (a) Absorption due to *D1* transitions in $^{87}$Rb atoms detected by photodiode as function of laser drive current (un-coupled spectrum), (b) Corresponding RF coupled hyperfine absorption spectrum. The complex absorption spectrum is due to the transitions from ground states to excited state by laser carrier and sidebands.

To stabilize the laser emission frequency, laser drive current would need to be controlled precisely which can be done by locking its injection current to the peak of RF coupled hyperfine absorption spectrum. To facilitate this, Phase Sensitive Detection (PSD) technique is employed to lock the laser drive current. This is achieved by modulating the laser current with a reference frequency of ~ kHz (also known as dither frequency) and then demodulating the detector output with reference dither using a PSD scheme. The output of PSD would serve as input to the servo control wherein the correction signal generated which subsequently employed as feedback to the injection current. The PSD implementation scheme employed for laser frequency stabilization is explained below.

PSD is a sensitive detection technique to detect and amplify very weak signals that are buried in noise. The functional block diagram of PSD scheme employed in this study is shown in Figure 3.12. Laser current is modulated with a dither signal (sinusoidal wave @ ~10 kHz) that is generated by a Wien bridge oscillator. The frequency modulated laser light passes through atomic cell and the transmitted light is collected by the photodetector. The output signal from TIA passes through a band-pass filter (BPF), mixer, low pass filter (LPF) and an amplifier. BPF is designed to be centred around modulation dither frequency such that any unwanted frequency can be attenuated (~ 50 dB). Filtered signal is directed to multiplier, where it undergoes multiplication with a reference signal to generate both sum and difference frequencies. To optimize the output of the multiplier, a phase shifter is employed to adjust the phase of input value with respect to reference dither. Higher frequency components are

removed by using two stage Sallen-key configuration of LPF (80 dB roll off) such that only DC component of the signal is allowed to pass through. This DC signal is further amplified using DC amplifier and fed to servo controller. This input PSD signal is compared with a reference PSD value (set point) to generate an error signal. The error signal is fed to a PI controller which provides the required servo control signal (correction) to the laser drive current.

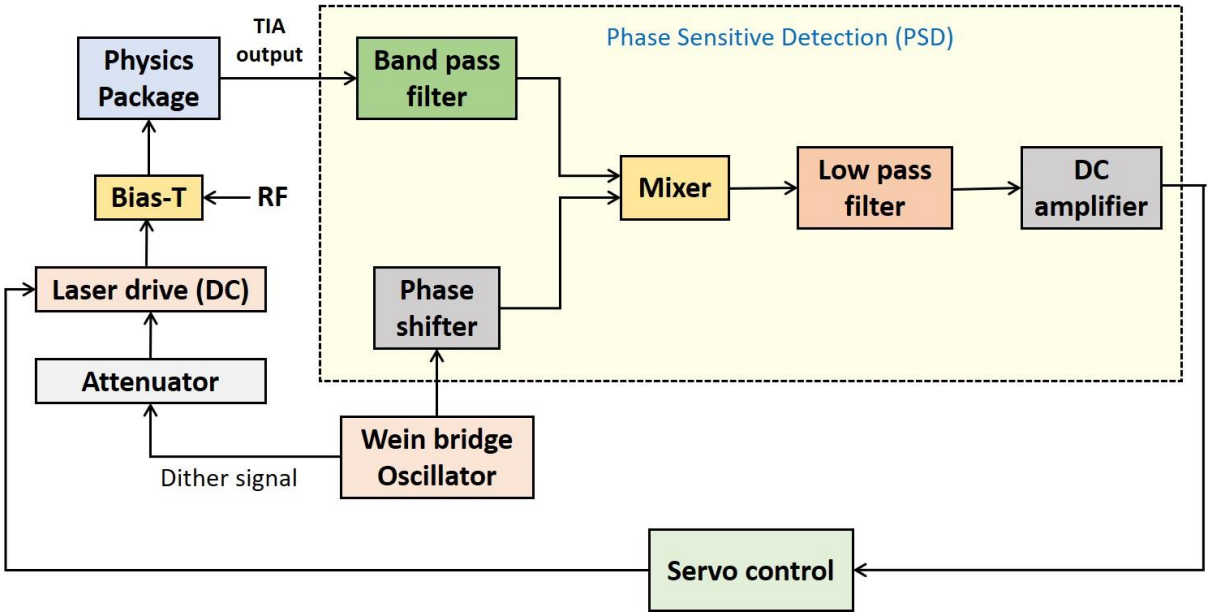


Figure 3.12: Functional block diagram of laser frequency stabilization by implementing PSD technique [115].

Figure 3.13 shows the measured hyperfine absorption spectrum and its corresponding PSD signal in $^{87}$Rb atoms. It can be observed that PSD signal appears as a differential of absorption spectrum. Hence, the peak of absorption spectrum corresponds to zero crossing of PSD signal. When the system is put in servo-control mode, the measured PSD signal is continuously tracked and compared with the reference voltage (corresponding to chosen absorption peak). The deviation in PSD signal due to any drift or fluctuation in laser frequency is generated as an error signal and fed to PI controller in a feedback manner. PI controller provides the servo signal (correction) that is added to the laser drive voltage to correct for any fluctuation and stabilize the laser frequency.

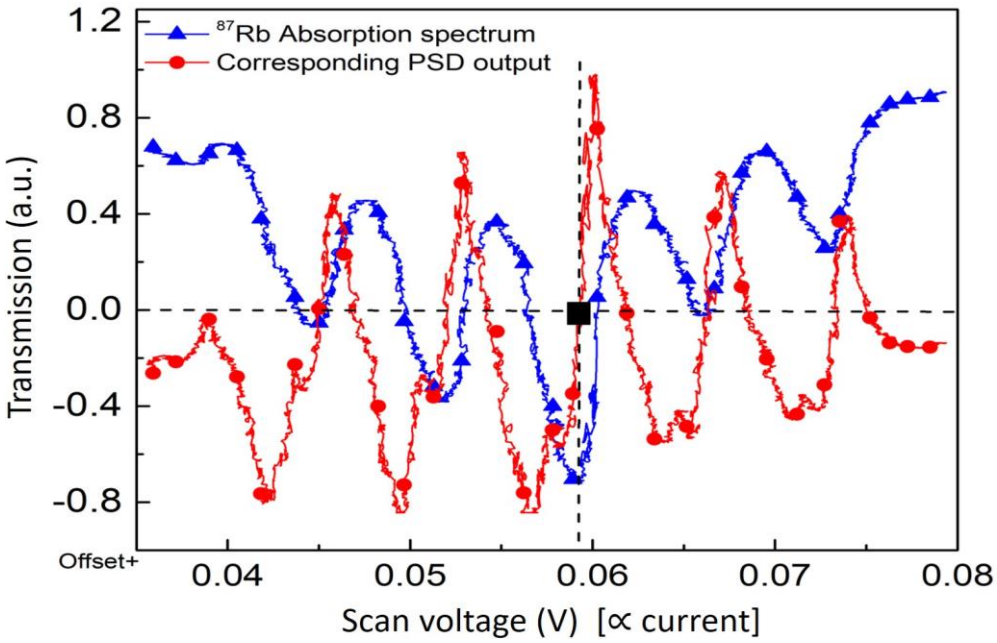


Figure 3.13: RF coupled hyperfine absorption spectrum of $^{87}$Rb and its corresponding PSD output signal. The black square box indicates the zero crossing of PSD output signal corresponding to the chosen coupled absorption peak.

Following the laser frequency stabilization, CPT resonance can be observed by sweeping RF modulation frequency via scanning the tune voltage of OCXO. For application in atomic clock, OCXO frequency stabilization is carried out with reference to the peak of CPT resonance using PSD and servo control in a mechanism similar to that used for laser frequency stabilization. Figure 3.14 shows the measured CPT resonance along with the corresponding PSD signal. OCXO tuning voltage is locked to the peak of the CPT resonance, i.e., zero crossing of the PSD signal. Any deviation with respect to this zero crossing is provided as a correction signal to stabilize the OCXO output frequency.

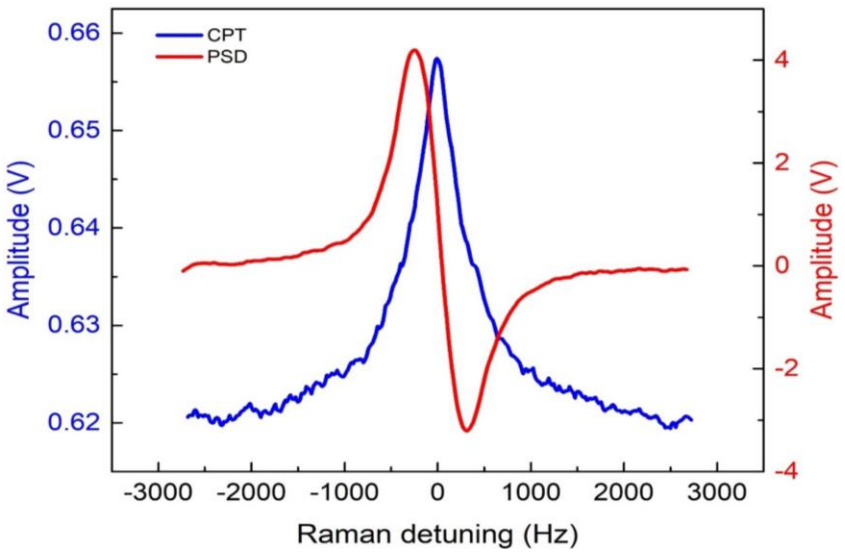


Figure 3.14: Typical measured CPT resonance (left y-axis) with corresponding PSD signal output (right y-axis) as function of Raman detuning. Zero crossing of PSD output signal is used as a reference for OCXO stabilization.

Figure 3.15 shows the table top experimental setup utilized to investigate the CPT resonance characteristics with respect various operating parameters discussed in this thesis.

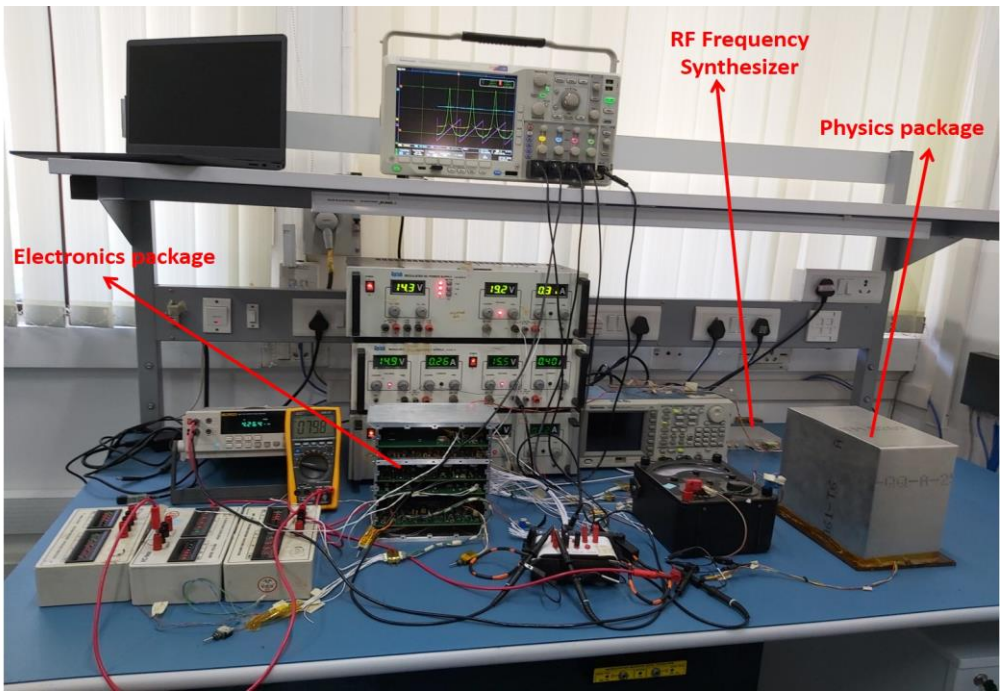


Figure 3.15: Photograph showing the experimental setup for realization and characterization of CPT resonance.

## 3.6 Investigation Plan

The work carried out in this thesis emphasizes the experiments with respect to vapor cell dimension, laser intensity, cell temperature, RF power, and buffer gas pressure. Preliminary experiments are carried out to derive the nominal operating range of these parameters to observe the CPT resonance in Rb atoms. Table 3.1 shows the experimental range of the above parameters considered for the experimental analysis.

Table 3.1: Range of operating parameters used in the experiments for each cell.

| Parameter | Range |
|---|---|
| Laser intensity | 4 to 22 $W/m^2$ |
| Cell temperature | 48 to 72 $^0C$ |
| RF power | 0.5 to 4 dBm |

Seven Rb vapor cells with different dimensions and buffer gas pressure values are used in the experiments. The first three cells have different radii (R=12.5 mm, 7.5 mm and 5.0 mm) but same length (L=25 mm) and are filled with Ne buffer gas at a pressure of 50 Torr. The remaining four cells have the same dimension (R=12.5 mm and L=25 mm) and are filled with the mixture of $Ar+N_2$ buffer gas at different buffer gas pressure values varying from 15 to 22 Torr. Figure 3.16 shows the list of various combinations operating parameters considered in the experiments. The characteristics of all CPT resonances are extracted as explained in Section 3.7 and analyzed. If the CPT characteristics are deviated from expected behaviour, the corresponding measurement is repeated before changing to the next parameter value. This process is iteratively performed for all the operating parameters of the cell.

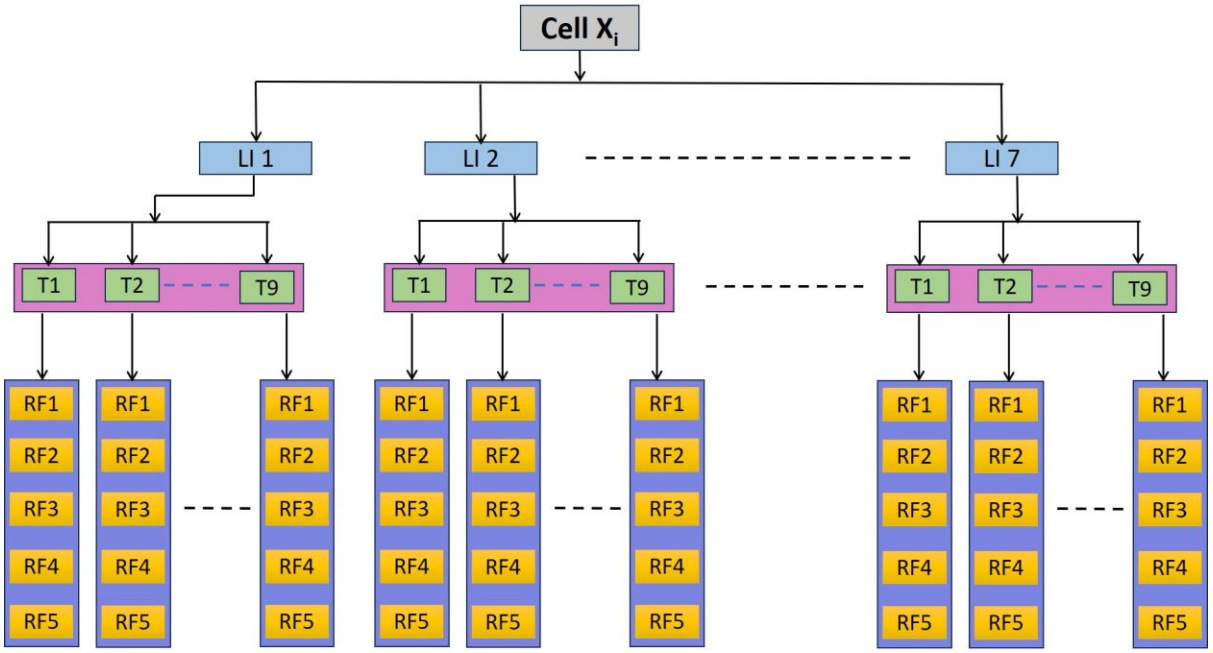


Figure 3.16: Various combinations of different operating parameters chosen for experiment. $X_i$ indicates the cell number (i=1,2…7). LI is laser intensity, T is cell temperature and RF indicates power of RF.

## 3.7 Extraction of resonance parameters

Subsequent to the measurement of CPT resonance, the acquired data undergoes processing to extract its characteristics and study their behaviour with various operating parameters. CPT resonance follows a Lorentzian form as shown in Figure 3.17. The mathematical formula defining the Lorentzian curve is given in Equation 3.1 [117], [118].

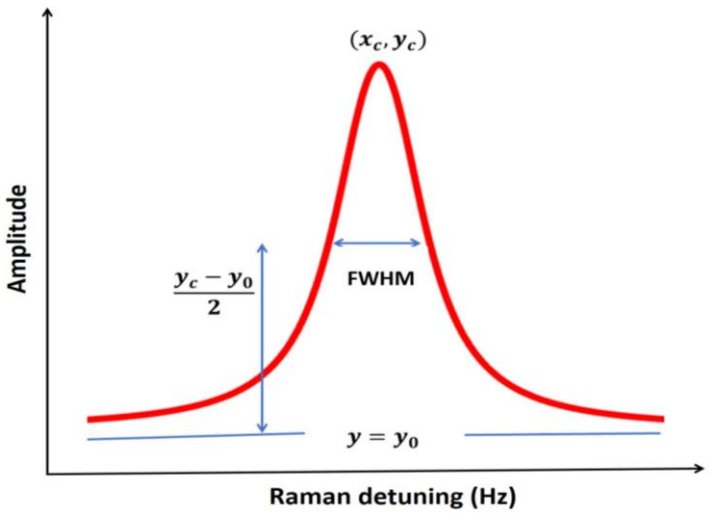


Figure 3.17: Geometrical shape for Lorentzian curve. Here, ($x_c$, $y_c$) is the peak point, $y_0$ is background, FWHM is full width at half maximum and amplitude is given by ($y_c$-$y_0$).

$$y = y_0 + \frac{2A}{\pi}\left(\frac{w}{4(x - x_c)^2 + w^2}\right) \quad (3.1)$$

Here, $y_0$ is background, $A$ is the area under the curve, $w$ is the FWHM, $x_c$ is the center frequency. At the center frequency i.e., at $x = x_c$, the amplitude corresponding to peak point is $y_c = y_0 + \frac{2A}{w\pi}$. Therefore, amplitude of the resonance is given by $y_c - y_0 = \frac{2A}{w\pi}$. The characteristics of CPT resonance are given by, $C = \frac{y_c - y_0}{y_0}$ (contrast), $q = \frac{C}{FWHM}$ (quality figure), and $x_c$ (center frequency). Thus, $y_0$, $x_c$, $w$ and $A$ are the required parameters to compute the characteristics of CPT resonance.

In order to extract these characteristics, Lorentzian fit has to be performed on each CPT resonance. As discussed in Section 3.6, multiple combinations of experiments are considered and at least four measurements are taken for each of these combinations to ensure data consistency. An in-house software is developed in MATLAB to process and extract the characteristics of all CPT resonance from the acquired measurement data. This software is designed to handle the input data collected from the oscilloscope for each combination of measurements (Figure 3.16) in file mode. It partitions the input data into discrete sets corresponding to four CPT resonances and extracts their characteristics by performing appropriate curve fitting. Furthermore, the software computes the mean value for each characteristic parameter extracted from four CPT resonances.

Lorentzian curve fitting is performed on each of the CPT resonances using batch least square technique and then extracted the parameters, such as $y_0$, $x_c$, $w$ and $A$**.** Same procedure is applied to all the measurement data sets provided as input to the software. The concept of batch least square technique and its implementation is discussed in the following sections.

### 3.7.1 Batch least square technique

The batch least square (BLS) technique is used to estimate the optimal values of variables in a model that represents the given data set. The variables corresponding to a chosen model that represent the given input measurement data set are indicated by a vector known as state parameters or the state vector indicated by $X$. Likewise, the measurements are represented by a vector called as measurement vector $Y$. The measurement model matrix ($H$) provides the relationship between measurements and state vector as shown in Equation 3.2.

$$Y = HX + \in \tag{3.2}$$

Here, $\in$ is the measurement noise vector. In general, an exact solution for $X$ is not possible due to uncertainty in the measurements and model. However, the closest possible estimate of $X$ (denoted by $\hat{X}$) is possible using the measurements and a suitable model. Estimated state parameters ($\hat{X}$) of model are used to construct the data referred to as model data. Estimation is said to be optimum if the error (also referred to as residuals) between true data, $Y$ (observed measurement data) and model data, $\hat{Y} = H\hat{X}$ (computed data using $\hat{X}$) is minimum. More specifically, $\hat{X}$ is estimated to minimize the sum of the squares of the residuals, indicated by a performance index (called the cost function) as given in Equation 3.3.

$$J = \frac{1}{2} {e_Y}^T e_Y = \frac{1}{2}[Y - H\hat{X}]^T[Y - H\hat{X}] \tag{3.3}$$

Here, $e_Y = Y - \hat{Y}$ is error vector. A necessary condition for a minimum of '$J$' is that its first derivative with respect to $X$ should be zero that is $\frac{dJ}{d\hat{X}}$=0, leads to the solution as given in Equation 3.4 [119]. Equation 3.4 is implemented in an iterative process until the value of '$J$' is minimized.

$$\hat{X} = (H^T H)^{-1} H^T Y \tag{3.4}$$

## 3.7.2 Implementation of the batch least square technique

The mathematical model used to represent the CPT resonance is Lorentzian curve as given in Equation 3.1. The state vector matrix that contains the required parameters to be estimated is given by Equation 3.5.

$$X = \begin{bmatrix} y_0 \\ x_c \\ w \\ A \end{bmatrix} \tag{3.5}$$

The measurement model matrix ($H$) is constructed by taking the partial derivative of model with respect to each variable of the state vector as given in Equation 3.6.

$$H = \left[\frac{\partial y}{\partial y_0} \quad \frac{\partial y}{\partial x_c} \quad \frac{\partial y}{\partial w} \quad \frac{\partial y}{\partial A}\right] \tag{3.6}$$

$$H = \left[1 \quad \frac{16A}{\pi}\left(\frac{w(x-x_c)}{(4(x-x_c)^2+w^2)^2}\right) \quad \frac{2A}{\pi}\left(\frac{4(x-x_c)^2-w^2}{(4(x-x_c)^2+w^2)^2}\right) \quad \frac{2}{\pi}\left(\frac{w}{4(x-x_c)^2+w^2}\right)\right]$$

Equation 3.4 together with Equations 3.5 and 3.6 are employed in an iterative process to fit the measured CPT resonance data with Equation 3.1 and estimate the state vector parameters (Equation 3.5). Figure 3.18 shows the CPT resonance data with Lorentzian curve fit which are closely matched with each other.

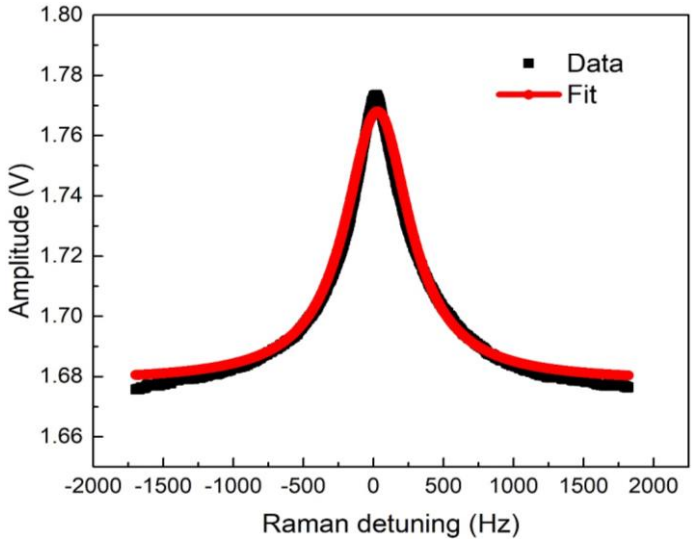


Figure 3.18: Typical CPT resonance data (black) and its fit (red) with the Lorentzian curve by employing Equation 3.4 together with Equations 3.5 and 3.6. The extracted parameters are C=5.36%, FWHM=558 Hz, $q$=9.6E-5 $Hz^{-1}$ and frequency shift of 35 Hz.

## 3.8 Clock characterization setup

Throughout the development of CPT based atomic clock, characterization of its output frequency performance with respect to a superior frequency reference is crucial. This characterization provides valuable insight into understanding its behaviour with respect to various perturbing parameters that require optimization. This section describes the test bed setup established for the real-time characterization of CPT based clock. A Passive Hydrogen Maser (PHM) is used as reference for evaluating the performance of CPT clock. Frequency outputs of 10 MHz from both PHM and CPT clock are provided as inputs to the phase comparator device. The output of this device corresponds to the phase difference between two input 10 MHz signals. Devised and developed algorithms to process and evaluate the CPT

clock performance with reference to PHM. These algorithms include the following processing steps as shown in Figure 3.19.

**Acquisition of phase difference:** Real-time acquisition of phase difference from the phase comparator to a computer with a sampling period of one second.

**Conversion of phase difference to fractional frequency:** The acquired phase difference is converted into fractional frequency, serving as input for clock characterization.

**Processing fractional frequency data:** Outliers are removed from the fractional frequency data using statistical measures such as mean and standard deviation. Further, frequency drift is computed from outlier free fractional frequency data.

**Computation of frequency stability:** Frequency stability is computed using Overlapping Allan deviation (OADEV) technique (Equation 1.11) from outlier free fractional frequency data.

**Real-time graphical display:** Real time graphical presentation illustrating the performance of fractional frequency and frequency stability.

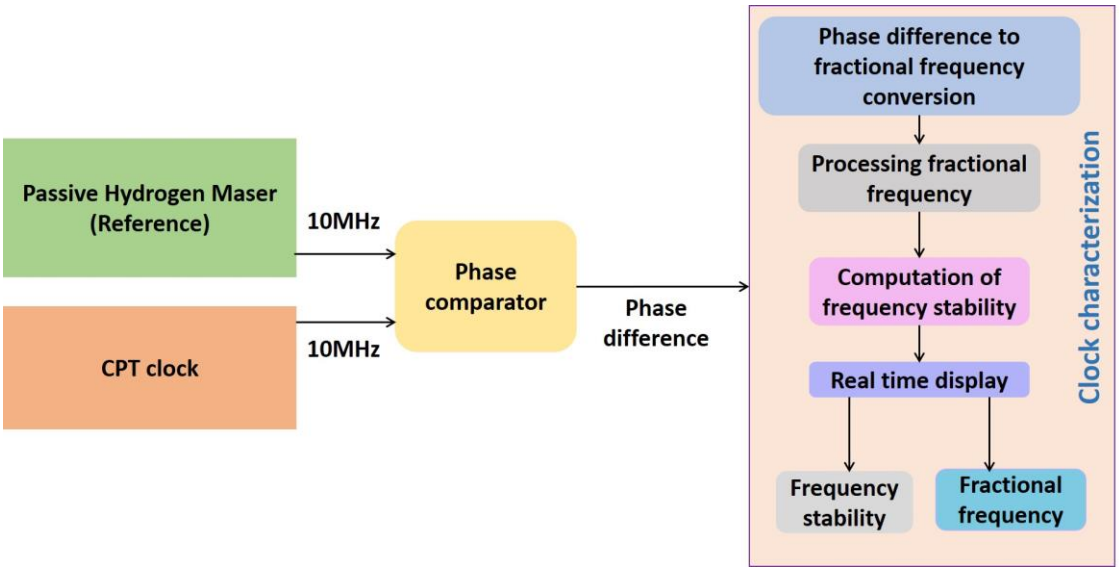


Figure 3.19: Characterization setup for CPT clock. Here, phase difference is the difference of phase between two 10 MHz signals from passive hydrogen maser and CPT clock.

Figure 3.20 shows the preliminary output frequency and corresponding frequency stability of CPT clock during its initial testing.

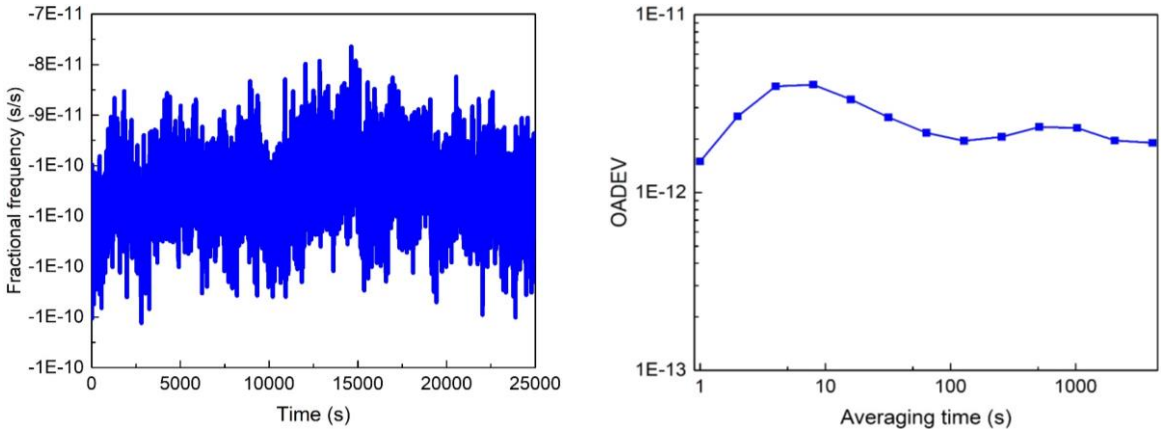


(a) (b)

Figure 3.20: Preliminary data measured using the characterization setup. (a) Fractional frequency of CPT clock during initial testing. (b) Corresponding frequency stability.

This chapter provided a detailed description of the experimental methods employed for the realization of CPT resonance. An experimental procedure is evolved and implemented to characterize the CPT resonance by considering various combinations of the operating parameters. Detailed methodology on CPT resonance data processing is provided. The data processing algorithm is implemented by developing in-house software to extract the CPT resonance characteristics with respect to all operating parameters. The impact of various operating parameters on CPT resonance characteristics is thoroughly studied using these experimental methods, as discussed thoroughly in chapter-4. Furthermore, the chapter concludes with a description on the test bed setup for characterization of CPT clock.

# Chapter-4

# Parametric Study of CPT Characteristics

As explained in Section 2.3, the characteristics of CPT resonance are influenced by various operating parameters such as dimension of vapor cell, laser excitation intensity, cell temperature, RF power, buffer gas and its pressure inside cell. A systematic study on the variation of CPT characteristics is essential for optimizing these parameters. This chapter discusses the experimental investigation carried out to study the CPT resonance characteristics, particularly focusing on the variation of quality figure ($q$), frequency shift, and rate of frequency shift with respect to the operating parameters. The experiments mainly focus on two objectives. The first objective involves the optimization of cell dimension by studying CPT characteristics in cells with different dimensions (radii). The second objective aims to optimize the operating parameters with respect to buffer gas pressure in an $^{87}$Rb atomic cell filled with Ar+$N_2$ buffer gas mixture. The mixture of Ar and $N_2$ was chosen such that their combination provides a minimum net frequency shift owing to their complementary (negative and positive) temperature dependent frequency shift values, as detailed in Section 2.3.4. Table 4.1 shows the details of the Rb vapor cells used in the experimental investigation. The cell numbers specified in this table are referred as their identifier throughout this chapter.

Table 4.1: Details of the Rb vapor cells used in the experimental study.

| **Cell number** | **Length (mm)** | **Radius (mm)** | **Atomic vapor** | **Buffer gas** | **Total pressure (Torr)** |
|---|---|---|---|---|---|
| C1 | 25 | 12.5 | Natural Rb | Ne | 50 |
| C2 | 25 | 7.5 | Natural Rb | Ne | 50 |
| C3 | 25 | 5.0 | Natural Rb | Ne | 50 |
| C4 | 25 | 12.5 | Enriched $^{87}$Rb | Ar+$N_2$ | 15 |
| C5 | 25 | 12.5 | Enriched $^{87}$Rb | Ar+$N_2$ | 17 |
| C6 | 25 | 12.5 | Enriched $^{87}$Rb | Ar+$N_2$ | 20 |
| C7 | 25 | 12.5 | Enriched $^{87}$Rb | Ar+$N_2$ | 22 |

This chapter further addresses the theoretically computed $q$ with different dimensions of cell, cell temperature and buffer gas pressure. Theoretical computation of $q$ is based on four-level atomic model as discussed in Section 2.2. Excited state decay rate ($\Gamma^*$) and ground state relaxation rate ($\gamma_2$) are the primary inputs to this model which are derived from measured FWHM with respect to laser intensity. Following sections provide a systematic description on the experimental investigation of CPT resonance characteristics in Rb cells as mentioned in Table 4.1.

## 4.1 Quality figure

According to Equation 2.12, the short-term frequency stability depends mainly on $q$. To achieve the improved short-term stability $q$ must be maximized. As discussed in Section 2.1.2, $q$ is the ratio between contrast and FWHM of CPT resonance (See Equation 2.11). Thus, short-term stability is improved when CPT resonance exhibits increased contrast and reduced FWHM, which depends on operating parameters. The variation of $q$ is investigated experimentally and the appropriate operating parameters are derived that provide its optimum value.

### 4.1.1 Laser excitation intensity

The effect of laser excitation intensity on $q$ of CPT resonance is studied experimentally by measuring laser light transmitted through the vapor cell under resonant excitation condition as function of excitation intensities while maintaining the vapor cell at a constant temperature. Theoretical computation of quality figure is carried out and compared with experimental results. To compute the theoretical quality figure, $\gamma_2$ and $\Gamma^*$ must be extracted from experimental data using the relationship between FWHM and laser excitation intensity (See Equations 2.18 and 2.7). Using equations 2.7 and 2.14, mathematical expression for FWHM can be represented by Equation 4.1. Thus, measured FWHM with respect to laser intensity is used to derive the values of $\gamma_2$ and $\Gamma^*$ using Equation 4.1 and the extraction methodology as explained in the following paragraphs.

$$\Delta\nu_{FWHM} = \frac{1}{\pi}\left(\gamma_2 + \frac{2I_L {d_{ij}}^2}{c\varepsilon_0\hbar^2\Gamma^*}\right) \tag{4.1}$$

FWHM is extracted from CPT resonances measured at different laser excitation intensities

while maintaining the cell temperature at 71 $^0$C. Figure 4.1 shows the variation of FWHM with incident laser intensity, measured in vapor cells with radius, $R$ = 12.5 mm, 7.5 mm and 5 mm (cells C1, C2 and C3). It is observed that the FWHM increases linearly with laser intensity which agrees well with the theoretical fit (solid line) according to Equation 2.7.

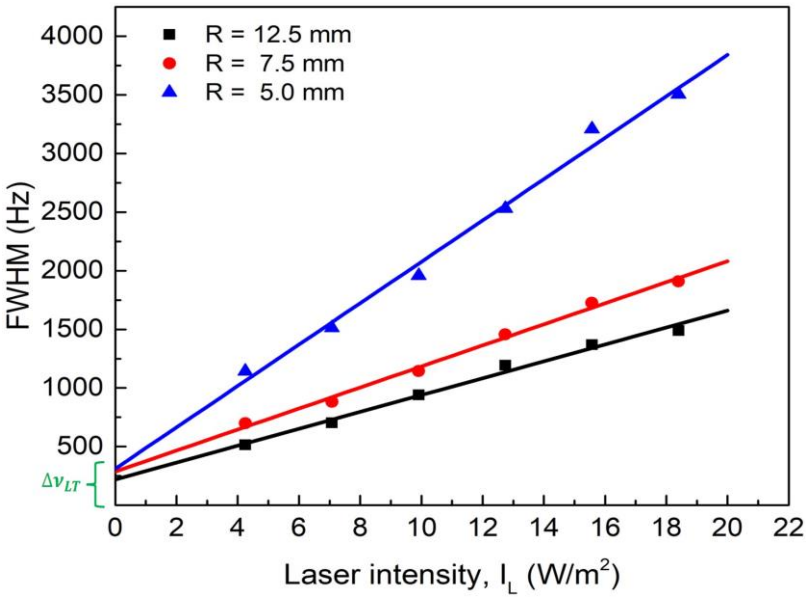


Figure 4.1: FWHM of CPT resonance (linewidth) with incident laser intensity for vapor cells with radius (R) values of 12.5 mm, 7.5 mm and 5.0 mm (cell numbers C1, C2, and C3). Data symbols indicate the measured values and solid lines correspond to theoretical fits (Equation 2.7). The cell temperature is maintained at 71 $^0$C during the measurements. $\Delta\nu_{LT}$ is linewidth threshold.

Figure 4.1 shows that each linear fit has its corresponding slope and intercept at $I_L$ = 0. These intercept values represent the minimum FWHM of CPT resonance (Linewidth Threshold, LT), i.e., $\Delta\nu_{LT} = \frac{\gamma_2}{\pi}$ = 220.48 Hz, 286.55 Hz and 311.74 Hz for cells with radius (*R)* values of 12.5 mm, 7.5 mm and 5 mm, respectively. These values also reflect the life time of the dark state. These values indicate the lower limit of FWHM under the experimental conditions (i.e., choice of cell dimension, temperature, and buffer gas, etc.). $\Delta\nu_{LT}$ is higher for cells with smaller radius. This is due to the higher $\gamma_2$ as a result of increased atom-wall collisions in cells with smaller dimension which would affect the coherence. The slope and intercept at $I_L$ = 0 from experimental data shown in Figure 4.1 are used to derive $\gamma_2$ and $\Gamma^*$ using Equation 4.1. These derived values are used in the theoretical computation of CPT resonance and its characteristics.

Theoretical quality figure for cell numbers C1, C2 and C3 is computed as follows. For each incident laser excitation intensity, the Rabi frequency of the transmitted laser light at the

exit of the vapor cell ($L$=25 mm) is calculated using the theoretical model explained in Section 2.2. When this estimated Rabi frequency is plotted as function of Raman detuning, it represents the CPT resonance, like in Figure 2.8. The quality figure of the corresponding CPT resonance is extracted by performing a Lorentzian fit (see Section 3.7).

Figure 4.2 shows the graphical representation of the experimental and computed $q$ as function of incident laser excitation intensity. The variation of the measured $q$ with excitation intensity is consistent with the theoretical predictions. In addition, $q$ decreases as cell size (radius) decreases due to higher FWHM in cells with lower dimension. As shown in Figure 4.2, although $q$ value improves by reducing the laser excitation intensity, measuring CPT resonances at lower intensities would require a more sensitive detection scheme. In this study, the optimum laser intensity with maximum quality figure is 4.25 W/m$^2$ for the cell with radius of 12.5 mm. However, the computation of theoretical values is extended to even further lower intensities, and it is observed that the quality figure deteriorates below an optimum laser intensity, as shown in Figure 4.2.

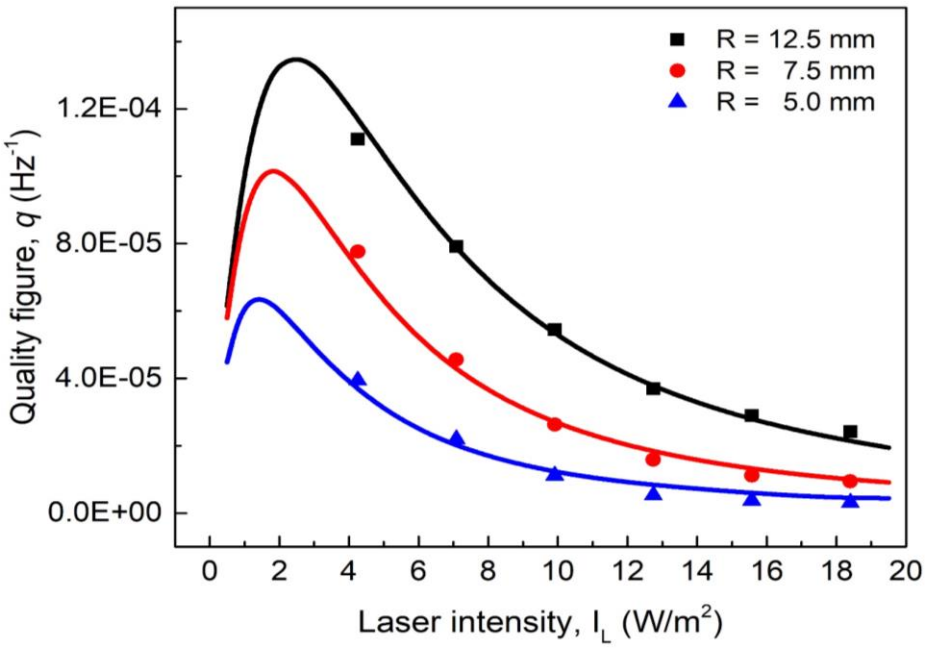


Figure 4.2: Variation of the experimentally measured quality figure with incident laser intensity for three cells with radius (R) values of 12.5 mm, 7.5 mm, and 5 mm (cells C1, C2, and C3) all kept at T = 71$^0$ C. Solid lines are computed from the theoretical model using Equations 2.18 and 2.23 as explained in Section 2.2.

The buffer gas pressure inside the Rb vapor cell also influences the variation of $q$ with respect to laser intensity. Figure 4.3 shows the variation of $q$ with laser intensity at different

buffer gas pressure ($Ar+N_2$) while maintaining a constant cell temperature (63 $^0$C) and RF power (1.51 dBm). Data points with symbols represent the experimental values, and the dotted curves are computed from the theoretical model. The results indicate that $q$ increases with buffer gas pressure at lower intensities but decreases with buffer gas pressure at higher laser intensities. Furthermore, the peak of $q$ shifts towards lower intensity as the pressure of buffer gas increases.

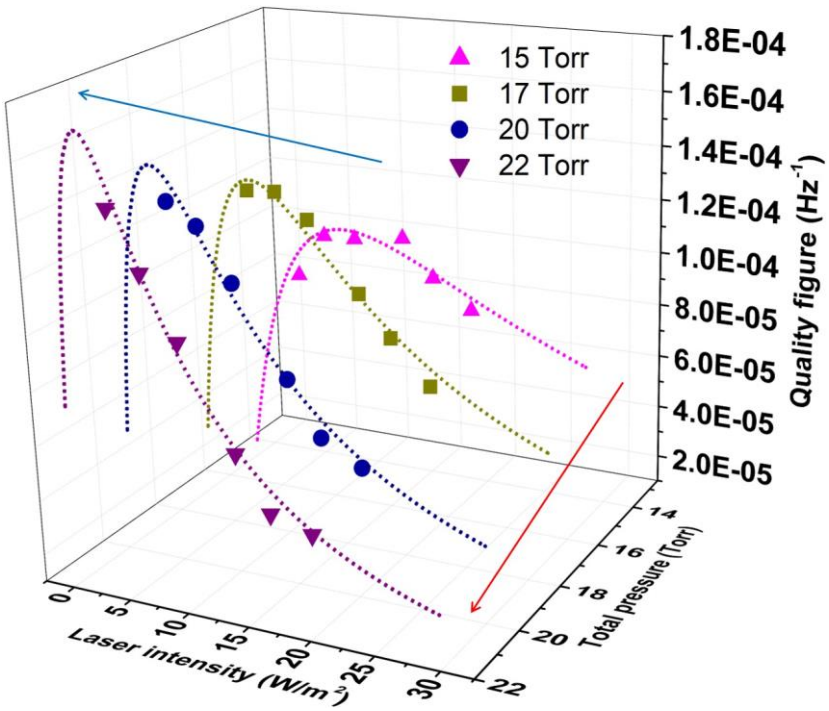


Figure 4.3: The variation in the quality figure with respect to laser intensity at different buffer gas pressure ($Ar+N_2$). Data points in solid symbols represent the measured values, while the dotted lines are computed from the theoretical model. Arrows indicate the direction of increase and decrease in magnitude of quality figure.

The behaviour of quality figure with laser intensity also exhibits dependence on the cell temperature. Figure 4.4 illustrates the variation of both measured and computed $q$ for cell C4 at different temperatures as function of laser intensity. Data points with solid symbols indicate the experimental data, while the 3D surface represents the theoretical model. Experimentally, laser intensities varied from 5 W/m$^2$ to 20 W/m$^2$, and the measured and theoretical data are in good agreement. At lower temperatures, $q$ increases with laser intensity until it reaches a peak value, beyond which it decreases with further increases in laser intensity. However, as the cell temperature increases, the trend of $q$ variation changes, and at high temperatures, it increases

with laser intensity. More details on variation of $q$ with cell temperature is discussed in the following section.

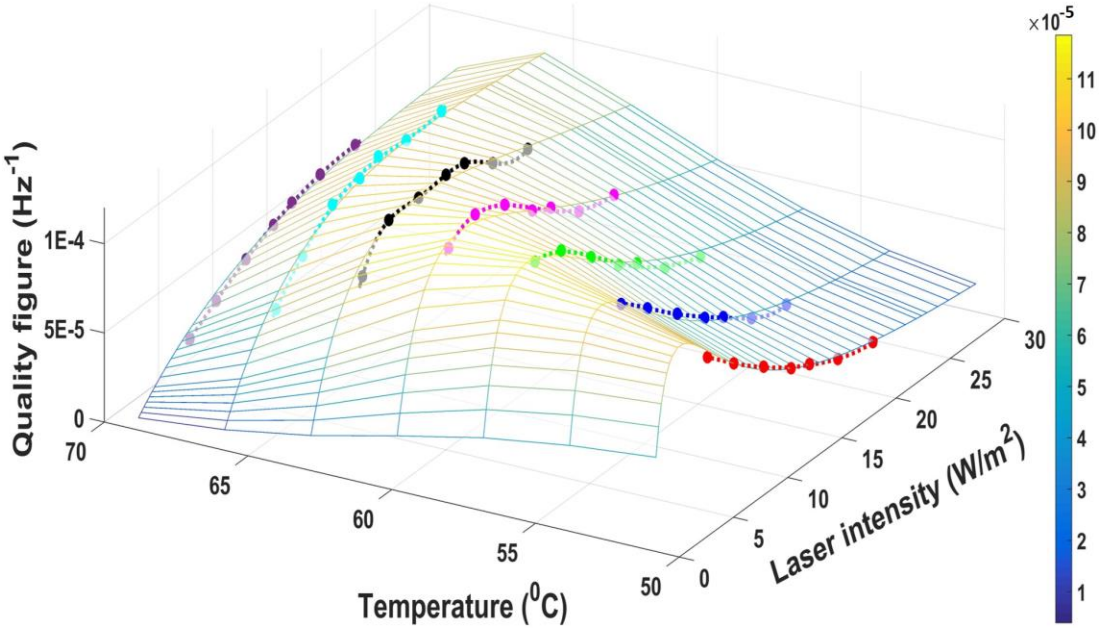


Figure 4.4: The behaviour of the quality figure with respect to laser intensity at different cell temperature while keeping the RF power constant (1.51 dBm) and maintaining the buffer gas pressure inside the cell @ 15 Torr. Data points with solid symbols connected with dotted lines represent the experimental data, while the 3D surface is simulated using the theoretical model.

## 4.1.2 Temperature of vapor cell

The amplitude of CPT resonance, and thus its contrast, depends on the number of atoms participating in the CPT phenomena. This atomic number density varies with cell temperature ($T$) (see Equation 2.27). In this regard, the influence of cell temperature on the characteristics of CPT resonance is studied experimentally in Rb cells.

Figure 4.5 shows variation of $q$ and the corresponding contrast (shown in inset) with cell temperature for three cells (C1, C2, and C3). In each cell, the contrast increases with temperature and reaches a maximum value ($C_{pk}$), from which it decreases with temperature [76], [92], [93], [120]. Contrast reaches maximum value at *optimum number density*. The temperature at which this *optimum number density* is attained is defined as *Optimum Temperature* ($T_{opt}$). $T_{opt}$ varies depending on cell dimension ($R$) and laser excitation intensity ($I_L$). At cell temperatures below $T_{opt}$, contrast increases with temperature, as more and more atoms are available for interaction with the laser field. At temperatures above $T_{opt}$, the contrast

reduces with increase in temperature due to the ravaging contribution of number density dependent mechanisms such as enhanced spin exchange collision and increase in optical thickness of medium [58], [62], [76], [92], [93], [121]. Therefore, at higher temperatures, the absorption of light increases along the length of vapor cell as a result of increase in optical thickness that leads to reduction in contrast [122].

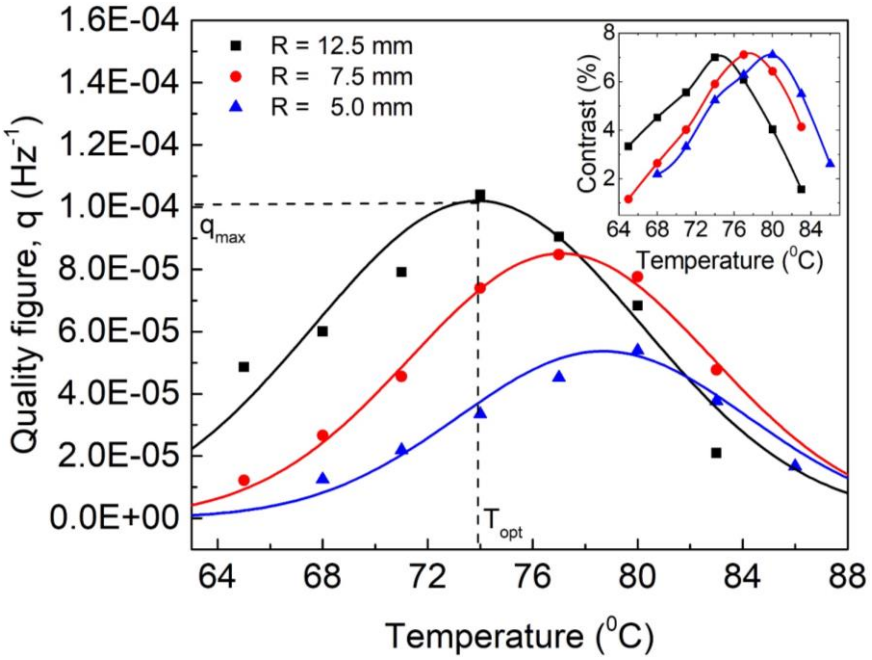


Figure 4.5: Measured quality figure (data symbols) as function of temperature for three cells, C1, C2, and C3 (filled with natural Rb and Ne buffer gas @ 50 Torr) at a laser intensity of 7.08 W/m$^2$. The solid curves indicate the Gaussian fit to the experimental data. Inset: The corresponding CPT resonance contrast as function of temperature.

For a given cell dimension, the variation in magnitude of $q$ with temperature is determined primarily by changes in contrast. This contrast has a characteristic temperature dependent peak at $T_{opt}$ as explained above. However, when compared between cells with different dimensions, the value of $T_{opt}$ shifts to a higher temperature for cells with lower dimension. The magnitude of $q_{max}$ at $T_{opt}$ decreases for lower dimension cells, whereas magnitude of corresponding contrast at $T_{opt}$ is similar for all the cells. The reduction in overall magnitude of $q$ among lower dimension cells is attributed to the increased FWHM (see Figure 4.7). Detailed description on variation of FWHM with cell temperature is provided subsequently. At a given temperature, the effect of wall collision is more pronounced for cells with lower dimension. The increase in temperature affects the confinement time of the atoms within the laser beam. In order to achieve

a similar contrast value as in larger cells, the temperature of smaller cells would have to be increased which leads to a higher optimum temperature ($T_{opt}$) [92].

The solid curves shown in Figure 4.5 are the curve fit to measured data points using the Gaussian function according to Equation 4.2 [117], [118], [123].

$$q(T) = q_{max}.exp[-\frac{1}{2}\left(\frac{T - T_{Opt}}{T_w}\right)^2] \quad (4.2)$$

where fitting parameter $q_{max}$ is the optimum $q$ value, i.e., the peak amplitude of quality figure at $T_{opt}$ and $T_w$ represents the peak width (1-sigma). The values of fitting parameters are extracted from the curves shown in Figure 4.5 and provided in Table 4.2. Amplitude of $q_{max}$ reduces with decrease in cell dimension due to increase in FWHM as shown in Figure 4.7. The optimum $q$ value is maximum for cell with higher dimension. Therefore, cells with larger radius are ideal for realizing CPT with optimized resonance characteristics which in turn helps in improving the frequency stability of atomic clock.

Table 4.2: Fitting parameters for the curve fittings in Figure 4.5.

| **Cell radius (mm)** | **$q_{max}$ ($Hz^{-1}$)** | **$T_{opt}$ ($^0C$)** | **$T_w$ ($^0C$)** |
|---|---|---|---|
| 12.5 | 1.0E-4 | 73.93 | 5.66 |
| 7.5 | 8.9E-5 | 77.15 | 5.19 |
| 5.0 | 5.3E-5 | 78.58 | 5.04 |

The value $q_{max}$ and the corresponding temperature, $T_{opt}$, also depend on laser intensity [121], [124]. Similar to Table 4.2, the values of $q_{max}$ and $T_{opt}$ are extracted at different laser intensities for all the three cells. Figure 4.6 depicts the variation of fit value of $q_{max}$ (solid line, left y-axis) and its corresponding $T_{opt}$ (dotted line, right y-axis) as function of laser excitation intensity for three cell dimensions. It is observed that the value of $q_{max}$ is higher and $T_{opt}$ value is lower for cells with higher dimension at lower excitation intensity. Thus, the optimum values of $q_{max}$ and $T_{opt}$ are achieved with higher dimension cell at lower laser excitation intensity.

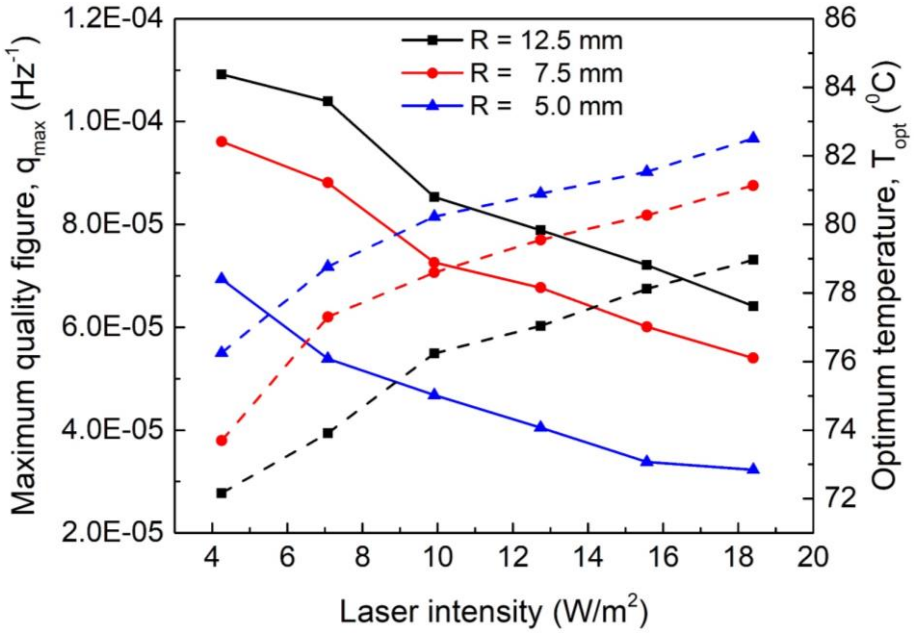


Figure 4.6: The plot of the maximum quality figure, $q_{max}$, (solid lines, left y-axis) of CPT resonance and corresponding optimum temperature, $T_{opt}$, (dashed lines, right y-axis) as function of laser excitation intensity for cells C1, C2 and C3 (filled with natural Rb and Ne buffer gas @ 50 Torr).

Figure 4.7 shows FWHM as function of cell temperature at a laser excitation intensity of 7.08 $W/m^2$ for cells with three different dimensions. FWHM is higher for cells with lower dimension due to enhanced wall collisions which destroy the coherence. For a given cell size, FWHM decreases marginally with increase in temperature. A higher cell temperature increases the collision between Rb-Rb atoms and Rb-buffer gas. The higher Rb-Rb collision rate would lead to an increase in FWHM of CPT resonance. On the other hand, the higher Rb-buffer gas atoms collision results in a tighter confinement of the Rb atoms in the probing volume which leads to an increase in the transit time (interrogation time) and thus a reduction in FWHM. The net reduction in the FWHM observed in this experiment indicates that Rb-buffer gas collision has a greater influence on CPT resonance characteristics under these operating conditions, especially the temperature range. Furthermore, a similar variation of FWHM with respect to temperature is also reported in Reference [121]. In addition, the rate of reduction in FWHM is higher in cell with lower dimension due to stronger confinement effect with increase in temperature.

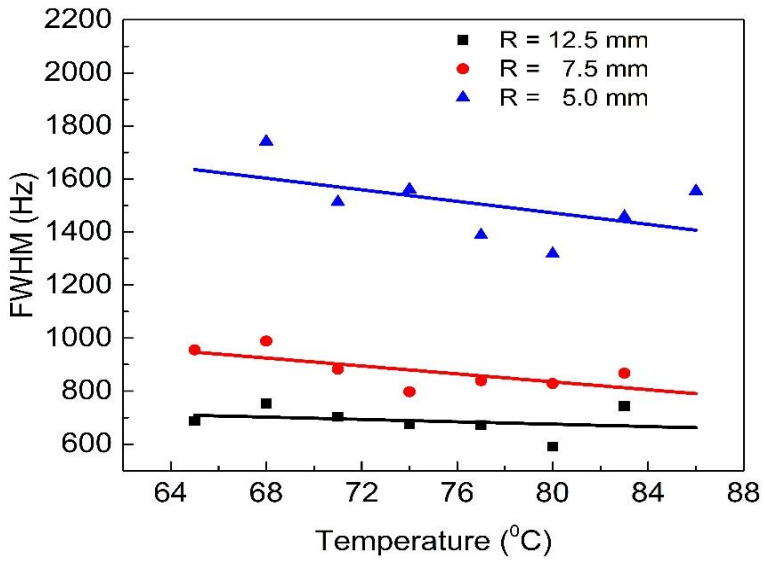


Figure 4.7: Measured FWHM of CPT resonance as function of temperature in cells C1, C2, and C3 (radius, R=12.5 mm, 7.5 mm and 5.0 mm) at a laser excitation intensity of 7.08 W/m$^2$. FWHM is higher for lower dimension cells. Here, the solid lines represent the corresponding linear fit.

For a given cell dimension, the $q_{max}$ and $T_{opt}$ also depend on the pressure of the buffer gas inside the cell. Like in Figure 4.6, $q_{max}$ and $T_{opt}$ are determined at all laser intensities for four cells (cell numbers C4, C5, C6, and C7) with different buffer gas pressures. Figure 4.8 depicts the relationship between $T_{opt}$ and laser intensity in these cells. The experimental data is fitted using a linear model and represented by solid lines. The results indicate that $T_{opt}$ increases with laser intensity and buffer gas pressure. From Figure 4.8, the observed $T_{opt}$ at lower intensity is around 60 $^0$C. Conversely, at similar laser intensity, $T_{opt}$ for cell number C1 is around 72 $^0$C as shown in Figure 4.6. Possible reason for this difference in magnitude of $T_{opt}$ is attributed to the type of Rb filled in these cells (see Table 4.1). Cell numbers from C4 to C7 are filled with enriched $^{87}$Rb, facilitating the availability of *optimum number density* at lower temperature. In contrast, cell numbers from C1 to C3 filled with natural Rb (containing 28% of $^{87}$Rb + 72% of $^{85}$Rb), achieve *optimum number density* at higher temperature due to lower percentage of $^{87}$Rb i.e., around 28%.

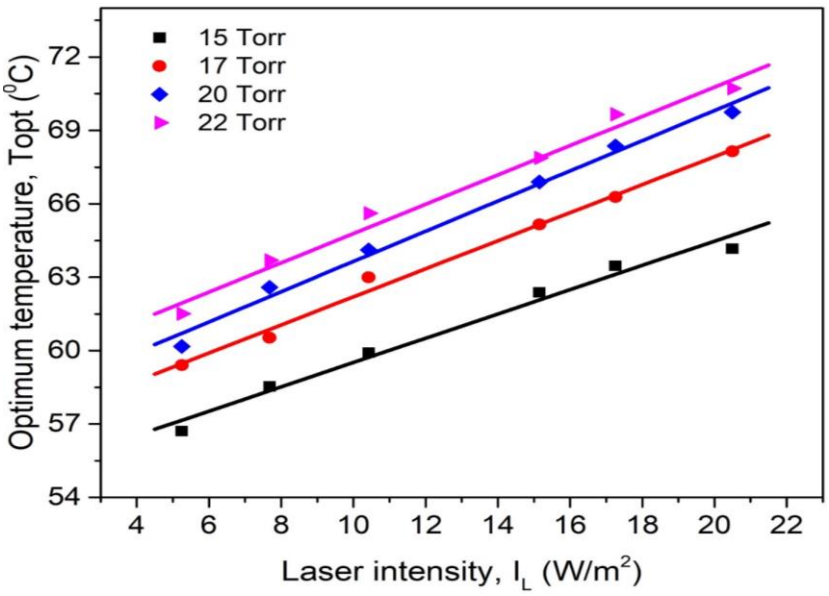


Figure 4.8: Variation of optimum temperature with respect to incident laser intensity for four cells with buffer gas pressure, 15 Torr (square), 17 Torr (circle), 20 Torr (diamond), and 22 Torr (right triangle), all kept at RF power 1.51 dBm. Solid lines represent the linear fit to the experimental data.

Figure 4.9 illustrates the variation of $q_{max}$ with laser intensity among four cells. Solid lines represent the fit to the experimental data using linear or quadratic models. As the Figure 4.9 shows, $q_{max}$ decreases with laser intensity, and the decrease is more pronounced for cells with higher buffer gas pressure. The cell with a buffer gas pressure of 15 Torr is preferable as the variation in its $q_{max}$ is minimal with a change in laser intensity.

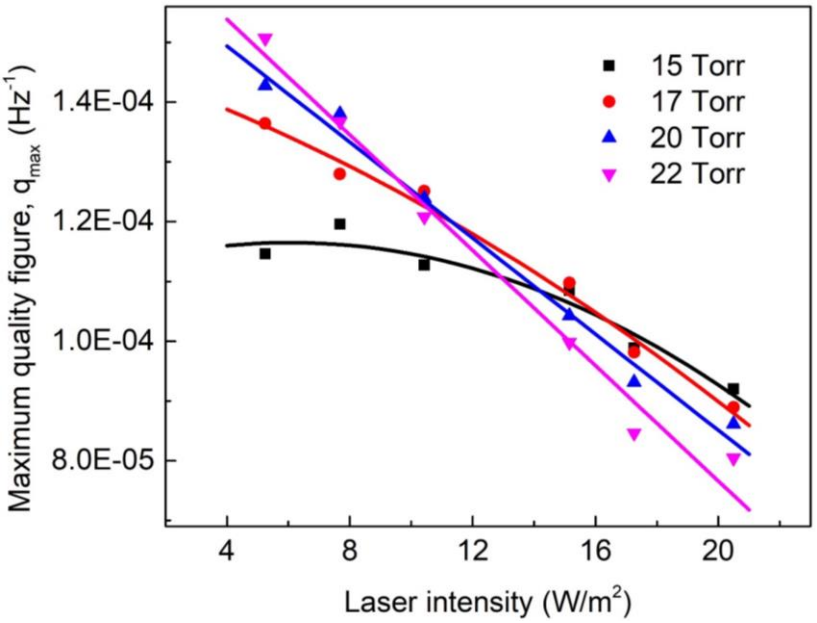


Figure 4.9: Maximum quality figure ($q_{max}$) of CPT resonance as function of laser intensity for cells with different pressure values, 15 Torr (squares), 17 Torr (circles), 20 Torr (up triangles), and 22 Torr (down triangles). The solid lines are the corresponding linear or quadratic fit.

### 4.1.3 RF power

The RF power that couples to laser diode also influences the CPT characteristics (See Section 2.3.5) [103], [105], [122]. Figure 4.10 shows the quality figure as function of RF power for cell number C4 at cell temperature 63 $^0$C, and laser intensity of 13 W/m$^2$. At lower RF power, the quality figure increases with increase in RF power and reaches a maximum value, after which it decreases. At higher RF power values, the quality figure exhibits rapid reduction. Optimum quality figure is achieved for RF power values between 0.8 to 1.6 dBm.

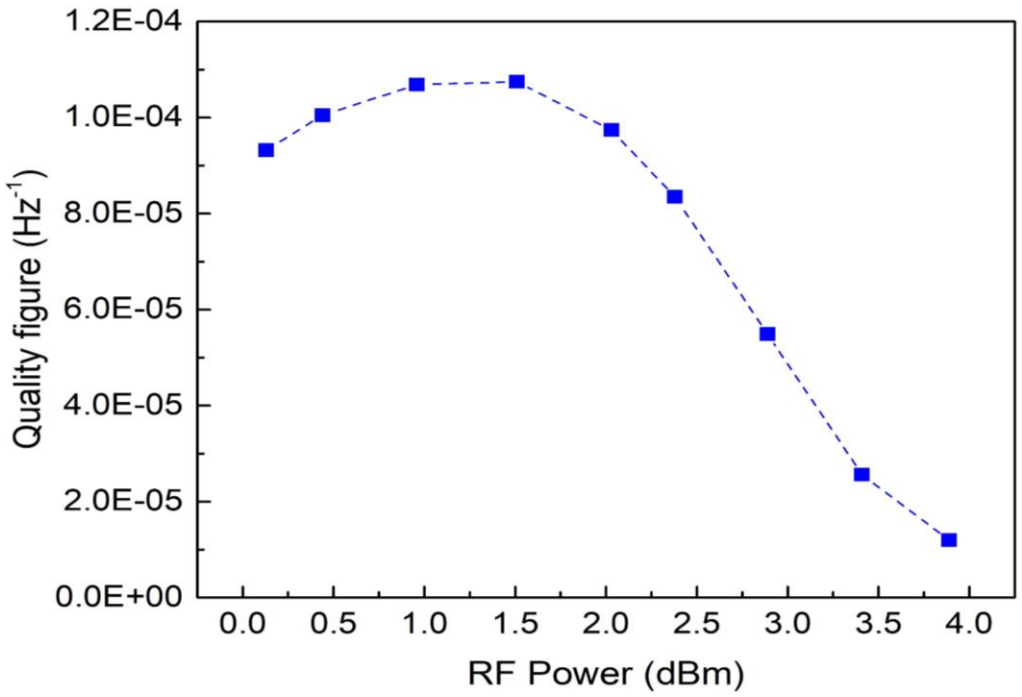


Figure 4.10: Quality figure of CPT resonance as function of RF power for cell C4 at temperature 63 $^0$C and laser intensity 13 W/m$^2$. The dashed line connecting the data points serves as a guide to eye.

## 4.2 CPT resonance frequency shift

The deviation of CPT resonance centre (peak) frequency from theoretical reference ($\nu_{ref}$) is defined as frequency shift. The laser excitation intensity, cell temperature and RF power are the primary contributing operating parameters to this frequency shift [53], [90], [103], [104], [125]. Laser intensity induces frequency shift as a result of AC stark effect (see Section 2.3.1) [90]. Temperature dependent frequency shift arises from the collisional interaction between $^{87}$Rb atoms and buffer gas. RF power influences the amplitude of the harmonics of modulated laser spectrum. Hence, its influence on frequency shift is in similar way to that of laser

intensity. As discussed in Section 3.5, output frequency of atomic clock is stabilized with reference to the peak of CPT resonance. Hence, any shift in resonance centre frequency leads to a shift in output frequency of atomic clock. Frequency shift in atomic clock influences its stochastic (medium to long-term frequency stability) as well as deterministic behaviour which induces error in timing applications such as satellite navigation. Hence, optimizing CPT resonance frequency shift is important in timing applications of CPT based atomic clock.

The fluctuations in center frequency are caused by the variations in operating parameters [90]. In this section, an investigation is reported on frequency shift, particularly the rate of frequency shift to study its sensitivity with respect to operating parameters. Frequency shift is calculated by taking the difference between observed resonance centre frequency and the reference frequency ($\nu_{ref}$=3.417341305 GHz). Systematic study on rate of frequency shift with different operating parameters is carried out. In this regard, following notations are used in the subsequent sections.

The rate of frequency shift with respect to laser intensity can be computed as $\frac{d\nu_{I_L}}{dI_L}$, which is called as intensity light shift coefficient ($\alpha_{I_L}$) [90]. Here, $\nu_{I_L}$ is frequency shift with respect to laser intensity. Similarly, the rate of frequency shift with respect to cell temperature and RF power are represented by $m_T = \frac{d\nu_T}{dT}$ and $m_{RF} = \frac{d\nu_{RF}}{dRF}$. Here, $\nu_T$ and $\nu_{RF}$ are frequency shift as function of cell temperature and RF power, respectively.

## 4.2.1 Frequency shift Vs Laser excitation intensity

The fluctuations in laser intensity can contribute to shift in the center frequency of CPT resonance that could manifest as noise and drift in the clock frequency. Light shift induced by laser intensity is a major contributor to the frequency instability. It is sum of the shifts induced by all possible sidebands of the laser spectrum. The laser intensity shift also depends on cell temperature [90], [124].

Figure 4.11 shows the CPT resonance center frequency shift in cell number C1 as function of laser intensity. Here, C1 is with radius 12.5 mm and containing natural Rb with Ne buffer gas @ 50 Torr. Measured frequency shift values are shown at two temperature values i.e., 65 $^0$C and 83 $^0$C. The magnitude of resonance frequency shift decreases at lower temperatures and increases at higher temperatures with laser intensity. Computed values of rate of frequency shift with laser intensity i.e., $\alpha_{I_L}$ at 65 $^0$C and 85 $^0$C are -8.964 Hz/Wm$^{-2}$ and 7.805 Hz/Wm$^{-2}$,

respectively. Thus, negative and positive $\alpha_{I_L}$ are observed at lower and higher temperatures. Sensitivity of $\alpha_{I_L}$ with respect to cell temperature is discussed in the following section.

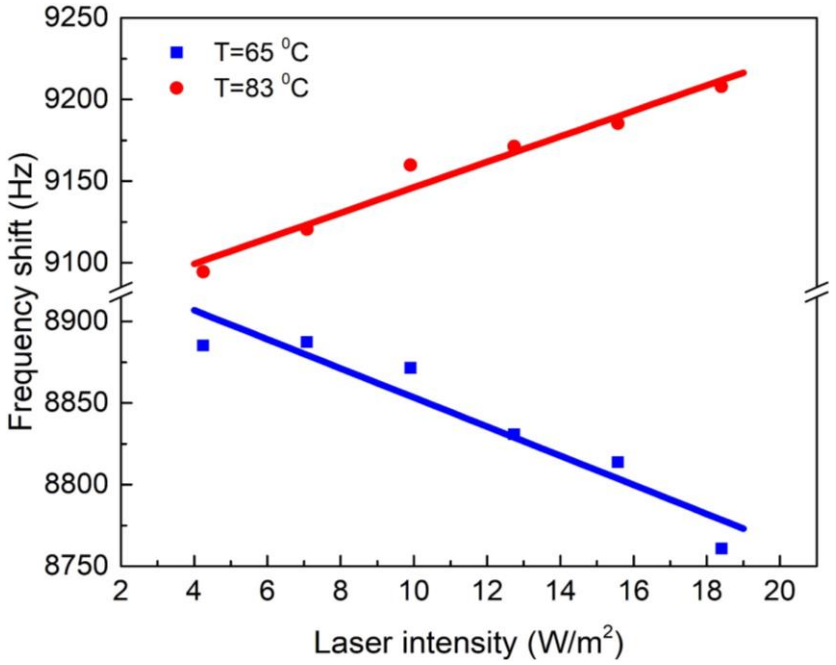


Figure 4.11: CPT resonance frequency shift as function of laser intensity at temperature, T = 65 $^0$C (squares) and 83 $^0$C (circles) measured in C1 containing natural Rb with Ne buffer gas @ 50 Torr. Solid lines represent linear fit to the measured data.

## 4.2.2 Frequency shift Vs Cell temperature

The intensity light shift coefficient, $\alpha_{I_L}$ values for cell C1 are computed for different operating cell temperatures and plotted as shown in Figure 4.12. As temperature increases, $\alpha_{I_L}$ changes from negative to positive value. Intensity light shift coefficient also depends on the absorption of resonant light (first order sidebands) by $^{87}$Rb atoms. However, the absorption depends on number density which increases with cell temperature. As the temperature increases, the intensity light shift coefficient induced by first order sidebands changes from negative to positive [90]. A minimum or near zero $\alpha_{I_L}$ ($LS_{min}$) is observed at temperature ~72 $^0$C. The temperature corresponding to $LS_{min}$ is termed as *optimum temperature for minimum light shift* ($T_{LS\text{-}opt}$) at which frequency shift due to laser intensity is minimum. From Figure 4.6, it can be seen that for the same cell (C1) the maximum quality figure is also observed at temperature ~72 $^0$C which also corresponds to the observed $T_{LS\text{-}opt}$.

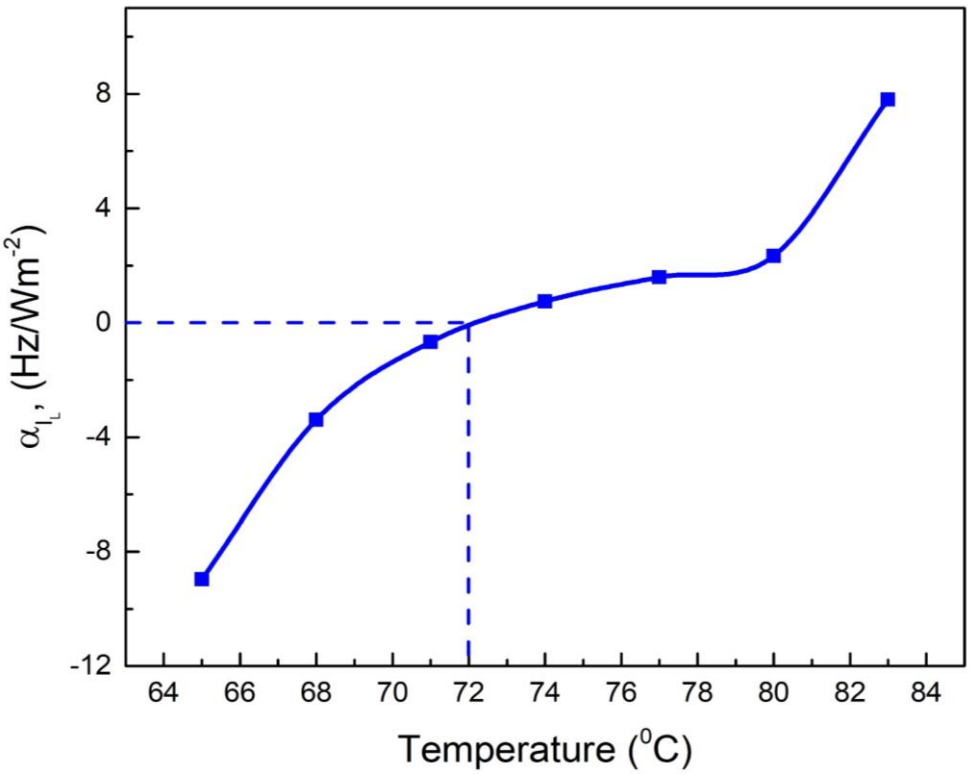


Figure 4.12: Intensity light shift coefficient $\boldsymbol{\alpha_{I_L}}$ as function of temperature for cell C1 with natural Rb and Ne buffer gas @ 50 Torr. Minimum intensity light shift coefficient is observed at temperature ~ 72 $^0$C.

The collisions between Rb atoms and buffer gas atoms in the vapor cell also induce frequency shift in the CPT resonance. This frequency shift is known as pressure shift of the ground-state hyperfine splitting [63] and it depends on temperature. Thus, any fluctuations in temperature affects the frequency shift and thus long-term frequency stability [94]. Frequency shift at a given temperature comprises the contribution arising from both laser intensity as well as cell temperature. In order to obtain the temperature dependent frequency shift, laser intensity contribution to frequency shift must be isolated. Laser intensity induced frequency shift at any temperature can be computed by multiplying the rate, $\frac{dv_{I_L}}{dI_L}$ (i.e., $\alpha_{I_L}$) at that temperature with given laser intensity. Figure 4.13 shows these intensity light shift contributions with respect to cell temperature at different laser intensity values.

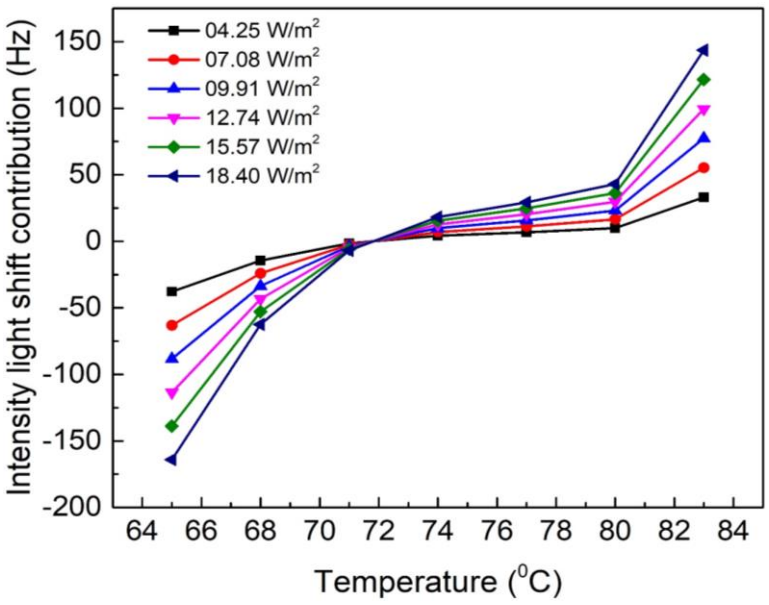


Figure 4.13: Intensity light shift contribution at each cell temperature corresponding to different laser intensity values.

Figure 4.14 shows the temperature dependent induced frequency shift (after separating the contribution of intensity light shift values, as shown in Figure 4.13) as function of temperature at laser intensity of 4.25 W/m$^2$. The observed rate of the frequency shift is +9.95 Hz/$^0$C whose sign (i.e., a positive slope) is consistent with the theory that the Ne buffer gas induces a positive temperature dependent frequency shift [9], [46], [63].

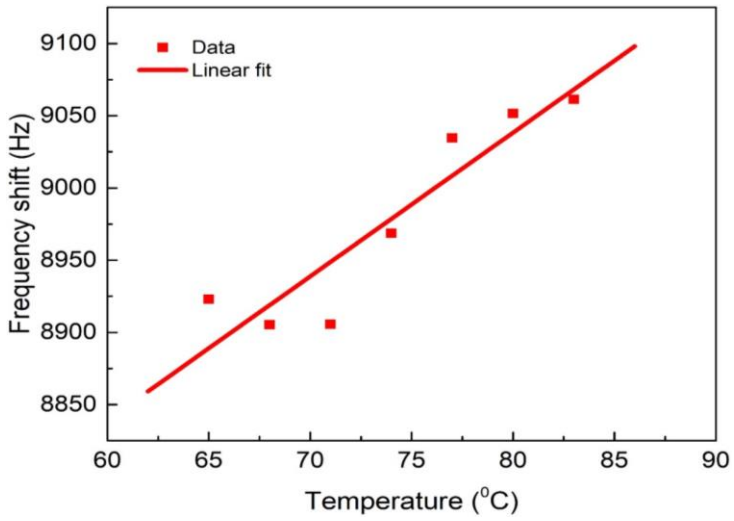


Figure 4.14: CPT resonance frequency shift as function of temperature at laser intensity 4.25 W/m$^2$ (light shift contribution is separated with reference to Figure 4.13)). The solid line is the linear fit to the measured data.

From Figure 4.14, the rate of frequency shift with temperature can be computed as $\frac{dv_T}{dT}$, i.e., $m_T$ at different laser intensity values. These $m_T$ values are plotted as function of laser

intensity as shown in Figure 4.15. The minimum rate of shift due to temperature is observed for light intensity range from 9.9 to 13 W/m$^2$ for cell C1.

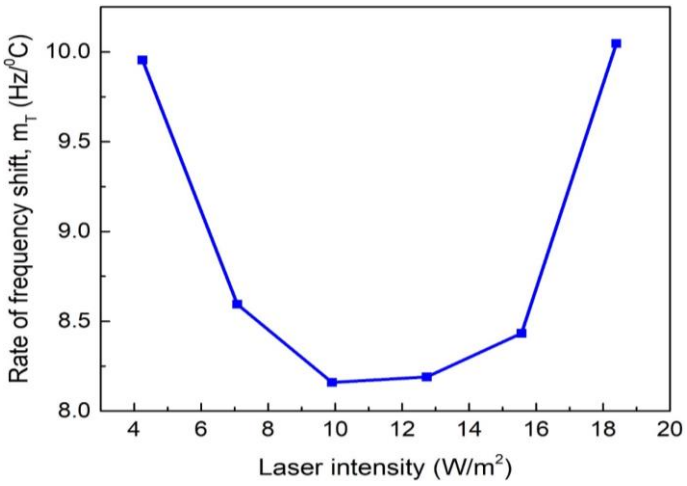


Figure 4.15: Rate of frequency shift, $\boldsymbol{m_T}$ as function of laser intensity. Minimum rate of temperature shift is observed for the laser intensity range from 9.9 to 13 W/m$^2$.

### 4.2.3 Frequency shift Vs RF power

Intensity light shift coefficient ($\alpha_{I_L}$) is also computed at different RF power values for four cells (C4, C5, C6, and C7) and plotted in Figure 4.16. These cells are filled with enriched $^{87}$Rb and (Ar+$N_2$) buffer gas at different pressure values. Figure 4.16 shows that the intensity light shift coefficient decreases with increase in RF power and is lower for cell with lower buffer gas pressure.

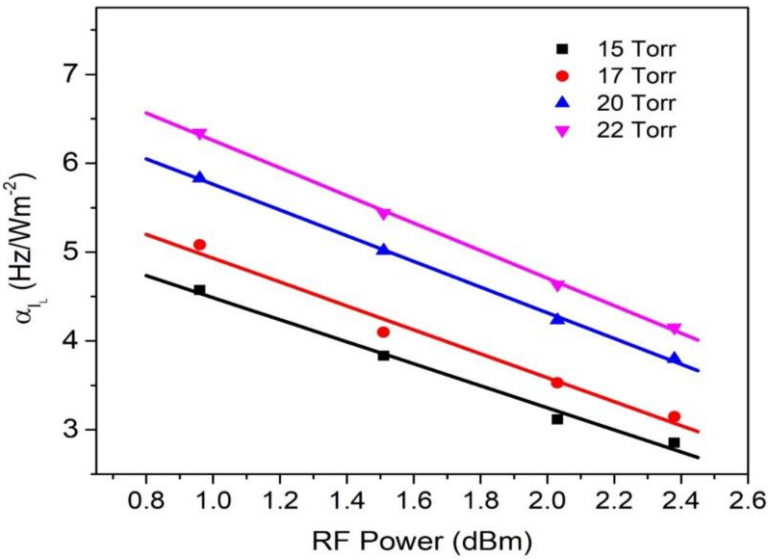


Figure 4.16: Variation of intensity light shift coefficient, $\alpha_{I_L}$ with RF power at T=63 $^0$C for four cells (C4, C5, C6 and C7). Solid lines are the linear fit to the experimental data. These four cells are filled with enriched $^{87}$Rb and (Ar+$N_2$) buffer gas.

Figure 4.17a shows the variation of frequency shift with RF power at laser intensity 7.08 W/m$^2$ for a cell with a buffer gas pressure of 22 Torr (C7). The data indicates a linear decrease in frequency shift with increase in RF power. The rate of frequency shift, $m_{RF}$ is computed at each laser intensity for four cells and presented in Figure 4.17b. Here, solid lines are the linear fit to the data. The results indicate that $m_{RF}$ depends significantly on laser intensity. Furthermore, the magnitude of $m_{RF}$ and its variation increases with buffer gas pressure. Minimum rate of frequency shift is observed for the cell with buffer gas pressure 15 Torr.

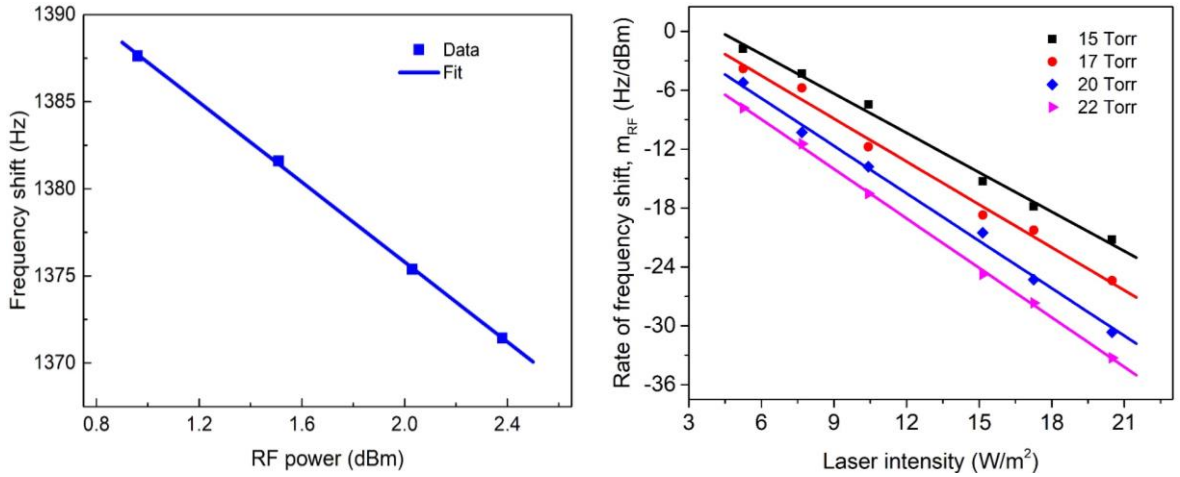


**(a)** **(b)**

Figure 4.17: (a) Frequency shift with RF power. (b) Variation of $m_{RF}$ as a function of laser intensity at cell temperature 63 $^0$C for four cells. Solid lines are the linear fit to the experimental data.

The experimental study discussed in this chapter is focused on practical ways to optimize the operating parameters that would affect the CPT resonance which in turn impact the stability of atomic clock. Experimental results are compared with four-level atomic model and the results are in good agreement. Further, these experimental results are utilized to understand the dependency of CPT resonance characteristics on operating parameters. Based on experimental results in this study optimum cell radius is 12.5 mm and cell with 15 Torr buffer gas pressure exhibit corresponding optimum $q_{max}$ (1.2E-4 Hz$^{-1}$) and $T_{opt}$ (~59 $^0$C) values. In addition, minimum rate of frequency shift is observed for this cell which provides the optimum trade-off among different operating parameters. These optimized parameters are appropriate for the excitation scheme and Rb cells considered in this study.

Shot-noise limited theoretical frequency stability of this scheme can then be estimated using an optimum '$q_{max}$' value obtained from the above experimental results. Equation 4.3 provides the shot-noise limited frequency stability [48].

$$\sigma(\tau) \approx \frac{1}{\sqrt{2}} \frac{(RIN)^{1/2}}{4q\nu_{hfs}} \tau^{-1/2} \tag{4.3}$$

Here, *RIN* is the Relative Intensity Noise for VCSEL, $q$ is quality figure, $\nu_{hfs}$ is $^{87}$Rb hyper fine ground state splitting, and $\tau$ is averaging time. Optimum '$q_{max}$' and *RIN* values considered in the calculation are, 1.2E-4 Hz$^{-1}$ and -120 dB/Hz [Manufacturer specification], respectively. Figure 4.18 shows the theoretical estimated shot-noise limited frequency stability.

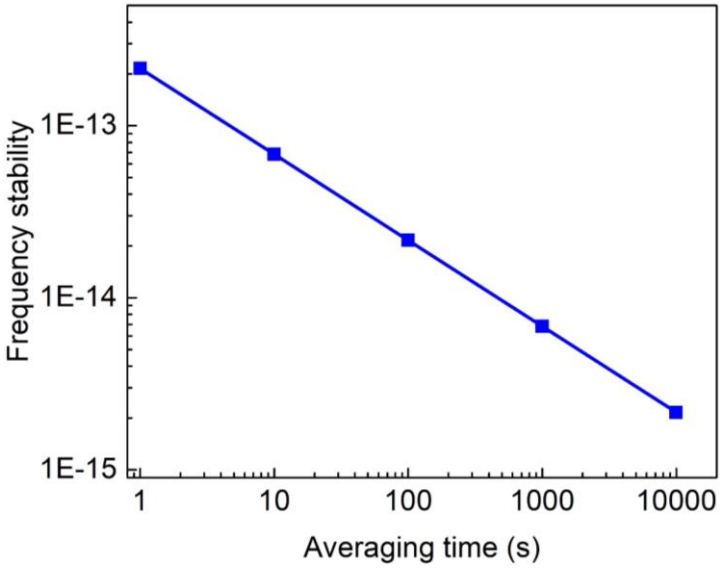


Figure 4.18: Shot-noise limited theoretical frequency stability corresponding to the optimum $q_{max}$.

This theoretical computation is purely based on the characteristics of laser source and parametric values of Rb vapour cell employed in the system. However, in reality the contributions from other system noises, like EM coupling, and servo control, would also affect the long-term frequency stability significantly.

When the atomic clock is used as on-board timing source in satellite navigation, its stochastic and deterministic behaviour is crucial for smooth functioning of navigation service. On-board clock characterization and continuous monitoring of its performance is critical in satellite navigation. Chapters 5 and 6 describe the real time characterization of satellite clock and timekeeping methodology for satellite navigation to provide the uninterrupted service to the user.

# Chapter-5

# Characterization of On-board Clocks

In satellite navigation system, atomic clock is used as on-board source for the generation of *satellite time*. Optimal performance of this on-board clock (satellite clock) is critical for smooth functioning of navigation system as its performance degradation, like instability, can directly affect the user positioning accuracy (see Equation 1.18). Typically, satellite clock exhibits stochastic and deterministic behaviour. The stochastic behaviour is studied by measuring the frequency stability using overlapping Allan deviation (OADEV). *Satellite time* can also deviate from ground reference time due to deterministic behaviour of satellite clock. This deterministic behaviour is characterized by satellite clock offset, $\delta t^s$ which is expressed using quadratic polynomial coefficients (see Equation 1.19) referred to as clock correction parameters. These correction parameters are predicted for a future period and broadcasted to the user. User receiver computes its position and timing information by applying these corrections, as explained in Section 1.5.2. More details on $\delta t^s$ and clock correction parameters are provided in Chapter-6.

Under nominal behaviour (with intended behaviour without any anomalies) of satellite clock, the user position is maintained within the desired accuracy if the predicted clock behaviour closely matches with the observed behaviour. Any deviation in observed clock behaviour from predicted behaviour would lead to an error in user position [126], [127]. Hence, accurate real-time characterization and monitoring of satellite clock behaviour is crucial in satellite navigation system. Characterization of satellite clock includes computation of its fractional frequency (commonly referred to as frequency in this chapter) and detection of anomalies such as outlier (an abnormal data point), phase jump (abrupt change in clock offset) and frequency jump (abrupt change in clock drift), as well as monitoring clock frequency stability against desired specifications. These anomalies cannot be corrected and consequently, the broadcasted clock parameters could become invalid after the occurrence of anomalies if they are untreated. Hence, any deviation in the frequency of satellite clock from its nominal

behaviour must be identified immediately and the user must be provided with a new set of suitable correction parameters to avoid degradation in position accuracy.

This chapter discusses the detailed algorithms to characterise on-board clocks that include: 1) real-time computation of frequency of satellite clock through one-way carrier phase measurements, 2) resolving the integer ambiguity issue associated with these one-way carrier phase measurements, and 3) detection of anomalies. These algorithms have been devised, implemented, and operationalized in Indian Regional Navigational Satellite System (IRNSS), also known as Navigation with Indian Constellation (NavIC). Further, the stochastic behaviour of satellite clocks is analysed by computing the frequency stability using OADEV and Dynamic Allan deviation (DADEV), and identifying the noise types using Lag-1 auto-correlation method. In essence, this chapter highlights the characterization methodology for on-board clocks using one-way carrier phase measurement data from NavIC satellites.

## 5.1 Navigation with Indian constellation

IRNSS/NavIC is developed by the Indian Space Research Organization (ISRO) to provide navigation service to users over the Indian region as well as the region extending up to 1500 km from its geopolitical boundary. Like other satellite navigation systems, NavIC also consists of three segments, namely space segment, ground segment and user segment as shown in Figure 5.1. The ground segment consists of IRNSS Network Timing Centre (IRNWT) to provide the ground reference time (also referred to as IRNSS system time), IRNSS Range and Integrity Monitoring Stations (IRIMS) which provide one-way range measurements and are also used to monitor the reliability of navigation signals. Code Division Multiple Access (CDMA) ranging stations provide two-way range measurements for independent orbit determination [128]. The satellite ephemeris and clock parameters are estimated at ISRO Navigation Centre (INC) i.e., NavIC service provider, with respect to IRNWT (NavIC reference time). These parameters are up-linked to the NavIC satellites via ground uplink stations, i.e., spacecraft control centre (SCC) [129], [130].

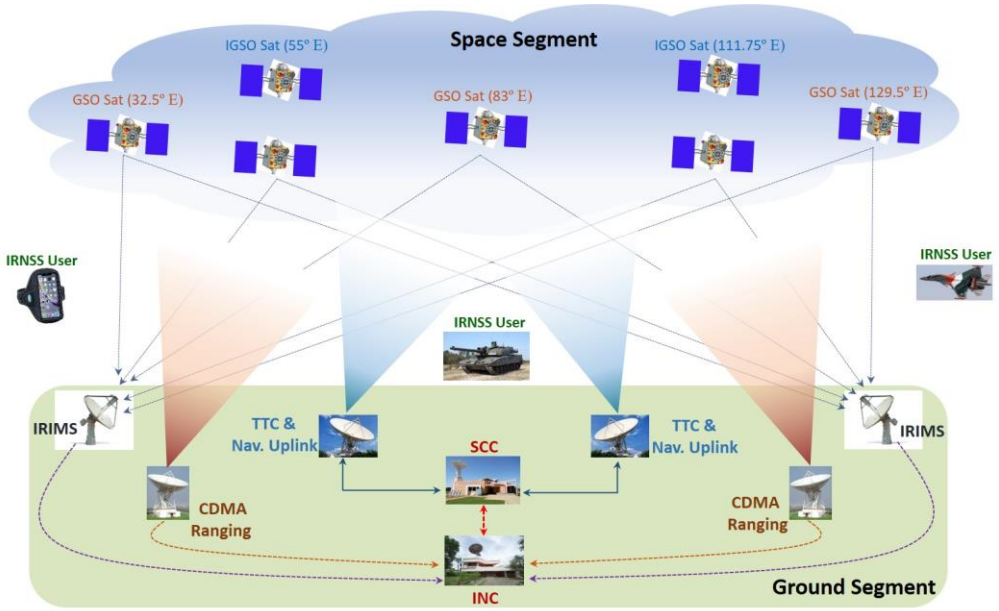


Figure 5.1: Architecture of IRNSS/NavIC. TTC: Telemetry, Tracking and Commanding.

The space segment consists of seven satellites such that three satellites are in geosynchronous orbits (GSO) with an inclination of $5^0$ and four satellites are in inclined geosynchronous orbits (IGSO) with an inclination of $29^0$. Three GSO satellites are located with longitude crossings at $32.5^0$ E, $83^0$ E, $129.5^0$ E and four IGSO satellites at $55^0$ E and $111.75^0$ E as shown in Figure 5.1 [130], [131]. NavIC user segment consists of NavIC receivers that provide the Standard Positioning Service (SPS), an open service to all users, and the Restricted Service (RS) only to authorized users.

Within the NavIC system, IRIMS reference receiver provides code ($\rho$) and carrier ($\varphi$) one way range measurements. NavIC service provider (or INC) uses these measurement data to estimate the satellite ephemeris and clock parameters which are referred to as primary navigation parameters. These navigation parameters will be embedded in navigation signal which are generated and transmitted by navigation payload on-board. One way carrier measurement data provided by IRIMS receivers would serve as input data to the algorithms discussed in this chapter.

## 5.2 NavIC navigation payload

Figure 5.2 shows the schematic of NavIC navigation payload that generates and transmits the navigation signals. Each NavIC satellite carries Rb Atomic Frequency Standard (AFS) whose output frequency (10 MHz) is fed to the Atomic Clock Monitoring Unit (ACMU). ACMU converts 10 MHz to the fundamental frequency, $f_0$ (10.23 MHz) using frequency

synthesizer. All carrier frequencies and satellite PRN (Pseudo-Random-Noise) codes are generated using this fundamental frequency via clock distribution unit. Navigation parameters uplinked to the satellite is received by Navigation Signal Generating Unit (NSGU) via telemetry and telecommand (TM and TC) unit. Navigation parameters and PRN codes are modulated on the carrier signals and then upconverted to L5 (1176.45 MHz) and S (2492.028 MHz) navigation signal frequencies [130], [131], [132], [133]. These L5 and S signals are amplified to the required power level by high power amplifiers and then transmitted through antenna. These navigation signals are received and processed by the NavIC user receiver on ground and the receiver then computes its position and timing information.

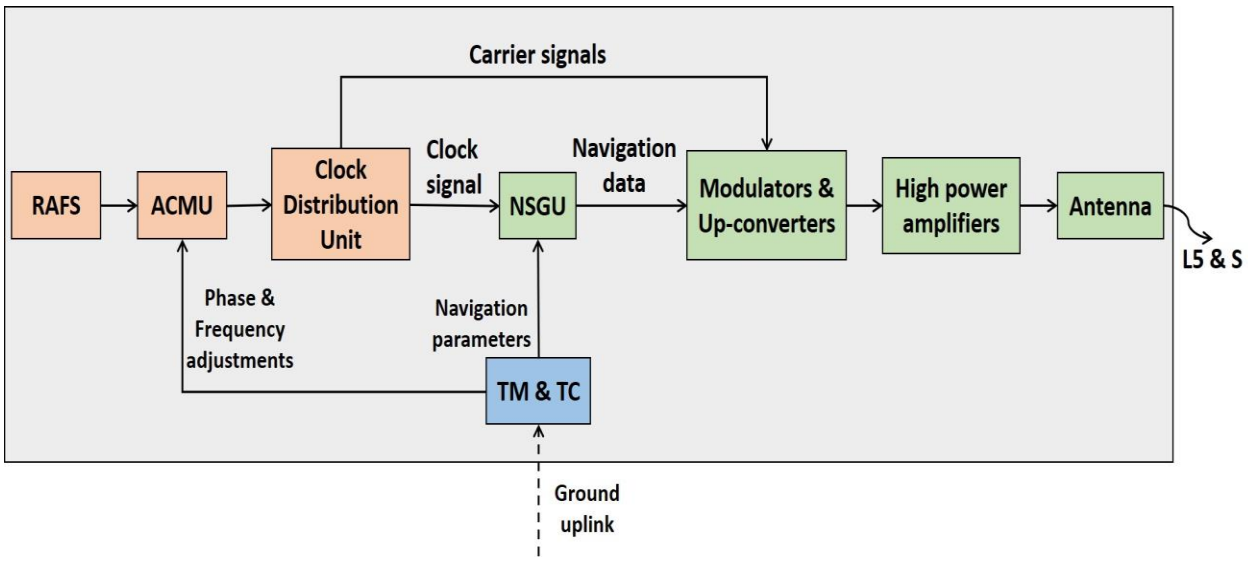


Figure 5.2: Block diagram of navigation payload of NavIC satellite.

After launch, the NavIC satellite becomes operational once the satellite is put in its final orbit. Subsequently, *satellite time* is synchronized with ground reference time (see Section 6.2.1) [131]. Frequency, frequency stability and drift of on-board Rb AFS are then continuously measured and monitored on ground by processing one-way range measurement data downlinked via L5 and S signals. The following sections describe the detailed methodology on characterization of on-board clock using one-way measurement data.

## 5.3 Criticality of clock characterization

As explained in Section 1.5.2.1, satellite clock offset, $\delta t^s$ plays a crucial role in computation of user equivalent range error (UERE), which determines the accuracy of the user position (see Equation 1.20). Navigation service provider estimates the clock correction

parameters based on the $\delta t^s$ accumulated over 24 hours (typically) which is called as estimation period. Subsequently, these corrections are predicted for the next 24 hours (called as prediction period) and uplinked to the satellite. In real-time, user receiver employs these broadcasted corrections to derive the $\delta t^s$ (see Equation 1.19) and then the computation of its position. The alignment of predicted clock behaviour with real-time observed behaviour is imperative for precise user positioning. However, the occurrences of clock anomalies can lead to deviation of observed clock offset from the prediction that creates error in user position. Hence, it is critical to detect these anomalies and promptly generate new clock parameters after the event of clock anomaly and uplink as well as broadcast to avoid degradation in user position.

### 5.3.1 Prediction error with nominal behaviour

Under nominal behaviour, observed clock offset generally aligns closely with the predicted offset. Figure 5.3a shows typical nominal behaviour of $\delta t^s$ of IRNSS-1E satellite during estimation period (say Day1) and prediction period (say Day2). The corresponding frequency data is the derivative of clock offset (see Equation 1.5) and shown in Figure 5.3b.

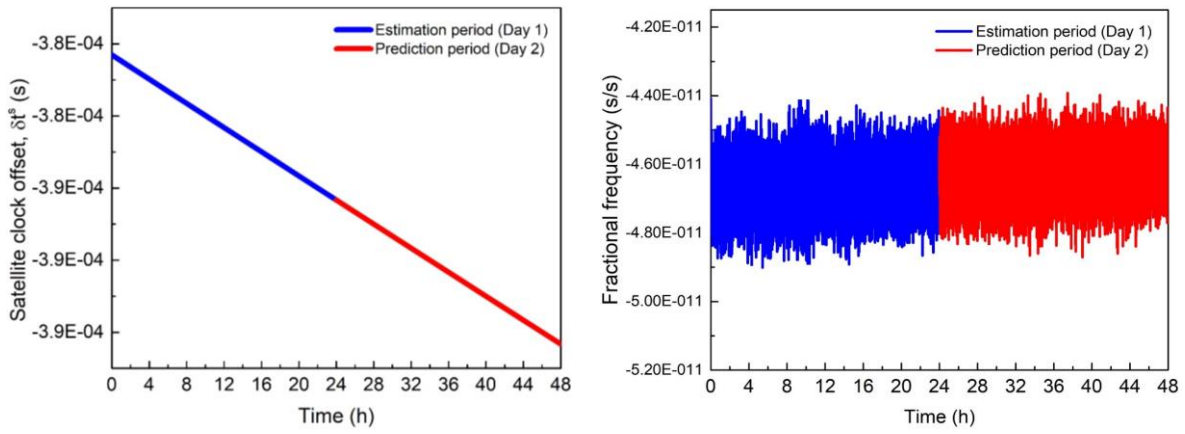


(a) (b)

Figure 5.3: (a) Satellite clock offset ($\boldsymbol{\delta t^s}$) of IRNSS-1E during the estimation and prediction period, with nominal behaviour. (b) Corresponding clock frequency data.

The difference between observed clock offset and predicted clock offset (computed with clock corrections using Equation 1.19) is referred to as prediction error, which contributes directly to the UERE. Figure 5.4a shows the schematic representation of observed and predicted (for 24 hours) clock offset with nominal behaviour, i.e., without any anomalies.

Figure 5.4b illustrates the typical prediction error corresponding to the data shown in Figure 5.3, for the duration of 24 hours (Day2). The prediction error is well within 5 ns over the period of 24 hours. The prediction error under nominal behaviour is due to the contribution from both uncertainty in the estimation model and frequency stability of clock.

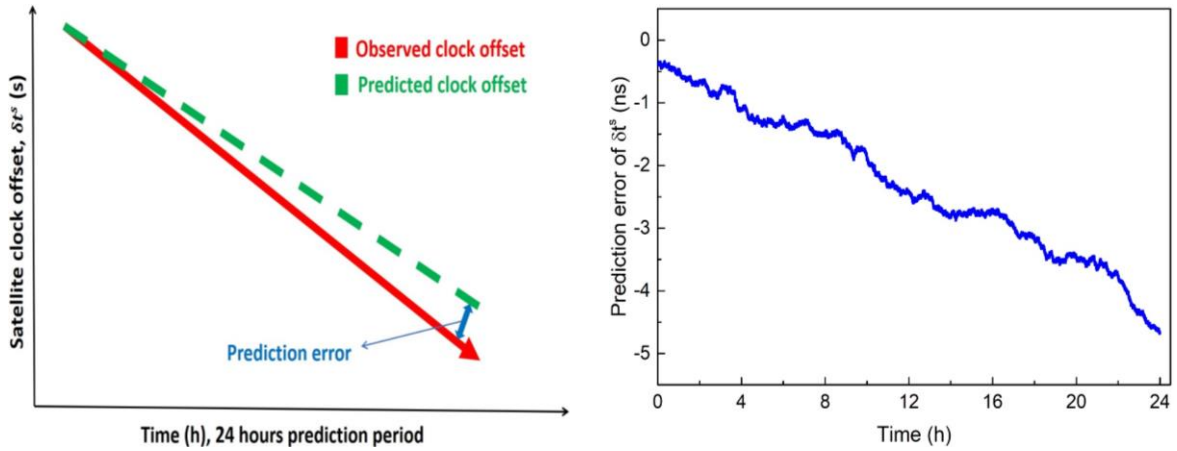


(a) (b)

Figure 5.4: (a) Schematic representation of observed and predicted clock offset with nominal behaviour during the prediction period. (b) Prediction error of IRNSS-1E clock offset, $\boldsymbol{\delta t^s}$ over 24 hours prediction period with respect to the data presented in Day2 of Figure 5.3.

## 5.3.2 Prediction error with anomalies

This section describes the impact of clock anomalies such as frequency jump and phase jump on prediction error during the prediction period. The impact is studied by simulating frequency jump and phase jump within the prediction period of IRNSS-1E clock data shown in Figure 5.3. Figure 5.5 shows the clock frequency with a simulated frequency jump at $T_{epoch}$ = 2 hours during Day2 with magnitude of 1.0E-12 s/s.

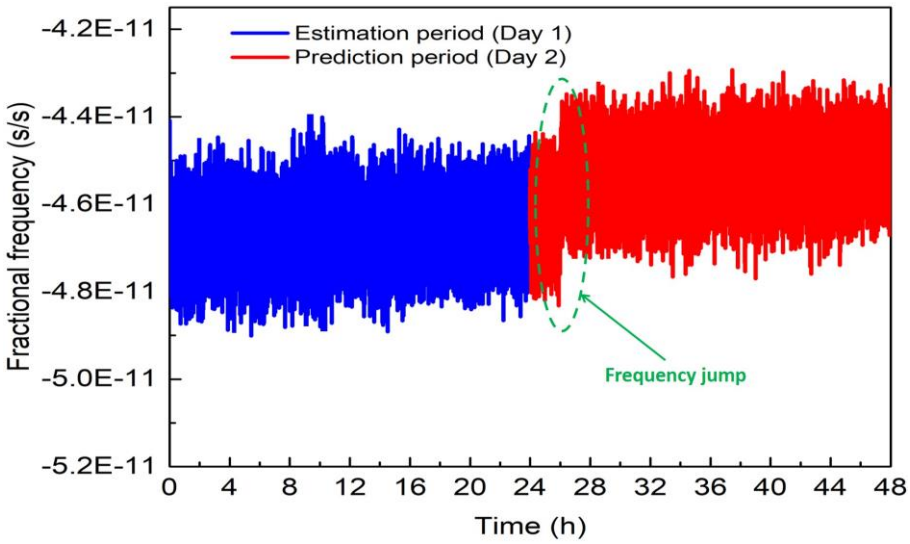


Figure 5.5: IRNSS-1E satellite clock frequency (corresponding to Figure 5.3b) with a simulated frequency jump at epoch, $T_{epoch}$ = 2 hour during the prediction period (Day2).

Figure 5.6 shows the prediction error in the observed clock offset during the nominal behaviour (circles) and in the presence of frequency jump (triangles). This prediction error (triangles) is corresponding to the data shown in Figure 5.5 during the prediction period. The error accumulates rapidly following the frequency jump. The accumulated error at the end of 24 hours is ~85 ns.

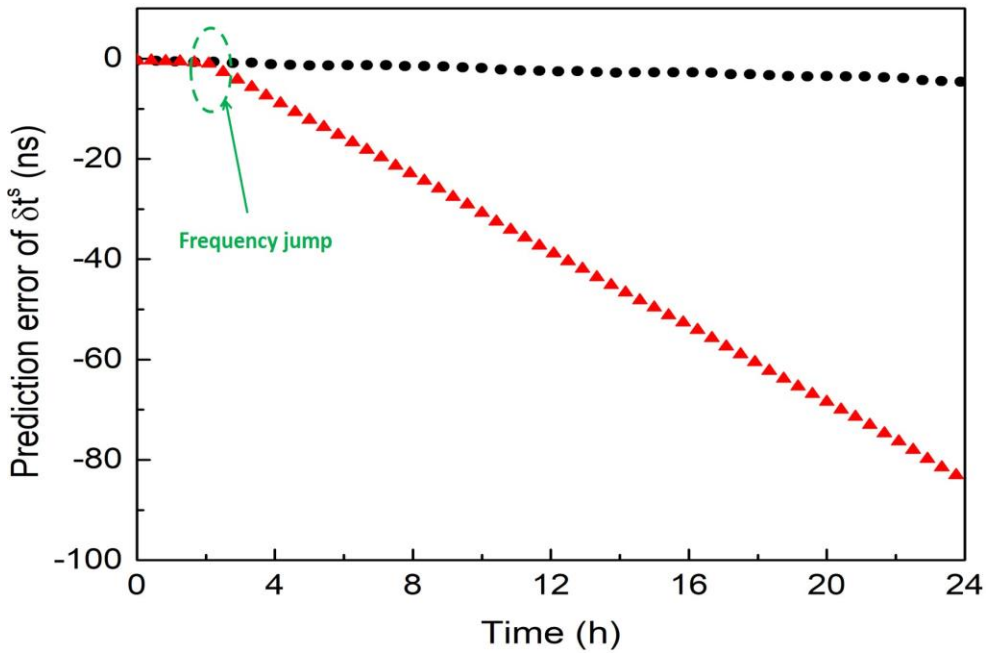


Figure 5.6: Prediction error without any anomaly (circles) and with frequency jump (triangles). It demonstrates the accumulation of clock offset prediction error (triangles) due to frequency jump.

Similarly, Figure 5.7 illustrates prediction error with nominal behaviour (circles) and with the phase jump (squares) in the observed clock offset. Here, the phase jump is simulated at epoch, $T_{epoch}$ = 2 hours during Day2, in data shown in Figure 5.3a with a magnitude of 10 ns. Due to this phase jump, same magnitude is observed in prediction error as an offset as shown in Figure 5.7.

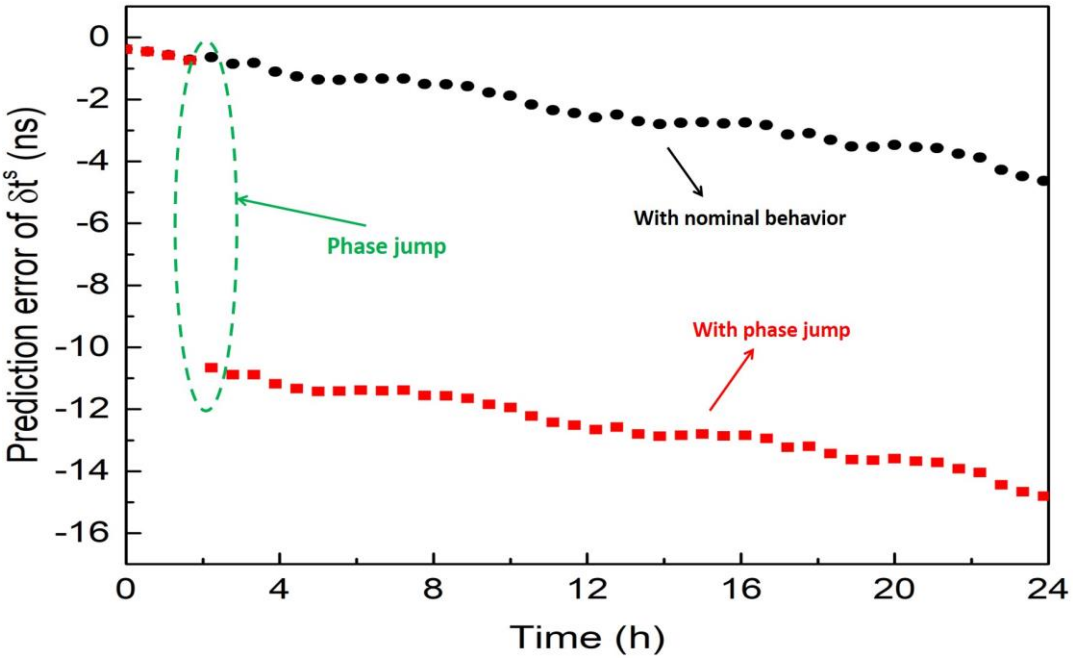


Figure 5.7: Prediction error of satellite clock offset with nominal behaviour (circles) and with a phase jump (squares) at the 2nd hour (epoch) within the prediction period.

Figures 5.6 and 5.7 clearly indicate that the clock prediction error increases rapidly following the anomaly events which invalidates clock corrections after the occurrence of anomaly. The magnitude of this error depends on the size of anomaly event, and the accuracy of user position thus degrades accordingly. These events must be detected immediately and followed by the generation of new clock correction parameters and their up-linking to the satellite to maintain the user position accuracy within the desired limit. The following sections provide the real-time characterization of clock using NavIC navigation signals and detection of anomalies.

## 5.4 Computation of on-board clock frequency

NavIC satellite provides one-way code and carrier range measurements on *L5* and *S* frequencies. Code measurements are accurate but noisy, while carrier measurements are precise

but ambiguous [134], [135], [136]. Therefore, standalone carrier phase measurements are preferable for clock characterization as they are less noisy compared to code measurements.

Carrier phase measurement by a receiver is the measure of phase difference between the navigation carrier signal received and the reference signal generated by itself. It is the sum of accumulated number of cycles and the instantaneous phase difference. The initial value of integer number of cycles is unknown and is called as integer ambiguity and denoted by $N$. For a given line of sight from satellite to receiver, this $N$ remains constant until the receiver continuously tracks the satellite without any interruption. If tracking is interrupted, the $N$ changes to a new value $N'$, which is referred as cycle slip [137], [138]. The possible reasons for occurrence of cycle slip are, severe ionospheric conditions, low signal to noise ratio, high multipath, high noise due to interference, and failure of receiver processing software [137], [139], [140]. Thus, the limitation with carrier phase measurement is that it contains unknown integer ambiguity [141], [142]. In this study, a new methodology is proposed in which the effect of integer ambiguity can be eliminated by using clock frequency data computed from carrier phase measurements. Detailed description of this methodology is provided below.

The carrier phase range measurement from NavIC satellite to IRIMS receiver is represented by following equation known as "*observation equation*" [141].

$$\varphi_j = r + \mathrm{c}(\delta t_u - \delta t^s) + \mathrm{T} - I_j + \lambda_j N_j + \varepsilon_{\varphi,j} \tag{5.1}$$

Here, $j$ is the signal identifier (*L5* or *S*), $\varphi_j$ is carrier phase range measurement, $r$ is true (geometric) range, $c$ is speed of light, $\delta t_u$ is receiver clock offset, $\delta t^s$ is satellite clock offset, $T$ is tropospheric delay, $I_j$ is ionospheric delay, $\lambda_j$ is wavelength of signal $j$, $N_j$ is integer carrier-phase ambiguity, and $\varepsilon_{\varphi,j}$ is unmodeled error. Figure 5.8 shows the carrier phase range data of IRNSS-1I satellite measured by IRIMS receiver at *L5* and *S* frequencies.

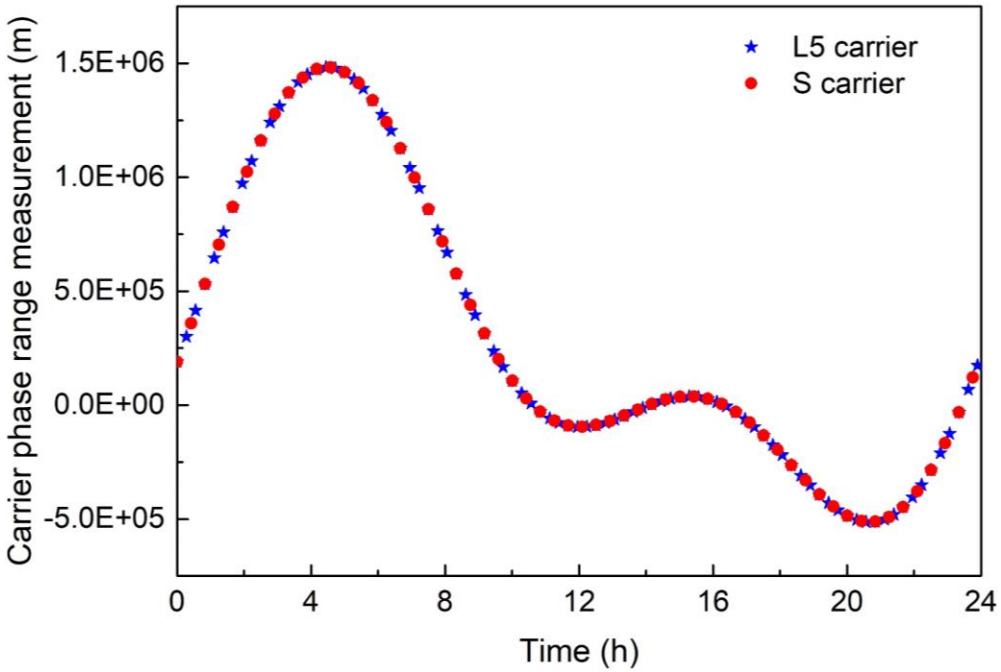


Figure 5.8: Carrier phase range data of IRNSS-1I satellite measured by IRIMS receiver at *L5* and *S* frequencies.

In this range data, ionospheric delay is the dominant source of error which can be eliminated by a linear combination of dual frequency measurements, known as iono-free linear combination [133], [143], [144], [145]. The iono-free carrier phase ($\varphi_{IF}$) measurement is given by Equation 5.2, in the units of metres [133].

$$\begin{aligned}\varphi_{IF} &= C_{L5}\varphi_{L5} - C_S\varphi_S \\ &= r + c[\delta t_u - \delta t^s] + T + C_{L5}\lambda_{L5}N_{L5} - C_S\lambda_S N_S + \varepsilon_{\varphi,IF}\end{aligned} \tag{5.2}$$

where $\varphi_{L5}$ and $\varphi_S$ are carrier phase range measurements at $L5$ and $S$ frequencies indicated by $f_{L5}$ and $f_S$, $\lambda_{L5}$ and $\lambda_S$ are corresponding wavelengths, $N_{L5}$ and $N_S$ are corresponding unknown integer number of cycles, and $\varepsilon_{\varphi,IF}$ represents unmodeled errors. Here, $C_{L5} = \frac{f_{L5}^2}{f_{L5}^2 - f_S^2}$ and $C_S = \frac{f_S^2}{f_{L5}^2 - f_S^2}$ are frequency dependent scale factors. Equation 5.2 can be rearranged as shown in Equation 5.3.

$$c\delta t^s{}_{\varphi} = c\delta t^s - C_{L5}\lambda_{L5}N_{L5} + C_S\lambda_S N_S = (r + c[\delta t_u] + T + \varepsilon_{\varphi,IF}) - \varphi_{IF} \tag{5.3}$$

Here, $c\delta t^s{}_\varphi$ is the satellite clock offset along with the integer ambiguity terms. Therefore, the satellite clock offset computed from carrier phase measurements ($c\delta t^s{}_\varphi$) is equivalent to the observed satellite clock offset ($c\delta t^s$) summed with unknown integer ambiguities. These ambiguities are multiplied by corresponding wavelengths, as given in Equation 5.3. This $c\delta t^s{}_\varphi$ is computed from carrier phase measurement by correcting it with known/computed values of $r$, $\delta t_u$ and $T$ [131].

True range ($r$) is calculated using satellite ephemeris [128] and known coordinates of IRIMS. Precise value of $\delta t_u$ is available for selected IRIMS. The Sastamoinen model is used to correct for tropospheric delay [146]. The value of $c\delta t^s{}_\varphi$ in units of seconds is computed using Equation 5.4.

$$\delta t^s{}_\varphi = \delta t^s + \frac{1}{c}(C_S\lambda_S N_S - C_{L5}\lambda_{L5}N_{L5}) \tag{5.4}$$

$$\delta t^s{}_\varphi = \delta t^s + \delta t^s{}_B \tag{5.5}$$

Here, $\delta t^s{}_B = \frac{1}{c}(C_S\lambda_S N_S - C_{L5}\lambda_{L5}N_{L5})$ is the bias due to the integer ambiguities present in the carrier phase measurements data. The existence of integer ambiguities ($N_{L5}$ and $N_S$) in Equation 5.4 can be resolved by using satellite clock frequency data. This frequency can be computed by taking the derivative of clock offset as given below (see Equation 1.5).

$$y = \frac{d\delta t^s{}_\varphi}{dt} = \frac{d\delta t^s}{dt} + \frac{1}{c}(C_S\lambda_S\frac{dN_S}{dt} - C_{L5}\lambda_{L5}\frac{dN_{L5}}{dt}) \tag{5.6}$$

If there is no cycle slip (i.e., no change in integer ambiguity) in carrier phase measurements from both signals, then the rate of $N_{L5}$ or $N_S$ (i.e., $\frac{dN_{L5}}{dt}$ or $\frac{dN_S}{dt}$), is zero. Therefore, the satellite clock frequency is not affected. If there is a cycle slip in *L5* or *S*, or in both, then the frequency is affected by an outlier with a magnitude represented by $y_{\Delta N}$.

Here, $y_{\Delta N} = -\frac{1}{c}(C_{L5}\lambda_{L5}\frac{dN_{L5}}{dt})$ or $\frac{1}{c}(C_S\lambda_S\frac{dN_S}{dt})$ , or $\frac{1}{c}(C_S\lambda_S\frac{dN_S}{dt} - C_{L5}\lambda_{L5}\frac{dN_{L5}}{dt})$ , respectively. Hence, the frequency can alternatively be represented using Equation 5.7.

$$y = \begin{cases} \dfrac{d\delta t^s}{dt}, & Without\ cycle\ slip \\ \dfrac{d\delta t^s}{dt} + y_{\Delta N}, & With\ Cycle\ slip \end{cases} \quad (5.7)$$

Satellite clock offset and frequency for IRNSS-1I satellite are computed using equations 5.5 and 5.7. Carrier phase measurement data shown in Figure 5.8 is input to this computation. Figure 5.9 shows the typical satellite clock offset and its frequency corresponding to data shown in Figure 5.8.

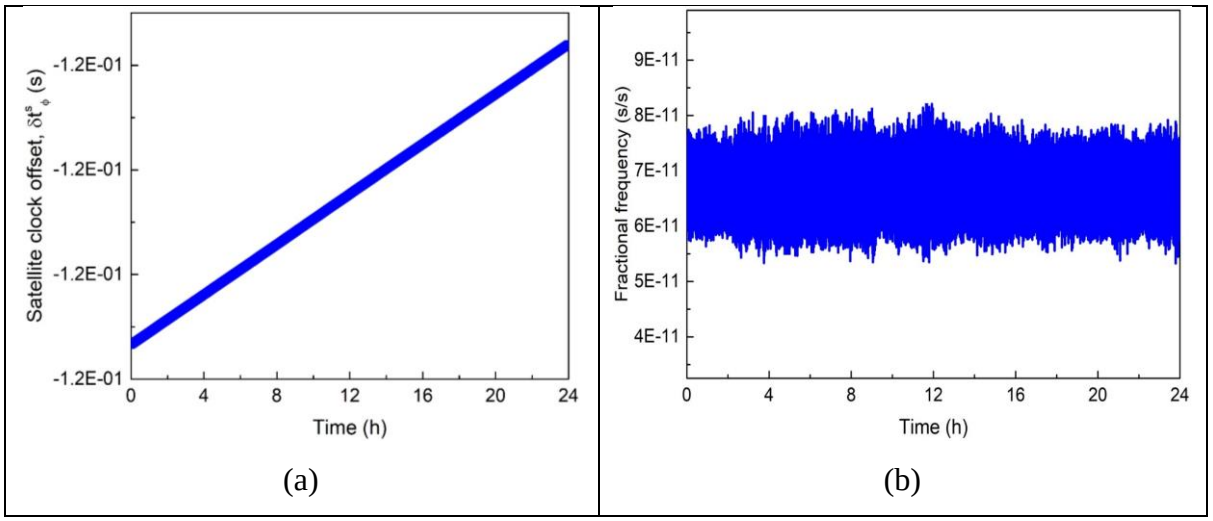


Figure 5.9: (a) IRNSS-1I satellite clock offset computed from carrier phase measurement data shown in Figure 5.8. (b) Corresponding frequency. These offset and frequency are computed using Equations 5.5 and 5.7, respectively.

Figure 5.10 shows the satellite clock offset in the presence of a cycle slip. This data corresponds to IRNSS-1I satellite (Figure 5.8) in which 10 cycles are simulated on L5 carrier phase measurement data.

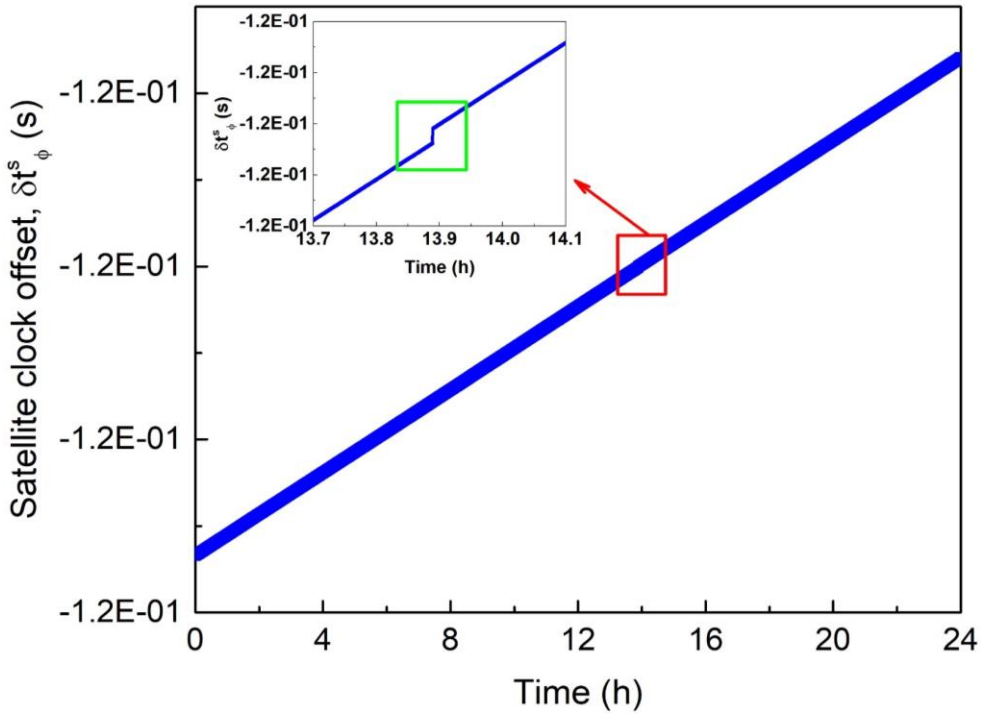


Figure 5.10: IRNSS-1I satellite clock offset in the presence of simulated cycle slip in carrier phase measurement. The inset shows the zoomed region around the cycle slip.

## 5.5 Clock anomalies

### 5.5.1 Classification of clock anomalies

Satellite clock offset ($\delta t^s$) can exhibit anomalies such as outlier, phase jump and frequency jump mainly due to environmental variations and internal malfunctioning. A single algorithm is developed for real-time detection of these anomalies. Frequency data derived from carrier phase measurements is the input to the developed methodology. Therefore, it is crucial to understand the relationship between clock offset and frequency data with respect to different anomalies. To understand this relationship, the anomalies are simulated and compared between clock offset and corresponding frequency data. These anomalies are simulated using the real clock data from one of the NavIC satellites.

Figure 5.11 indicates the presence of outlier in clock offset and its effect on corresponding frequency data. The presence of an outlier in clock offset is validated through the identification of successive outliers with opposite polarity in the clock frequency data.

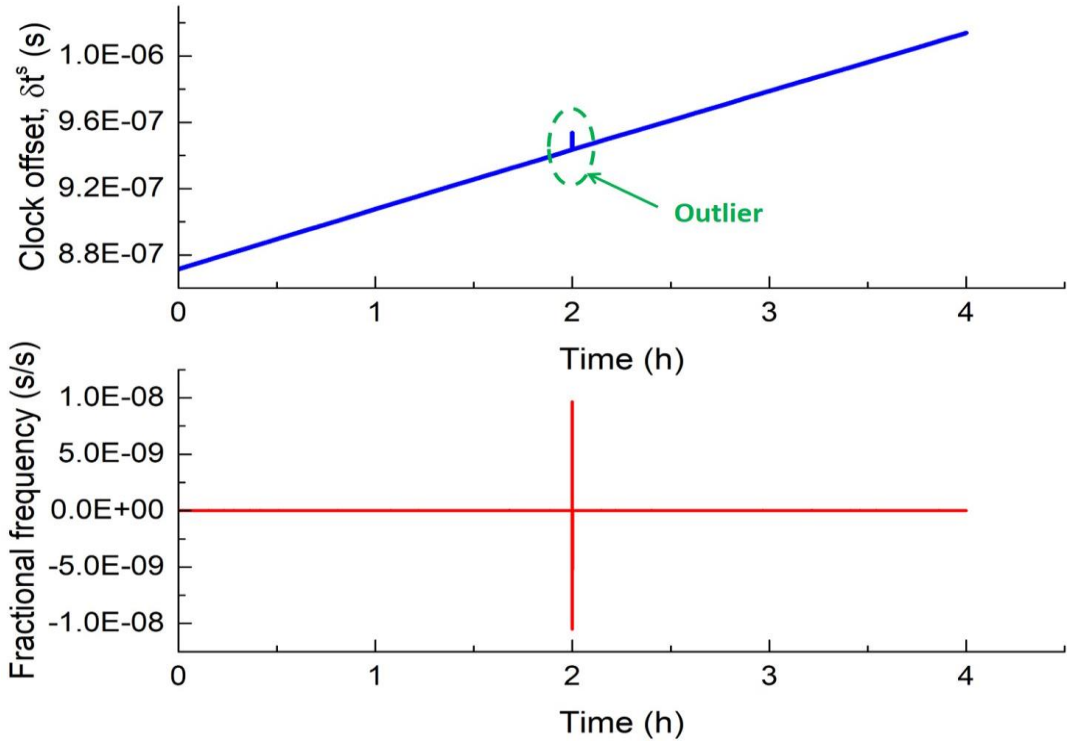


Figure 5.11: IRNSS-1D clock offset and frequency data with respect to simulated outlier during the first 4 hours.

Figure 5.12 shows the presence of phase jump in clock offset and corresponding frequency data. A phase jump in clock offset is reflected as a single outlier in frequency data. From Figures 5.10 and 5.12, it is observed that the presence of both cycle slip in the carrier phase measurement and phase jump in clock offset would impact the clock frequency data with a similar outlier. Thus, cycle slip also can be identified as a phase jump as they are indistinguishable. In order to mitigate this issue, frequency data derived from multiple receivers are processed to distinguish between phase jump and cycle slip in satellite clock offset data. If multiple receivers detect a phase jump at the same epoch, it is confirmed as an actual phase jump in satellite clock. Conversely, if a phase jump is not observed by multiple receivers, it is identified as a cycle slip occurred in that particular receiver.

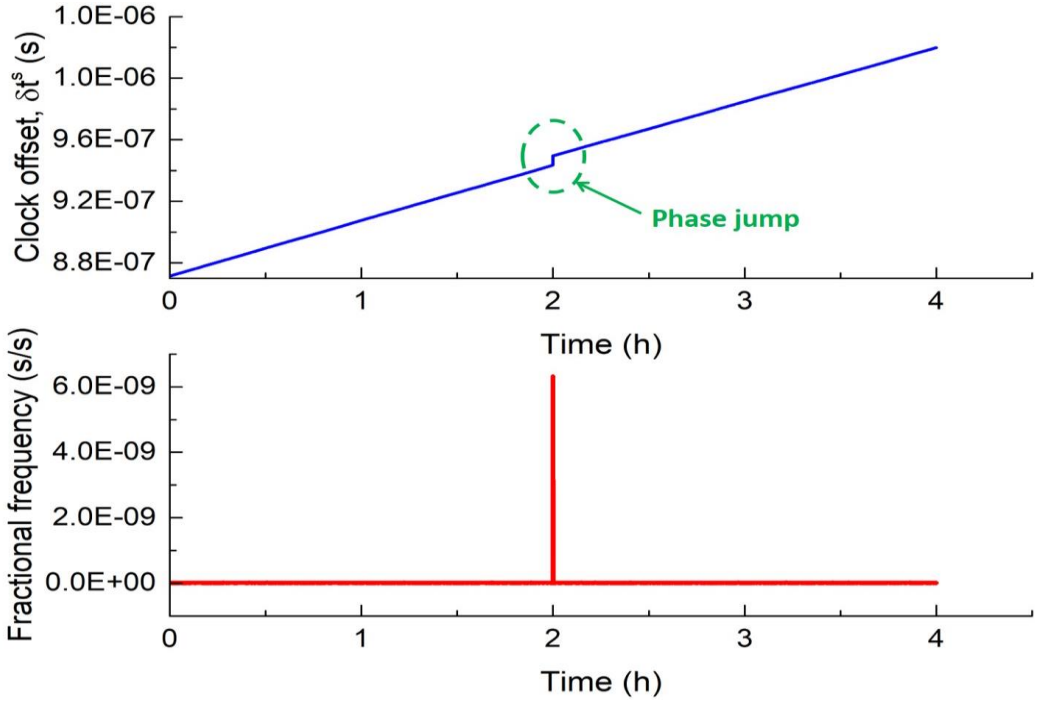


Figure 5.12: IRNSS-1D clock offset and frequency data with respect to phase jump during the first 4 hours.

Figure 5.13 shows the presence of a simulated frequency jump with magnitude 1.0E-11 s/s in both clock offset and frequency data. The frequency jump is detected by continuously verifying that the frequency error is beyond the threshold value.

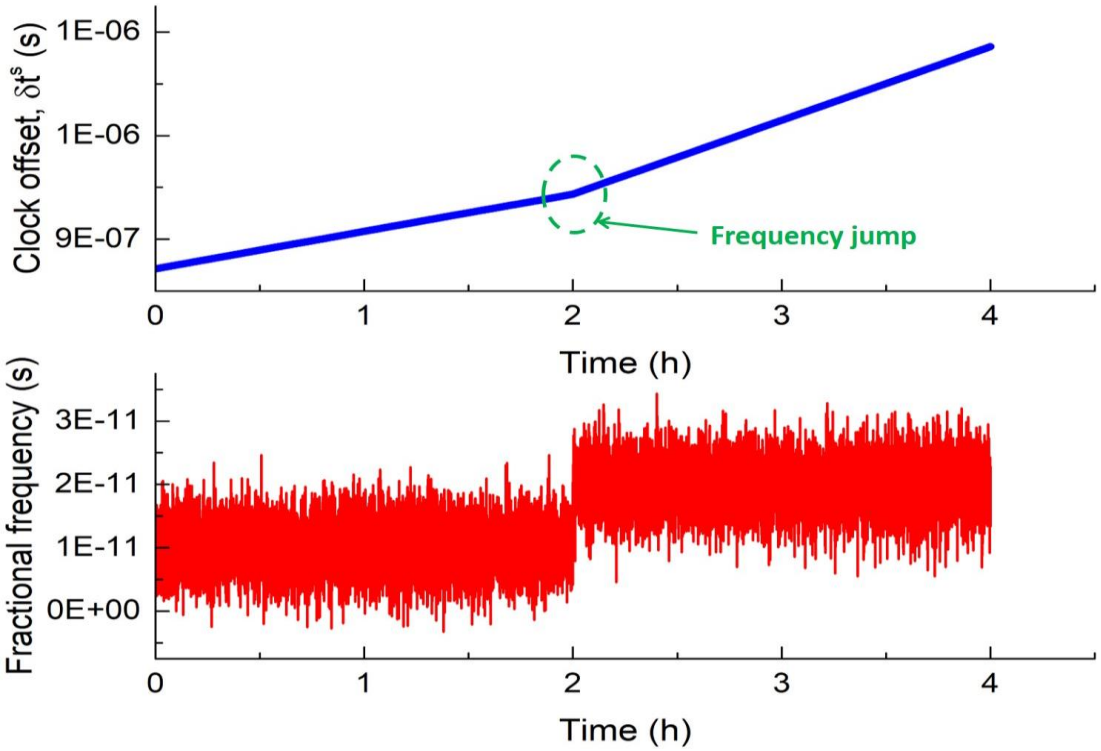


Figure 5.13: IRNSS-1D clock offset and frequency data with respect to simulated frequency jump during the first 4 hours.

### 5.5.2 Detection of clock anomalies

Detection of clock anomalies in frequency data is developed based on a linear prediction method. Satellite clock frequency can be well predicted using a linear model [147]. In the absence of anomaly, the observed and predicted frequency data are close to each other. Conversely, in the presence of an anomaly, the observed frequency data deviates from the predicted value. Anomalies are detected based on an error threshold limit between observed and predicted frequency data. Additionally, smoothening is applied to the computed raw frequency data using Equation 5.8, to enhance the confidence in detecting anomalies. The parameter $\beta$ in Equation 5.8 indicates the smoothening constant which decides the amount of smoothing of raw frequency data. $y_i$ and $\hat{y}_i$ are the raw and smoothened frequency values at i$^{th}$ epoch. Smoothened frequency data is input to the algorithm for anomaly detection.

$$\hat{y}_{i+1} = \hat{y}_i + \beta(y_i - \hat{y}_i) \tag{5.8}$$

The anomaly detection methodology can be divided into three sequential steps. Initially, the process involves in performing a linear fit to smoothened frequency data. Subsequently, statistical analysis would be performed on the fitting residuals. Finally, the presence of anomalies is detected based on these statistics. The detailed flow chart illustrating the methodology for detecting anomalies is presented in Figure 5.14. Following are the corresponding steps involved in the procedure.

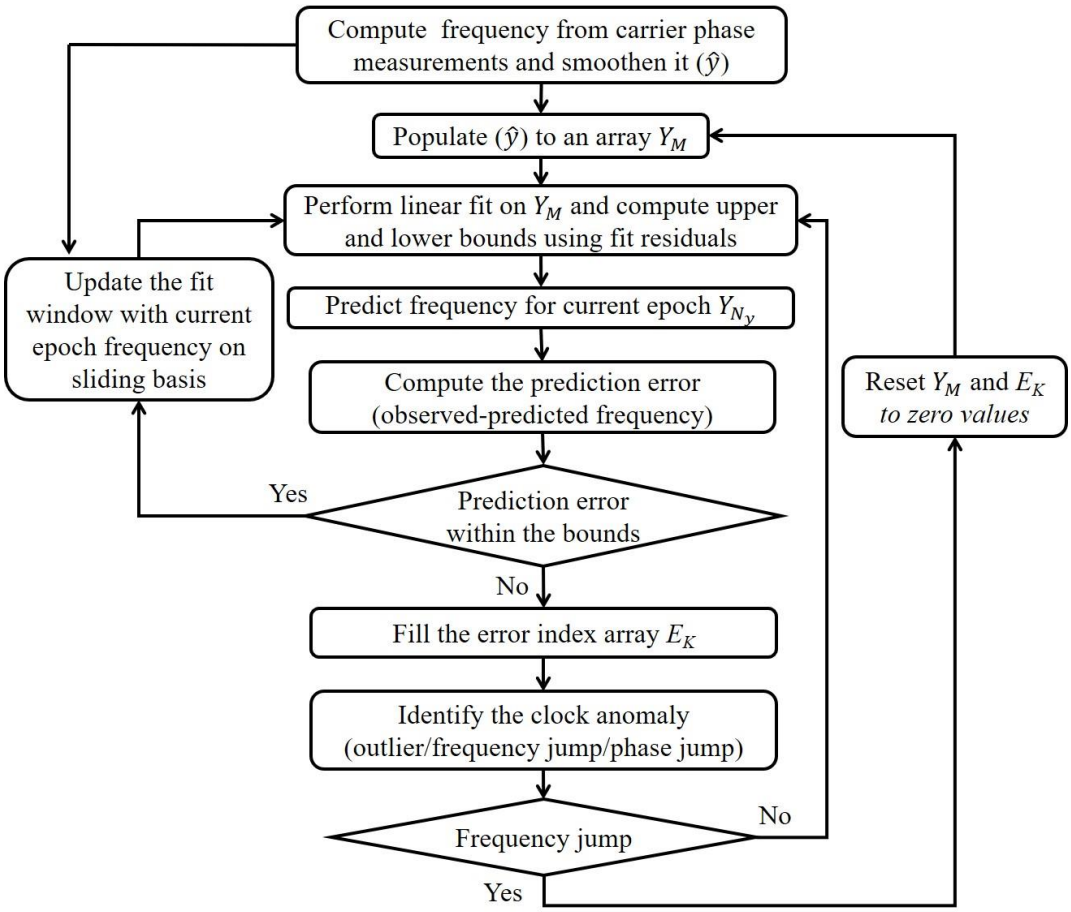


Figure 5.14: Flow chart for detecting and removing anomalies in satellite clock frequency data.

**Step 1:** Satellite clock frequency data is computed from carrier phase measurements with a sampling period of one second using Equation 5.7. Subsequently, the obtained frequency data is smoothened using Equation 5.8 which is input to the algorithm for anomaly detection. The frequency data is populated in a fitting array ($Y_M$) up to a predefined duration, $M$, to start the initial fitting, as shown below.

$$Y_1 = \hat{y}_1,\ Y_2 = \hat{y}_2,\ \ldots\ldots\ldots,\ Y_M = \hat{y}_M$$

Where $M$ is the duration of the data for fitting. Consider $N_y = M+1$ as the current epoch in real-time. The removal of outliers in the initial fit period of $M$ is carried out by deriving threshold value from mean ($\bar{y}$) and three times of standard deviation (STD) '$\sigma$' on smoothened frequency ($Y_M$) data as given in Equation 5.9.

$$Threshold = \bar{y} + 3\sigma \tag{5.9}$$

Given $\hat{y}_i$ is treated as an outlier if its absolute value i.e., $|\hat{y}_i|$ is more than threshold. After removing any possible outliers, linear fitting is performed on fitting array, $Y_M$.

**Step2:** Statistical analysis is performed on fit residuals ($y_e$) to compute mean ($\overline{y_e}$) and STD ($\sigma_e$) for the fit residuals of fitting duration *M*. Positive and negative threshold values are then determined based on fit residuals statistics as given in Equation 5.10, referred to as upper bound (UB) and lower bound (LB), respectively. In real-time, frequency value for the current epoch $N_y$ is predicted ($\tilde{y}_{N_y}$) using linear fit coefficients generated from frequency data of length *M*. Prediction error, i.e., the error between predicted ($\tilde{y}_{N_y}$) and observed ($\hat{y}_{N_y}$) frequency data is then computed at current epoch.

$$UB = \bar{y}_e + 3\sigma_e$$
$$LB = \bar{y}_e - 3\sigma_e \tag{5.10}$$

**Step-3**: Prediction error is compared with the upper and lower bound values to determine the categorization of the observed frequency data. When prediction error falls within the bounds, the observed frequency is classified as good data or non-anomalous. Conversely, if the magnitude of the prediction error exceeds the bound values, the observed frequency data is considered as anomalous. An array of length *K* is populated with error index $E_i$ =+/-1 ($i$=0,1,2, …., *K*). Here, +1(-1) represents the prediction error is above (below) the upper (lower) bound. In this context, *K* represents the predefined optimum duration to confirm the occurrence of a frequency jump.

If the frequency data is not anomalous at current epoch, the fitting array ($Y_M$) is populated with the sliding frequency data, as illustrated below. The process then proceeds iteratively from step 1.

$$Y_1=\hat{y}_2,\ Y_2=\hat{y}_3,\ldots\ldots\ldots..,Y_M=\hat{y}_{N_y}.$$

Upon addition of each new epoch, the dynamic computation of mean and STD on fitting residuals is carried out without incorporating all fitting residuals data, as shown below.

$$\bar{y}_{N_y} = \bar{y}_M + \frac{1}{M}(y_e - \bar{y}_M)$$
$$S_N = \sqrt{\frac{M-1}{M}\left[\sigma_M{}^2 + \frac{1}{M}(y_e - \bar{y}_M)^2\right]}$$

Here, $y_e$ is the fitting residue with respect to current epoch. $\bar{y}_M$ and ${\sigma_M}^2$ are previously calculated mean and STD of fit residuals for length *M*.

As an example, the scheme for identification of anomalies using error index array is depicted in Figure 5.15 by considering the prediction error is above UB. In this representation, green and red colours correspond to error index values +1 and -1, respectively. An anomaly is identified as an outlier if the adjacent $E_K$ values are +1 and -1, respectively as shown in Figure 5.15a. A phase jump is detected when the last three $E_K$ values are 0, +1 and 0 (Figure 5.15b). Finally, a frequency jump is detected when the sum of all $E_K$ values is equal to $+K$ (Figure 5.15c). If the outlier or phase jump is confirmed, the corresponding epoch is discarded without storing it in $Y_M$ and proceeds to the next epoch. However, if the frequency jump is confirmed, the fitting array $Y_M$ and error index array $E_K$ are reset to zeros and the procedure as explained above restarts again. If the prediction error is below the LB, the above explanation changes by interchanging the green and red colours in Figure 5.15.

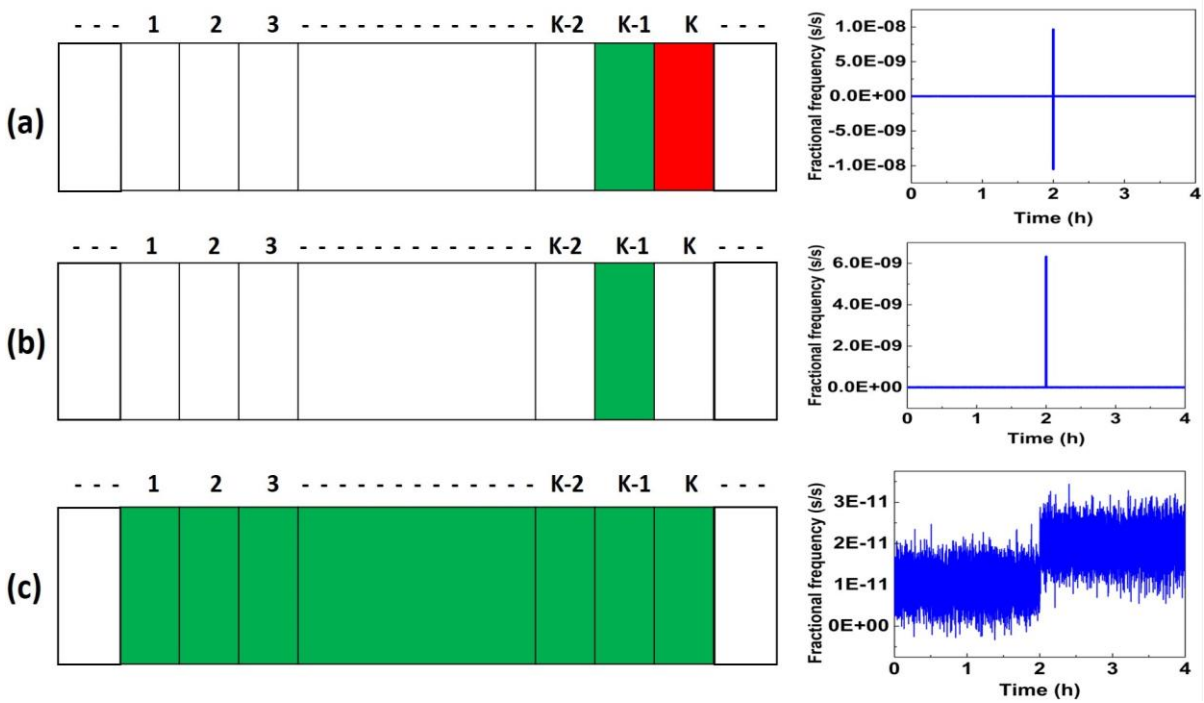


Figure 5.15: Graphical representation of anomaly detection with error index array ($E_K$). Green and red colours represent error index values of +1 and -1, respectively. Parts (a), (b) and (c) highlight the anomalies with outlier, phase jump, and frequency jump. The corresponding anomalies in frequency data are shown in the right side against (a), (b) and (c), respectively.

To validate the developed algorithm, frequency data from IRNSS-1D with frequency jump is considered. Figure 5.16 indicates the frequency computed using Equation 5.7 for IRNSS-1D satellite clock, where a frequency jump is observed at around 20 hours.

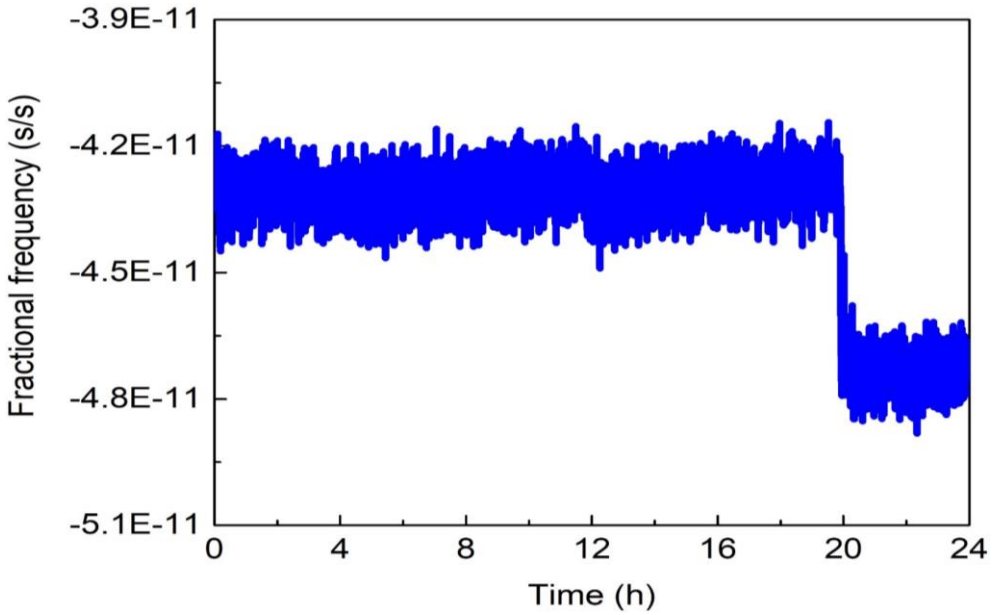


Figure 5.16: Satellite clock frequency data for IRNSS-1D with an observed frequency jump around 20 hours.

Data shown in Figure 5.16 is used to demonstrates the efficacy of frequency jump detection algorithm as explained above. Figure 5.17 indicates that the prediction error along with lower and upper bounds, computed using Equation 5.10. It can be observed that around 20 hours, the prediction error is consistently above the threshold value (upper bound) for successive epochs up to *K*, as shown in Figure 5.17. Thus, it is detected as a frequency jump. Here, the considered *K* value is 60 s.

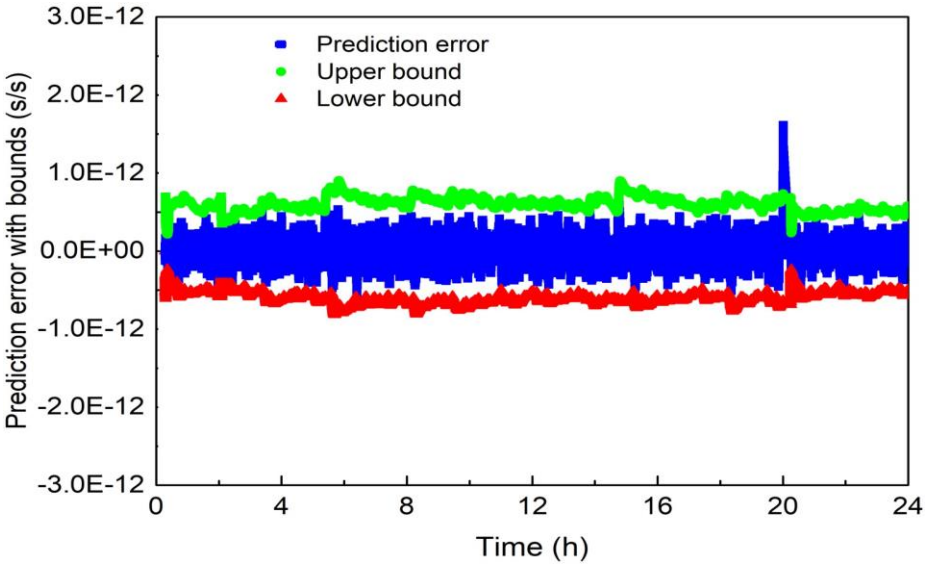


Figure 5.17: Prediction error of IRNSS-1D satellite clock frequency data shown in Figure 5.16 with corresponding lower and upper threshold values. The prediction error exceeds threshold value and confirms the presence of frequency jump.

## 5.6 Monitoring on-board clock performance

Algorithms for computing satellite clock frequency and detecting anomalies as explained above are successfully implemented and operationalized in NavIC constellation. These algorithms facilitate the routine characterization and monitoring of satellite clocks in operational satellites. Long term behaviour of clock frequency and frequency drift is systematically monitored. In addition, algorithms implemented to analyse the stochastic behaviour using overlapping Allan deviation (OADEV), dynamic Allan deviation (DADEV) and identification of noises present in frequency data. The following sections provide the aforementioned analysis using data from NavIC operational satellites (IRNSS-1C and IRNSS-1I).

### 5.6.1 Frequency

NavIC satellite clock frequency computed using Equation 5.7 is used to study its long-term behaviour. Figure 5.18a shows the frequency data computed from one-way carrier phase measurements for one of the GSO (IRNSS-1C) and IGSO (IRNSS-1I) satellites over a six months period from 21 May (MJD: 59720) to 17 November (MJD: 59900), 2022. Figure 5.18b shows the typical overlapping Allan deviation for these data. Here, frequency with drift removed is input to compute the frequency stability based on Equation 1.11. Frequency stability value for averaging time of one day is approximately 3.0E-14.

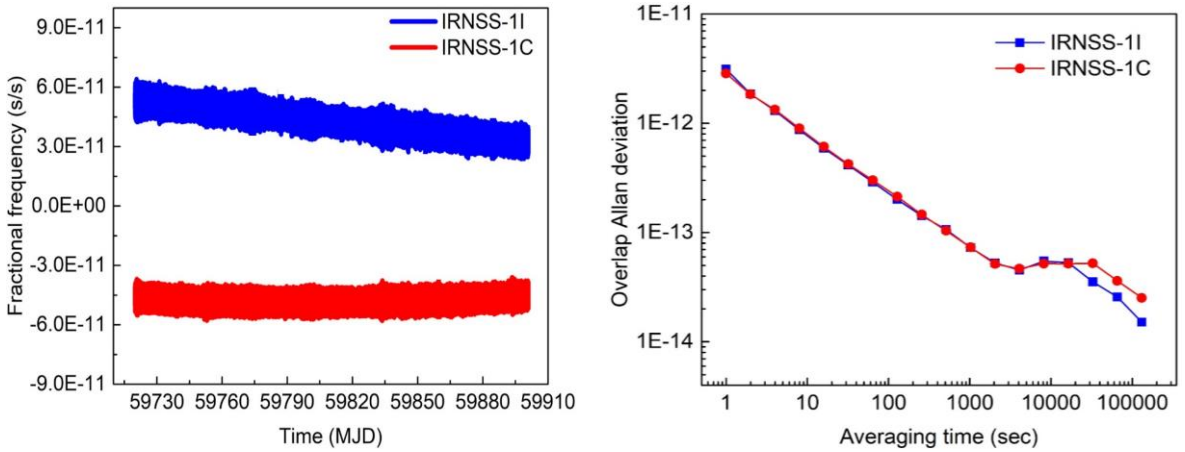


Figure 5.18: (a) Satellite clock frequency data for IRNSS-1C (bottom) and IRNSS-1I (top) for six months from 21 May to 17 November 2022. (b) Typical frequency stability (OADEV) of Rb AFS (drift removed) used in IRNSS-1C (circles) and IRNSS-1I (squares) measured on ground.

Figure 5.19 shows the frequency drift values for IRNSS-1C and IRNSS-1I during the period mentioned in Figure 5.18a. Each data point in Figure 5.19 represents the computed frequency drift value, derived from the frequency data of previous seven days. IRNSS-1I is observed to have a negative frequency drift value during this period and its magnitude is higher than that of IRNSS-1C. Frequency drift for IRNSS-1C is negative during the initial period and then changed to a positive value.

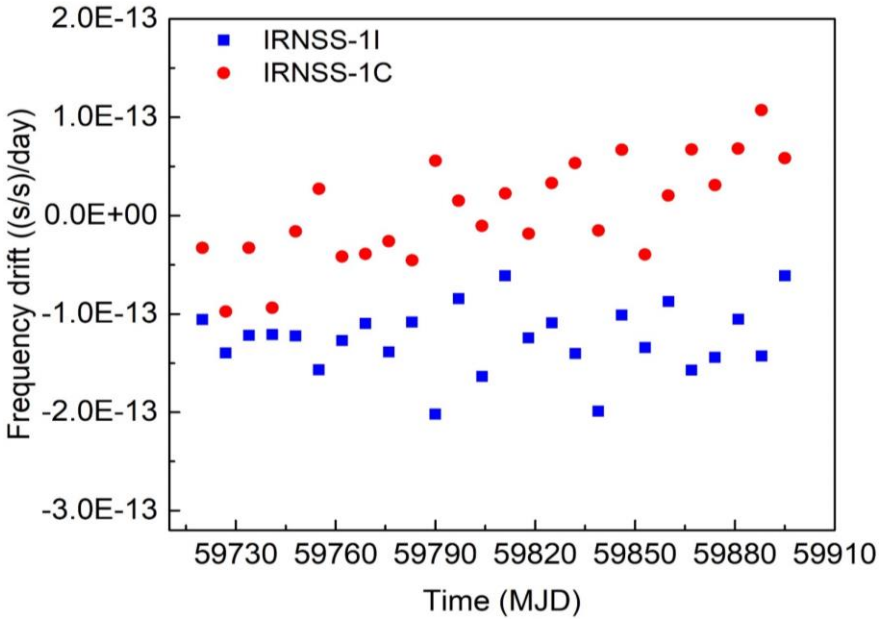


Figure 5.19: Variation of frequency drift for IRNSS-1C (circles) and IRNSS-1I (squares) computed from the frequency data indicated in Figure 5.18a.

Additionally, an algorithm based on DADEV [28], [29], [30], [31] is employed to monitor the influence of instantaneous clock frequency variations on frequency stability. It provides the real-time frequency stability corresponding to the frequency. Figure 5.20 shows the three-dimensional DADEV (refer to Section 1.3.3) for the frequency data shown in Figure 5.16. It shows a peak during the occurrence of frequency jump, while indicating nominal behaviour for the remaining duration. DADEV is useful for real-time monitoring of clock frequency stability performance in the presence of frequency jump, phase jump and sudden increase in noise. Its ability to capture such dynamic variations makes it valuable tool for continuously monitoring the frequency stability of clock in operational satellites.

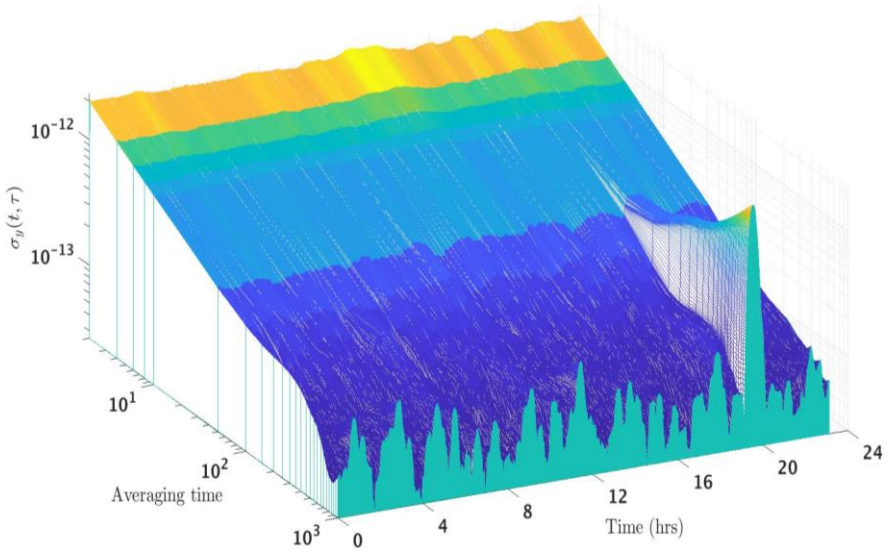


Figure 5.20: DADEV for frequency data corresponding to Figure 5.16. During frequency jump (at ~20 hours), DADEV shows a peak with increasing magnitude, while remaining period exhibits nominal behaviour.

## 5.6.2 Noise identification in frequency

As discussed in Section 1.3.2, different types of noises present in on-board clock frequency data such as White phase modulation (PM), Flicker PM, White frequency modulation (FM), Flicker FM, Random walk FM and Random run FM (or frequency drift). Generally, these noises are derived by computing the slopes of averaging time versus modified Allan deviation graph. This manual process of noise identification depends on frequency stability. Analytical algorithms that are independent of frequency stability data are implemented to identify the noises in NavIC satellite clocks (refer to Section 1.3.4). Figure 5.21 shows the noise coefficient, alpha (α) obtained using both non-overlap (squares) and overlap (circles) Lag-1 autocorrelation

methods [16], [36] at different averaging times for IRNSS-1C and IRNSS-1I, respectively. α values computed using non-overlap Lag-1 method show frequent variations with increase in averaging time, which is resolved by overlap method. Figure 5.21a illustrates that Rb AFS in IRNSS-1C shows α values corresponding to white frequency modulation (FM) up to 1000 s averaging time, Flicker FM and Random walk FM from 1000 to 10000 s and white phase modulation at around 100000 s. Similar observations of noise types are also evident in the case of IRNSS-1I as shown in Figure 5.21b.

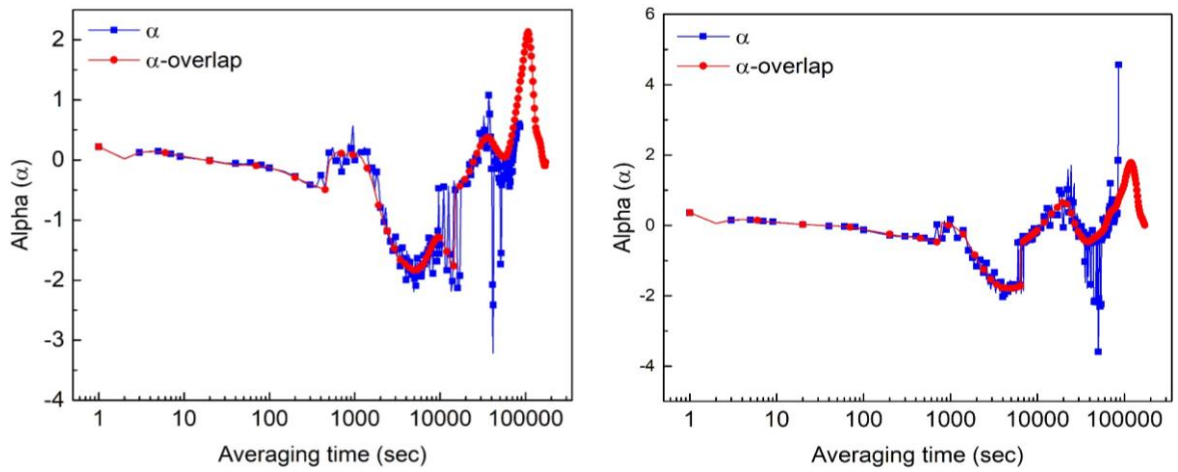


(a) (b)

Figure 5.21: Variation of alpha (α) value using non-overlapping samples (squares) and overlapping samples (circles) with respect to averaging time for (a) IRNSS-1C and (b) IRNSS-1I.

In this chapter, a methodology for clock characterization based on carrier phase measurement data is discussed. Described a single algorithm that is used to detect outliers, phase jumps, and frequency jumps. As part of routine characterization and monitoring, the frequency and frequency drift behaviour of the on-board clock for IRNSS-1C (GSO) and IRNSS-1I (IGSO) are provided over a period of six months. In addition, the performance of on-board clock stochastic behaviour is presented using the OADEV technique to study the long-term frequency stability and DADEV technique to monitor instantaneous clock stability which reflects variations in the frequency data. Finally, the Lag-1 autocorrelation method is implemented using overlap method to identify the noises present in the clock.

In every GNSS/RNSS, a predefined maximum range (i.e., broadcast limit) is allocated for the satellite clock correction parameters broadcasted by the navigation satellites. Satellite clock offset accumulates gradually over time due to its frequency drift and ageing. To provide

uninterrupted service to the user, satellite clock offset must be maintained within the allocated broadcast limit. Chapter-6 provides a detailed methodology for maintaining clock offset within the broadcast limit, specifically considering NavIC constellation.

# Chapter-6

# Satellite Timekeeping Methodology

Many of the global and regional satellite navigation systems use atomic clocks as their stable on-board frequency reference (see Table 1.2) to generate *satellite time* (*on-board time*) [148]. NavIC *satellite time* is generated from Rb AFS. This chapter discusses the NavIC *satellite time*, initial time synchronization of satellite clock and methods to apply frequency corrections to mitigate satellite clock errors with respect to ground reference. The discussion includes computation of satellite clock offset, $\delta t^s$ (considered as error due to the difference between ground reference time and *satellite time* that needs to be corrected/maintained) and strategy for up-linking of clock correction parameters (as given in Equation 1.19). Even though $\delta t^s$ is made close to zero during the initial synchronization, it tends to accumulate over time due to drift in clock frequency and ageing [149]. However, $\delta t^s$ needs to be maintained within the broadcast limit allocated by navigation system which is referred to as *satellite timekeeping*. This chapter describes the designing and development of a reliable satellite timekeeping methodology that is employed in NavIC constellation. This involves the development of a new mathematical model to compute the optimal correction to be applied that would reduce the service outage. The detailed methodology for timekeeping is discussed using the observed satellite clock offset data from NavIC satellites.

## 6.1 NavIC satellite time

Navigation Signal Generating Unit (NSGU) on-board navigation satellite generates the NavIC *satellite time* using fundamental frequency (10.23 MHz) generated from 10 MHz output of Rb AFS (refer Section 5.2). This *satellite time* is defined with respect to Week Number (WN) and Time of Week Count (TOWC) [132] and generated using a set of three time counters as shown in Figure 6.1. Time in counter-1, which receives fundamental frequency as its input, is incremented after every ~ 100 ns, i.e., time period of fundamental frequency (10.23 MHz) is 97.7517 ns. The output of counter-1 is provided as input to counter-2. Time in counter-2 is

incremented after every one *millisecond* and is therefore also referred to as *millisecond* counter. The *millisecond* counter input enables counter-3 to increment after every 12 seconds i.e., increment in TOWC. The Week Number is then incremented by one when TOWC count reaches 50400 (i.e., 604800/12, here 604800 is total number of seconds in a week). Thus, the satellite clock (Rb AFS) is the frequency source for satellite time generation. The IRIMS receivers on ground extract the WN and TOWC of satellite time from navigation signals broadcasted at L5 and S frequencies.

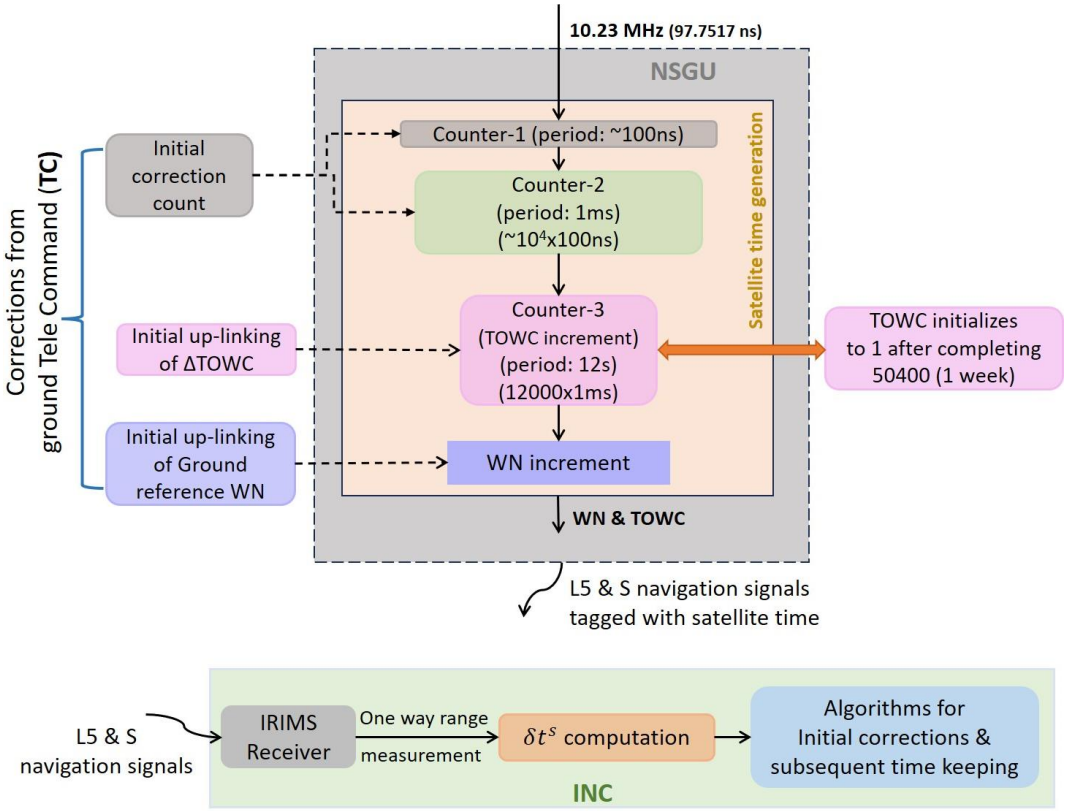


Figure 6.1: Schematic of NavIC satellite time generation and provision for applying corrections to NSGU. ΔTOWC: Difference between ground and satellite TOWC. NSGU and INC are Navigation Signal Generating Unit and ISRO Navigation Centre.

## 6.2 Initial time and frequency corrections to NavIC satellite clock

This section addresses the initial time and frequency corrections applied to NavIC satellite once it is placed in the designated orbit. Once the navigation payload is powered on the satellite time counters that are sourced from on-board atomic frequency standard start incrementing time from zero. In order to achieve valid one-way range measurements, the satellite time needs

to be synchronized with ground reference time initially which is referred to as *initial satellite time synchronization*. Additionally, fractional frequency of satellite clock measured using ground receivers also exhibits an offset with respect to ground reference due to relativistic effects. Thus, prior to the operationalization of a navigation satellite, initial corrections corresponding to both time and relativistic frequency offset need to be applied to navigation payload.

### 6.2.1 Initial satellite time synchronization

Satellite time synchronization is achieved by synchronizing three time counters in the NSGU (see Figure 6.1) with respect to ground reference via a three-step process. These three steps are referred to as coarse correction (setting WN and TOWC), *millisecond* correction (time setting with accuracy one millisecond), and fine correction (time setting with accuracy less than 100 ns). In each step, the difference between ground reference time and satellite time is computed and uplinked to the satellite to adjust the corresponding counter [131] as shown in Figure 6.1.

IRIMS receiver driven by ground reference time provides WN and TOWC of both ground reference time and satellite time. The difference between ground and satellite TOWC (ΔTOWC) is computed. This ΔTOWC together with WN of ground reference time are uplinked as coarse corrections to NSGU (see Figure 6.1) which corrects its WN and TOWC to match with those of ground reference.

*Millisecond* and fine corrections are generated by computing difference between satellite time and ground reference, i.e., satellite clock offset ($\delta t^s$) using one-way range measurements (see Section 6.3). For *millisecond* correction, $\delta t^s$ is converted to an equivalent number of *millisecond* count and uplinked to the satellite as correction count to adjust the time counter-2 as shown in Figure 6.1. After this correction, the satellite time is set with an accuracy better than one *millisecond*. Following this $\delta t^s$ is computed again and converted to an equivalent correction count of ~100 ns and uplinked to the satellite which corrects the time counter-1 as shown in Figure 6.1. With this final correction, satellite time is synchronized to ground reference with an accuracy better than 100 ns. Figure 6.2 illustrates typical time synchronization carried out for IRNSS-1B satellite with ground reference.

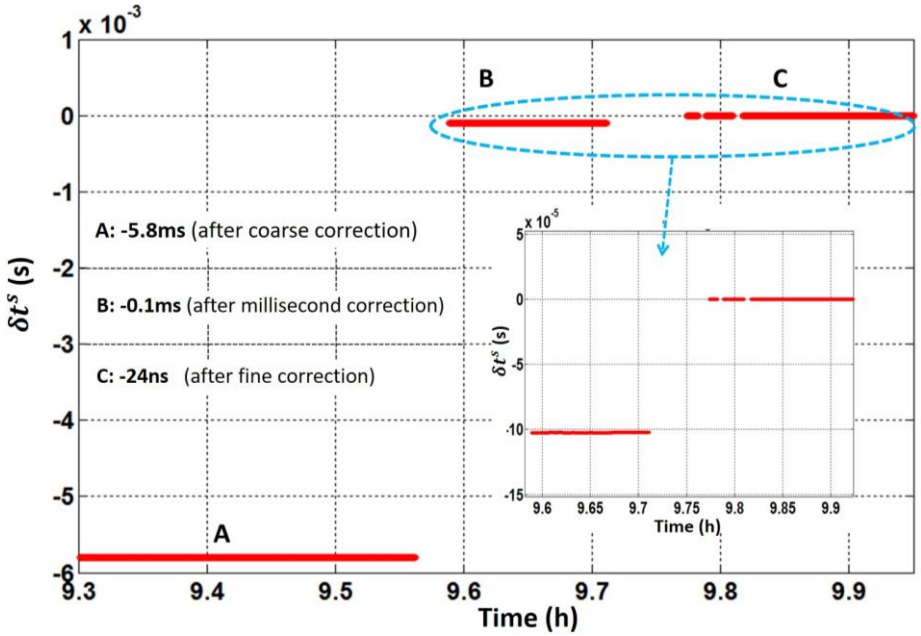


Figure 6.2: Initial synchronization of NavIC (IRNSS-1B) satellite time with respect to ground reference [131]. A, B and C represent the satellite clock offset ($\boldsymbol{\delta t^s}$) after coarse, millisecond and fine corrections, respectively.

## 6.2.2 Initial correction to clock frequency offset

Atomic clocks in an orbiting satellite experience relativistic effects due to satellite orbital velocity and its altitude. According to the special theory of relativity (STR) a clock in a moving reference frame tics slower than clock in rest frame. As per general theory of relativity (GTR) clock in weak gravitational field tics faster than the clock in strong gravitational field. Following equation provides the fractional frequency offset due to the above effects for circular orbits [150], [151].

$$\frac{\Delta f}{f_0} = \frac{-3GM}{2ac^2} + \frac{GM}{a_1 c^2}\left(1 + \frac{J_2}{2}\right) + \frac{(\omega a_1)^2}{2c^2} \tag{6.1}$$

Where, $\frac{\Delta f}{f_0}, a, c, GM, \omega, a_1 \; and \; J_2$ are fractional frequency offset, semi major axis, speed of light, gravitational constant for Earth, Earth rotation rate, equatorial radius of Earth and Earth's quadrupole moment coefficient, respectively. The values of these parameters are provided in Table 6.1 and the calculated $\frac{\Delta f}{f_0}$ for NavIC satellite is 5.3877E-10 s/s. Thus, due to the relativistic effect, a frequency offset of +5.5115 mHz ($\frac{\Delta f}{f_0} * f_0$) can be observed in NavIC

satellite's fundamental frequency when received on ground which would result in an error of 46.55 $\mu$s/day (i.e. 13.95 km/day) if not corrected.

Table 6.1: Parameters considered to compute relativistic fractional frequency offset for NavIC satellite.

| Parameter | Value |
|---|---|
| Gravitational constant for Earth | 3.986004415E14 $m^3/s^2$ |
| Semi major axis | 4.2164E7 m |
| Speed of light | 299792458 m/s |
| Equatorial radius of Earth | 6.3781363E6 m |
| Earth's quadrupole moment coefficient | 1.0826269E-6 |
| Earth rotation rate | 7.2921151467E-5 rad/s |

Provision exists in NavIC payload to provide frequency offset correction to ACMU through telecommands (see Figure 5.2). This correction is applied to frequency synthesizer which will change the fundamental frequency accordingly. To compensate the error due to relativistic effect as discussed above, frequency offset correction value of -5.5115 mHz is applied to ACMU in which $f_0$ is adjusted accordingly.

Practically, the orbits of NavIC satellites are eccentric (non-circular). However, Equation 6.1 is for a circular orbit and hence, the effect of orbit eccentricity needs to be corrected. User receiver computes correction to this eccentricity as per signal in space interface control document [133] and Equation 6.2.

$$\Delta t_r = Fe\sqrt{A}\sin E_k \tag{6.2}$$

where, $e$, $A$ and $E_k$ are eccentricity, semi-major axis and eccentric anomaly, while $F$ is a constant given by -4.442807633E-10 $s/\sqrt{m}$ [133].

## 6.3 Clock correction parameters for NavIC satellite

After the initial satellite time synchronization with ground reference, $\delta t^s$ tends to deviate with respect to ground reference over time due to drift in clock frequency which is an inherent characteristic of on-board atomic clock and its ageing over time [149]. NavIC ground control facility (service provider) computes $\delta t^s$ using one-way code range data measured by selected IRIMS. The receiver clock offset ($\delta t_u$) of these selected IRIMS with respect to ground

reference is known precisely. The pseudo range equation for any given ground IRIMS receiver with respect to satellite can be represented as in Equation 6.3 [39]

$$\rho = r + c[\delta t_u - \delta t^s] + I + T + \varepsilon \tag{6.3}$$

where $\rho$ is pseudo range (code measurement), $r$, $I$, and $T$ are as defined in Equation 5.1, and $\varepsilon$ represents the unmodelled error. The noise in code range measurement can be reduced by employing code-carrier smoothening based on Hatch-filter [135], [136], [152], [153] .

$\delta t^s$ is computed using smoothened pseudo range data by correcting the known/computed values of $r$, $\delta t_u$, $I$ and $T$ as explained in section 5.4. This computed $\delta t^s$ is used to estimate satellite clock correction parameters, namely time offset or clock time bias ($af_0$), fractional frequency offset or clock drift ($af_1$) and frequency drift or clock drift rate ($af_2$). These correction parameters would be predicted for the next 24 hours and broadcasted to the user. Estimation of these clock correction parameters is carried out by employing a quadratic polynomial model (Equation 1.19) using standard batch least square technique [147]. Input to this estimation technique is $\delta t^s$ collected over a period of 24 hours.

In NavIC, predicted satellite clock correction parameters for next 24 hours are up-linked to satellites during their continuous visibility via up-linking ground station. Figure 6.3 indicates the strategy for generating and up-linking satellite clock correction parameters employed in NavIC. Here, Group-1 indicates 12 sets of clock correction parameters predicted for next 24 hours starting from $n^{th}$ hour on any arbitrary day with each set valid for 2 hours. However, after 4 hours, i.e., at $n+4$ hours, the next set (Group-2) of clock correction parameters are estimated again by incorporating measurement data from recent 4 hours and freshly predicted for the next 24 hours. This procedure is repeated every 4 hours in sliding mode as shown in Figure 6.3.

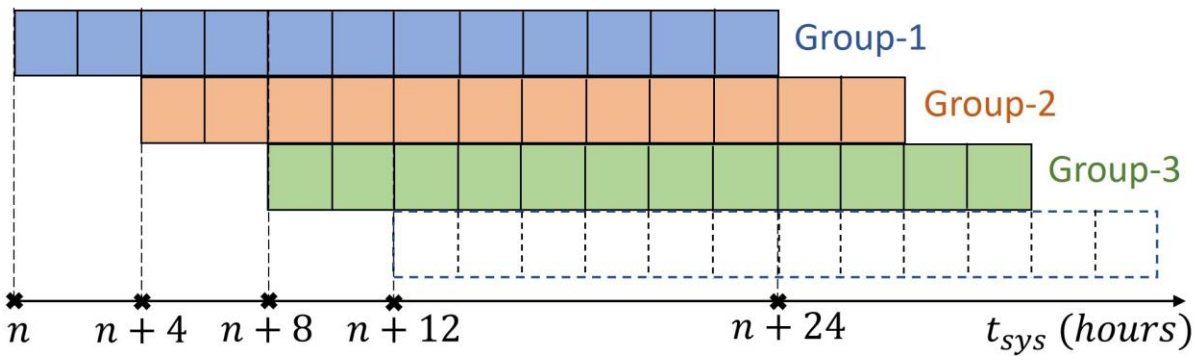


Figure 6.3: Strategy for generating and up-linking of clock correction parameters in NavIC. Group-1, Group-2 and Group-3 indicate predicted clock correction parameters of 12 sets with a sliding time interval of four hours.

In each navigation satellite system $\delta t^s$ accumulates over time due to frequency offset and frequency drift. Figure 6.4 shows the accumulation of $\delta t^s$ due to clock coefficients $af_1$ and $af_2$ with time $t_{sys}$ expressed in days. Here, $t_{sys}$ is ground reference time as explained in Section 1.5.1. Consider an arbitrary day $d_n$ where the clock coefficients are given by $af_0(n)$, $af_1(n)$ and $af_2(n)$ corresponding to the start of that day. As shown in Figure 6.4, at the start of day $d_{n+1}$, coefficient $af_0(n+1)$ would be the accumulated clock offset ($\delta t^s(n)$) by the end of previous day (i.e., $d_n$).

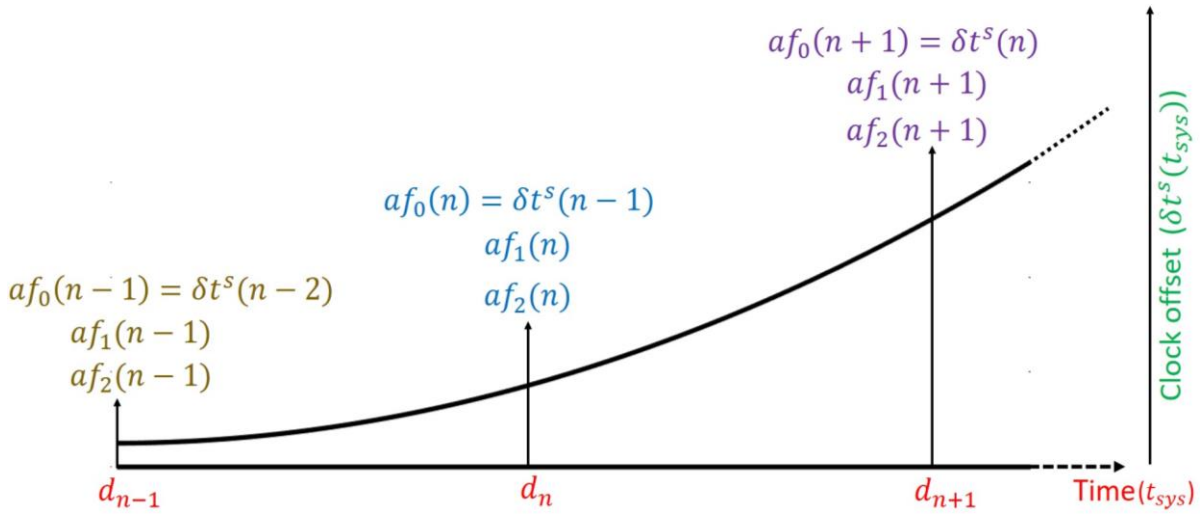


Figure 6.4: Schematic representation of typical accumulation pattern of satellite clock offset ($\boldsymbol{\delta t^s}$).

In any navigation satellite system, the $\delta t^s$ is allowed to accumulate only up to the pre-allocated broadcast limit. The range measurements by a user receiver are not reliable if the satellite clock offset is beyond maximum allocated broadcast limit and the clock offset would become invalid (see Equation 1.18). This situation leads to a large error in user position. Hence, the clock offset needs to be maintained within the allocated broadcast limit which is referred to as satellite timekeeping. Satellite timekeeping is done by applying corrections to navigation payload on-board the satellite. Based on provisions available on-board various methods are available to apply the corrections, such as 1) Re-initializing time offset, 2) Adjusting fractional frequency offset, 3) Adjusting time offset together with fractional frequency offset, and 4) Adjusting frequency drift. Method (1) is implemented in GPS-IIA block satellites [154], GPS-IIR block satellites employ method (4) [155] and Beidou uses (2) and (3) [156], [157], [158] for satellite timekeeping.

During the implementation of correction to the satellite using any of the methods mentioned above, navigation service from corresponding satellite is not available to the user for a certain period. In addition, the service outage from satellite also depends on how frequently these corrections are applied. Hence, satellite service outage is influenced by two factors. First is the time elapsed from application of the correction to the resumption of services, which depends on type of method chosen for the correction. Second, the number of corrections applied during the lifetime of the satellite which depends on change in frequency drift but primarily the magnitude of correction. The magnitude of correction would be such that the time interval between two consecutive corrections should be as long as possible. Such correction is called as *optimum correction*.

Table 6.2: Maximum permissible values allocated for individual clock coefficients in NavIC satellites.

| Parameter | Maximum value |
|---|---|
| $af_0$ | $\pm$9.76560E-04 s |
| $af_1$ | $\pm$3.72529E-09 s/s |
| $af_2$ | $\pm$3.72529E-09 s/s |

Table 6.2 shows the allocated limit for broadcast parameters $af_0$, $af_1$ and $af_2$ in NavIC satellites [133]. The accumulated $af_0$ over time i.e., satellite clock offset, would need to be maintained within the broadcast limit ($\pm$9.7656E-04 sec). The following section provides the description on optimum timekeeping methodology devised and employed in NavIC constellation.

## 6.4 Timekeeping methodology

Based on the provisions exist on-board, two approaches are employed in NavIC satellites to maintain the satellite clock offset ($\delta t^s$) within the broadcast limit: 1) re-initializing satellite time (i.e., re-initializing $\delta t^s$) and 2) correcting the fractional frequency offset ($af_1$) which in turn modifies $\delta t^s$ as described in Equation 1.19.

### 6.4.1 Reinitializing satellite time

In this approach, satellite clock offset is synchronized (re-initialized) with ground reference time whenever it is approaching close to the broadcast limit. In this method

corrections to NSGU are provided by a three-step process as discussed in Section 6.2.1. Each time, the implementation of this synchronization process lasts for about 4-6 hours during which the satellite service is unavailable for users. Frequent satellite time synchronization is not recommended as it leads to discontinuity in the range measurements (due to adjustment in NSGU time counters, see Figure 6.2) as well as long downtime of satellite's service. Therefore, this scheme is employed in NavIC only during the initial operational phase following the launch of satellites and not for subsequent satellite timekeeping.

## 6.4.2 Correcting fractional frequency offset

In this method, correction to $af_1$ is done by applying an appropriate frequency offset ($\Delta f = af_1 * f_0$) to ACMU which then synthesizes corresponding revised $f_0$ so as to maintain $\delta t^s$ within limit (see Figure 5.2). This method requires only couple of minutes to implement the corrections and the satellite service can be resumed within 20 minutes. The sign and magnitude of correction to the frequency offset depend on the accumulated values of $\delta t^s$ and $af_2$ at the time of correction. The value of the frequency offset (FO) correction would be optimized such that the time interval between two consecutive corrections should be as long as possible. Such correction is called as *optimum frequency offset correction.*

The mathematical expression employed in computing optimal value of $af_1$ is described below. The quadratic polynomial that is used to predict the clock offset (as given in Equation 1.19) can also be represented in a generalized form as given by Equation 6.4.

$$\delta t^s(t_{sys}) = af_2(t - t_{OL})^2 + {\delta t^s}_{OL} \tag{6.4}$$

where, $t = t_{sys} - t_c$, $t_c$ is the time $t_{sys}$ at which the recent clock correction parameters are applicable and $(t_{OL}, {\delta t^s}_{OL})$ is the vertex of this polynomial such that,

$$(t_{OL}, {\delta t^s}_{OL}) = (-\frac{af_1}{2af_2}, \frac{4af_0af_2 - {af_1}^2}{4af_2}) \tag{6.5}$$

Here, $t_{OL}$ is the time at which $\delta t^s$ reaches the maxima/minima and is denoted as ${\delta t^s}_{OL}$ (See Figure 6.5). The ${\delta t^s}_{OL}$ corresponds to the Operating Limit (OL) of $\delta t^s$ which is positive when $af_2 < 0$ and negative for $af_2 > 0$ as shown in Figure 6.5. Setting up of OL is necessary to keep a safe margin with respect to the broadcast limit (BL) and avoid any overshooting of $\delta t^s$ due

to the random variation of $af_2$. From Equation 6.5, the optimum value of $af_1$ corresponding to the desired operating limit (i.e., $\delta t^s{}_{OL}$) is given by

$$af_1 = \begin{cases} +2\sqrt{af_2(af_0 - \delta t^s{}_{OL})}, & af_2 < 0 \\ -2\sqrt{af_2(af_0 - \delta t^s{}_{OL})}, & af_2 > 0 \end{cases} \tag{6.6}$$

The parameters $af_0$ and $af_2$ in Equation 6.6 are the observed values whereas $\delta t^s{}_{OL}$ is a desired set parameter. The magnitude of $af_0$ and $af_2$ at any given time depend on the characteristic behavior of observed $\delta t^s$.

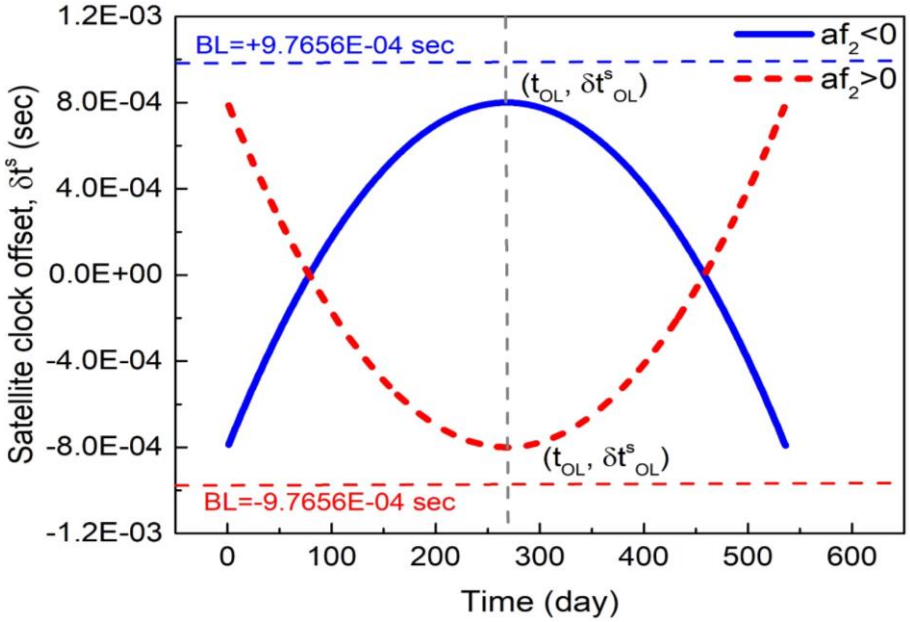


Figure 6.5: A representative data plot on the variation of $\boldsymbol{\delta t^s}$ as function of time, computed using Equation 1.19 and 6.6. The computation uses a typical value of $\boldsymbol{af_2}$ ($\pm$ 2.57E-13/day) and desired magnitude of $\boldsymbol{\delta t^s{}_{OL}}$. Here, $\boldsymbol{\delta t^s{}_{OL}}$ = +8.0E-4 sec if $\boldsymbol{af_2}$ <0 and -8.0E-4 sec if $\boldsymbol{af_2}$ >0.

## 6.5 Implementation of frequency offset correction

Initially, the computed values of $\delta t^s$ and the corresponding $af_1$ and $af_2$ are closely monitored for a certain period of time. At a suitable time, by incorporating appropriate magnitude of $af_1$ but with a sign opposite to that of $af_2$, an optimum FO (corrected $af_1$) is estimated which depends critically on the sign and magnitude of $af_2$ at the time of applying correction (see Equation 6.6). After the FO correction, $\delta t^s$ is then predicted for future time using Equation 1.19 which accumulates over time with a rate and direction proportional to the magnitude and sign of corrected $af_1$, respectively.

The implementation of satellite timekeeping methodology is described using a typical case of IRNSS-1B satellite. In this satellite, $\delta t^s$ was first observed closely over a period of 8½ months (from January 1, 2019 to September 16, 2019). On September 17, 2019, the observed values of $af_0$, $af_1$ and $af_2$ were -2.50E-4 sec, -4.01E-11 s/s and -3.30E-14/day, respectively. Using the above values of $af_0$ and $af_2$, an optimum value of $af_1$ (+4.0E-11 s/s) is computed by setting $\delta t^s{}_{OL}$ = 8.0E-4 sec as the desired operating limit in Equation 6.6. Here, the corrected value of $af_1$ is positive since $af_2$ is negative. The FO correction was then applied on September 17, 2019 which is termed as correction date/time, $T_C$. With the above correction, the predicted $\delta t^s$ using Equation 1.19 is plotted in Figure 6.6 (curve C1). The curve C0 is the prediction of uncorrected $\delta t^s$ which would have reached the broadcast limit after a time period of only 185 days.

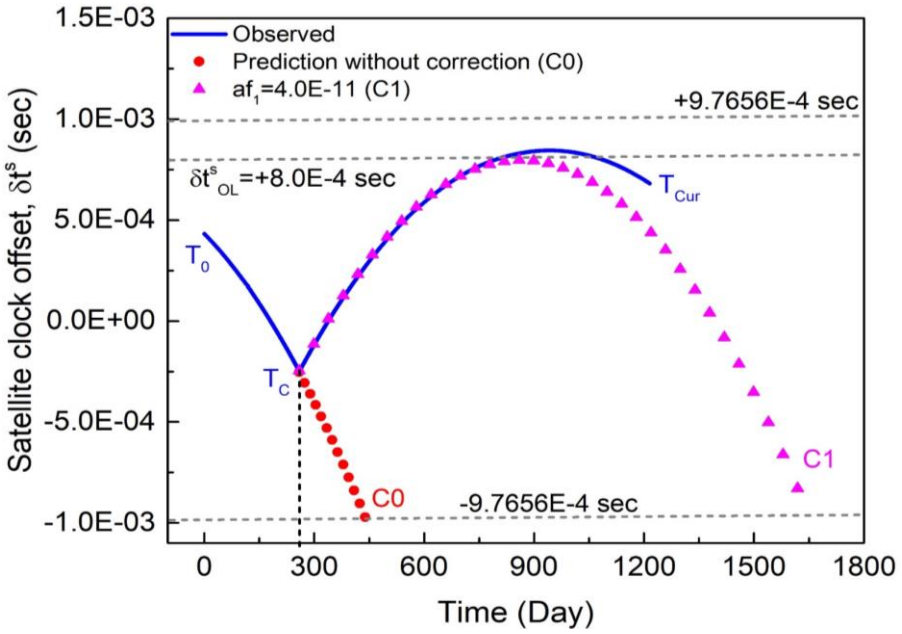


Figure 6.6: Prediction of satellite clock offset in IRNSS-1B satellite without any correction (C0) and with an optimum correction value at $\boldsymbol{T_C}$ (C1). The plot $\overline{\boldsymbol{T_0 T_C T_{Cur}}}$ shows observed clock offsets before and after the correction.

It can be observed that the applied optimum FO correction provides a maximum time period (1400 days) to reach the broadcast limit. However, the behavior of observed $\delta t^s$ after FO correction depends on the variation of $af_2$ over time. The plot $\overline{T_C T_{Cur}}$ as shown in Figure 6.6 is the observed $\delta t^s$ after correction which is in good agreement with the predicted offset up to 490 days. After that, the observed offset slowly deviates from the predicted value owing to change in the magnitude of $af_2$. Consequently, the maximum value of observed $\delta t^s$ (plot $\overline{T_C T_{cur}}$) changes to 8.45E-04 s, which is higher than $\delta t^s{}_{OL}$ but still within the broadcast limit.

The selection of suitable time to apply the FO correction is based on the trade-off between magnitude of correction and the estimated time period for the accumulated $\delta t^s$ to reach the broadcast limit following the application of correction. The correction applied too quickly (for example, much before $T_C$ as in Figure 6.6) would result in shorter time interval between the two corrections. On the other hand, this time interval could increase if the correction is applied much later compared to $T_C$ as in Figure 6.6. However, this would necessitate a correction with higher magnitude. Additionally, in the latter case, the accumulation of $\delta t^s$ becomes more susceptible for any changes in $af_2$ over time.

The efficacy of applied optimum correction as explained above depends on the variation of $af_2$ over time. After the correction, both $\delta t^s$ and $af_2$ are monitored continuously. If the observed variation of $af_2$ is significant, $\delta t^s$ accumulates rapidly to reach the broadcast limit. In such cases, intermediate corrections are applied to arrest the accumulation of $\delta t^s$ within the broadcast limit. For example, in the case of IRNSS-1I satellite, an optimum correction was applied at $T_{C1}$ as shown in Figure 6.7. The data plot $\overline{T_{C1}T_{C2}}$ indicates the observed $\delta t^s$ after this correction. Owing to variation in $af_2$ over time, $\delta t^s$ deviated from its predicted characteristic behavior and required further correction at $T_{C2}$ (349 days after $T_{C1}$) to arrest the accumulation of $\delta t^s$ within the broadcast limit. Data plots $P_1$ ($\overline{T_{C1}P_1}$) and $P_2$ ($\overline{T_{C1}P_2}$) in Figure 6.7 are the predictions of $\delta t^s$ without and with variation in $af_2$ over time. The mismatch between these two data is due to the change in $af_2$ and untreated variation due to $af_2$ would have resulted in accumulation of $\delta t^s$ beyond the broadcast limit (as shown in data plot $P_2$).

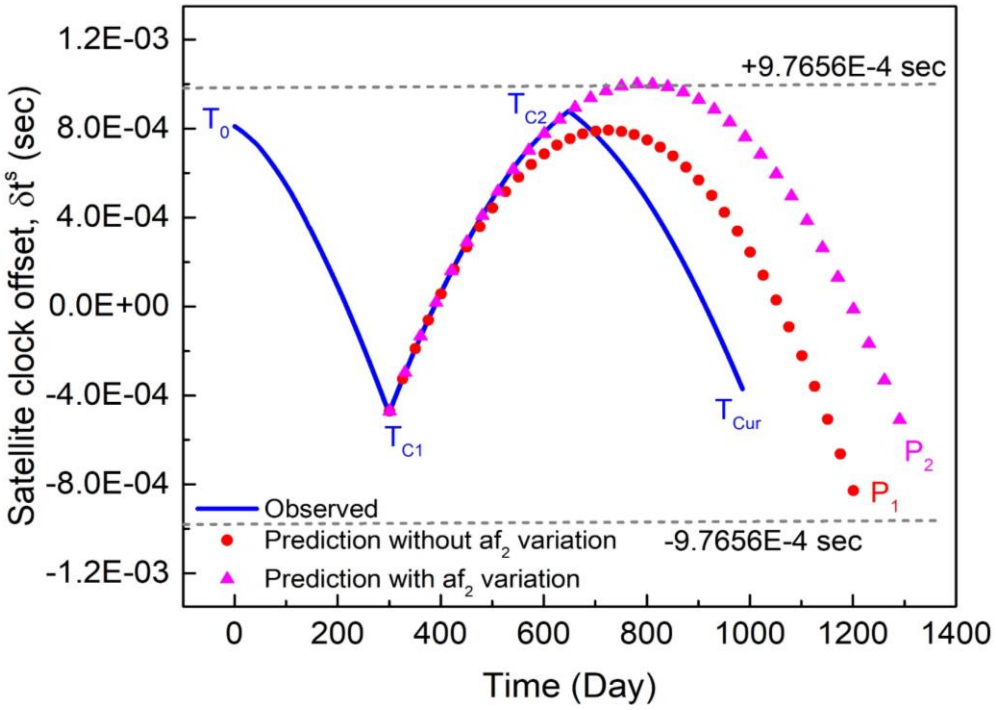


Figure 6.7: Observed and predicted $\boldsymbol{\delta t^s}$ in IRNSS-1I satellite. Data plots $\overline{\boldsymbol{T_0 T_{C1}}}$ and $\overline{\boldsymbol{T_{C1} T_{C2}}}$ are the observed $\boldsymbol{\delta t^s}$ before and after applying the FO correction, respectively. Plots $P_1$ and $P_2$ are the predicted $\boldsymbol{\delta t^s}$ without and with variation in $\boldsymbol{af_2}$, respectively.

In this chapter optimum satellite timekeeping methodology is described for NavIC satellite constellation. The strategy for generation and up-linking of NavIC clock correction parameters is discussed. Details provided on provisions available in NavIC navigation payload for satellite timekeeping and their limitations. A new strategy is devised and implemented in NavIC satellites by applying optimal frequency offset correction to maintain the satellite clock offset within the broadcast limit. The methodology for NavIC satellite timekeeping discussed in this chapter reduces the satellite operational time outage, and hence the performance degradation.

# Chapter-7

# Summary

CPT phenomena in $^{87}$Rb atoms is employed in this study to characterize the performance of CPT resonance for application in atomic clock. CPT excitation scheme implemented in this study is based on the direct current modulation of drive current of a VCSEL diode. CPT resonance characteristics are studied in vapor cells containing natural Rb with Ne buffer gas and enriched $^{87}$Rb with Ar+$N_2$ buffer gas mixture. An inhouse developed MATLAB software is utilized to extract and analyse the CPT resonance characteristics.

Experimental study is carried out to investigate the dependence of CPT resonance characteristics i.e., quality figure ($q$) and frequency shift on critical operating parameters. These parameters include laser excitation intensity, cell temperature and RF power for Rb vapor cells with different dimension and buffer gas pressure. CPT resonance and its corresponding $q$ are modelled with respect to cell length and radius using a four-level atomic system. A new scaling parameter ($\beta$) is introduced to account for the cell dimension (radius) which would reflect the influence of collisional dynamics, particularly wall collisions. Developed a mechanism to extract the excited state decay rate ($\Gamma^*$) and ground state relaxation ($\gamma_2$) parameters which are inputs to the four-level atomic system.

The study revealed that, for a given laser intensity, magnitude of $q$ value decreases with decrease in cell radius due to higher FWHM. Higher FWHM in cells with lower dimension is due to increased atom wall collisions which would affect the coherence. For a cell with given radius, the $q$ value decreases with increase in laser intensity. However, the variation of $q$ with laser intensity depends on cell temperature. The dependency of $q$ on laser excitation intensity and cell temperatures is in good agreement with the theoretical model. This study shows that $q$ exhibits a maximum ($q_{max}$) at an optimum temperature ($T_{opt}$) that depends on laser excitation intensity, cell dimension (radius) and buffer gas pressure. The quality figure also exhibits a maximum at an optimum RF power.

Experimental investigation of CPT characteristics in Rb cell (R=12.5 mm, L=25 mm) filled with natural Rb and Ne buffer gas at 50 Torr pressure shows that the intensity light shift coefficient is temperature dependent and is minimum at an optimum temperature 72 $^0$C at which quality figure is also optimum. The observed temperature shift for Ne buffer gas is positive and its value is minimum as well as less sensitive to laser intensity when operated from 9.9 to 13 W/m$^2$. Further, investigation is carried out on rate of frequency shift in Rb cells (R=12.5 mm, L=25 mm) filled with Ar+$N_2$ buffer gas mixture at different buffer gas pressures to derive optimum operating parameters. Rate of frequency shift is measured in these cells with respect to laser intensity, cell temperature, and RF power. Further, cell filled with enriched $^{87}$Rb and Ar+$N_2$ buffer gas at pressure 15 Torr shows the optimum performance with respect to quality figure as well as frequency shift. The optimum quality figure achieved in this study, i.e., $q_{max}$ ~ 1.2E-4 Hz$^{-1}$, would enable short-term stability of CPT clock < 2 x $10^{-12}$ per sec. In essence, this study facilitated the understanding of light absorption, collisional dynamics in atomic vapor cell and then enabled the optimization of operating parameters of CPT based atomic clock.

Further, a methodology for real-time characterization and continuous monitoring of on-board clock using one way carrier phase range measurement is developed. This methodology addresses the issue regarding the presence of integer ambiguity in carrier phase measurement data. Devised and developed a single algorithm to detect outliers, phase jump and frequency jumps. Stochastic behaviour of on-board clock is characterized by implementing the OADEV technique to study the long-term behaviour and DADEV to monitor instantaneous clock stability that reflects the variations in the frequency data. Additionally, Lag-1 autocorrelation method using overlapping samples of frequency data is implemented to estimate the types of noises exhibited by the on-board clock. All these algorithms are implemented and operationalized in NavIC constellation. As part of routine characterization and monitoring the frequency and frequency drift behaviour of the on-board clock for IRNSS-1C (GSO) and IRNSS-1I (IGSO) are analysed over a period of six months which validated the efficacy of implementation of these algorithms. Finally, typical results of frequency stability and different types of noises in NavIC on-board clocks are presented.

Satellite clock offset accumulates over time due to its frequency offset and frequency drift. The strategy for generation and up-linking of NavIC clock correction parameters is discussed. Devised and developed an optimal satellite timekeeping methodology that is implemented in NavIC constellation. This timekeeping methodology is successfully demonstrated utilizing IRNSS-1B satellite offset data. Further, successfully demonstrated the additional intervening

frequency correction when the observed satellite clock offset deviates from the predicted clock offset due to change in frequency drift. The developed methodology for NavIC satellite timekeeping discussed in this thesis reduces the satellite operational time outage and hence, minimize the performance degradation.

## Scope for future work

CPT clocks with superior frequency stability are highly desired for application both on ground as well as space. In this regard, investigation on other variants of CPT clocks would be pursued in future.

**Ramsey interrogation technique**

This technique is widely used as it reduces the frequency shift due to AC stark effect and power broadening. In Ramsey CPT, the interaction with the CPT driving field is split into two pulses, separated by a delay time say $T_R$. The first pulse pumps the atoms in to the dark state. After the first pulse turned off, the atoms under go free evolution during time $T_R$. A second pulse of light acts as a probe used for the detection of transmitted beam under CPT condition. This technique could enable the development of clocks with frequency stability in the order of $10^{-13}$ to $10^{-14}$.

**CPT maser**

The self-sustained oscillations in masers are established through stimulated emission when the ensemble of atoms is placed in a microwave cavity that is tuned to the resonant frequency of these atoms. CPT maser is also based on the similar scheme. CPT masers are reported to give superior frequency stability.

# Publications

Papers published in peer-reviewed journals:

1. Rajaiah K., Manjula R., Tiwari P., Kappen M. J., Biswas S., Raha B., Pradhan S., Venkatappa Rao Tumu, Umesh S. B., Elumalai S., Kalpana Arvind P., Sriram K. V. and Prashanth C Upadhya, **"Parametric Study of CPT Resonance in Rubidium Vapor Cell for Application in Atomic Clock"** Indian Journal of Pure & Applied Physics, Vol. 60, pp. 489-496, June 2022. SCIE, IF:0.846
2. Rajaiah K., Manamohan K., Nirmala S., Venkatappa Rao T., and Upadhya P C., **"Satellite Time Keeping Methodology for IRNSS/NavIC constellation",** Gyroscopy and Navigation, ISSN 2075-1087, Vol. 13, No. 3, pp. 149–154, 2022. SCOPUS, IF:1.46

Book chapter:

1. Rajaiah K., Tiwari P., Manjula R., Thakur N., Kappen M. J., Umesh S. B., Selvaraj P., Nirmala S., Pradhan S., Venkatappa Rao T., Kalpana Arvind P., Sriram K. V., Laxmi Prasad A. S. and Upadhya P. C., "**"Coherent Population Trapping Based Atomic Sensors for Space Application",** Book chapter, In: Advances in Small Satellite Technologies. Lecture Notes in Mechanical Engineering. Springer, Singapore. pp: 247-253 (2020).

Conference papers:

1. Rajaiah K., Manjula R., Tiwari P., Kappen M. J., Biswas S., Pradhan S., T. Venkatappa Rao, Umesh S. B., Kalpana Arvind P., Elumalai S., Sriram K V and Upadhya P C**,** "**CPT Resonance Frequency shift in Rb-Ne Vapor Cell for Application in Atomic Clock**", presented in National Laser Symposium -30 (NLS-30) during January 2022. This paper was selected for ***best paper award***.
2. Rajaiah K, Manjula R, Tiwari P, Kappen M J, Biswas S, Praveen K C, Nirmala S, Pradhan S., Venkatappa Rao T, Umesh S B, Sriram K V and Upadhya P C**,** "**Coherent population trapping in Rubidium vapor cells filled with Ar+$N_2$ buffer gas for application in atomic clock**", presented in OPTIQ-2023 (International conference on Optics, Photonics and Quantum Information). This paper was selected for ***best paper award***.

Papers under preparation (internal review):

1. Rajaiah K, Manamohan K, Nirmala S, Venkatappa Rao T, Hemanth Kumar Reddy N, Upadhya P C, "**Satellite clock characterization for NavIC constellation**"
2. Rajaiah K, Manjula R, Tiwari P, Kappen M J, Biswas S, Praveen K. C., Nirmala S., Pradhan S, Venkatappa Rao T, Umesh S B, Sriram K V and Upadhya P C, "**Characterization of CPT resonance in Rb vapor cells with Ar+$N_2$ buffer gas for application in atomic clock**".

# References


[1] F. Riehle, *Frequency Standards: Basics and Applications*. Wiley, 2003. doi: 10.1002/3527605991.

[2] J. Jespersen and J. Fitz-Randolph, “From sundials to atomic clocks :,” Gaithersburg, MD, 1999. doi: 10.6028/NBS.MONO.155e1999.

[3] M. Kajita, *Measuring Time-Frequency measurements and related developments in physics*. IOP Publishing, 2018. doi: 10.1088/978-0-7503-2124-2.

[4] F. G. Major, *The Quantum Beat-principles and applications of atomic clocks*. New York, NY: Springer New York, 2007. doi: 10.1007/978-0-387-69534-1.

[5] T. N. Bandi, “A Comprehensive Overview of Atomic Clocks and their Applications,” *Biology, Engineering, Medicine and Science Reports*, vol. 9, no. 1, pp. 01–10, Jan. 2023, doi: 10.5530/bems.9.1.1.

[6] L. S. Cutler, “Fifty years of commercial caesium clocks,” *Metrologia*, vol. 42, no. 3, pp. S90–S99, Jun. 2005, doi: 10.1088/0026-1394/42/3/S10.

[7] R. Beard and K. Senior, “Clocks,” in *Springer Handbook of Global Navigation Satellite Systems*, P. J. G. Teunissen and O. Montenbruck, Eds., Cham: Springer International Publishing, 2017, pp. 121–164. doi: 10.1007/978-3-319-42928-1_5.

[8] E. Batori, N. Almat, C. Affolderbach, and G. Mileti, “GNSS-grade space atomic frequency standards: Current status and ongoing developments,” *Advances in Space Research*, vol. 68, no. 12, pp. 4723–4733, Dec. 2021, doi: 10.1016/j.asr.2020.09.012.

[9] T. LINDVALL, M. MERIMAA, I. TITTONEN, and E. IKONEN, “ALL-OPTICAL ATOMIC CLOCK BASED ON DARK STATES OF Rb-85,” in *Frequency Standards and Metrology*, WORLD SCIENTIFIC, May 2002, pp. 183–190. doi: 10.1142/9789812777713_0022.

[10] J. A. Wisnia, “CAFS-A Cesium Atomic Frequency Standard for GPS Block IIR,” in *24th Annual Precise Time and Time Interval Systems and Applications Meeting*, Virginia: ION, Dec. 1992, pp. 199–208.

[11] P. Rochat *et al.*, “The onboard galileo rubidium and passive maser, status & amp; performance,” in *Proceedings of the 2005 IEEE International Frequency Control Symposium and Exposition, 2005.*, IEEE, 2005, pp. 26–32. doi: 10.1109/FREQ.2005.1573898.

[12] B. L. S. Marlow and D. R. Scherer, “A Review of Commercial and Emerging Atomic Frequency Standards,” *IEEE Trans Ultrason Ferroelectr Freq Control*, vol. 68, no. 6, pp. 2007–2022, Jun. 2021, doi: 10.1109/TUFFC.2021.3049713.

[13] John R. Vig, “Quartz Crystal Resonators and Oscillators for Frequency Control and Timing Applications - A Tutorial.” 2004 IEEE International Frequency Control Symposium Tutorials, May 2004.

[14] “IEEE Standard Definitions of Physical Quantities for Fundamental Frequency and Time Metrology-Random Instabilities,” *IEEE Std 1139-1999*, pp. 1–40, 1999, doi: 10.1109/IEEESTD.1999.90575.

[15] J. A. Barnes *et al.*, “Characterization of Frequency Stability,” *IEEE Trans Instrum Meas*, vol. IM–20, no. 2, pp. 105–120, May 1971, doi: 10.1109/TIM.1971.5570702.

[16] Riley W. J., *Handbook of Frequency Stability Analysis*. 2008.

[17] E. Rubiola, *Phase Noise and Frequency Stability in Oscillators*. Cambridge University Press, 2008. doi: 10.1017/CBO9780511812798.

[18] D. Sullivan, D. Allan, D. Howe, and F. L. Walls, “Characterization of Clocks and Oscillators,” *NASA STI/Recon Technical Report N*, vol. 1337, Nov. 1990.

[19] D. W. Allan, “Time and Frequency (Time-Domain) Characterization, Estimation, and Prediction of Precision Clocks and Oscillators,” *IEEE Trans Ultrason Ferroelectr Freq Control*, vol. 34, no. 6, pp. 647–654, Nov. 1987, doi: 10.1109/T-UFFC.1987.26997.

[20] D. W. Allan, “Statistics of atomic frequency standards,” *Proceedings of the IEEE*, vol. 54, no. 2, pp. 221–230, 1966, doi: 10.1109/PROC.1966.4634.

[21] D. W. Allan, “Should the classical variance be used as a basic measure in standards metrology?,” *IEEE Trans Instrum Meas*, vol. IM–36, no. 2, pp. 646–654, Jun. 1987, doi: 10.1109/TIM.1987.6312761.

[22] J. Mcgee and D. Howe, “TheoH and allan deviation as power-law noise estimators,” *IEEE Trans Ultrason Ferroelectr Freq Control*, vol. 54, no. 2, pp. 448–452, Feb. 2007, doi: 10.1109/TUFFC.2007.260.

[23] D. Calero and E. Fernandez, “Characterization of Chip-Scale Atomic Clock for GNSS navigation solutions,” in *2015 International Association of Institutes of Navigation World Congress (IAIN)*, IEEE, Oct. 2015, pp. 1–8. doi: 10.1109/IAIN.2015.7352264.

[24] D. W. Allan and J. A. Barnes, “A Modified ‘Allan Variance’ with Increased Oscillator Characterization Ability,” in *Thirty Fifth Annual Frequency Control Symposium*, IEEE, 1981, pp. 470–475. doi: 10.1109/FREQ.1981.200514.

[25] R. A. Baugh, “Frequency Modulation Analysis with the Hadamard Variance,” in *25th Annual Symposium on Frequency Control*, IEEE, 1971, pp. 222–225. doi: 10.1109/FREQ.1971.199860.

[26] S. Hutsell, “Relating the Hadamard Variance to MCS Kalman Filter Clock Estimation,” 1995. [Online]. Available: https://api.semanticscholar.org/CorpusID:84181602

[27] S. Hutsell, W. Reid, J. Crum, H. Mobbs, and J. Buisson, “Operational Use of the Hadamard Variance in GPS,” p. 15, Nov. 1996.

[28] L. Galleani and P. Tavella, “The characterization of clock behavior with the Dynamic Allan Variance,” in *IEEE International Frequency Control Sympposium and PDA Exhibition Jointly with the 17th European Frequency and Time Forum, 2003. Proceedings of the 2003*, IEEE, pp. 239–244. doi: 10.1109/FREQ.2003.1275096.

[29] L. Galleani and P. Tavella, “Tracking nonstationarities in clock noises using the dynamic allan variance,” in *Proceedings of the 2005 IEEE International Frequency Control Symposium and Exposition, 2005.*, IEEE, pp. 392–396. doi: 10.1109/FREQ.2005.1573964.

[30] I. Sesia, L. Galleani, and P. Tavella, “Implementation of the dynamic Allan variance for the Galileo System Test Bed V2,” in *2007 IEEE International Frequency Control Symposium Joint with the 21st European Frequency and Time Forum*, IEEE, May 2007, pp. 946–949. doi: 10.1109/FREQ.2007.4319219.

[31] I. Sesia, L. Galleani, and P. Tavella, “Application of the Dynamic Allan Variance for the Characterization of Space Clock Behavior,” *IEEE Trans Aerosp Electron Syst*, vol. 47, no. 2, pp. 884–895, Apr. 2011, doi: 10.1109/TAES.2011.5751232.

[32] L. Galleani and P. Tavella, “Identifying Nonstationary Clock Noises in Navigation Systems,” *International Journal of Navigation and Observation*, vol. 2008, pp. 1–5, Apr. 2008, doi: 10.1155/2008/524317.

[33] L. Galleani, “The dynamic Allan variance II: a fast computational algorithm,” *IEEE Trans Ultrason Ferroelectr Freq Control*, vol. 57, no. 1, pp. 182–188, Jan. 2010, doi: 10.1109/TUFFC.2010.1396.

[34] D. A. Howe, R. L. Beard, C. A. Greenhall, F. Vernotte, W. J. Riley, and T. K. Peppler, “Enhancements to GPS operations and clock evaluations using a ‘total’ Hadamard deviation,” *IEEE Trans Ultrason Ferroelectr Freq Control*, vol. 52, no. 8, pp. 1253–1261, Aug. 2005, doi: 10.1109/TUFFC.2005.1509784.

[35] W. J. Riley and C. A. Greenhal, “Power law noise identification using the lag 1 autocorrelation,” in *18th European Frequency and Time Forum (EFTF 2004)*, IEE, 2004, pp. 576–580. doi: 10.1049/cp:20040932.

[36] Q. Ai, Y. Yuan, T. Xu, and B. Zhang, “Time and frequency characterization of GLONASS and Galileo on-board clocks,” *Meas Sci Technol*, vol. 31, no. 6, p. 065003, Jun. 2020, doi: 10.1088/1361-6501/ab69d3.

[37] J. Levine, “The history of time and frequency from antiquity to the present day,” *The European Physical Journal H*, vol. 41, no. 1, pp. 1–67, Apr. 2016, doi: 10.1140/epjh/e2016-70004-3.

[38] J. Sanz Subirana, J.M. Juan Zornoza, and M. Hernández-Pajares, *GNSS Data Processing, Vol. I: Fundamentals and Algorithms*. ESA Communications, 2013.

[39] Pratap Misra and Per Enge, *Global Positioning System: Signals, Measurements, and Performance*, 2nd ed. Gnaga-Jamuna, 2011.

[40] US Air Force, “Navstar GPS Space Segment/Navigation User Segment Interfaces, Interface Specification, IS-GPS-200H,” 2013.

[41] J. Saastamoinen, “Atmospheric Correction for the Troposphere and Stratosphere in Radio Ranging Satellites,” 2013, pp. 247–251. doi: 10.1029/GM015p0247.

[42] J. W. Marini, “Correction of Satellite Tracking Data for an Arbitrary Tropospheric Profile,” *Radio Sci*, vol. 7, no. 2, pp. 223–231, Feb. 1972, doi: 10.1029/RS007i002p00223.

[43] V. B. Mendes and E. C. Pavlis, “High-accuracy zenith delay prediction at optical wavelengths,” *Geophys Res Lett*, vol. 31, no. 14, Jul. 2004, doi: 10.1029/2004GL020308.

[44] Kaplan Elliot and Hegarty Christopher, *Understanding GPS: Principles and Applications*. Artech House, 2006.

[45] R. B. Langley, P. J. G. Teunissen, and O. Montenbruck, “Introduction to GNSS,” in *Springer Handbook of Global Navigation Satellite Systems*, Cham: Springer International Publishing, 2017, pp. 3–23. doi: 10.1007/978-3-319-42928-1_1.

[46] M. Merimaa, T. Lindvall, I. Tittonen, and E. Ikonen, “All-optical atomic clock based on coherent population trapping in 85Rb,” *J. Opt. Soc. Am. B*, vol. 20, no. 2, pp. 273–279, Feb. 2003, doi: 10.1364/JOSAB.20.000273.

[47] J. Kitching, S. Knappe, M. Vukicevic, L. Hollberg, R. Wynands, and W. Weidmann, “A microwave frequency reference based on VCSEL-driven dark line resonances in Cs vapor,” *IEEE Trans Instrum Meas*, vol. 49, no. 6, pp. 1313–1317, 2000, doi: 10.1109/19.893276.

[48] J. Vanier, “Atomic clocks based on coherent population trapping: a review,” *Applied Physics B*, vol. 81, no. 4, pp. 421–442, Aug. 2005, doi: 10.1007/s00340-005-1905-3.

[49] G. Alzetta, A. Gozzini, L. Moi, and G. Orriols, “An experimental method for the observation of r.f. transitions and laser beat resonances in oriented Na vapour,” *Il Nuovo Cimento B Series 11*, vol. 36, no. 1, pp. 5–20, Nov. 1976, doi: 10.1007/BF02749417.

[50] Daniel A. Steck, *Rubidium 87 D Line Data*, Revision 2.3.3. 2023. Accessed: Nov. 19, 2023. [Online]. Available: https://steck.us/alkalidata/rubidium87numbers.pdf

[51] M. Stähler *et al.*, “Coherent population trapping resonances in thermal ^85Rb vapor: D1 versus D2 line excitation,” *Opt Lett*, vol. 27, no. 16, p. 1472, Aug. 2002, doi: 10.1364/OL.27.001472.

[52] E. Arimondo, “Relaxation processes in coherent-population trapping,” *Phys Rev A (Coll Park)*, vol. 54, no. 3, pp. 2216–2223, Sep. 1996, doi: 10.1103/PhysRevA.54.2216.

[53] V. Shah and J. Kitching, “Advances in Coherent Population Trapping for Atomic Clocks,” 2010, pp. 21–74. doi: 10.1016/S1049-250X(10)59002-5.

[54] S. Pradhan, A. Kani, H. Wanare, R. Behera, and A. K. Das, “Nonlinear magneto-optic and self-polarization rotation by superposition of states,” *Phys Rev A (Coll Park)*, vol. 85, no. 6, p. 063805, Jun. 2012, doi: 10.1103/PhysRevA.85.063805.

[55] S. Pradhan, A. Kani, H. Wanare, S. Mishra, and A. K. Das, “Magic frequency enabled by quantum interference for a dual atomic device,” *Journal of Physics B: Atomic, Molecular and Optical Physics*, vol. 48, no. 7, Apr. 2015, doi: 10.1088/0953-4075/48/7/075502.

[56] M. Zhu, “High contrast signal in a coherent population trapping based atomic frequency standard application,” in *IEEE International Frequency Control Sympposium and PDA Exhibition Jointly with the 17th European Frequency and Time Forum, 2003. Proceedings of the 2003*, IEEE, pp. 16–21. doi: 10.1109/FREQ.2003.1274978.

[57] E. Arimondo, “V Coherent Population Trapping in Laser Spectroscopy,” 1996, pp. 257–354. doi: 10.1016/S0079-6638(08)70531-6.

[58] S. Knappe, R. Wynands, J. Kitching, H. G. Robinson, and L. Hollberg, “Characterization of coherent population-trapping resonances as atomic frequency references,” *Journal of the Optical Society of America B*, vol. 18, no. 11, p. 1545, Nov. 2001, doi: 10.1364/JOSAB.18.001545.

[59] J. Vanier, A. Godone, and F. Levi, “Coherent population trapping in cesium: Dark lines and coherent microwave emission,” *Phys Rev A (Coll Park)*, vol. 58, no. 3, pp. 2345–2358, Sep. 1998, doi: 10.1103/PhysRevA.58.2345.

[60] J. Vanier, M. W. Levine, D. Janssen, and M. J. Delaney, “On the use of intensity optical pumping and coherent population trapping techniques in the implementation of atomic

frequency standards," *IEEE Trans Instrum Meas*, vol. 52, no. 3, pp. 822–831, Jun. 2003, doi: 10.1109/TIM.2003.814687.

[61] S. Micalizio, A. Godone, F. Levi, and J. Vanier, "Spin-exchange frequency shift in alkali-metal-vapor cell frequency standards," *Phys Rev A*, vol. 73, no. 3, 2006, doi: 10.1103/PhysRevA.73.033414.

[62] R. Boudot *et al.*, "Coherent population trapping resonances in Cs-Ne vapor microcells for miniature clocks applications," *J Appl Phys*, vol. 109, no. 1, Jan. 2011, doi: 10.1063/1.3530951.

[63] J. Vanier and C. Audoin, *The Quantum Physics of Atomic Frequency Standards*. CRC Press, 1989. doi: 10.1201/9781003041085.

[64] S. E. Harris, "Electromagnetically Induced Transparency," *Phys Today*, vol. 50, no. 7, pp. 36–42, Jul. 1997, doi: 10.1063/1.881806.

[65] M. Fleischhauer, A. Imamoglu, and J. P. Marangos, "Electromagnetically induced transparency: Optics in coherent media," *Rev Mod Phys*, vol. 77, no. 2, pp. 633–673, Jul. 2005, doi: 10.1103/RevModPhys.77.633.

[66] S. Khan, M. P. Kumar, V. Bharti, and V. Natarajan, "Coherent population trapping (CPT) versus electromagnetically induced transparency (EIT)," *The European Physical Journal D*, vol. 71, no. 2, p. 38, Feb. 2017, doi: 10.1140/epjd/e2017-70676-x.

[67] R. Finkelstein, S. Bali, O. Firstenberg, and I. Novikova, "A practical guide to electromagnetically induced transparency in atomic vapor," *New J Phys*, vol. 25, no. 3, p. 035001, Mar. 2023, doi: 10.1088/1367-2630/acbc40.

[68] H. Lee, M. Fleischhauer, and M. O. Scully, "Sensitive detection of magnetic fields including their orientation with a magnetometer based on atomic phase coherence," *Phys Rev A (Coll Park)*, vol. 58, no. 3, pp. 2587–2595, Sep. 1998, doi: 10.1103/PhysRevA.58.2587.

[69] K. Cox, V. I. Yudin, A. V. Taichenachev, I. Novikova, and E. E. Mikhailov, "Measurements of the magnetic field vector using multiple electromagnetically induced transparency resonances in Rb vapor," *Phys Rev A (Coll Park)*, vol. 83, no. 1, p. 015801, Jan. 2011, doi: 10.1103/PhysRevA.83.015801.

[70] R. G. Beausoleil, W. J. Munro, D. A. Rodrigues, and T. P. Spiller, "Applications of electromagnetically induced transparency to quantum information processing," *J Mod Opt*, vol. 51, no. 16–18, pp. 2441–2448, Nov. 2004, doi: 10.1080/09500340408231802.

[71] L. Ma, O. Slattery, and X. Tang, “Optical quantum memory based on electromagnetically induced transparency,” *Journal of Optics*, vol. 19, no. 4, p. 043001, Apr. 2017, doi: 10.1088/2040-8986/19/4/043001.

[72] D. Budker, D. F. Kimball, S. M. Rochester, and V. V. Yashchuk, “Nonlinear Magneto-optics and Reduced Group Velocity of Light in Atomic Vapor with Slow Ground State Relaxation,” *Phys Rev Lett*, vol. 83, no. 9, pp. 1767–1770, Aug. 1999, doi: 10.1103/PhysRevLett.83.1767.

[73] D. F. Phillips, A. Fleischhauer, A. Mair, R. L. Walsworth, and M. D. Lukin, “Storage of Light in Atomic Vapor,” *Phys Rev Lett*, vol. 86, no. 5, pp. 783–786, Jan. 2001, doi: 10.1103/PhysRevLett.86.783.

[74] S.-W. Su, Y.-H. Chen, S.-C. Gou, T.-L. Horng, and I. A. Yu, “Dynamics of slow light and light storage in a Doppler-broadened electromagnetically-induced-transparency medium: A numerical approach,” *Phys Rev A (Coll Park)*, vol. 83, no. 1, p. 013827, Jan. 2011, doi: 10.1103/PhysRevA.83.013827.

[75] B. D. Clader, S. M. Hendrickson, R. M. Camacho, and B. C. Jacobs, “All-optical microdisk switch using EIT,” *Opt Express*, vol. 21, no. 5, p. 6169, Mar. 2013, doi: 10.1364/OE.21.006169.

[76] N. Castagna, R. Boudot, S. Guérandel, E. De Clercq, N. Dimarcq, and A. Clairon, “Investigations on continuous and pulsed interrogation for a CPT atomic clock,” *IEEE Trans Ultrason Ferroelectr Freq Control*, vol. 56, no. 2, pp. 246–253, Feb. 2009, doi: 10.1109/TUFFC.2009.1033.

[77] A. Nagel *et al.*, “Experimental realization of coherent dark-state magnetometers,” *Europhysics Letters (EPL)*, vol. 44, no. 1, pp. 31–36, Oct. 1998, doi: 10.1209/epl/i1998-00430-0.

[78] P. D. D. Schwindt *et al.*, “Chip-scale atomic magnetometer,” *Appl Phys Lett*, vol. 85, no. 26, pp. 6409–6411, Dec. 2004, doi: 10.1063/1.1839274.

[79] J. Belfi, G. Bevilacqua, V. Biancalana, Y. Dancheva, and L. Moi, “All optical sensor for automated magnetometry based on coherent population trapping,” *Journal of the Optical Society of America B*, vol. 24, no. 7, p. 1482, Jul. 2007, doi: 10.1364/JOSAB.24.001482.

[80] J. Kitching, “Chip-scale atomic devices,” *Appl Phys Rev*, vol. 5, no. 3, p. 031302, Sep. 2018, doi: 10.1063/1.5026238.

[81] A. Aspect, E. Arimondo, R. Kaiser, N. Vansteenkiste, and C. Cohen-Tannoudji, “Laser Cooling below the One-Photon Recoil Energy by Velocity-Selective Coherent Population

Trapping," *Phys Rev Lett*, vol. 61, no. 7, pp. 826–829, Aug. 1988, doi: 10.1103/PhysRevLett.61.826.

[82] A. V. Taichenachev, A. M. Tumaikin, and V. I. Yudin, "Quantum theory of cooling of atoms below the one-photon recoil energy by a pulsed field," *Journal of Experimental and Theoretical Physics Letters*, vol. 65, no. 10, pp. 779–784, May 1997, doi: 10.1134/1.567426.

[83] M. Fleischhauer and M. D. Lukin, "Dark-State Polaritons in Electromagnetically Induced Transparency," *Phys Rev Lett*, vol. 84, no. 22, pp. 5094–5097, May 2000, doi: 10.1103/PhysRevLett.84.5094.

[84] R. Wynands and A. Nagel, "Precision spectroscopy with coherent dark states," *Appl Phys B*, vol. 68, no. 1, pp. 1–25, Jan. 1999, doi: 10.1007/s003400050581.

[85] M. A. Hafiz and R. Boudot, "A coherent population trapping Cs vapor cell atomic clock based on push-pull optical pumping," *J Appl Phys*, vol. 118, no. 12, p. 124903, 2015.

[86] Z. Warren, M. S. Shahriar, R. Tripathi, and G. S. Pati, "Experimental and theoretical comparison of different optical excitation schemes for a compact coherent population trapping Rb vapor clock," *Metrologia*, vol. 54, no. 4, pp. 418–431, Aug. 2017, doi: 10.1088/1681-7575/aa72bb.

[87] J. Vanier, M. W. Levine, D. Janssen, and M. Delaney, "Contrast and linewidth of the coherent population trapping transmission hyperfine resonance line in [Formula Presented] Effect of optical pumping," *Phys Rev A*, vol. 67, no. 6, p. 4, 2003, doi: 10.1103/PhysRevA.67.065801.

[88] A. Godone, F. Levi, S. Micalizio, and J. Vanier, "Dark-line in optically-thick vapors: Inversion phenomena and line width narrowing," *European Physical Journal D*, vol. 18, no. 1, pp. 5–13, 2002, doi: 10.1140/e10053-002-0001-z.

[89] ARFKEN GEORGE, *Mathematical Methods for Physicists*, 3rd ed. Academic Press, 1985.

[90] D. Miletic, C. Affolderbach, M. Hasegawa, R. Boudot, C. Gorecki, and G. Mileti, "AC Stark-shift in CPT-based Cs miniature atomic clocks," *Applied Physics B*, vol. 109, no. 1, pp. 89–97, Oct. 2012, doi: 10.1007/s00340-012-5121-7.

[91] J. Vanier, M. W. Levine, D. Janssen, and M. J. Delaney, "The coherent population trapping passive frequency standard," *IEEE Trans Instrum Meas*, vol. 52, no. 2, pp. 258–262, Apr. 2003, doi: 10.1109/TIM.2003.810005.

[92] S. Knappe, J. Kitching, L. Hollberg, and R. Wynands, "Temperature dependence of coherent population trapping resonances," *Appl Phys B*, vol. 74, no. 3, pp. 217–222, Mar. 2002, doi: 10.1007/s003400200800.

[93] D. Jian-Liao, H. Zheng-Feng, H. Hui-Juan, and W. Yu-Zhu, “Temperature Dependence of Dark Lines in Coherent Population Trapping,” *Chinese Physics Letters*, vol. 23, no. 7, pp. 1745–1748, Jul. 2006, doi: 10.1088/0256-307X/23/7/025.

[94] H. S. Moon, S. E. Park, Y.-H. Park, L. Lee, and J. B. Kim, “Passive atomic frequency standard based on coherent population trapping in Rb-87 using injection-locked lasers,” 2006.

[95] F. Levi, A. Godone, and J. Vanier, “The light shift effect in the coherent population trapping cesium maser,” *IEEE Trans Ultrason Ferroelectr Freq Control*, vol. 47, no. 2, pp. 466–470, Mar. 2000, doi: 10.1109/58.827437.

[96] Jinquan Deng, “Light shift compensation in a Rb gas cell frequency standard with two-laser pumping,” *IEEE Trans Ultrason Ferroelectr Freq Control*, vol. 48, no. 6, pp. 1657–1661, Nov. 2001, doi: 10.1109/58.971718.

[97] P. Siddons, C. S. Adams, C. Ge, and I. G. Hughes, “Absolute absorption on rubidium D lines: comparison between theory and experiment,” *Journal of Physics B: Atomic, Molecular and Optical Physics*, vol. 41, no. 15, p. 155004, Aug. 2008, doi: 10.1088/0953-4075/41/15/155004.

[98] J. Vanier, J.-F. Simard, and J.-S. Boulanger, “Relaxation and frequency shifts in the ground state of Rb-85,” *Phys Rev A (Coll Park)*, vol. 9, no. 3, pp. 1031–1040, Mar. 1974, doi: 10.1103/PhysRevA.9.1031.

[99] E. Kuchina, E. E. Mikhailov, and I. Novikova, “Effect of atomic diffusion on the Raman–Ramsey coherent population trapping resonances,” *Journal of the Optical Society of America B*, vol. 33, no. 4, p. 610, Apr. 2016, doi: 10.1364/JOSAB.33.000610.

[100] O. Kozlova, S. Guérandel, and E. De Clercq, “Temperature and pressure shift of the Cs clock transition in the presence of buffer gases: Ne, N2, Ar,” *Phys Rev A*, vol. 83, no. 6, Jun. 2011, doi: 10.1103/PhysRevA.83.062714.

[101] K. Deng *et al.*, “Effect of buffer gas ratios on the relationship between cell temperature and frequency shifts of the coherent population trapping resonance,” *Appl Phys Lett*, vol. 92, no. 21, 2008, doi: 10.1063/1.2937407.

[102] J. Vanier, R. Kunski, N. Cyr, J. Y. Savard, and M. Têtu, “On hyperfine frequency shifts caused by buffer gases: Application to the optically pumped passive rubidium frequency standard,” *J Appl Phys*, vol. 53, no. 8, pp. 5387–5391, 1982, doi: 10.1063/1.331467.

[103] V. Shah, P. D. Schwindt, V. Gerginov, S. Knappe, L. Hollberg, and J. Kitching, “Active light shift stabilization in modulated CPT clocks.,” in *2006 IEEE International Frequency*

*Control Symposium and Exposition*, IEEE, Jun. 2006, pp. 699–701. doi: 10.1109/FREQ.2006.275473.

[104] D. Radnatarov, S. Kobtsev, V. Andryushkov, S. Khripunov, E. Baklanov, and A. Yakovlev, "Properties of Rb CPT Atomic Clock at Subharmonic Microwave Modulation Frequencies," *IEEE Photonics J*, vol. 11, no. 4, pp. 1–11, Aug. 2019, doi: 10.1109/JPHOT.2019.2925012.

[105] Y. Li, K. Deng, Q. Meng, D. Shi, X. Chen, and Z. Wang, "Temperature compensation via RF power adjusting in Chip Scale Atomic Clocks," in *2011 Joint Conference of the IEEE International Frequency Control and the European Frequency and Time Forum (FCS) Proceedings*, IEEE, May 2011, pp. 1–4. doi: 10.1109/FCS.2011.5977802.

[106] R. Boudot, S. Guerandel, E. de Clercq, N. Dimarcq, and A. Clairon, "Current Status of a Pulsed CPT Cs Cell Clock," *IEEE Trans Instrum Meas*, vol. 58, no. 4, pp. 1217–1222, Apr. 2009, doi: 10.1109/TIM.2008.2009918.

[107] J.-M. Danet, O. Kozlova, P. Yun, S. Guérande, and E. de Clercq, "Compact atomic clock prototype based on coherent population trapping," *EPJ Web Conf*, vol. 77, p. 00017, Aug. 2014, doi: 10.1051/epjconf/20147700017.

[108] S. H. Yim, S.-B. Lee, T. Y. Kwon, K. M. Shim, and S. E. Park, "Optical phase-locking of two extended-cavity diode lasers by serrodyne modulation," *Appl Opt*, vol. 58, no. 10, p. 2481, Apr. 2019, doi: 10.1364/AO.58.002481.

[109] X. Liu, J.-M. Mérolla, S. Guérandel, C. Gorecki, E. de Clercq, and R. Boudot, "Coherent-population-trapping resonances in buffer-gas-filled Cs-vapor cells with push-pull optical pumping," *Phys Rev A (Coll Park)*, vol. 87, no. 1, p. 013416, Jan. 2013, doi: 10.1103/PhysRevA.87.013416.

[110] C. Affolderbach, A. Nagel, S. Knappe, C. Jung, D. Wiedenmann, and R. Wynands, "Nonlinear spectroscopy with a vertical-cavity surface-emitting laser (VCSEL)," *Appl Phys B*, vol. 70, no. 3, pp. 407–413, Mar. 2000, doi: 10.1007/s003400050066.

[111] N. Cyr, M. Tctu, and M. Breton, "All-Optical Microwave Frequency Standard: A Proposal," 1993.

[112] P. Tiwari *et al.*, "Atomic Frequency Standard based on Coherent Population Trapping in Rb-87 Atoms for Space Application," in *2019 URSI Asia-Pacific Radio Science Conference (AP-RASC)*, IEEE, Mar. 2019, pp. 1–1. doi: 10.23919/URSIAP-RASC.2019.8738229.

[113] J. Vanier, "Atomic clocks based on coherent population trapping: A review," *Applied Physics B: Lasers and Optics*, vol. 81, no. 4. pp. 421–442, Aug. 2005. doi: 10.1007/s00340-005-1905-3.

[114] M. Ellmeier *et al.*, “Frequency shift compensation for single and dual laser beam pass sensors of a coherent population trapping resonance based coupled dark state magnetometer,” *Measurement: Sensors*, vol. 25, p. 100606, Feb. 2023, doi: 10.1016/j.measen.2022.100606.

[115] R. Manjula, T. Pragya, T. Nikhil, M. Madan Mohan, R. Bijay, and U. Prashanth, “Development of Precision Atomic Optical Systems,” Aug. 2019.

[116] B. Weigl *et al.*, “High-performance oxide-confined GaAs VCSELs,” *IEEE Journal of Selected Topics in Quantum Electronics*, vol. 3, no. 2, pp. 409–415, Apr. 1997, doi: 10.1109/2944.605686.

[117] V. Jain, M. C. Biesinger, and M. R. Linford, “The Gaussian-Lorentzian Sum, Product, and Convolution (Voigt) functions in the context of peak fitting X-ray photoelectron spectroscopy (XPS) narrow scans,” *Appl Surf Sci*, vol. 447, pp. 548–553, Jul. 2018, doi: 10.1016/j.apsusc.2018.03.190.

[118] G. H. Major, V. Fernandez, N. Fairley, and M. R. Linford, “A detailed view of the Gaussian–Lorentzian sum and product functions and their comparison with the Voigt function,” *Surface and Interface Analysis*, vol. 54, no. 3, pp. 262–269, Mar. 2022, doi: 10.1002/sia.7050.

[119] Byron D. Tapley, Bob E. Schutz, and George H. Born, *Statistical Orbit Determination*. Elsevier, 2004. doi: 10.1016/B978-0-12-683630-1.X5019-X.

[120] S. Micalizio and A. Godone, “Raman-Ramsey resonances in atomic vapor cells: Rabi pulling and optical-density effects,” *Phys Rev A (Coll Park)*, vol. 99, no. 4, p. 043425, Apr. 2019, doi: 10.1103/PhysRevA.99.043425.

[121] P. Yun *et al.*, “High-performance coherent population trapping clock with polarization modulation,” Oct. 2016, doi: 10.1103/PhysRevApplied.7.014018.

[122] R. Boudot *et al.*, “A high-performance frequency stability compact CPT clock based on a Cs-Ne microcell,” *IEEE Transactions on Ultrasonics, Ferroelectrics, and Frequency Control*, vol. 59, no. 11. pp. 2584–2587, 2012. doi: 10.1109/TUFFC.2012.2493.

[123] I. Al-Nahhal, O. A. Dobre, E. Basar, C. Moloney, and S. Ikki, “A Fast, Accurate, and Separable Method for Fitting a Gaussian Function [Tips & Tricks],” *IEEE Signal Process Mag*, vol. 36, no. 6, pp. 157–163, Nov. 2019, doi: 10.1109/MSP.2019.2927685.

[124] O. Kozlova, J. M. Danet, S. Guerandel, and E. De Clercq, “Limitations of long-term stability in a coherent population trapping Cs Clock,” *IEEE Trans Instrum Meas*, vol. 63, no. 7, pp. 1863–1870, 2014, doi: 10.1109/TIM.2014.2298672.

[125] D. S. Chuchelov *et al.*, “Study of factors affecting the light shift of the CPT resonance,” *J Phys Conf Ser*, vol. 1686, no. 1, p. 012029, Dec. 2020, doi: 10.1088/1742-6596/1686/1/012029.

[126] A. Cernigliaro and I. Sesia, “Satellite clocks characterization and monitoring for global navigation satellite systems,” in *2011 XXXth URSI General Assembly and Scientific Symposium*, IEEE, Aug. 2011, pp. 1–4. doi: 10.1109/URSIGASS.2011.6050279.

[127] A. Cernigliaro and I. Sesia, “INRIM tool for satellite clock characterization in GNSS,” in *2012 European Frequency and Time Forum*, IEEE, Apr. 2012, pp. 133–135. doi: 10.1109/EFTF.2012.6502350.

[128] K. Rajaiah, K. Manamohan, S. Nirmala, and S. C. Ratnakara, “Modified empirical Solar Radiation Pressure model for IRNSS constellation,” *Advances in Space Research*, vol. 60, no. 10, pp. 2146–2154, Nov. 2017, doi: 10.1016/j.asr.2017.08.020.

[129] A. S. Ganeshan, S. C. Ratnakara, S. Nirmala, R. Babu, T. Neetha, and A. Kartik, “‘Successful proof of concept demonstration First Position Fix with IRNSS,’” *Inside GNSS*, pp. 48–52, Aug. 2015.

[130] S. Kogure, A. S. Ganeshan, and O. Montenbruck, “Regional Systems,” in *Springer Handbook of Global Navigation Satellite Systems*, Cham: Springer International Publishing, 2017, pp. 305–337. doi: 10.1007/978-3-319-42928-1_11.

[131] K. Rajaiah, K. Manamohan, and S. Nirmala, “‘IRNSS/NavIC on-board time synchronization with ground reference time,’” *Journal of Spacecraft Technology*, vol. 31, no. 2, pp. 01–05, 2020.

[132] D. Durga, A. Rajat, K. Vijay V., K. Gopichand, M. Sanjay D., and R. T.V.S., “Design, Implementation and Realization of Navigation Signal Generation Unit for IRNSS Payload,” *Journal of Spacecraft Technology*, vol. 21, no. 2, pp. 25–29, Jul. 2011.

[133] ISRO, “Indian Regional Navigation Satellite System, Signal In Space ICD for Standard Positioning Service,” *U R Rao Satellite Centre*, vol. 1, no. 2, 2017.

[134] H. Zhang, S. Ji, Z. Wang, and W. Chen, “Detailed assessment of GNSS observation noise based using zero baseline data,” *Advances in Space Research*, vol. 62, no. 9, pp. 2454–2466, Nov. 2018, doi: 10.1016/j.asr.2018.07.023.

[135] R. Hatch, “‘The synergism of GPS code and carrier measurements,’” in *Proceedings of 3rd International Geodetic Symposium on Satellite Doppler Positioning*, New Mexico State University, 1982, pp. 1213–1231.

[136] Q. Zhang, Z. Chen, F. Rong, and Y. Cui, “An improved Hatch filter and its application in kinematic positioning with single-frequency GPS,” *Measurement*, vol. 146, pp. 868–878, Nov. 2019, doi: 10.1016/j.measurement.2019.07.030.

[137] J.-H. Won and T. Pany, “Signal Processing,” in *Springer Handbook of Global Navigation Satellite Systems*, Cham: Springer International Publishing, 2017, pp. 401–442. doi: 10.1007/978-3-319-42928-1_14.

[138] G. Xu and Y. Xu, “Cycle Slip Detection and Ambiguity Resolution,” in *GPS*, Berlin, Heidelberg: Springer Berlin Heidelberg, 2016, pp. 229–261. doi: 10.1007/978-3-662-50367-6_8.

[139] G. HUO and L. MIAO, “Cycle-slip Detection of GPS Carrier Phase with Methodology of SA4 Multi-wavelet Transform,” *Chinese Journal of Aeronautics*, vol. 25, no. 2, pp. 227–235, Apr. 2012, doi: 10.1016/S1000-9361(11)60382-8.

[140] X. Tu and Z. Lei, “Cycle-slip detection and correction of GPS single-frequency carrier phase based on wavelet transform and LS-SVM,” *The Journal of Engineering*, vol. 2019, no. 20, pp. 6995–6999, Oct. 2019, doi: 10.1049/joe.2019.0525.

[141] R. B. Langley, P. J. G. Teunissen, and O. Montenbruck, “Introduction to GNSS,” in *Springer Handbook of Global Navigation Satellite Systems*, Cham: Springer International Publishing, 2017, pp. 3–23. doi: 10.1007/978-3-319-42928-1_1.

[142] G. Xu and Y. Xu, “GPS Observables,” in *GPS*, Berlin, Heidelberg: Springer Berlin Heidelberg, 2016, pp. 55–61. doi: 10.1007/978-3-662-50367-6_4.

[143] G. A. Zhbankov, N. P. Danilkin, and O. A. Maltseva, “Influence of the ionosphere on the accuracy of the satellite navigation system,” *Acta Astronaut*, vol. 190, pp. 194–201, Jan. 2022, doi: 10.1016/j.actaastro.2021.10.004.

[144] A. Rovira-Garcia, D. Ibáñez-Segura, R. Orús-Perez, J. M. Juan, J. Sanz, and G. González-Casado, “Assessing the quality of ionospheric models through GNSS positioning error: methodology and results,” *GPS Solutions*, vol. 24, no. 1, p. 4, Jan. 2020, doi: 10.1007/s10291-019-0918-z.

[145] Mohinder S. Grewal, Angus P. Andrews, and Chris G. Bartone, “GNSS Measurement Errors,” in *Global Navigation Satellite Systems, Inertial Navigation, and Integration*, Wiley Telecom, 2020, pp. 249–292. doi: 10.1002/9781119547860.ch7.

[146] J. Saastamoinen, “Atmospheric Correction for the Troposphere and Stratosphere in Radio Ranging Satellites,” in *The Use of Artificial Satellites for Geodesy*, vol. 15, 1972, pp. 247–251. doi: 10.1029/GM015p0247.

[147] G. B. Mansur and L. D. D. Ferreira, “ERROR BEHAVIOR OF ATOMIC CLOCKS ABOARD GPS SATELLITES,” *Boletim de Ciências Geodésicas*, vol. 25, no. 4, 2019, doi: 10.1590/s1982-21702019000400027.

[148] L. A. Mallette, J. White, and P. Rochat, “Space qualified frequency sources (clocks) for current and future GNSS applications,” in *IEEE/ION Position, Location and Navigation Symposium*, IEEE, May 2010, pp. 903–908. doi: 10.1109/PLANS.2010.5507225.

[149] C. Liu *et al.*, “Analysis on Factors Influencing Frequency Drift of Rubidium Clocks for Satellite Navigation,” in *China Satellite Navigation Conference (CSNC) 2016 Proceedings*, Springer, 2016, pp. 645–652. doi: 10.1007/978-981-10-0940-2_56.

[150] N. Ashby, “Relativity in the Global Positioning System,” *Living Rev Relativ*, vol. 6, no. 1, p. 1, Dec. 2003, doi: 10.12942/lrr-2003-1.

[151] R. Babu, T. Rethika, and S. C. Rathnakara, “Onboard Atomic Clock Frequency Offset for Indian Regional Navigation Satellite System,” *International Journal of Applied Physics and Mathematics*, pp. 270–272, 2012, doi: 10.7763/IJAPM.2012.V2.109.

[152] C. Chen, G. Chang, S. Zhang, G. Chen, and F. Luo, “New range domain carrier-smoothed code filtering with dual-frequency BDS data,” *Asian J Control*, vol. 21, no. 4, pp. 1496–1505, Jul. 2019, doi: 10.1002/asjc.1996.

[153] B. Park, C. Lim, Y. Yun, E. Kim, and C. Kee, “Optimal Divergence-Free Hatch Filter for GNSS Single-Frequency Measurement,” *Sensors*, vol. 17, no. 3, p. 448, Feb. 2017, doi: 10.3390/s17030448.

[154] Epstein, Marvin, Dass, and Todd, “‘Management of Phase and Frequency for GPS IIR Satellites,’” in *Proceedings of the 33th Annual Precise Time and Time Interval Systems and Applications Meeting*, California, 2001, pp. 481–492.

[155] J. Phelan, T. Dass, G. Freed, J. Rajan, J. D’Agostino, and M. Epstein, “GPS block IIR clocks in space: current performance and plans for the future,” in *Proceedings of the 2005 IEEE International Frequency Control Symposium and Exposition, 2005.*, IEEE, 2005, p. 19. doi: 10.1109/FREQ.2005.1573897.

[156] G. Huang, B. Cui, Q. Zhang, P. Li, and W. Xie, “Switching and performance variations of on-orbit BDS satellite clocks,” *Advances in Space Research*, vol. 63, no. 5, pp. 1681–1696, Mar. 2019, doi: 10.1016/j.asr.2018.10.047.

[157] J. Kudrys, D. Prochniewicz, F. Zhang, M. Jakubiak, and K. Maciuk, “Identification of BDS Satellite Clock Periodic Signals Based on Lomb-Scargle Power Spectrum and Continuous Wavelet Transform,” *Energies (Basel)*, vol. 14, no. 21, p. 7155, Nov. 2021, doi: 10.3390/en14217155.

[158] T. Geng, R. Jiang, Y. Lv, and X. Xie, “Analysis of BDS-3 Onboard Clocks Based on GFZ Precise Clock Products,” *Remote Sens (Basel)*, vol. 14, no. 6, p. 1389, Mar. 2022, doi: 10.3390/rs14061389.